Magnetic and Microwave Properties of Transition Metal Oxide Based Nanostructures

Thesis submitted for the degree of

Doctor of Philosophy (Science)

in

Physics (Experimental)

by

Anupam Gorai

Department of Physics
University of Calcutta
2023

Dedicated to THE Universe……

ABSTRACT

With the massive development of technologies like wireless information transfer, worldwide navigation, and radar (radio detection and ranging) communication, high-frequency electromagnetic radiation is having a detrimental effect on the environment. Therefore, a thorough search is being conducted for microwave absorption materials (MAMs) that are both extremely effective and inexpensive to produce. The efficacy of the solution depends not only on its quality, but also on its price, sustainability, and device portability. A recent study indicates that around 23 percent of engineering research focuses on ferrites, which improves the manufacture of microwave devices and reduces their cost. Ferrites are iron-based ferrimagnetic oxides that possess both magnetic and insulating characteristics. They let electromagnetic (EM) waves to pass through the material and, because to their high dielectric constant, increase dielectric loss, hence expanding the range of applications for high-frequency devices. In this dissertation, the characteristics of nanostructures based on transition metal oxides are examined in depth. With previous knowledge of the excellent microwave absorption qualities of manganese ferrite ($MnFe_2O_4$, MnFO) nanohollowspheres, this material is selected to synthesize bilayer by depositing highly effective materials to improve electromagnetic wave absorption capabilities. Initially, a comparative investigation is conducted to determine the impact of covering MnFO nanohollowspheres (NHSs) with a magnetic ($CoFe_2O4$, CFO) and a nonmagnetic but highly dielectric (SiO_2) material on the electromagnetic characteristics. In order to attain ideal thicknesses at which electromagnetic wave absorption is greatest, the thicknesses of the coated materials are further changed. Detailed investigations suggest that the MnFO@CFO-35 sample with a 35 nm coating thickness of CFO (out of 15 nm, 35 nm, and 50 nm) exhibits a reflection loss (RL) of -66.48 dB (shielding > 99.999 percent) at 6.01 GHz with only 20 wt.% filler concentration in an epoxy matrix and a composite length of 4.46 mm. The MnFO@CFO-35 NHS has an effective total bandwidth of about 1.88 GHz ($RL < -10$ dB). A sample with a coating thickness of 35 nm of SiO_2, MnFO/SiO-35 exhibits RL values as high as -61.02 dB at 11.7 GHz with only a 20 wt.% filler concentration in an epoxy matrix and a composite length of 4.40 mm. Total effective bandwidth ($RL < -10$ dB) for MnFO/SiO-35 NHS becomes 3.10 GHz. It is inferred that the existence of magnetic characteristics in CFO coating as opposed to non-magnetic SiO_2 is the fundamental explanation for the greater reflection loss seen in CFO-coated MnFO NHSs. In addition, it is proven that an optimum layer of CFO on MnFO NHS has enhanced EM wave absorption capabilities significantly. Similarly, a research is conducted on ferroelectric sodium bismuth titanate, $Sr_x(Na_{0.5}Bi_{0.5})_{1-x}TiO_3$, with

different doping concentrations of strontium, SNBT(x*100) ($0.25 \leq x \leq 0.75$), to achieve a high dielectric constant at ambient temperature, which is required for strong microwave absorption. Due to the diamagnetic nature of SNBT materials, a layer of CFO is deposited to increase the microwave absorption through implementation of magnetic parameters. It is observed that the magnitudes of ε'_m, the maximum value of dielectric constant and T_m, the temperature corresponding to ε'_m are decreased with an increase of Sr^{2+} ion in the materials. Investigation of microwave absorption characteristics of the SNBT materials with increasing Sr^{2+} doping concentration demonstrates that SNBT50 (x = 0.5) is a more promising material for microwave applications than the other two SNBT materials with high ferroelectricity at room temperature and a decent permittivity value. The CFO coating applied to SNBT50, SNBT50@CFO, increases the composites' permittivity and adds permeability and magnetic loss. CFO being a good MAM due to its optimal permittivity and permeability properties, due to interfacial polarization, the synergistic effect between the core and shell, and the introduction of magnetic loss in the sample, the electromagnetic absorption properties of SNBT50@CFO composite with a length as short as 2.7 mm exhibit a reflection loss of -20.19 dB with an increased effective absorption bandwidth of 4.56 GHz. In addition, it exhibits a constant attenuation that rises constantly over the observed frequency range. Due to its increased EM wave absorption capabilities and significant ferroelectricity at room temperature, SNBT50@CFO is a particularly attractive alternative for high-frequency multi-disciplinary applications. In the final study, metallic Ni nanoparticles, a soft magnetic material, are coated with CFO, a hard magnetic material to accomplish efficient exchange coupling by effectively synthesizing the core-shell nanostructure. The single-phase nature of the hysteresis loop revealed by the Ni@CFO core-shell structure, together with higher saturation and residual magnetization, and a coercivity with a value between that of Ni and CFO, provides evidence for exchange coupling between the magnetic spins of Ni and CFO. The thickness-dependent electromagnetic wave absorption characteristics of Ni@CFO exchange-coupled core-shell nanostructures and its shell material as a CFO nanoparticle are studied comprehensively. As a consequence of the urchin-like structure of metallic Ni nanoparticles, the real part of dielectric permittivity is enhanced and eddy current loss mostly contributes to the magnetic loss. Ni@CFO core-shell is discovered to have a minimal reflection loss (RL) of -84.01 dB at 9.57 GHz and the overall effective bandwidth measured for $RL < -10$ dB is 6.25 GHz. The outstanding EM wave absorption of Ni@CFO makes it a mass-efficient and economically beneficial EMA material for a number of high-frequency applications.

সারাংশ

বেতার তথ্য স্থানান্তর, বিশ্বব্যাপী নেভিগেশন এবং রাডার (রেডিও সনাক্তকরণ এবং রেঞ্জিং) যোগাযোগের মতো প্রযুক্তির ব্যাপক বিকাশের সাথে, উচ্চ কম্পাঙ্কের তড়িৎচৌম্বকীয় বিকিরণ পরিবেশের উপর ক্ষতিকারক প্রভাব ফেলে। অতএব, অত্যন্ত কার্যকরী উৎপাদনক্ষম এবং স্বল্পমূল্য মাইক্রোতরঙ্গ শোষক পদার্থের (MAMs) একটি পুঙ্খানুপুঙ্খ অনুসন্ধান আবশ্যক। এই সমাধানের কার্যকারিতা শুধুমাত্র এর মানের উপর নয়, এর মূল্য, স্থায়িত্ব এবং যন্ত্রের প্রান্যমাণ যোগ্যতার ওপরও নির্ভর করে। একটি সাম্প্রতিক সমীক্ষা ইঙ্গিত করে যে প্রায় ২৩ শতাংশ প্রকৌশল গবেষণা হয় ফেরাইট যৌগগুলিকে কেন্দ্র করে, যা মাইক্রোতরঙ্গ সমন্বিত যন্ত্রগুলির উৎপাদনকে উন্নত করে এবং তাদের খরচ কমায়। ফেরাইট হল লৌহচুম্বকীয় ফেরিচৌম্বকীয় অক্সাইড যা চৌম্বকীয় এবং অন্তরক উভয় বৈশিষ্ট্যের অধিকারী। এই পদার্থগুলি তড়িৎচৌম্বকীয় তরঙ্গকে নিজেদের মধ্যে গ্রহণ করে এবং এদের উচ্চ অন্তরক ধ্রুবকের কারণে অন্তরক ক্ষয় বৃদ্ধি হয়, ফলে এটি উচ্চ কম্পাঙ্ক সমন্বিত যন্ত্রের ব্যবহারিক পরিসর প্রসারিত করে। এই গবেষণায়, রূপান্তর ধাতব অক্সাইডের উপর ভিত্তি করে ন্যানো গঠনের বৈশিষ্ট্যগুলি গভীরভাবে পরীক্ষা করা হয়েছে। ম্যাঙ্গানিজ ফেরাইটের ($MnFe_2O_4$, MnFO) ন্যানো ফাঁপা গোলকের উৎকৃষ্ট মাইক্রোতরঙ্গ শোষণের গুণাবলীর পূর্ববর্তী জ্ঞানের ওপর ভিত্তি করে এই পদার্থটিকে তড়িৎচৌম্বকীয় তরঙ্গ শোষণ ক্ষমতা আরও উন্নত করার জন্য অত্যন্ত উপযুক্ত পদার্থের প্রলেপ দিয়ে দ্বী-স্তর সংশ্লেষিত করার জন্য নির্বাচন করা হয়েছে। প্রাথমিকভাবে, MnFO ন্যানো ফাঁপা গোলকের (NHS) ওপর তড়িৎচৌম্বকীয় বৈশিষ্ট্যের উপর ভিত্তি করে একটি চৌম্বকীয় ($CoFe_2O_4$, CFO) এবং একটি অচৌম্বকীয় কিন্তু অত্যন্ত অন্তরক (SiO_2) পদার্থ দিয়ে আবরণের প্রভাব নির্ধারণের জন্য একটি তুলনামূলক তদন্ত করা হয়। সর্বোচ্চ তড়িৎচৌম্বকীয় তরঙ্গ শোষণ ক্ষমতার জন্য আদর্শ বেধ পেতে প্রলিপ্ত পদার্থের বেধ আরও পরিবর্তন করা হয়। বিশদ তদন্ত দেখা গেছে যে, একটি ৩৫ ন্যানোমিটার (nm) পুরু CFO (১৫ nm, ৩৫ nm, এবং ৫০ nm এর মধ্যে) এর আবরণ দিয়ে তৈরী MnFO@CFO-৩৫ নমুনাটি ৬.০১ গিগাহার্জ (GHz) কম্পাঙ্কে ইপোক্সি রজনের ছাঁচে মাত্র ২০ শতাংশ পদার্থের মনস্থবিশিষ্ট একটি যৌগিক শোষকের ৪.৪৬ মিলিমিটার এর দৈর্ঘ্যে -৬৬.৪৮ ডেসিবেল (dB) এর মতো প্রতিফলন ক্ষয় (RL) প্রদর্শন করে (রক্ষণ > 99.999 শতাংশ)। MnFO@CFO-৩৫ NHS-এর কার্যকর মোট

ব্যান্ডউইথ প্রায় ১.৮৮ GHz (RL <-১০ dB)। SiO_2 এর ৩৫ nm পুরু আবরণ সহ একটি নমুনা, MnFO@SiO-৩৫ ইপোক্সি রজনের ছাঁচে শুধুমাত্র ২০ শতাংশ পদার্থের ঘনত্ববিশিষ্ট এবং ৪.৪০ মিলিমিটার দীর্ঘ যৌগিক শোষকে ১১.৭ GHz এ RL এর মান -৬১.০২ dB পর্যন্ত প্রদর্শন করে। MnFO@SiO-৩৫ NHS-এর জন্য মোট কার্যকর ব্যান্ডউইথ (RL <-১০ dB) হয় ৩.১০ GHz। অচৌম্বকীয় SiO_2 এর বিরুদ্ধে CFO আবরণের চৌম্বকীয় বৈশিষ্ট্যের অস্তিত্ব CFO প্রলিপ্ত MnFO NHS-এ দেখা ব্যুৎক্রম প্রতিফলন ক্ষয়ের জন্য মৌলিক ব্যাখ্যা হিসেবে অনুমান করা যায়। উপরন্তু, এটি প্রমাণিত হয় যে MnFO NHS-এ CFO-এর একটি যথাযথ স্তর EM তরঙ্গ শোষণ ক্ষমতাকে উল্লেখযোগ্য ভাবে বৃদ্ধি করেছে। একইভাবে, শক্তিশালী মাইক্রোতরঙ্গ শোষণের জন্য প্রয়োজনীয় পরিবেষ্টিত তাপমাত্রায় উচ্চ অন্তরক ধ্রুবক অর্জনের জন্য ফেরোবৈদ্যুতিক সোডিয়াম বিসমাথ টাইটানেট, $Sr_x(Na_{0.5}Bi_{0.5})_{1-x}TiO_3$ এ স্ট্রন্টিয়ামের বিভিন্ন ডোপিং ঘনত্ব যুক্ত SNBT(x*১০০) ($0.২৫ \leq x \leq 0.৭৫$) নিয়ে একটি গবেষণা পরিচালিত হয়, যা । যেহেতু SNBT পদার্থের ডায়াচৌম্বকীয় বৈশিষ্ট্য আছে, তাই এতে চৌম্বকীয় পরামিতি সম্পাদনের মাধ্যমে মাইক্রোতরঙ্গ শোষণ বাড়ানোর জন্য CFO-এর একটি স্তরের প্রলেপ দেওয়া হয়। এটা দেখা যায় যে, অন্তরক ধ্রুবকের সর্বোচ্চ মান ε'_m এবং ε'_m এর সাথে সংশ্লিষ্ট তাপমাত্রা T_m পদার্থে Sr^{2+} আয়নের বৃদ্ধির সাথে হ্রাস পেয়েছে। ক্রমবর্ধমান Sr^{2+} এর ডোপিং ঘনত্বের সাথে SNBT পদার্থগুলির মাইক্রোতরঙ্গ শোষণের বৈশিষ্ট্যের তদন্ত প্রমাণ করে যে মাইক্রোতরঙ্গের ব্যবহারিক বিষয়ে ঘরের তাপমাত্রায় উচ্চ ফেরোবিদ্যুৎ এবং তড়িৎভেদ্যতার উপযুক্ত মান সহ অন্য দুটি SNBT পদার্থের তুলনায় SNBT50 ($x = 0.৫$) একটি বেশি প্রতিশ্রুতিশীল পদার্থ। SNBT৫০ এর উপর CFO এর আবরণ দিয়ে প্রস্তুত করা SNBT৫০@CFO-এ যৌগিক পদার্থটির তড়িৎভেদ্যতা বাড়ায় এবং চৌম্বকপ্রবেশ্যতা ও চৌম্বকীয় ক্ষতি যোগ হয়। CFO এর যথাযথ তড়িৎভেদ্যতা এবং চৌম্বকপ্রবেশ্যতা বৈশিষ্ট্যের কারণে একটা ভালো MAM হওয়ায়, অন্তপৃষ্ঠীয় সমবর্তন, অন্তস্তল ও খোলকের মধ্যে আন্তক্রিয়ার প্রভাব এবং নমুনায় চৌম্বকীয় ক্ষয়ের প্রবর্তনের কারণে ক্ষুদ্র ২.৭ মিলিমিটার দৈর্ঘ্যের যৌগিক পদার্থ SNBT৫০@CFO বর্ধিত কার্যকরী শোষণ ব্যান্ডউইডথ ৪.৫৬ GHz সহ -২০.১৯ dB প্রতিফলন ক্ষয় প্রদর্শন করে। উপরন্তু, এটি পর্যবেক্ষিত বস্পাঙ্কের পরিসরে উপশম ধ্রুবকের ক্রমাগত বৃদ্ধি প্রদর্শন করে যা। এর বর্ধিত EM তরঙ্গ শোষণ ক্ষমতা এবং ঘরের তাপমাত্রায় উল্লেখযোগ্য ফেরোবিদ্যুৎ

যোগ্যতার কারণে, SNBT৫০@CFO উচ্চ কম্পাঙ্কের বিভিন্ন অন্তর্বিষয়িক ব্যবহারিক প্রয়োগের জন্য একটি বিশেষ আকর্ষণীয় বিকল্প। চূড়ান্ত গবেষণায়, কার্যকর বিনিময় সংযোজন সম্পন্ন করার জন্য একটি নরম চৌম্বকীয় পদার্থ ধাতব নিকেল (Ni) ন্যানোকণা কে একটি শক্তি চৌম্বকীয় পদার্থ CFO দিয়ে প্রলিপ্ত করে কার্যকরভাবে অন্তস্তল-খোলক ন্যানোগঠন সংশ্লেষ করা হয়। উচ্চতর সম্পৃক্ত ও অবশিষ্ট চৌম্বকীয়করণ এবং Ni ও CFO এর মাঝামাঝি চৌম্বকীয় বাধ্যকারীতার মান সহ, Ni@CFO অন্তস্তল-খোলক কাঠামো দ্বারা প্রকাশিত হিস্টেরেসিস লুপের একক দশা Ni ও CFO-এর মূর্তির মধ্যে বিনিময় সংযোজনের প্রমাণ দেয়। Ni@CFO বিনিময় সংযোজিত অন্তস্তল- খোলক ন্যানোগঠন এবং খোলক উপাদান হিসেবে CFO ন্যানোকণার পুরুত্ব-নির্ভর তড়িৎচৌম্বকীয় তরঙ্গ শোষণের বৈশিষ্ট্যগুলির গভীরভাবে পরীক্ষা করা হয়। ধাতব Ni-এর কাঁঠাল সদৃশ কাঠামোর ফলস্বরূপ অন্তরক তড়িৎভেদ্যতার বাস্তবিক অংশটি উন্নত হয় এবং এডি তড়িৎপ্রবাহের ক্ষয় বেশিরভাগ চৌম্বকীয় ক্ষয়ে অবদান রাখে। Ni@CFO অন্তস্তল-খোলকে ৯.৫৭ GHz এ -৮৪.০১ dB-এর ন্যূনতম প্রতিফলন ক্ষয় খুঁজে পাওয়া গেছে এবং RL <-১০ dB-এর জন্য সামগ্রিক কার্যকর ব্যান্ডউইথ ৬.২৫ GHz পরিমাপ করা হয়েছে। Ni@CFO এর অসামান্য EM তরঙ্গ শোষণ গুণটিকে অনেকগুলি উচ্চ কম্পাঙ্কের ব্যবহারিক কাজের জন্য একটি ব্যাপক কার্যক্ষম এবং অর্থনৈতিকভাবে উপকারী EMA উপাদান হিসেবে গড়ে তুলেছে।

LIST OF PUBLICATIONS

(Included in Thesis)

1. **Gorai, A.**, Mandal, D., & Mandal, K. (2021). Multi-layered nano-hollow spheres for efficient electromagnetic wave absorption. *Nanotechnology*, 32(34), 345707.
2. Dutta, A., **Gorai, A.**, Mandal, D., & Mandal, K. (2021). Dielectric and microwave absorption properties of Na0.5Bi0.5TiO3–SrTiO3 system. *Ferroelectrics, 583*(1), 252–263.
3. **Gorai, A.**, Mandal, R., & Mandal, D. (2022). Enhanced Electromagnetic Wave Absorption by Bi-layered Nano-hollow Spheres. *IEEE Transactions on Magnetics* 58, 1–6.
4. **Gorai, A.**, Hait, S., Taute, W., Höft, M., & Mandal, K. (2023). Optimization of Magnetic Coating for Improved Electromagnetic Wave Absorption in Bi-layered Nano-hollow Spheres (**Accepted at IEEE Transactions on Magnetics**).
5. **Gorai, A.**, Dutta, A. & Mandal, K., Enhancement of Microwave Absorption Properties of Crystal-Engineered Perovskite Oxide using Cobalt Ferrite **(Manuscript Submitted)**.
6. **Gorai, A.** & Mandal, K., Tuning of Magnetic Properties in Exchange Coupled Core-shell Nanostructures **(Manuscript Under Preparation)**

(Not Included in Thesis)

1. Mandal, D., **Gorai, A.**, & Mandal, K. (2019). Electromagnetic wave trapping in NiFe2O4 nano-hollow spheres: An efficient microwave absorber. *Journal of Magnetism and Magnetic Materials*, 485(April), 43–48
2. Chakraborty, I., Majumder, D., Rakshit, R., Alam, M., Mukherjee, S., **Gorai, A.**, & Mandal, K. (2021). Magnetic Field-Dependent Photoluminescence of Tartrate-Functionalized Gadolinium-Doped Manganese Ferrite Nanoparticles: A Potential Therapeutic Agent for Hyperbilirubinemia Treatment. *ACS Applied Nano Materials*, 4(5), 4379–4387
3. Saha, P., Rakshit, R., **Gorai, A.**, Mandal, D., & Mandal, K. (2022). Unusual dielectric properties of hollow magnesium ferrite nanospheres: a potential lightweight microwave absorber. *Journal of Materials Science 2022 57:7*, ***57***(7), 4569–4582

4. Hait, S., **Gorai, A.**, & Mandal, K. (2023). Origin of different microwave absorption in multiferroic Bismuth and Gallium Ferrite, *Materials Letters* ***331***, 133520.
5. Hait, S., **Gorai, A.**, & Mandal, K. (2023). Barium and Yttrium Co-doping in Bismuth Ferrite Nanoparticles to Enhance Microwave Properties, *Physica Scripta* ***98***(9), 095940.

ACKNOWLDEGEMENT

My years at the S. N. Bose National Centre for Basic Sciences have shaped me into a new and much better person. On this campus, I had access to a huge array of academic, cultural, and social activities. I shall be eternally grateful to the S. N. Bose National Centre for Basic Sciences for giving me with the opportunity to discover who I am and to pursue my most audacious dreams, as well as the constraints that compelled me to be resourceful and independent.

Next, I would want to express my deep gratitude to Prof. Kalyan Mandal, who guided me through my Doctoral research. By allowing me to do extensive, time-independent research, he developed me into an experimental physicist who is capable of working alone and in teams from anywhere in the world. His influence pushed me to think critically and learn as much as I could about the topic I was investigating. Again, I would want to thank him for motivating me to plan and conduct my own study, as well as for our interesting conversations, which helped me to develop my thoughts and add depth to my studies. Finally, after a year of the COVID-19 pandemic, I have to admit that without his patience and full support, it would be difficult to complete my thesis.

I am eternally grateful to one of the most influential teachers in my life, Mr. Saikat Pal, without whom I would not be where I am now. I also want to thank his family, especially Rajarshi Pal, my childhood companion who always encouraged me to keep going forward. I shall be eternally grateful to Mr. Ashutosh Mukherjee for mentoring and inspiring me during this journey. I thank all the teachers who have influenced me at some point of my life. Only a few of the countless names are Mr. Rajib Kesh, Mr. Shibaprasad Mukherjee, Mr. Tapas Kesh, Mr. Subir Dhara for Sagarbhanga High School, Mr. Basudeb Dutta, Mr. Ramakrishna Biswas from Durgapur Taraknath High School, Dr. Debabrata Dutta, Dr. Malay Purkait from Ramakrishna Mission Residential College Narendrapur, Prof. Subhrangshu Sekhar Manna, Prof. Punnyabrata Pradhan, Prof. Ramkrishna Das, Prof. Samir Kumar Pal, Prof. Priya Mahadevan, Prof. Amitabha Lahiri, Prof. Suman Chakrabarty, Prof. Thirupathaiah Setti from my centre Satyendra Nath Bose National Centre for Basic Sciences, Mr. Naresh Sen, Mr. Sanjib Pal.

I have a deep and abiding appreciation for all the wonderful people I have met during my time at this centre and beyond. I thank my beloved friends Atul Rathor, Sudip Majumder, Surya Narayan Panda, Shantonu Mukherjee and Shashank Gupta from my Integrated PhD batchmates with whom I started my journey here, Dr. Subhamita Sengupta, Dhiraj Tapadar,

Dr. Priyanka Saha, Debayan Mondal, Dr. Sucheta Mondal, Anish Das, Arundhati Adhikari, Anusree Sen from SNB Dance group for lighting my dancing spirit, Abhik Ghosh Moulick, Amrita Mondal, Ria Saha, Animesh Hazra, Shivam Mishra, Avik Sasmal, Jayarshi Bhattacharya, Subhajit Singha from SNB Mess Committee 2020-2021 in my journey through development of management skills, Dr. Tuhin Maji, Ram Krishna Patra, Samrat Sen, Subhajit Singha, Ishita Jana, Sudip Chakraborty and Sourav Mandal from Photofest 2020, 2022, 2023 groups for emphasizing my artistic aspect, Rajdeep Biswas, Abhik Ghosh Moulick, Jayarshi Bhattacharya, Ardhendu Pal, Prapti Mukherjee, Arun Kumar Das from SNB Drama group for cultivating my performing ability, Dr. Subrata Dev, Dr. Sk Imadul Islam, Dr. Krishnendu Pal, Sayan Ghosh, Tanmoy Chakraborty, Krishnendu Sinha, Jayarshi Bhattacharya, Sabuj Mandal, Bidhan Kumbhakar, Samir Rom, Premashis Raj, Soumen Mondal, Pratap Pal, Anutosh Biswas, Riju Pal from Badminton, Football, Cricket, Table Tennis, Carrom and Chess Tournament groups for learning team work, Dr. Biplab Bhattacharya, Dr. Subhadip Chakraborti, Dr. Samrat Ghosh, Dr. Sumanta Kundu, Dr. Rakesh Das, Dr. Sandip Saha, Dr. Sayani Chatterjee, Dr. Subhashish Chakraborty, Dr. Arghya Das, Dr. Jayita Patwari, Dr. Rahul Bandyopadhyay, Dr. Prantik Nandi as my beloved seniors in my centre for their valuable suggestions, advices and discussions, Mr. Kaustav Bhattacharya and Mr. Ranjit Sengupta from swimming group for the fun but informative discussions and support, my facebook friends Tanushree Roy and Supti Das for helpful conversations and always staying by me and finally to my childhood buddies, Rajat Mukherjee, Kushankur Chakraborty and Ayan Mukherjee for always being there for me.

I thank all my labmates Dr. Dipanjan Maity, Dr. Dipika Mandal, Dr. Priyanka Saha, Saheli Samanta, Soham Saha, Ishita Jana, J Sridhar Mohanty, Sourav Sarkar for their cheerful company, help, and support. I thank my seniors Dr. Souvanik Talukdar, Dr. Rupali Rakshit, Dr. Dipika Mandal, Dr. Subrata Ghosh, Dr. Indranil Chakraborty, Dr. Mahebub Alam, Dr. Deblina Majumdar, Dr. Keshab Karmakar, Dr. Debasish Sarkar, Dr. Ashutosh Kumar Singh, Dr. Arka Chaudhuri and Dr. Srabantika Ghose.

I am indebted to the technical staff at my institution for their patience and helpfulness at various measurements: Mr. Debarghya Ghosh, Mr. Sourav Sinha, Mr. Shakti Nath Das, Mr. Amit Kumar Chanda, Mr. Joy Bandopadhyay, and Mrs. Urmi Chakrabarty. I am thankful to Ms. Nibedita Konar, Mr. Rupam Porel, Ms. Chandrakana Chatterjee for easing my administrative works and Abhijit Da from Computer Section for solving my computer related problems.

I would want to thank all of the SNB Mess Committees throughout my stay at this centre, all the cooking team members, Kamakhya Bagchi, cleaners of my hostel and campus,

gardeners, securities and every personnel working hard to sustain healthy and memorable life at SNBNCBS.

Now, I would want to express my heartfelt gratitude to Ms. Swarnali Hait, without whom I couldn't envision my existence at SNBNCBS. From being an IPhD batchmate to my solitary companion to every single aspect I mentioned above till now, from sports, to dancing, to swimming, to skating, to mess committee, from ups and downs to deep long philosophical discussion, she has always been there with me and she has always had my back when I needed it the most.

Finally, I want to thank my dear grandparents, Mrs. Lakshami Ghosh and Mr. Bodhan Ghosh, for all they've done for me and the incredible impact they've had on my life. I miss my aunt Mahuya Ghosh, who loved me and encouraged me throughout my childhood.

The names I have written above are just a tip of some icebergs. Many names are unwritten due to certain constraints. But I must mention a name, Dexter, a cartoon character from Dexter's Laboratory who inspired me from the beginning of my school to be a scientist, an inventor which led me to what I am today. I am thankful to the creator of that cartoon.

Anupam Gorai

LIST OF ABBREVIATIONS

	A
AFM	Antiferromagnetism
AC	Alternating Current
	B
BW	Bandwidth
BCO	$BiCrO_3$
BT	$BaTiO_3$
	C
CS	Core-Shell Nanostructure
CFO	Cobalt Ferrite, $CoFe_2O_4$
CFSE	Crystal Field Stabilization Energy
CPE	Converse Piezoelectric Effect
	D
DM	Dzyaloshinkii-Moriya
DC	Direct Current
DOS	Density of States
DUT	Device Under Test
	E
EDX	Energy Dispersive X-ray Analysis
EM	Electromagnetic
EMA	EM wave absorbing materials
EMI	EM wave interference
EMF	Electromotive Force
EG	Ethylene Glycol
EtOH	Ethyl Alcohol
	F
FC	Field Cooled
FM	Ferromagnetism
fM	Ferrimagnetism
FCC	Face Centered Cubic
FEG	Field Electron Gun

FMR	Ferromagnetic Resonance
FESEM	Field Emission Scanning Electron Microscope
FWHM	Full Width at Half Maxima
	G
GB	Grain Boundary
	H
HAADF	High-angle annular dark-field imaging
HRTEM	High Resolution Transmission Electron Microscope
	I
ICDD	The International Centre for Diffraction Data
	J
JCPDS	Joint Committee on Powder Diffraction Standards
	M
MD	Multi Domain
MUT	Material Under Test
MAM	Microwave Absorption Material
MLCT	Metal-ligand charge transfer
MH	Magnetic Hysteresis
MnFO	Manganese Ferrite
	N
NaOH	Sodium Hydroxide
NBT	Bismuth Sodium Titanate
NRW	Nicholson-Ross-Weir
NMs	Nanomaterials
NPs	Nano particles
NSs	Nanostructures
NHSs	Nanohollowspheres
	P
PM	Paramagnetic
PPMS	Physical Property Measurement System
PVP	Polyvinylpyrrolidone
	R
RT	Room Temperature

RF	Radio Frequency
RL	Reflection Loss
	S
SD	Single Domain
SE	Shielding Efficiency
SNBT50	$Sr_{0.5}Bi_{0.25}Na_{0.25}TiO_3$
SAED	Selected Area Electron Diffraction
ST, STO	Strontium Titanate
SWR	Standing Wave Ratio
STV Ratio	Surface-to-Volume Ratio
	T
TE	Transverse Electric
TEM	Transverse Electromagnetic
TEOS	Tetraethyl Ortho Silicate
TM	Transition Metal, Transverse Magnetic
	V
VNA	Vector Network Analyser
VSM	Vibrating Sample Magnetometer
	X
XRD	X-ray Diffractometer
	Z
ZFC	Zero Field Cooled

LIST OF SYMBOLS

a	Lattice Constant (Å)
A	Area
B	Magnetic Flux Density (T)
BW_{eff}	Total Effective Bandwidth
c	Lattice Constant (Å), Speed of Light ($3x10^8$ m/s)
C	Capacitance (F)
C_g	Grain Capacitance
C_{gb}	Grain Boundary Capacitance
d	Inter-Planar Spacing
d_c	Critical Diameter
d_{in}	Inner Diameter (mm)
d_{out}	Outer Diameter (mm)
D	Crystallite Size (nm), Electric Displacement
e	Electronic Charge (1.602×10^{-19} C)
E	Electric Field (kV/cm)
E_a	Activation Energy (eV)
E_I	Incoming Electromagnetic Wave
E_R	Reflected Electromagnetic Wave
E_T	Transmitted Electromagnetic Wave
E_A	Attenuated Electromagnetic Wave
f	Frequency (Hz)
f_C	Cut-Off Frequency (Hz)
f_r	Resonance Frequency
f_m	Frequency of Minimum Reflection Loss
F	Landau's Free Energy
F_0	Ground State Free Energy
G	Conductance
H	Magnetic Field
H_C	Coercivity
H_0	Externally Applied Field
H_A	Anisotropy Field

H_D	Demagnetization Field
H_{ex}	Exchange Hamiltonian
I	Electric Current (A)
J	Exchange Constant
J_e	Isotropic Exchange Integral
k_B	Boltzmann Constant (1.3806488×10^{-23} J/K)
k	Wave Number
k_C	Cut-Off Wave Number (Hz)
K	Magnetic Anisotropy, Dielectric Constant
K_V	Bulk or Volume Anisotropy Constant
K_S	Surface Anisotropy Constant
K_{eff}	Total Effective Anisotropy Constant
L	Inductance
M	Magnetization (emu/g)
M_S	Saturation Magnetization
M_R	Remnant Magnetization
N	Number of Loops in Pickup Coils
P	Electric Polarization ($\mu C/cm^2$)
P_T	Transmitted Power
P_I	Incident Power
Q	Charge
r	Distance Vector
R	Resistance (Ω)
R_g	Grain Resistance
R_{gb}	Grain Boundary Resistance
RL_{min}	Minimum Reflection Loss
s	Temperature Dependent Parameter of Conduction
S	Spin Operator
S_{ij}	Scattering Parameters
t	Time, Thickness of Absorbers
t_m	Absorber Thickness of Minimum Reflection Loss
T	Temperature (K), Torque

T_C	Curie Temperature
T_B	Blocking Temperature
T_N	Neel Temperature
T_m	Temperature at which Dielectric Constant becomes Maximum
V	Volume, Electric Voltage (V)
W	Energy Dissipation
Z	Complex Impedance
Z'	Real Part of Complex Impedance
Z''	Imaginary Part of Complex Impedance
Z_{in}	Input Impedance
Z_0	Output Impedance
α	Attenuation Constant
β	Phase Constant
η	Intrinsic Impedance of Conducting Medium
η_0	Intrinsic Impedance of Free Space (~ 377 Ω).
γ	Gyromagnetic Ratio, Gilbert Damping Coefficient
δ	Nano particles
ε	Complex Electric Permittivity
ε_0	Free Space Permittivity (8.854×10^{-12} F/m)
ε_r	Relative Complex Permittivity
ε'_∞	Permittivity at Infinitely High Frequency
ε'	Real Part of Complex Electric Permittivity
ε''	Imaginary Part of Complex Electric Permittivity
ε'_m	The Maximum Value of Dielectric Constant
$\tan\delta_\varepsilon$	Electric Loss Tangent
$\tan\delta_\mu$	Magnetic Loss Tangent
$\tan\delta$	Dielectric Tangent Loss at Low Frequency
θ	Phase, Angle
λ	Wave Length
μ	Complex Magnetic Permeability, Effective Mass
μ_0	Free Space Permeability ($4\pi \times 10^{-7}$ H/m)
μ_r	Relative Complex Permeability

μ'	Real Part of Complex Magnetic Permeability
μ''	Imaginary Part of Complex Magnetic Permeability
ω	Angular Frequency, Octahedral Tilt
ν_0	The Attempt Frequency
χ	Susceptibility
φ	Radio Frequency
τ	Relaxation Time Constant (s)
σ	Conductivity, Saturation Magnetostriction
σ_{ac}	AC Conductivity
σ_{dc}	DC Conductivity
ρ	Resistivity, Free Charge Density
Γ	Reflection Coefficient
Γ_{in}	Total Reflected Fields at the Interface
T	Transmission Coefficient
Φ	Magnetic Flux

CONTENTS

LIST OF FIGURES

CHAPTER 1

INTRODUCTION

This introduction chapter includes a comprehensive literature review, theoretical background, and motivation to work in this specific topic, as well as a quick overview of the whole project.

1.1 IMPORTANCE OF MICROWAVE STUDY

The microwave region of electromagnetic spectrum ranges from 1 GHz to 300 GHz (or 30 cm to 1 mm in wavelength) [1], [2]. Although Hertz produced and studied microwaves for the first time in 1886, their practical application required the invention of suitable generators, such as the klystron and magnetron. Microwaves are the primary medium for high-speed data transmissions between earth-based stations, satellites, and space probes. A system of synchronous satellites approximately 36,000 kilometres above the Earth is utilised for international broadband communications of all types, including television and telephone.

Antennas for microwave transmitters and receivers are of parabolic dish shape [3]. They generate microwave radiation with a spreading angle proportional to the ratio of the wavelength of the constituent waves to the dish's diameter. Thus, the beams can be directed similar to a searchlight. Radar rays comprise of brief microwave pulses. The distance of an aircraft or ship can be determined by measuring the time it takes for a radar pulse to travel to the object and, after reflection, back to the radar dish antenna. In addition, the velocity of objects can be measured by utilising the change in frequency of the reflected wave pulse caused by the Doppler effect. Therefore, microwave radar is extensively utilised for guiding aircraft and vessels and detecting speeding commuters. Since microwaves can penetrate smoke clouds but are dispersed by water particles, they are utilised for mapping meteorological disturbances and forecasting the weather. Microwaves perform an expanding function in food heating and preparation. They are absorbed by the water and lipids in foods (such as in the tissue of proteins) and generate heat from the inside. In most instances, this reduces cooking time by a factor of one hundred. In contrast, dried objects such as glass and ceramics are not heated during the procedure, and metal foils are not pierced at all.

Multiple varieties of microwave generators and amplifiers have been created. Vacuum-tube devices, such as the klystron and the magnetron, continue to be widely utilised, particularly for high-power applications. Magnetrons have been adopted for radar systems and microwave cookers, whereas klystrons are predominantly utilised as amplifiers in radio relay systems and for dielectric heating. Multiple devices capable of producing, amplifying, detecting, and controlling microwaves have been created by solid-state technology. Notable examples include the Gunn and tunnel (or Esaki) diodes. The maser (short for "microwave amplification by stimulated emission of radiation") has proven useful in radio astronomy, microwave radiometry, and long-distance communications, among other fields.

1.2 RELEVANCE OF NANOTECHNOLOGY

Physicist Richard P. Feynman initially introduced the concept of nanotechnology in his lecture titled "There is plenty of space at the bottom," in which he underlined the need for nanoscale materials to create better and smaller devices. Norio Taniguchi coined the word "nanotechnology" in 1974 to describe the study of the characteristics and uses of diverse materials with very small dimensions, in the range of 1 to 100 nm. These size restrictions shown by nanostructures (NSs) often result in qualitatively distinct behaviour compared to their bulk equivalent. For instance, Cox and his colleagues discovered that bare Rhodium (Rh) clusters have a non-zero magnetic moment for fewer than 60 atoms, indicating either ferro- or ferrimagnetic ordering despite the fact that Rh in bulk is a Pauli paramagnet at all temperatures [4]. When the size of these functional nanomaterials (NMs) is equivalent to specific physical length scales, such as the carrier mean free path, superconducting coherence length, magnetic domain wall width, and spin diffusion length, etc., [5] these unique features emerge. Moreover, the reduction in size of materials confines them in confinement zones where quantum phenomena play a significant role, resulting in the density of states (DOS) of electrons in the material changing from a continuous function ($D \propto E^{1/2}$) to a delta function as we move from bulk to nanoscale, as depicted in Fig. 1.1 [6]. Since the ratio of surface area (A) to volume (V) in nanoscale greatly increases with size reduction ($A/V \propto 1/r$ for spherical particles), a greater amount of material can come into contact with surrounding materials, thereby influencing properties such as transition temperatures, fluorescence, electronic excitation, electrical conductivity, magnetic permeability, and chemical reactivity [7]–[11].

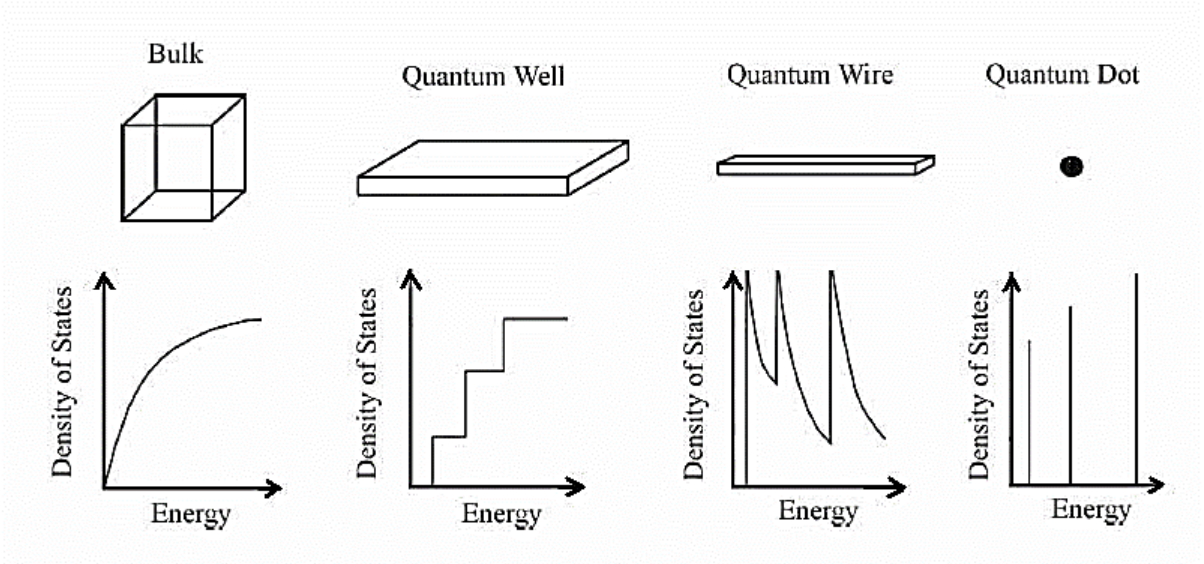

Figure 1.1. Change in density of states (DOS) with decreasing size: from bulk to quantum dots

The ability to modify and alter the characteristics and characteristic parameters of engineered nanomaterials makes them even more intriguing, since variations in nanoscale lead to their diverse uses [8], [12]–[19]. In this regard, size, shape, content, and functionalization of nanomaterials are presented as potential techniques [15], [20], [21]. The synthesis and characterisation of nanostructures of various functional materials is crucial and difficult due to the need to precisely regulate their defect states, nanoscale architectures, and consequently their characteristics [22]. For example, reducing the size of ferrites to a particular level induces superparamagnetism, making them more appropriate as biosensors [23], [24]. Although Iron (Fe), Cobalt (Co), and Nickel (Ni) are all ferromagnetic, the replacement of Co or Ni cations in typical magnetite creates hard magnetic and soft magnetic substances, respectively [11], [25]. Due to surface modification and charge transfer, magnetic or non-magnetic layer capping on nanostructures also has a dramatic influence on their characteristics [26], [27].

Nanotechnology is significantly enhancing and even revolutionizing several fields, including information technology, health, transportation, energy, and environmental research. Nanomaterials are employed everywhere [14], [28], [29], from components in high frequency devices to the biomedical area and even the production of "smart textiles" to "anti-friction fluids." In addition, their lightweight, space-efficient, low-cost, but effective nature enables the

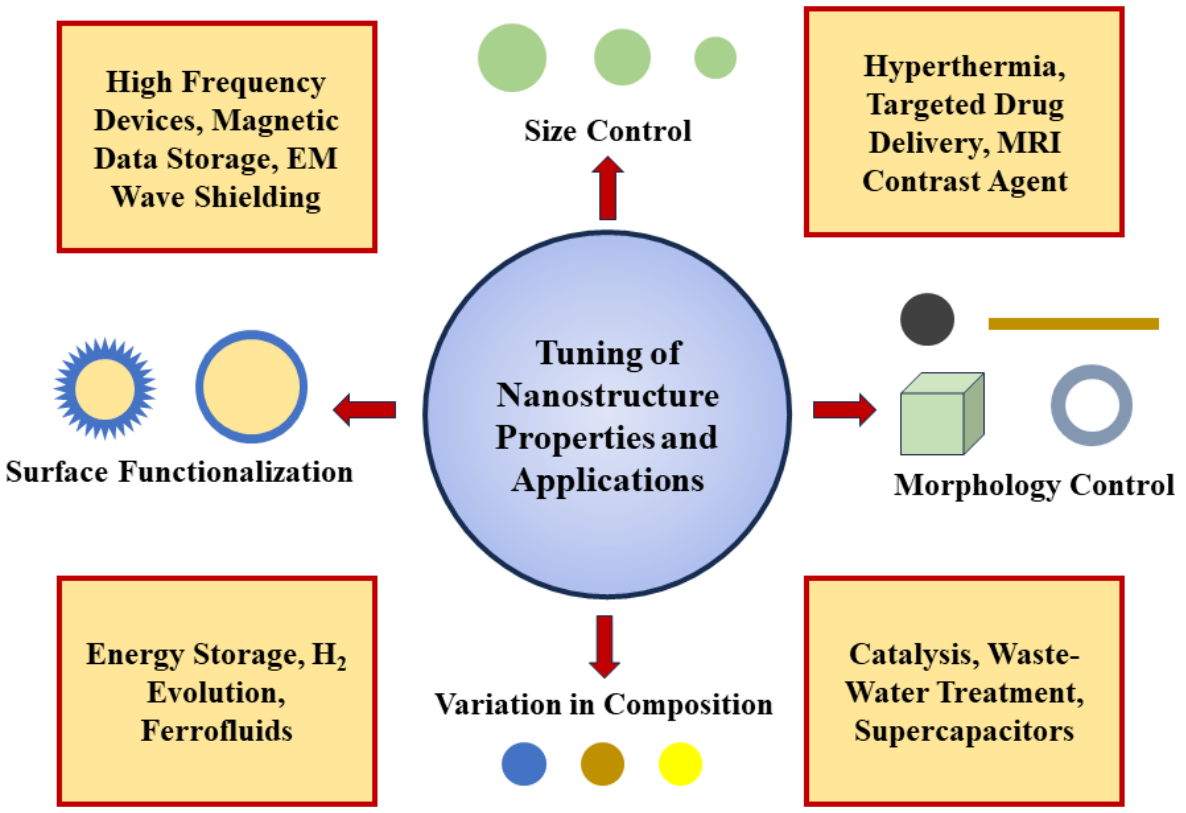

Figure 1.2. Schematic illustration of potential nanostructure tuning methods and their applications

creation of superior and productive technologies. Fig. 1.2 is a schematic representation of nanomaterial tuning and applications in many sectors. Even if a number of commercial applications have been successfully implemented, research on nanoscale materials is not at yet saturated and remains tremendously enthusiastic.

1.3 NANOSTRUCTURES

The nanohollowspheres (NHSs), nanocubes, core-shell, and nanorods morphologies of polymer, carbon, and other nanomaterials are shown in Fig. 1.3 [30]–[32]. Despite having identical building components, these nanostructures display distinct thermodynamic, physical, and mechanical characteristics [22], [33] owing to changes in boundary restrictions, defect states, etc. For instance, Ba and Y co-doped bismuth ferrite nanoparticles show stronger ferromagnetism and spontaneous ferroelectricity than its bulk counterpart [34].

1.3.1 NANO-HOLLOW SPHERES

In the past few years, nanostructure researchers have gravitated toward the fabrication of nano hollow spheres (NHSs) due to their hollow interior, which increases their effective surface area while their density is much lower than that of their dense solid counterparts [33], [35]. Due to their high saturation magnetization (M_S), large surface area and pore volume, low density, and ability to withstand volume changes due to temperature and pressure, NHSs are able to be used in a wide variety of applications in the fields of biomedical research [8], high frequency magnetic devices [36], energy storage [13], ferro-fluids [14], Hydrogen evolution reaction [20], supercapacitors [15], and chemical sensors [17]. Large void space and the outer surface of NHSs may be used for the encapsulation and controlled release of pharmaceuticals [37], [38]. Moreover, numerous internal reflections of EM waves in the inner hollow core of NHS lengthen their overall path length and enhance their absorption, hence enhancing EM wave shielding [39].

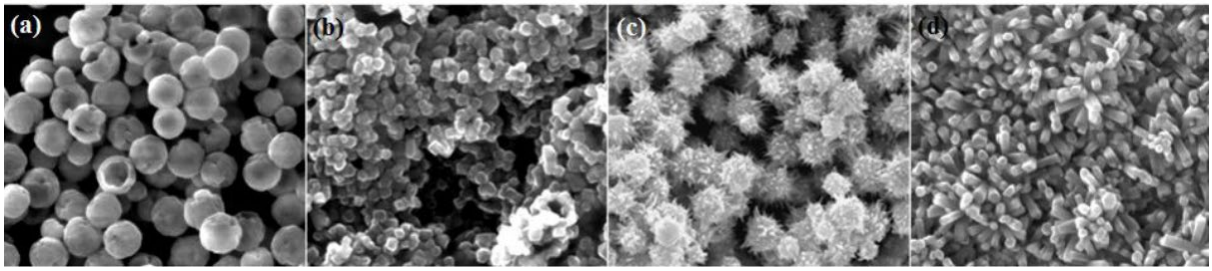

Figure 1.3. Different nanostructure morphologies (a) nano-hollow spheres (b) nanocubes (c) etching core-shell structure (d) nanorods

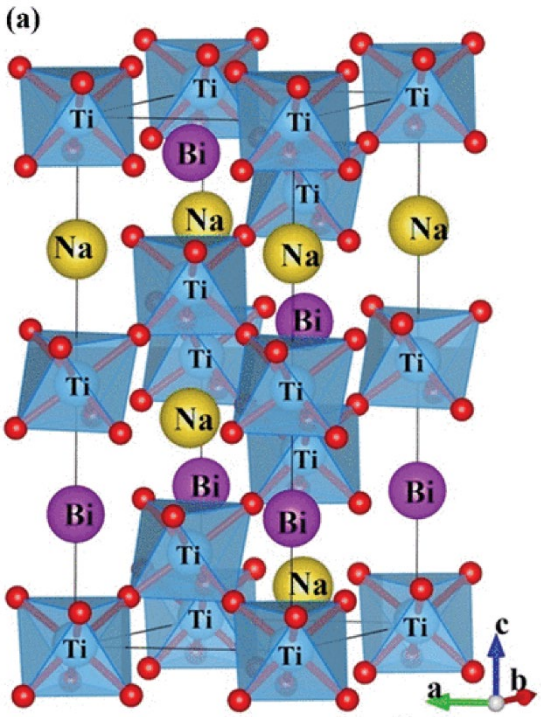

Figure 1.4. Crystal structure of NBT system

Despite the fact that, by definition, nanomaterials must have dimensions ≤100 nm, NHS with sizes >100 nm behave similarly to nanomaterials since their shell thickness is less than 100 nm; this feature relaxes their nanoscale range and expands their application space [27], [40]. Possibilities of different configurations of hollow spheres, such as single-shell, multi-shell, yolk-shell, and rattle-type, among others, also contribute to the growth of this morphology as a study area [35].

1.3.2 TRANSITION METAL OXIDE BASED MATERIALS

It is well-known that traditional iron oxide, Fe_3O_4, also known as 'loadstone' from ancient period, is a versatile substance that is utilized extensively as an MRI contrast agent for early-stage cancer diagnosis and production of metamaterials [41], [42]. Ferrites are excellent in high frequency components due to their very high DC electrical resistivity and thus minimal loss [43]. In addition, recently reported phenomena such as enormous magnetoresistance rely on magnetic nanoparticles. Ferrites with considerably superior permittivity (ε) and permeability (μ) provide broader bandwidth (BW), greater impedance matching, and EM wave absorption compared to conventional EM wave absorbing materials, such as carbon-based materials and metal powders [44], [45]. Due to their adjustable absorption bands, EM wave absorbing materials (EMA) are extensively employed in both military and civilian applications, including stealth technologies, anti-radiation sheets, and anechoic chambers. Both dielectric and magnetic losses are important sources, and large ε and μ values reduce the needed thickness (t) of EMA, hence enhancing its space-efficiency [46]. Consequently, a comprehensive investigation of the structural, magnetic, dielectric, and microwave absorption characteristics of transition metal-based materials is crucial.

Bismuth sodium titanate ($Na_{0.5}Bi_{0.5}TiO_3$, often known as NBT) is an additional fascinating material to explore owing to its high dielectric constant. It possesses a perovskite *R*3*c* structure at room temperature, however beyond 225 °C it changes to a tetragonal phase. In the past, solid solutions of NBT containing a large number of perovskites were studied in an attempt to get

features suitable for technological applications [47]–[55]. Due to the high Curie temperature of NBT and the other perovskite materials used for the solid solution, the bulk of the compounds eventually possess high Curie temperatures [56]. $SrTiO_3$, which possesses a cubic-to-tetrahedral phase transition temperature of 105 K, is employed to generate the solid solution and reduce the Curie temperature to an appropriate level for technological purposes [57]–[60]. Sr^{2+}, whose ionic radii are between those of Na^{1+} and Bi^{3+}, settles in the Na/Bi sites of the NBT-ST solid solution at room temperature and changes the crystal structure of NBT [61]. As a result, varying the concentration of this ion makes it interesting to study to achieve a transition temperature that is sufficiently near to room temperature (300 K at 3 kHz) and a high enough dielectric constant at low frequency [47].

1.3.3 CORE-SHELL STRUCTURES

Core–shell nanoparticles are a form of biphasic material that consists of an inner core structure and an outside shell composed of various substances. As a result of the unique features that might result from the mix of core and shell material, shape, and design, these particles are of interest. In addition, they have been engineered such that the shell material may increase the reactivity, thermal stability, or oxidative stability of the core material, or so that a cheap core material can support a thin, more costly shell material. Consequently, they have found widespread use in domains such as biomedicine, electrical and semiconducting materials, and catalysts.

There are several core-shell nanostructure geometries [Fig. 1.5][62]–[64], including (a) spherical core/shell nanoparticles; (b) hexagonal core/shell nanoparticles; (c) numerous tiny core materials covered by single shell material; (d) nanomatryushka material; and (e) moveable core inside hollow shell material.

The qualities of nanoparticles are not only proportional to their size, but also to their form. For instance, the blocking temperature, magnetic saturation, and permanent magnetization of magnetic nanocrystals are all dependent on particle size, while the coercivity of the nanocrystals is entirely reliant on particle shape due to surface anisotropy effects. Other nanoparticle physical and chemical features, including catalytic activity and selectivity, electrical and optical properties, sensitivity to surface-enhanced Raman scattering (SERS), plasmon resonance, and melting temperature, are also significantly shape-dependent.

Importance of Core-shell nanostructures[65]–[67]:

- Core/shell nanoparticles are modified materials with excellent functionality.

- Due to the shell material coating, the core particle's attributes such as reactivity reduction or thermal stability may be adjusted, hence increasing the core particle's overall particle stability and dispersibility.
- The coating on the core particle serves several purposes, including surface modification, the capacity to boost functionality, stability, and dispersibility, controlled release of the core, and decrease in precious material consumption, among others.
- As micro-vessels, catalytic supports, adsorbents, lightweight structural materials, and thermal and electrical insulators, nano- and micro-sized hollow particles are employed for a variety of functions.

Nickel is magnetically softer than Cobalt ferrite, because of which exchange coupled Nickel core with Cobalt Ferrite shell nanostructures provide us with additional control over the magnetic features of the material which is beneficial for high microwave absorption. The formation of core-shell structure having $MnFe_2O_4$ nanohollowspheres as core and highly anisotropic $CoFe_2O_4$ and highly dielectric SiO_2 as shell is expected to effectively modify the dielectric and magnetic properties of the materials as a result of increased number of interfaces, and increased dielectric and magnetic losses. Therefore, the study of the optimization of thickness of these coatings with materials having different properties are extremely interesting and promising for application.

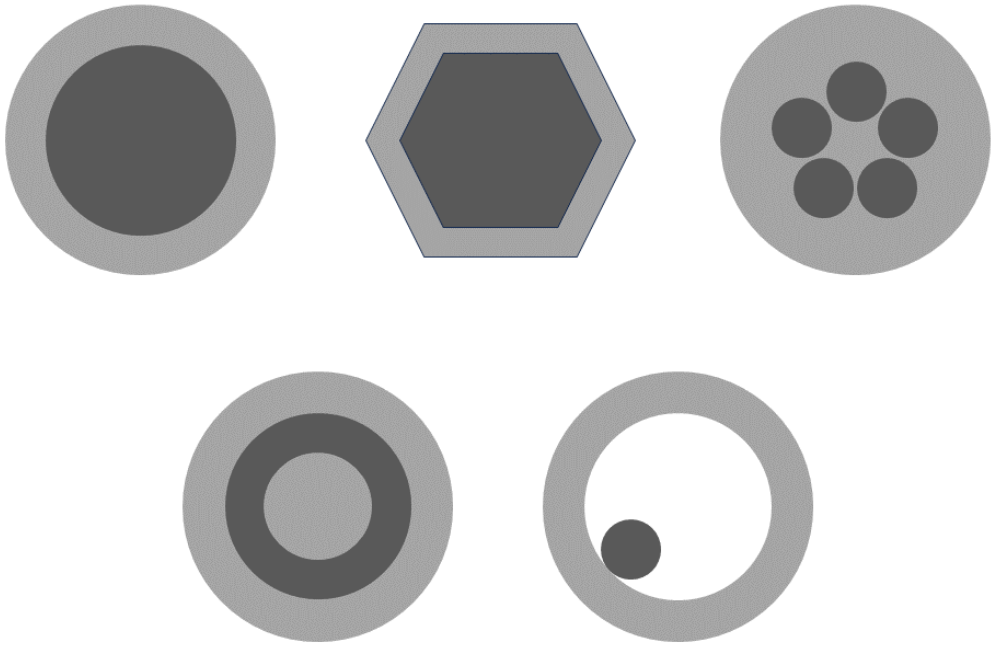

Figure 1.5. Different core/shell nanoparticles

1.4 CRYSTAL STRUCTURE

In general, based on structural properties there are three kinds of ferrites: (i) Spinels, (ii) Garnets, and (iii) Hexaferrites. Spinel ferrites with the formula TFe_2O_4 (T = transition metal ion) are 3d transition metal-based ferrites with space group $Fd3m$. As illustrated in Fig. 1.6, the cubic unit cell is composed of 56 atoms, 32 oxygen anions arranged in a cubic close-packed structure, and cations occupying 8 of the 64 available tetrahedral sites (A sites) and 16 of the 32 available octahedral sites (B sites). The limit of atomic radii included in the A-site is 0.30 Å, whereas the limit for the B-site is 0.55 Å. The structure may expand or shrink depending on the cationic radii positioned in the sites. Furthermore, in an oxygen closed pack shape comprised of intervening face-centered cubic (fcc) lattices, anions occupy the cube's corners and the cation occupies the space formed by these anions. The structural formula for the fundamental spinel compound TFe_2O_4 is [68]

$$[T_{(1-i)}Fe_i]^A[T_iFe_{(2-i)}]^B O_4 \tag{1.1}$$

where the amounts in brackets represent the average occupancy of A- and B- sites and i is the inversion parameter.

The distribution of cations in A- and B-sites is primarily determined by crystal field stabilization energy (CFSE) and relative cation size. The greater CFSE value of component cations determine their preference for a higher co-ordination site, i.e., the B-site; hence, Fe_3O_4,

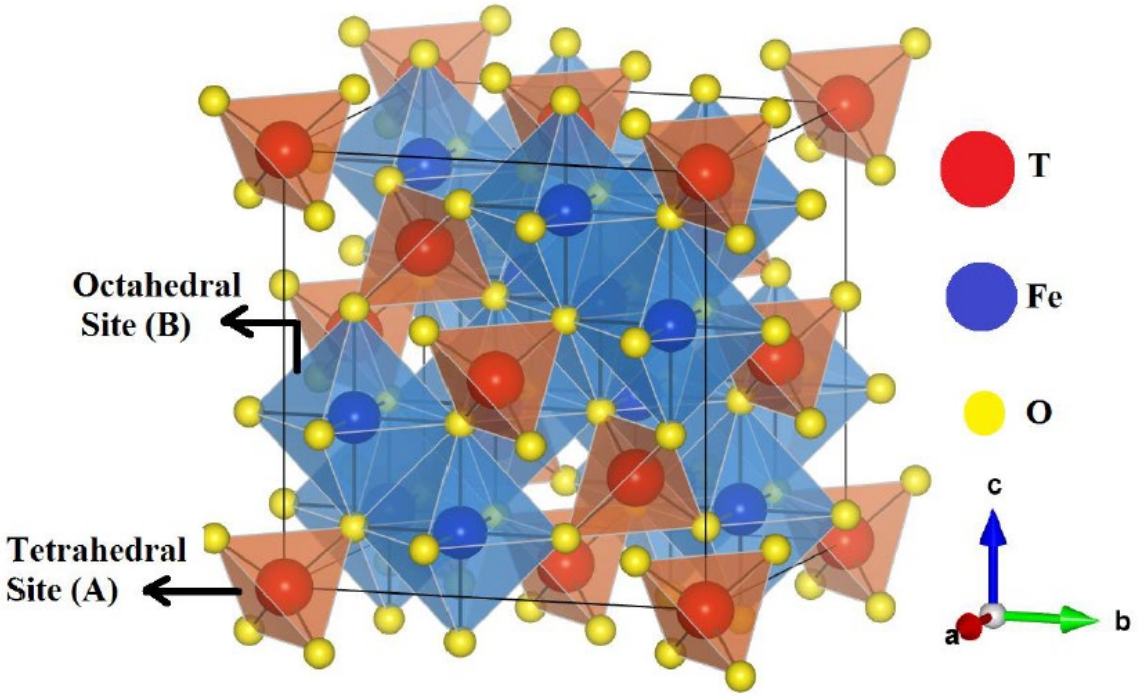

Figure 1.6. Crystal structure of a spinel ferrite, TFe_2O_4

$CoFe_2O_4$, $NiFe_2O_4$, and $CuFe_2O_4$ have inverted spinel structures [69]. However, in $ZnFe_2O_4$, Zn^{2+} with a d^0configuration and in $MnFe_2O_4$, both Fe^{3+} and Mn^{2+} with a d^5 state exhibit no preference for certain locations. $MnFe_2O_4$ and $ZnFe_2O_4$ thus have the potential to form a normal, inverse, or mixed spinel structure. In conjunction with CFSE, grain size reduction to less than 6.8 nm resulted in the transition of the majority of inverted spinel ferrite molecules to the regular spinel structure. Changes in cation distribution between tetrahedral (A) and octahedral (B) sites may have an effect on their structural characteristics, which in turn influence their magnetic and dielectric properties. Similar to Zn-doped Fe_3O_4, at a specific concentration of the non-magnetic element Zn, cation distribution fluctuates so that magnetic exchange interaction at the B-site increases the overall magnetic moment of the ferrite [70].

1.4.1 NORMAL SPINEL FERRITE

On the basis of cation distribution, a spinel ferrite can be of types normal, inverse, or mixed. In a normal spinel structure, 8 divalent cations are all located in tetrahedral sites and 16 trivalent cations are all located in octahedral sites; hence the inversion parameter (i) becomes 0 (schematically illustrated in Fig. 1.7(a)). In general, this type of distribution takes place in bulk zinc ferrites, $Zn^{2+}[Fe^{3+}Fe^{3+}]O_4^{2-}$.

1.4.2 INVERSE SPINEL FERRITE

T^{2+} ions, unlike regular spinels, occupy the octahedral voids, whereas half of the Fe^{3+} ions occupy the tetrahedral voids and the other half occupy the B sites. Therefore, the result of the inversion parameter (i) is 1. It is denoted by the formula $Fe^{3+}[T^{2+}Fe^{3+}]O_4^{2-}$. Inverse spinel structure is shown by Fe_3O_4, $CoFe_2O_4$, and $NiFe_2O_4$. In this kind of ferrites, the magnetic contribution from Fe^{3+} ions are cancelled out by inter-lattice super-exchange, leaving only the contribution from T^{2+} ions. This kind of spinel is shown schematically in Fig. 1.7(b).

1.4.3 MIXED SPINEL FERRITE

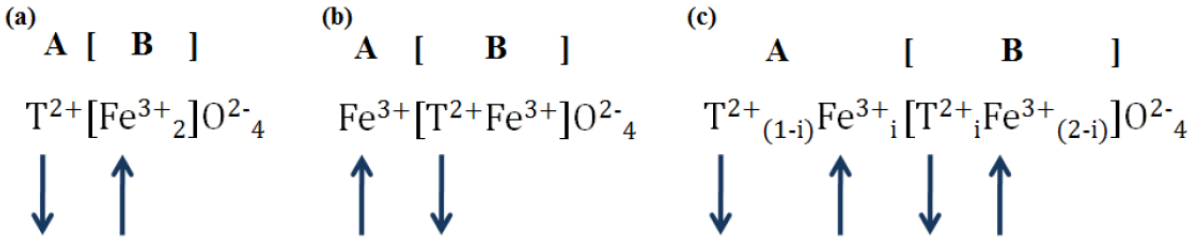

Figure 1.7. Cations distribution in (a) normal, (b) inverse, (c) mixed spinel ferrites

Mixed spinel structure or partially inverse spinel is formed when cations T^{2+} and Fe^{3+} are distributed in both A - and B - sites, and the structural formula of this ferrite is $T^{2+}_{(1-i)}Fe^{3+}_{i}[T^{2+}_{i}Fe^{3+}_{(2-i)}]O^{2-}_{4}$, where i is the degree of inversion (shown schematically in Fig. 1.7(c)). This structure is often represented by $MnFe_2O_4$, which has an inversion degree of i = 0.2 and the structural formula $Mn^{2+}_{0.8}Fe^{3+}_{0.2}[Mn^{2+}_{0.8}Fe^{3+}_{1.8}]O^{2-}_{4}$.

1.5 MAGNETIC PROPERTIES

This section will focus on the magnetic characteristics of nanostructures, notably spinels, in dc and ac magnetic fields, as well as their consequential importance. Spin and orbital angular momentum of electrons and nuclei are closely associated with the genesis of magnetism. Types of magnetism include paramagnetism, which is caused by the spin and angular momentum of individual electrons, diamagnetism, which is caused by the electron's orbital angular momentum, and ferromagnetism, which is caused by an internal field induced magnetic order in the spins giving rise to the formation of domains with a large number of aligned spins in each domain. Fig. 1.8 illustrates the magnetic behaviour of materials under the influence of an applied field, including the typical locations, saturation magnetization (M_S, maximum induced magnetization), remanent magnetization (M_R, remaining magnetization after an applied field is removed), and coercivity (H_C, magnetic field needed to demagnetize the sample). In terms of a material's susceptibility (χ), ferromagnets have $\chi \gg 0$. Spinel ferrites with anti-parallel distribution of divalent and trivalent cations in A- and B-sites are typically ferrimagnetic in nature, and the material exhibits anti-ferromagnetism if the magnetic moment of cations in anti-parallel distribution becomes equal. Individually, tetrahedral and octahedral sites exhibit direct exchange interactions between spins. Exchange Hamiltonian is given as $H_{ex} = -2J_e \sum_j S_i.S_j$, where S represents the spin operator and J_e represents the isotropic exchange integral [71]. Apart from this direct exchange, there are systems with indirect exchange, e.g. (1) Ruderman–Kittel–Kasuya–Yosida (RKKY) exchange, where the metallic ions are coupled via itinerant electrons, (2) super-exchange, here the exchange is mediated via different non-magnetic ions, (3) anisotropic exchange interaction (also known as Dzyaloshinskii-Moriya interaction), where the spin-orbit interaction plays a major role and often leads to canting of spins by small angle [71]. The super exchange mechanism couples the unpaired spins of inter-site cations via shared oxygen ions in spinels. This exchange constant (J) between A- and B-sites may be calculated using Bloch's theorem [43], which will be

addressed in further detail later. Consequently, for inverse spinel ferrites, TFe_2O_4 (T^{2+} = divalent ions such as Fe, Co, and Ni), ferromagnetic interactions are created when T^{2+} ions contain unpaired electrons. The size of NSs has a significant impact on their magnetic behaviour. Due to surface spin canting, the M_S of nanoparticles can be less than that of bulk particles [72]. In addition, at bulk sizes, the temperature dependence of M_S is observed to adhere to Bloch's $T^{3/2}$ law, but tiny nanoparticles exhibit a divergence from this $T^{3/2}$ nature, with a T^2 trend [43], [73]. In ferromagnetic materials, magnetic domains (10-1000 nm) are often divided by domain walls that contain energy associated with their development and continued presence. The domain-wall widths (wall energies) for hard magnetic materials range between 5 nm (50 mJ/m^3) and 100 nm (0.1 mJ/m^3) [74]. If the magnetic domain structure is well understood, analysing the magnetic hysteresis behaviour of ferro/ferrimagnets is made easier. Possible domain structures can be investigated using the Day plot, which is a graphical mapping of M_{RS}/M_S vs. H_{CR}/H_C, where H_{CR} is the field value at which the $M-H$ loop exhibits a remanence of $M_R = 0.5M_{RS}$ [75]. Naturally occurring hard magnets with a larger exchange interaction constant exhibit high magnetostriction and magneto-crystalline anisotropy [25]. When crystal grains are equivalent in size to magnetic domains, magnetic domains are trapped by crystal grain boundaries and exhibit significant inertia to an applied magnetic field. In addition, when the crystal size just reaches the single domain (SD) dimension from the multi-domain (MD) dimension upon scaling down the particle size of a ferromagnetic material, all the spins align to each other and only rotation of spins is possible, so demagnetization becomes more difficult as the H_C value increases [43]. Further particle size reduction results in the superparamagnetic character of ferro/ferrimagnetic NPs. In this situation, the NPs act as paramagnets in the absence of a magnetic field, and as strong ferromagnets without hysteresis loss in the presence of a magnetic field; this feature of NPs is widely used in switching devices and bio-medicine [31].

Moreover, magnetic characteristics are temperature dependant. As temperature increases, ferromagnetic crystals grow and spin-spin exchange weakens. Above a particular temperature, the Curie temperature (T_C), super-exchange totally disappears and the material becomes paramagnetic [76]. The freezing of spins on the surface of nanostructures as the temperature drops, increases the coercivity and magnetism of the material. The typical temperature for antiferromagnetism is known as the Néel temperature (T_N). Above the temperature known as the Blocking temperature (T_B), both ferro and ferrimagnetic nanoparticles display superparamagnetic behaviour characterized by fast and random magnetization reversals that

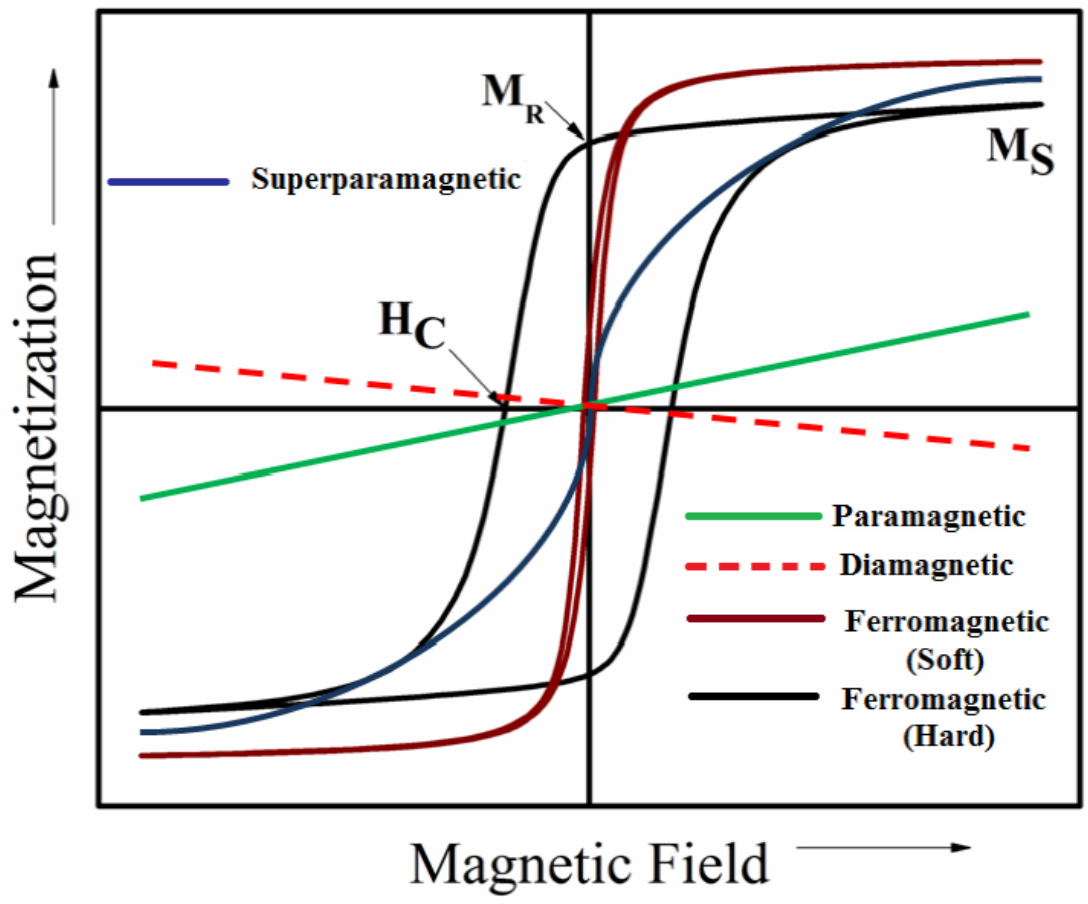

Figure 1.8. Magnetic behaviour of materials under the influence of an applied field

result in a zero time-average magnetic moment [24]. Magnetic property parameters are heavily influenced by anisotropy of the material, exchange interactions, and even measurement frequency. Therefore, detailed explanations of these events are provided below.

1.5.1 MAGNETIC ANISOTROPY

Magnetic anisotropy is the directional dependence of a material's magnetic moment in the absence of an external magnetic field. Magnetic anisotropy in a material may result from the crystalline lattice's symmetry or the nano-structured material's particular form.

1.5.1.1 MAGNETOCRYSTALLINE ANISOTROPY

Magnetocrystalline anisotropy is an inherent feature of the material and the major contributor to magnetic anisotropy, which is created by the spin-orbit interaction of electrons. Strong ties exist between the spatial arrangement of electron orbitals and the crystallographic structure. Therefore, when electron spins interact, they compel each other to align along well-defined, unidirectional crystallographic axes. The magnetic anisotropy is described by two models: (a) the Néel model, which states that magnetic anisotropy results from magnetic spin

pair interactions, and (b) the Single-ion or crystal field model, which describes crystal field interactions with atoms that are not fundamentally magnetic [71], [72]. As the magnetocrystalline energy is associated with the relative orientation of the total magnetization with respect to the magnetic easy axis of the crystal, i.e., θ. The magnetocrystalline anisotropy energy can be expressed as,

$$E_k = VK_n \sin^{2n}\theta \tag{1.2}$$

Where, $K_n(n = 0, 1, 2 \ldots)$ are the magnetocrystalline anisotropy constants. For a single crystallite, considering small θ value, from magnetocrystalline anisotropy energy expression, magnetization (M_H) at any applied magnetic field (H) can be written (neglecting higher order terms) as,

$$M_H = M_S\left[1 - \frac{a}{H} - \frac{b}{H^2}\right] + \chi H \tag{1.3}$$

Néel attribute the constant, a to the effect of inhomogeneity and defects inside the crystallites or grain boundary and b to the stress due to anisotropy in the material [61]. The b value is experimentally determined to be ($0.07619\ A^2/m^2$) and this law of approach to magnetic saturation (LAS) is used most effectively for measurement of the magnetocrystalline anisotropy on polycrystalline specimens [77], [78].

1.5.1.2 SHAPE ANISOTROPY

The magnetic dipolar anisotropy, or shape anisotropy, is mediated by the dipolar interaction of free magnetic poles causing stray or demagnetization fields. This interaction tends to direct magnetic moments parallel to the surfaces to minimize the magneto-static energy. The interaction is long range and hence its contribution is dependent upon the shape of the sample. Shape anisotropy becomes important in thin films and often produces in-plane alignment of moments. Due to shape anisotropy, demagnetization factor is 0 for long cylinders, 1/3 for spheres and 1 for plates [72].

1.5.1.3 SURFACE ANISOTROPY

Surface anisotropy, which was initially described by Néel, relates to the surface and interfaces of nanostructures and is most often exhibited in materials with complex structures and morphologies, such as metal films, multilayer, rough surfaces, and tiny particles. Generally, the surface anisotropy of nanoparticles is substantially greater than the bulk value,

as a result of the greater proportion of surface ions in smaller particles [79]. This surface spins are disordered because they reside in an uncompensated coordination sphere due to broken bonds, vacancies, and the formation of bonds with certain organic molecules. Thus, surface anisotropy makes the surface layer of a nanoparticle more magnetically resistant than the core area. The effective anisotropy energy (K_{eff}) of a spherical particle may be expressed as $K_{eff} = K_V + \frac{6}{D}K_S$, where K_V and K_S are the bulk (or volume) and surface anisotropy constants, respectively, and D is the particle's diameter.

1.5.2 SUPER-EXCHANGE INTERACTION & BLOCH'S THEOREM

In spinel ferrites, the intra-site interactions ($A-A$ and $B-B$) are direct exchange type, but inter-site interaction ($A-B$) interaction is of super-exchange type, with the interaction between $3d$ cations mediated through $2p$ spins of non-magnetic oxygen anions. Experimentally, the exchange constant (J_{AB}) between tetrahedral (A) and octahedral (B) sites may be determined by fitting Bloch's law to temperature vs. M_S curves.

According to the spin wave theory, demagnetization of a ferromagnetic material from $M_S(0)$ (M_S at T = 0 K) with temperature is caused by the excitation of spin waves with long wavelengths, and the excitation energy ε_k of the spin waves may be expressed as [23], [43],

$$\varepsilon_k = Dk^2 + Ek^4 + g\mu_B(H_0 + H_A + H_D) \tag{1.4}$$

Here D is the spin-wave stiffness coefficient, H_0 is the externally applied field, H_A is the anisotropy field, and H_D is the demagnetization field. Bloch's law describes the temperature dependence of saturation magnetization at temperatures much below T_C.

$$M_S(T) = M_S(0)(1 - BT^b) \tag{1.5}$$

where B is the Bloch constant proportional to the inverse of exchange constant (J) and b is the Bloch exponent for a three-dimensional system, which is 3/2 [79]. At low temperatures, it is possible to witness a distinct divergence from Bloch's rule in nanoparticles owing to the existence of magnons with wavelengths greater than the particle size, which cannot be stimulated. Bloch exponent is discovered to be highly dependent on particle size, chemical content, and synthesis technique, but independent of nanoparticle structure. The exchange constant between A- and B- sites (J_{AB}) may be computed using the following equation [23], [43]:

$$J_{AB} = \frac{16k_B(S_{B1}+S_{B2}-S_B)}{11S_A(S_{B1}+S_{B2})}\left[\frac{0.05864}{4B(S_{B1}+S_{B2}-S_A)}\right]^{2/3} \quad (1.6)$$

where S_A and S_{B1} are the spins of Fe^{3+} and equal 5/2 for magnetite. S_{B2} corresponds to the spin of Fe^{2+} ions in the octahedral location of the Fe_3O_4 lattice which is equal to 2.

1.5.3 SUPERPARAMAGNETISM

Below a certain critical diameter (d_c), a single domain ferromagnetic material becomes superparamagnetic. d_c may be computed using this equation: $d_c \approx \frac{\sqrt{JK}}{\mu_0 M_S^2}$, where K is the anisotropy constant, J is the exchange constant, μ_0 is the free-space permeability, and M_S is the saturation magnetization. Magnetostatic energy equals domain wall energy and magnetic anisotropy energy in a single domain. Below d_c and above T_B, thermal energy is sufficient to overcome the anisotropy barrier and reverse the spin orientation [24]. With the presence of an externally applied field, the magnetic moments of superparamagnetic nanoparticles acquire fast random saturation magnetization. As a result, superparamagnetic NPs provide more control over the application of their magnetic characteristics due to their high field response.

1.5.4 MAGNETIC RELAXATION

After the magnetic field is removed from nanoscale particles, the spin flips to a random location, and the reversal duration relies on external characteristics such as temperature and measurement frequency as well as internal parameters such as anisotropy energy, striction, etc. The average time between magnetization reversals is described by the Arrhenius-like Néel-Brown formula $\tau = \tau_0 e^{(\frac{KV}{k_B T})}$, where τ_0 is between 10^{-9} and 10^{-13} s, K is the anisotropy constant, and V is the particle's volume [80]. The magnetic relaxation curves (M versus time) of permanent magnetic materials are fascinating to analyse in order to evaluate their capacity to retain magnetization over time. Magnetization is observed to decline exponentially with time based on Brownian and Néel spin-spin relaxation, $M(t) = M_0 e^{-\frac{t}{\tau}}$, where $M(t)$ and M_0 are the magnetizations of the sample at time t and $t = 0$ and τ is the relaxation time constant.

1.5.5 DYNAMIC MAGNETIZATION

Ferrites are non-conducting oxides that, unlike metals, permit the whole penetration of electromagnetic fields, and their use in high-frequency applications such as

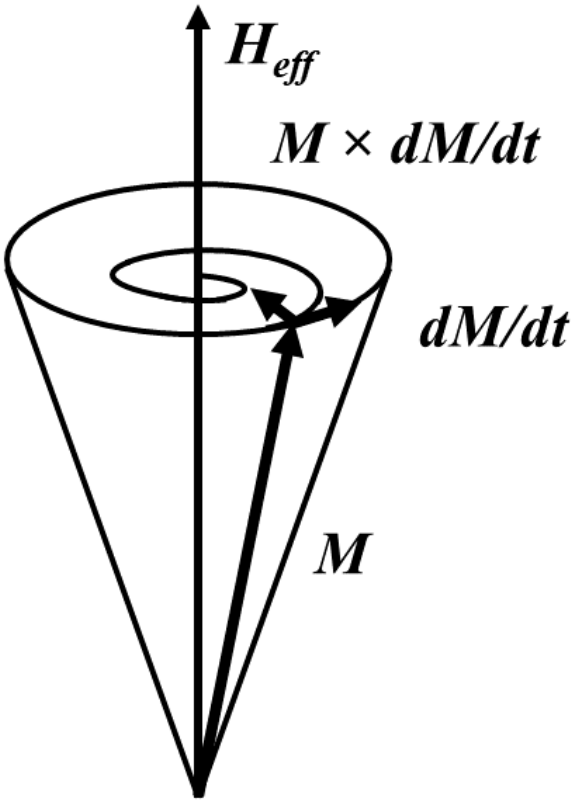

Figure 1.9. The precessional motion of the magnetization around the effective magnetic field direction when damping is included

telecommunications and radar systems is on the rise [81]. At such high frequencies, domain walls are unable to follow the field (average domain wall dispersion occurs at 10 GHz), and spin dynamics absorb microwave radiation [21]. To decrease Zeeman energy, magnetic spins precess about their equilibrium orientation in response to a torque at the frequency of an external field (as shown in Fig. 1.9). The Landau-Lifshitz-Gilbert (LLG) equation of motion [82] describes the overall behaviour of dynamic magnetization. Torque (T) associated with an electron spin (S) is given by $\frac{dS}{dt} = T = M \times H_{eff}$, where $M(= -\gamma S)$ is the magnetic moment of an electron and H_{eff} is the effective applied magnetic field. The magnetization's equation of motion with extra damping components looks like this:

$$\frac{dM}{dt} = -\gamma\left(M \times H_{eff}\right) + \frac{\alpha}{M_S}\left(M \times \frac{dM}{dt}\right) \tag{1.7}$$

Here, α is the Gilbert damping coefficient, $\gamma = ge/2mc$ is the gyromagnetic ratio, and H_{eff} is the total spin field (external and internal). This equation of motion's solution reproduces Globus' connection for the static case and demonstrates that the dispersion frequency (f_r) changes as $\sim D^{-1}$ (D = grain diameter) for small grains and as $\sim D^{-2}$ (D = grain diameter) for larger grains [83].

1.6 DIELECTRIC PROPERTIES

To build high-frequency circuits, one must have a comprehensive grasp of the electrical characteristics of materials, particularly the dielectric constant and loss tangent under working circumstances. On the basis of their conductivity, materials may be classified as conductors, semiconductors, or insulators, and as dielectric, paraelectric, or ferroelectric depending on their

polarizability [84]. Typically, ferrites are classified as semiconductors and dielectrics. The measurement of complicated dielectric characteristics of materials at radio frequency (RF) and microwave frequency is crucial in the study disciplines of material science, communication, and microwave circuit design [85]. Moreover, measurements at AC frequency offer insight into the microscopic nature of the ionic conducting process, while the technically more difficult DC measurements provide less information about the sample's overall dynamic behaviour. Thus, AC methods are utilized to determine material parameters such as bulk conductivity, surface, grain boundary effect, ionic transport, and double layer development at the electrode/sample interface, etc. [86]. Dielectric qualities relevant to polarization behaviour, conduction, and relaxation processes of a material are dependent on both external and internal factors such as frequency, temperature, and pressure, as well as sample orientation, composition, and molecule structure. Important concerns relevant to the dielectric characteristics of a material are explored in the section that follows.

1.6.1 IMPEDANCE SPECTROSCOPY

It is well known that impedance spectroscopy is an effective technique for exploring the dielectric characteristics of materials, such as conductivity (σ), dielectric constant (ε), transport processes, interfacial capacitance, mobility of charges and their equilibrium concentration, etc. When an AC signal with electric field intensity much below breakdown voltage is applied to a system, the system's impedance follows Ohm's law as the ratio of voltage (V) to current (I) in the time domain,

$$V(t) = V_0 \exp(j\omega t) \tag{1.8}$$

$$I(t) = I_0 \exp(j\omega t - \theta) \tag{1.9}$$

$$Z(\omega) = |Z|cos\theta - j|Z|sin\theta = Z' - jZ'' = \frac{1}{j\omega C} \tag{1.10}$$

Here, Z' and Z'' represent the real and imaginary components of the complex impedance (Z), ω ($= 2\pi f$) or the angular frequency of the signal, and C represents the complex capacitance of the dielectric sample. As the relative dielectric constant or permittivity (ε) of the material is proportional to the capacitance, $\varepsilon = C/C_0$, it may be determined from the impedance using the following formula,

$$\varepsilon = \frac{1}{j\omega C_0 Z} = \varepsilon' - j\varepsilon'' \tag{1.11}$$

Where, capacitance of free space, $C_0 = \frac{\varepsilon_0 A}{d}$, ε_0, A, and d represent the free space permittivity (8.854×10^{-12} F/m), active region area, and sample thickness, respectively. By expanding Eq. (1.11), the real and imaginary components of the dielectric constant may be expressed in terms of impedance as follows:

$$\varepsilon' = \frac{Z''}{\omega C_0 (Z'^2 + Z''^2)} \tag{1.12}$$

$$\varepsilon'' = \frac{Z'}{\omega C_0 (Z'^2 + Z''^2)} \tag{1.13}$$

In addition, the real component of conductivity may be calculated using the formula $\sigma = \omega\varepsilon_0\varepsilon''$[87]. Permittivity values reflect the interaction between an external field and the electric dipole moments of a sample. The ε' indicates the amount of dipole or charge alignment (both induced and permanent) as a result of polarization, whereas ε'' quantifies the energy necessary to align the dipoles or move the ions. Loss tangent ($\tan\delta_\varepsilon = \frac{\varepsilon''}{\varepsilon'}$) is a measurement of the energy lost by a substance owing to an external electric field. Generally, with rising temperatures, ε increases in dielectric material with an increase in participating dipoles or ions. According to the ideal Debye's dispersion equation, the frequency dependence of ε' is,

$$\varepsilon' = \varepsilon'_\infty + \frac{(\varepsilon'_0 - \varepsilon'_\infty)}{1+(\omega\tau)^2} \tag{1.14}$$

$$\varepsilon'' = \frac{(\varepsilon'_0 - \varepsilon'_\infty)\omega\tau}{1+(\omega\tau)^2} \tag{1.15}$$

Where, ε'_∞ and ε'_0 are the permittivity values at high and low frequency respectively, and τ is relaxation time constant. Due to the trailing of dipoles behind the field, ε' decreases with increasing frequency, whereas ε'' reaches its maximum at $\omega = {}^1/_\tau$, where the oscillating charges are linked with the oscillating field and absorb the most electrical energy. Numerous materials have a non-Debye dielectric behaviour defined by a wider asymmetric loss peak when several ions are responsible for dielectric dispersion [88]. Havriliak-Negami [89] provided the Cole-Cole, Davidson-Cole, and empirical expressions to characterise the non-Debye behaviour of a material. Electric modulus (M), which is defined as the inverse of relative permittivity, is used to analyse dielectric behaviour at comparatively higher temperatures, where ε becomes normally quite high owing to electrode polarization and carrier transport.

1.6.2 POLARIZATION

The cations in ferrites are surrounded by tightly packed oxygen anions and are thus regarded to be isolated. Therefore, the electrons or holes associated with a certain ion will stay isolated, resulting in the creation of a potential well. The transition to an adjacent lattice site for a trapped carrier charge at a lattice site in such a deep well might be induced by thermal activation or at a higher frequency. This trapped charge, known as a small polaron, is caused by the crystal lattice defect and, when an electric field is applied, polarization is generated [90]. The positioning of cations in A or B sites of ferrites have a substantial effect on the movement of charge carriers and the defining aspects of their dielectric properties. In addition, the interaction of electron hopping between cations produces dipole pairs in ferrites, which contribute to dipolar polarization [85]:

$$T^{2+} + Fe^{3+} \leftrightarrow T^{3+} + Fe^{2+} + E_a \tag{1.16}$$

Where E_a is the activation energy necessary for electron transfer from T^{2+} to Fe^{3+} and vice versa. Based on the source of origination, there are several kinds of polarization:

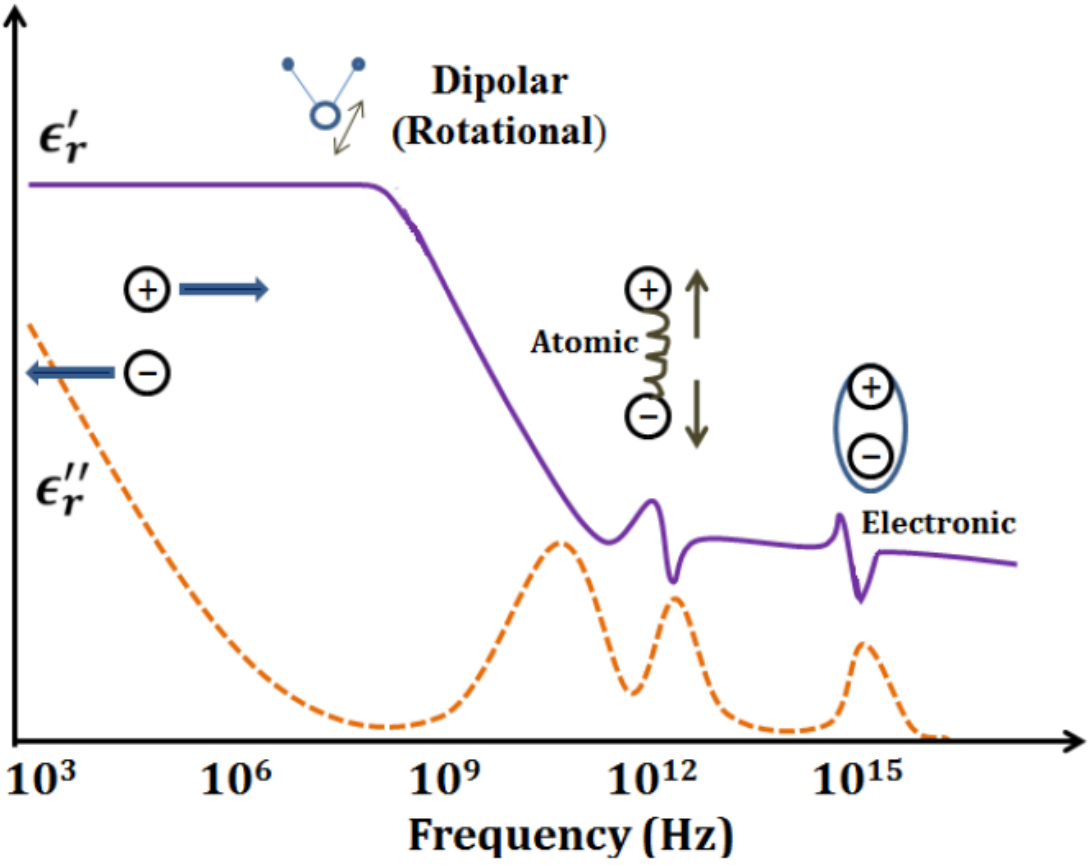

Figure 1.10. Dielectric response with varying frequency

- Electronic Polarization: When an external field is present, the electron cloud travels in relation to the nucleus. Electronic polarization is predominant at 10^{12} Hz; therefore, its negligible contribution at low frequencies is enhanced at optical frequencies. The reaction time of this polarisation is ~ 10^{-15} s.
- Atomic Polarization: Atomic polarization takes place when neighbouring positive and negative ions "stretch" in response to an applied electric field. This form of polarization is effective at THz and microwave frequencies, in addition to having a reaction time of 10^{-13} s and operating at frequencies between 10^{9} Hz and 10^{12} Hz. In addition to dielectric relaxation, high frequency dielectric systems exhibit a resonance-type dielectric response. Also, Tang *et al*. discussed the inertial effects in charge movement or anomalous dispersion [91].
- Dipolar Polarization: Dipolar or orientation polarization refers to the alignment of dipoles in an electric field by orientation. Orientation polarization typically takes about 10^{-9} s and predominates between 10^{3} Hz - 10^{9} Hz [92].
- Space Charge Polarization: Interfacial polarization is caused by the build-up of space charge at the structural interfaces of an inhomogeneous dielectric material. This process involves the trapped charge carriers, and as the temperature rises, more carriers are activated by thermal agitation which in turn increases the space charge polarization. Its operating frequency range is less than 10^{7} Hz at room temperature, and lies between the microwave and radio-wave frequency bands.

As frequency rises, slower processes disappear, leaving only quicker mechanisms to contribute to value. A schematic dielectric constant, ε, versus frequency curve exhibiting several forms of polarization is given in Fig. 1.10. The Maxwell-Wagner grain-grain boundary model for ferrites and the Cole-Cole plot may be used to describe this dielectric relaxation.

1.6.3 MAXWELL-WAGNER MODEL AND COLE-COLE PLOT

Conducting grains and grain boundary layers of ferrite material may be interpreted as an inhomogeneous polycrystalline dielectric structure established by Maxwell and Wagner, according to a theory provided by Koops[93]. When an external electric field is introduced, charge carriers travel easily from the grain and accumulate (space charge) at the grain's resistive boundaries. This method may generate a large polarization and a high ε' at low frequencies. In the presence of charge movement inertia, dipoles would relax relative to the polarizing field,

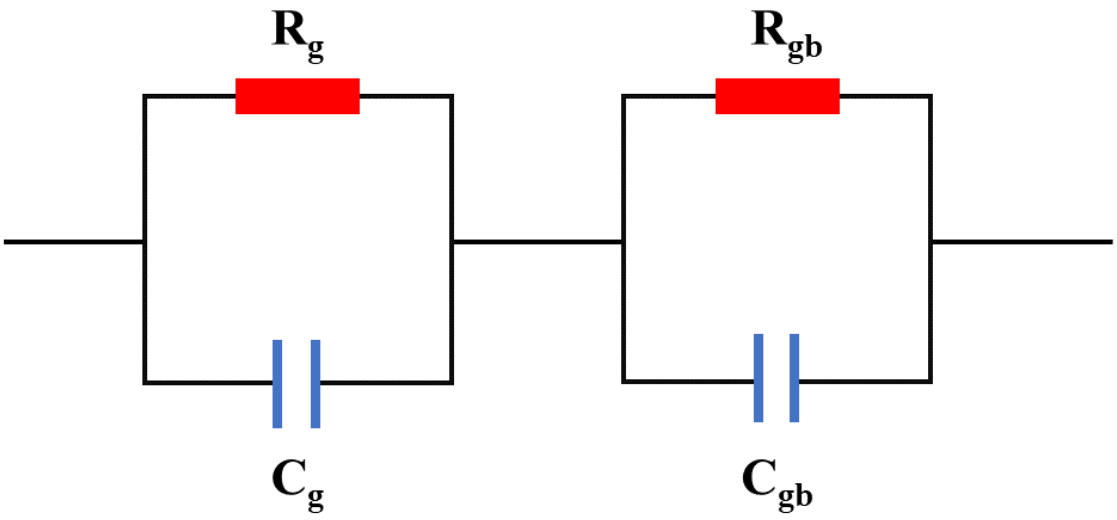

Figure 1.11. Equivalent circuit of grain and grain boundary resistances and capacitances in a material

resulting in a limited phase difference with the field. After a distinctive cut-off frequency that is sufficiently high, the phase lag in the carriers becomes evident, leading ε' to diminish. At these frequencies, conductive grains become more active and electron hopping takes place, which increases the conductivity of the material.

The Cole-Cole plot is essentially a simple real part of impedance (Z') versus imaginary part of impedance (Z'') plot that can represent the Maxwell-Wagner two-layer model and the electrical processes happening inside the system, and the relaxation mechanism. At a certain temperature, a Debye-type material displays a perfect semi-circular plot, but a non-Debye-type material displays a deformed semi-circle and an electrode-sample interface displays an inclined line plot.

Fig. 1.11 depicts the equivalent circuit of a grain and grain boundary model of a material, which may be used to analyse the resistive and capacitive components of the material's complex impedance (Z). The analogous circuit depicts the grain and grain boundaries with resistances, R_g and R_{gb} and capacitances, C_g and C_{gb}, respectively. Components of resistance and capacitance are linked in parallel, whereas the grains and grain boundaries are connected in series.

Therefore, the equivalent impedance may be calculated as,

$$Z = Z_g + Z_{gb} \tag{1.17}$$

Here, Z_g is the complex impedance of the grain and Z_{gb} is the complex impedance of the grain boundary.

Therefore,

$$\frac{1}{Z_g} = \frac{1}{R_g} + j\omega C_g \tag{1.18}$$

$$Z_g = \frac{R_g}{1+j\omega C_g R_g} \tag{1.19}$$

And,

$$\frac{1}{Z_{gb}} = \frac{1}{R_{gb}} + j\omega C_{gb} \tag{1.20}$$

$$Z_{gb} = \frac{R_{gb}}{1+j\omega C_{gb} R_{gb}} \tag{1.21}$$

Substituting these expressions in Eq. 1.17, we get,

$$Z = Z_g + Z_{gb} = \frac{R_g}{1+j\omega C_g R_g} + \frac{R_{gb}}{1+j\omega C_{gb} R_{gb}} \tag{1.22}$$

$$Z' - jZ'' = \frac{R_g(1-j\omega C_g R_g)}{1+\omega^2 C_g^2 R_g^2} + \frac{R_{gb}(1-j\omega C_{gb} R_{gb})}{1+\omega^2 C_{gb}^2 R_{gb}^2} \tag{1.23}$$

$$Z' - jZ'' = \left[\frac{R_g}{1+\omega^2 C_g^2 R_g^2} + \frac{R_{gb}}{1+\omega^2 C_{gb}^2 R_{gb}^2}\right] - j\omega\left[\frac{C_g R_g^2}{1+\omega^2 C_g^2 R_g^2} + \frac{C_{gb} R_{gb}^2}{1+\omega^2 C_{gb}^2 R_{gb}^2}\right] \tag{1.24}$$

Equating the real and imaginary parts from both sides of the above equation,

$$Z' = \left[\frac{R_g}{1+\omega^2 C_g^2 R_g^2} + \frac{R_{gb}}{1+\omega^2 C_{gb}^2 R_{gb}^2}\right] \tag{1.25}$$

$$Z'' = \left[\frac{\omega C_g R_g^2}{1+\omega^2 C_g^2 R_g^2} + \frac{\omega C_{gb} R_{gb}^2}{1+\omega^2 C_{gb}^2 R_{gb}^2}\right] \tag{1.26}$$

1.6.4 CONDUCTION

In dielectric ferrites, when the frequency of the applied field rises, the conductive grains become more active by promoting the hopping of electrons and holes between Fe^{2+} and T^{3+} ions and vice versa, hence speeding the hopping rate. As the frequency of the applied field rise, it is possible to witness a progressive increase in conductivity accompanied by a reduction in polarization. Jonscher's power law offers a simple formula for the frequency dependence of conductivity [94], [95],

$$\sigma_{ac}(\omega, T) = \sigma_{dc}(\omega, T) + A\omega^S(T) \tag{1.27}$$

Here, σ_{dc} is the material's DC conductivity, A is material-dependent constant, and s is a temperature-dependent parameter that fluctuates between 0 and 1 depending on the conduction mechanism. Even though grain boundaries are resistive and may hamper ionic transport, a high defect density in the interfacial areas adds to the high conduction path. Thermal excitation increases charge hopping by increasing charge carrier mobility and concentration. Fitting the Arrhenius equation of conductivity to $\ln(\sigma_{ac})$ vs. $1/k_BT$ plot at low frequency yield the activation energy (assuming it is thermally activated) for dc conduction (E_{dc}).

1.7 MICROWAVE PROPERTIES

With the extensive growth of technology, such as wireless information transmission, global navigation, and radar (radio detection and ranging) communication, the need for ferrites for high-frequency applications is fast increasing [96]–[98]. A recent study suggests that around 23 percent of engineering research focuses on ferrites, which enhances production and decreases the cost of microwave devices [99]. Ferrites are iron-based ferrimagnetic oxides that combine magnetic material and electrical insulator properties [100]. They allow electromagnetic (EM) waves to permeate the material and, because to their high resistivity, minimize eddy current loss, hence broadening the spectrum of applications for high-frequency devices. In non-reciprocal devices such as circulators, fast sensors with ferrite properties such as strong anisotropy, low FMR (ferromagnetic resonance) bandwidth, and low loss are required [100]–[102]. For microwave absorbers, on the other hand, lossy material with a large resonance bandwidth and a good matching of relative permittivity ($\varepsilon = \varepsilon' - j\varepsilon''$) and permeability ($\mu = \mu' - j\mu''$) are required.

Electromagnetic Interference (EMI) has become a serious issue recent years due to the proliferation of high-frequency devices [91]. Multiple forms of electromagnetic interference cause misunderstanding of transported information, noise, and thus a slowdown of electronic devices. Furthermore, this undesired wave pollution is harmful to the environment and human health. Electromagnetic absorbers (EMA) are thus essential for reducing and shielding harmful electromagnetic radiation [103], [104]. Films of EMA materials may be employed as frequency-selective band pass filters in circuit components. In addition, since the 19th century, the military has used EMA materials extensively in 'stealth technology' to render aircrafts and ships radar-invisible [105], [106]. Despite ferrite's prevalence in high-frequency devices, its weight is their principal disadvantage; for practical applications, thin, light, and affordable

microwave absorbers are expected to be most effective [96], [103], [107]. EMA materials based on ferrite inhibit the reflection of EM waves and transform the bulk of their energy into heat. In regard to this heat dissipation and material's temperature increase, ferrites with their lower thermal coefficient and stability may function satisfactorily up to 200 °C owing to their thermal resistance. For research and application purposes, ferrite fillers are typically disseminated and precisely formed inside a suitable polymer matrix. Numerous techniques for measuring permeability and permittivity have evolved throughout time. These approached include free-space methods, open-ended coaxial probe techniques, cavity resonators, full-body resonance techniques, and transmission-line techniques [108]. Each approach has its own application range and intrinsic constraints. For example, cavity-based approaches are accurate but not wideband [108]. Transmission line techniques are the straightforward and precise methods for measuring the defining characteristics of materials. In the next sections, transmission line method and electromagnetic wave theory are presented in depth in relation to microwave absorption.

1.7.1 RELATED ELECTROMAGNETIC THEORY

Electric and magnetic processes and electromagnetic wave propagation at the macroscopic level are described by Maxwell's equations, published in 1873, set the framework for the practical uses of guided waves and transmission lines. Following are the Maxwell's equations for a material:

$$\vec{\nabla}.\vec{D} = \rho \tag{1.28}$$

$$\vec{\nabla}.\vec{B} = 0 \tag{1.29}$$

$$\vec{\nabla} \times \vec{E} = -\frac{\partial \vec{B}}{\partial t} \tag{1.30}$$

$$\vec{\nabla} \times \vec{H} = \vec{J} + \frac{\partial \vec{D}}{\partial t} \tag{1.31}$$

Here, $\vec{D} = \varepsilon_0 \vec{E} + \vec{P} = \varepsilon \vec{E}$, represents electric displacement, $\vec{B} = \mu_0(\vec{H} + \vec{M})$, magnetic flux density, ρ, free charge density and $\vec{J} = \sigma \vec{E}$, current density in the material. Fig. 1.12 depicts the orientation of the $\vec{E}$, $\vec{H}$, and $\vec{k} = k\hat{n}$ vectors for a generic plane wave. $\vec{H}$ can be expressed in terms of $\vec{E}$ as,

$$\vec{H} = -\frac{1}{j\omega\mu_0}\vec{\nabla} \times (\vec{E}_0 e^{-j\vec{k}.\vec{r}}) \tag{1.32}$$

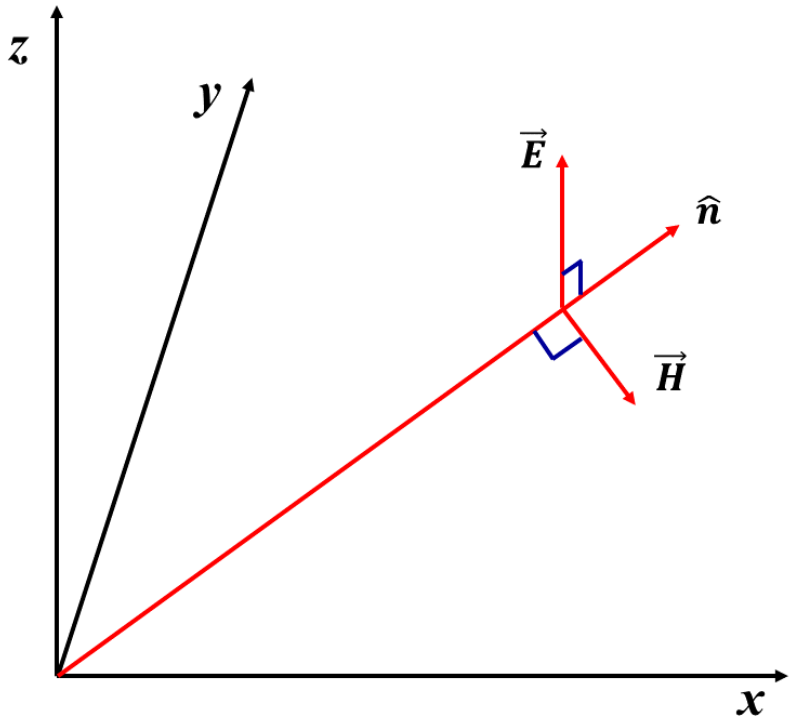

Figure 1.12. Orientation of the $\vec{E}$, $\vec{H}$, $\vec{k} = k\hat{n}$ vectors for a general plane wave

$$= \frac{1}{\omega\mu_0}\vec{k} \times \vec{E}_0 e^{-j\vec{k}.\vec{r}} \tag{1.33}$$

$$= \sqrt{\frac{\varepsilon_0}{\mu_0}}(\hat{n} \times \vec{E}) \tag{1.34}$$

Considering wave equation, $\vec{E} = E_0 \cos(\omega t + \varphi)\hat{x}$, Maxwell's equations are in phasor form,

$$\vec{\nabla}.\vec{D} = \rho \tag{1.35}$$

$$\vec{\nabla}.\vec{B} = 0 \tag{1.36}$$

$$\vec{\nabla} \times \vec{E} = -j\omega\vec{B} \tag{1.37}$$

$$\vec{\nabla} \times \vec{H} = \vec{J} + j\omega\vec{D} \tag{1.38}$$

The propagation of alternating EM waves shows that the permittivity of a material is complex in nature. In this situation, Eq. 1.38 takes the form below and dielectric loss tangent is defined as follows,

$$\vec{\nabla} \times \vec{H} = j\omega(\varepsilon' - j\varepsilon'')\vec{E} + \sigma\vec{E} \tag{1.39}$$

$$\tan\delta_\varepsilon = \frac{(\sigma + \omega\varepsilon'')}{\varepsilon'} \tag{1.40}$$

Solving for $\vec{E}$ or $\vec{H}$ from 1.37 and 1.38 gives Helmholtz wave equations:

$$\vec{\nabla} \times \vec{\nabla} \times \vec{E} = -j\omega\mu\vec{\nabla} \times \vec{H} = \omega^2\mu\varepsilon\vec{E}$$

$$\nabla^2\vec{E} + \omega^2\mu\varepsilon\vec{E} = 0 \tag{1.41}$$

A constant $k = \omega\sqrt{\mu\varepsilon}$ is defined as the propagation constant (also known as the phase constant, or wave number) of the medium. The resulting wave equation for $\vec{E}$ for plane waves in a general lossy (with finite conductivity σ) medium is:

$$\nabla^2\vec{E} + \omega^2\mu\varepsilon(1 - j\frac{\sigma}{\omega\varepsilon})\vec{E} = 0 \tag{1.42}$$

Then a complex propagation constant for the medium is defined as,

$$\gamma = \alpha + j\beta = j\omega\sqrt{\mu\varepsilon}\sqrt{1 - j\frac{\sigma}{\omega\varepsilon}} \tag{1.43}$$

where α is the attenuation constant and β is the phase constant.

The expression of complex propagation constant, γ, consists of real part, α, known as attenuation constant and imaginary part, β, known as phase constant.

From Fig. 1.12 and considering modified Helmholtz equation, relation between magnetic and electric field transforms to,

$$\vec{H} = \frac{\gamma}{j\omega\mu}\vec{E} \tag{1.44}$$

The intrinsic impedance of the conducting medium is denoted by, $\eta = \frac{j\omega\mu}{\gamma}$. As the skin-depth, $\delta = {}^{1}/_{\alpha} = \sqrt{{}^{2}/_{\omega\mu\sigma}}$ decreases for strongly conducting materials, such as metal (high σ), EM waves do not enter the substance. The average power (P_l) lost in a lossy medium with volume V due to conductivity, dielectric, and magnetic losses is,

$$P_l = \frac{\sigma}{2}\int E^2 dv + \frac{\omega}{2}\int(\varepsilon'' E^2 + \mu'' H^2)dv \tag{1.45}$$

However, magnetic hysteresis and domain wall resonance become less important at low fields and high frequencies ($f > 100$ MHz for ferrites), but typical FMR and eddy current loss become more pronounced in the gigahertz region [109], [110].

When a z-propagating EM wave reaches a media interface, part of the energy is reflected and some is transmitted through the medium. Assuming normal incidence (as shown in Fig. 1.13), the expressions for incident waves (E_i, H_i), reflected (E_r, H_r) and transmitted (E_t, H_t) will be,

(at $z < 0$)

$$\vec{E}_i = \hat{x} E_0 e^{-jk_0 z} \tag{1.46}$$

$$\vec{H}_i = \hat{y} \frac{1}{\eta_0} E_0 e^{-jk_0 z} \tag{1.47}$$

$$\vec{E}_r = \hat{x} \Gamma E_0 e^{jk_0 z} \tag{1.48}$$

$$\vec{H}_i = -\hat{y} \frac{\Gamma}{\eta_0} E_0 e^{jk_0 z} \tag{1.49}$$

(at $z > 0$)

$$\vec{E}_t = \hat{x} T E_0 e^{-\gamma z} \tag{1.50}$$

$$\vec{H}_t = \hat{y} \frac{T}{\eta} E_0 e^{-\gamma z} \tag{1.51}$$

Here, Γ represents the reflection coefficient, T, represents the transmission coefficient and η_0, represents the inherent impedance of free space ($\sim 377\ \Omega$). Since the tangential field components must be continuous at $z = 0$, the resulting equations are as follows,

$$1 + \Gamma = T \tag{1.52}$$

$$1 - \frac{\Gamma}{\eta_0} = \frac{T}{\eta} \tag{1.53}$$

Solving the equations, Γ and T can be expressed as,

$$\Gamma = \frac{\eta - \eta_0}{\eta + \eta_0} \tag{1.54}$$

$$T = \frac{2\eta}{\eta + \eta_0} = 1 + \Gamma \tag{1.55}$$

Reflection loss (RL) relating to the reflected power of an EM wave from a material is described as Γ value as, RL (in dB) $= -20\log|\Gamma|$. According to convention, the sign for RL is assumed to be negative $(-)$ in this thesis.

Different transverse modes are associated with an EM wave confined inside a waveguide, optical fibre, or resonator dependent on the transmission line boundary conditions. The topic will continue the subsequent section.

1.7.2 TRANSMISSION LINE ANALOGY

Typically, transmission lines consist of many conducting lines. Circuit components connected with such conductors include series resistance (R) for their length, series inductance (L) from conductors, shunt capacitance (C) from parallelly arranged conductors, and an additional shunt conductance (G) from added load [111]. Along the length of a transmission line, the amplitude and phase of voltages and currents can vary dramatically. Since these transmission lines are small, inexpensive, and can be easily integrated with active circuit devices; they are of tremendous importance in the study of microwave circuits and devices [112]. Transmission lines with multiple conductors can only sustain transverse electromagnetic (TEM) waves, since longitudinal field components are missing. Waveguides with a single conductor support transverse electric (TE) and/or transverse magnetic (TM) waves, which are distinguished by the existence of longitudinal magnetic or electric field components, respectively. According to the Maxwell equations, fields with their transverse components are [113],

$$\vec{E}(x,y,z) = [\overrightarrow{E_0}(x,y) + \hat{z}E_z(x,y)]e^{-j\beta z} \tag{1.56}$$

$$\vec{H}(x,y,z) = [\overrightarrow{H_0}(x,y) + \hat{z}H_z(x,y)]e^{-j\beta z} \tag{1.57}$$

And,

$$H_x = \frac{j}{k_c^2}\left(\omega\varepsilon\frac{\partial E_z}{\partial y} - \beta\frac{\partial H_z}{\partial x}\right) \tag{1.58}$$

$$H_y = -\frac{j}{k_c^2}\left(\omega\varepsilon\frac{\partial E_z}{\partial x} + \beta\frac{\partial H_z}{\partial y}\right) \tag{1.59}$$

$$E_x = -\frac{j}{k_c^2}\left(\beta\frac{\partial E_z}{\partial x} + \omega\mu\frac{\partial H_z}{\partial y}\right) \tag{1.60}$$

$$E_y = \frac{j}{k_c^2}\left(-\beta\frac{\partial E_z}{\partial y} + \omega\mu\frac{\partial H_z}{\partial x}\right) \tag{1.61}$$

where $k_c = \sqrt{k^2 - \beta^2}$, is cut-off wave number. Solution for TE mode characterized by $E_z = 0$ and $H_z \neq 0$, from $H_z(x,y,z) = h_z(x,y)e^{-j\beta z}$ and reduced Helmholtz wave equation,

$$\left(\frac{\partial^2}{\partial x^2} + \frac{\partial^2}{\partial y^2} + \frac{\partial^2}{\partial z^2}\right)h_z = 0 \tag{1.62}$$

For rectangular waveguide with breadth 'a' and width 'b', general solution of 1.62 gives,

$$h_z(x,y) = X(x)Y(y)$$

$$h_z(x,y) = (A\ cosk_x x + B\ sink_x x)(C\ cosk_y y + B\ sink_y y) \tag{1.63}$$

Considering the following boundary conditions on the electric field components tangential to the waveguide walls,

$$e_x(x,y) = 0\ at\ y = 0, b$$

$$e_y(x,y) = 0\ at\ x = 0, a$$

The final solution for H_z is,

$$H_z(x,y,z) = A_{mn} cos\frac{m\pi x}{a} cos\frac{n\pi y}{b} e^{-j\beta z} \tag{1.64}$$

Where, the propagation constant for TE_{mn} mode is $\beta = \sqrt{k^2 - \pi^2\left[\left(\frac{m}{a}\right)^2 + \left(\frac{n}{b}\right)^2\right]}$. The associated cut-off frequency is given by $f_{c_{mn}} = \frac{1}{2\pi\sqrt{\mu\varepsilon}}\pi^2\left[\left(\frac{m}{a}\right)^2 + \left(\frac{n}{b}\right)^2\right]$. The dominant mode is the mode with the lowest cut-off frequency, which is TE_{10} mode in this case. At a given operating frequency f only those modes having $f > f_c$ will propagate, modes with $f < f_c$ will lead to an imaginary β (or real α), that means all field components will decay exponentially from the source of excitation. Such modes are referred to as evanescent modes, which can lead

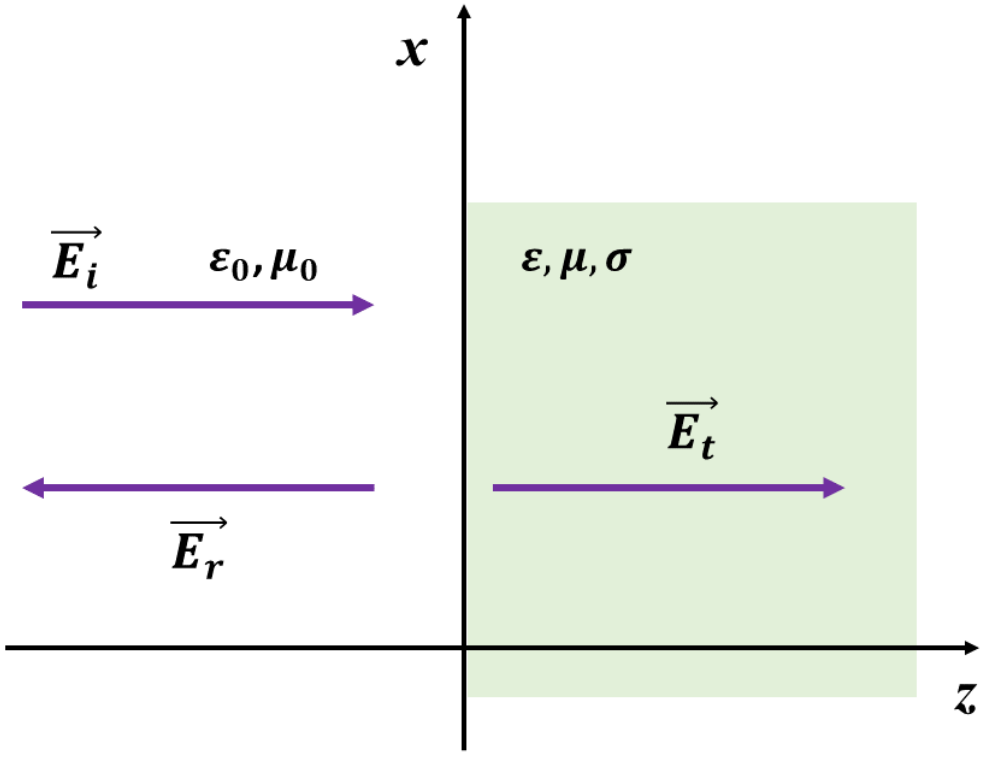

Figure 1.13. Plane wave reflection from an arbitrary medium: normal incidence

to overmodulation; as a result, signal noise can be generated.

Transverse electromagnetic (TEM) waves are characterized by $E_z = H_z = 0$. Here, from Equations 1.58-1.61, both k and β equals to $\omega\sqrt{\mu\varepsilon}$. The cut-off wave number, $k_c = \sqrt{k^2 - \beta^2}$, is thus zero for TEM waves. When a gradient of a scalar potential, $\varphi(x, y)$ arises between two conductors in a waveguide, TEM mode can propagate. Solving Laplace's equation between the two conductors,

$$\nabla_t^2 h(x, y) = 0 \tag{1.65}$$

$$\vec{E}(x, y) = \overrightarrow{\nabla_t}\varphi(x, y) \tag{1.66}$$

With an understanding of wave mode propagation in transmission lines, the voltage (v) and current (i) definitions of a two-wire line are derived through circuit analysis. Fig. 1.14 depicts the schematic representation of a transmission line and its components.

From the circuit diagram, Kirchhoff's voltage and current laws can be applied to give,

$$v(z, t) - R\Delta z i(z, t) - L\Delta z \frac{\partial i(z,t)}{\partial t} - v(z + \Delta z, t) = 0 \tag{1.67}$$

$$i(z, t) - G\Delta z v(z + \Delta z, t) - C\Delta z \frac{\partial v(z+\Delta z,t)}{\partial t} - i(z + \Delta z, t) = 0 \tag{1.68}$$

For the steady-state condition, the above equations can be simplified into their phasor forms,

$$\frac{dV(z)}{dz} + (R + j\omega L)I(z) = 0 \tag{1.69}$$

$$\frac{dI(z)}{dz} + (G + j\omega C)V(z) = 0 \tag{1.70}$$

Comparing these with wave equations for $V(z)$ and $I(z)$, with propagation constant, $\gamma = \sqrt{(R + j\omega L)(G + j\omega C)}$,

$$V(z) = V_0^+(e^{-\gamma z} + \Gamma e^{\gamma z}) \tag{1.71}$$

$$I(z) = \frac{V_0^+}{Z_0}(e^{-\gamma z} - \Gamma e^{\gamma z}) \tag{1.72}$$

where the $e^{-\gamma z}$ term represents wave propagation in the $+z$ direction, and the $e^{\gamma z}$ term, wave propagation in the $-z$ direction. Characteristic impedance (Z_0) of the circuit is defined as,

$$Z_0 = \frac{V_0^+}{I_0^+} = \sqrt{\frac{R+j\omega L}{G+j\omega C}} \tag{1.73}$$

For a coaxial line with inner diameter (a) and outer diameter (b), geometry dependent characteristic impedance is related to intrinsic or wave impedance in the way,

$$Z_0 = \frac{E_\rho \ln(\frac{b}{a})}{2\pi H_\varphi} = \sqrt{\frac{\mu}{\varepsilon}} \frac{\ln(\frac{b}{a})}{2\pi} = \eta \frac{\ln(\frac{b}{a})}{2\pi} \tag{1.74}$$

When transmission line is terminated in an arbitrary load impedance Z_L, at load point, $Z_L = \frac{V}{I} = \frac{V_0^+ + V_0^-}{V_0^+ - V_0^-} Z_0$. Therefore, solving for V_0^- gives,

$$\frac{V_0^-}{V_0^+} = \frac{Z_L - Z_0}{Z_L + Z_0} = \Gamma \tag{1.75}$$

At a distance $z = -l$ from the load, the input impedance (Z_{in}) seen looking toward the load is (from equations 1.71, 1.72, and 1.75),

$$Z_{in} = \frac{V(-l)}{I(-l)} = Z_0 \frac{Z_L + Z_0 \tanh \gamma L}{Z_0 + Z_L \tanh \gamma L} \tag{1.76}$$

As a special case of this transmission line impedance equation, a line is terminated in a short circuit, i.e., $Z_L = 0$, input impedance takes the form,

$$Z_{in} = Z_0 \tanh \gamma L \tag{1.77}$$

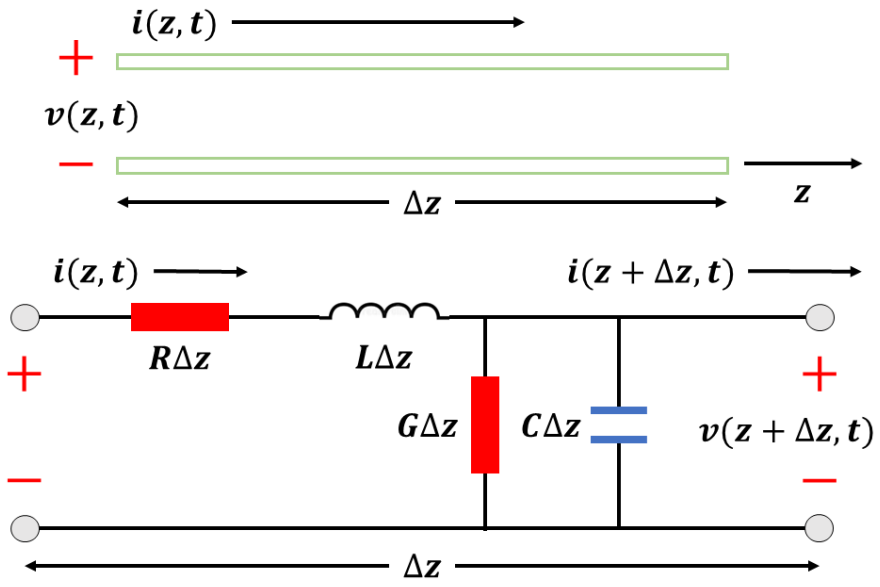

Figure 1.14. Equivalent circuit for an incremental length of transmission line

1.7.2.1 RECTANGULAR WAVEGUIDE

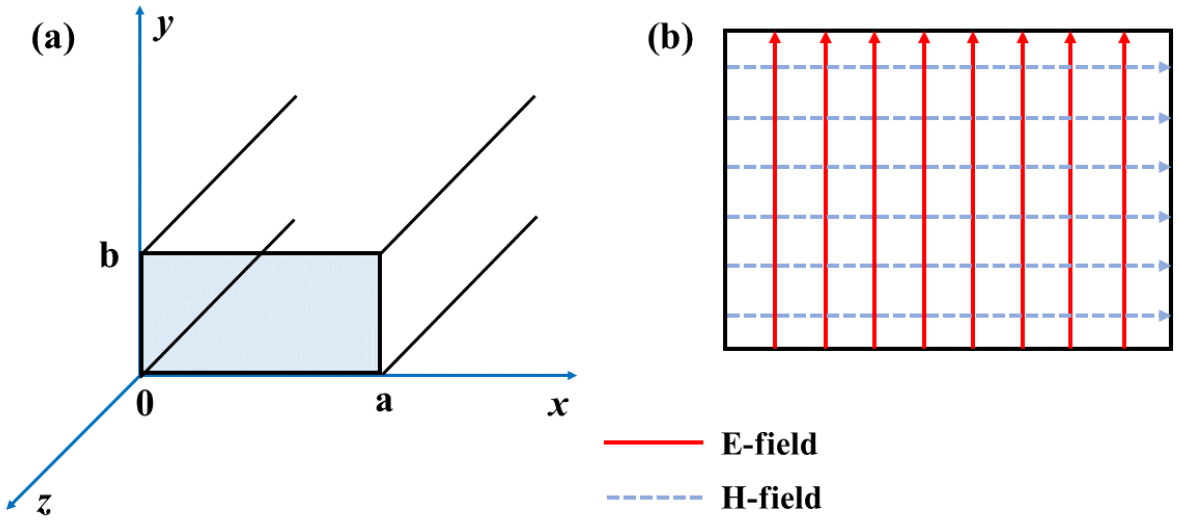

Figure 1.15. Geometry of a rectangular waveguide and field lines for TE_{10} mode

The simplest and most dominant mode of propagation in a rectangular waveguide with breadth (a) and width (b) ($a > b$) is the so-called TE_{10} mode, which is dependent on longer side 'a'. Even though TM mode may travel via this waveguide, its cut-off frequency is much greater than that of TE mode. Being a closed conductor, it cannot sustain TEM waves, as the static potential in such a region would be either zero or a constant. Rectangular waveguides are often used to transport large quantities of microwave power at high frequencies, and exact material characteristics may be determined using this kind of waveguide. Fig. 1.15 depicts a schematic representation of a rectangular waveguide and its field propagation.

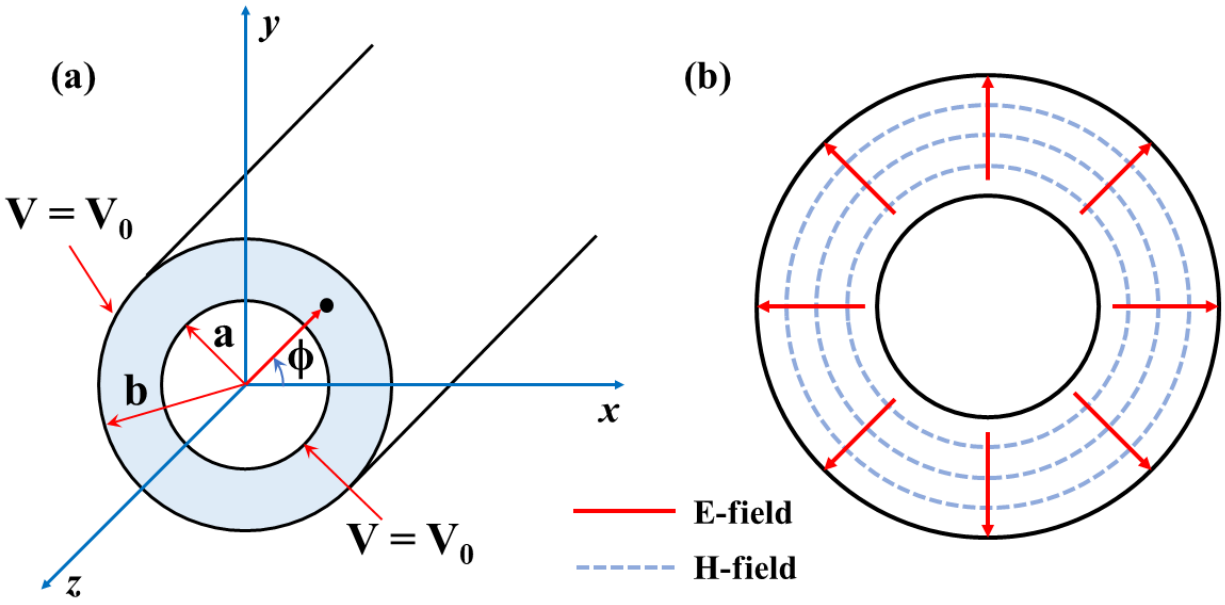

Figure 1.16. Geometry of a coaxial line and field lines for TEM mode

1.7.2.2 COAXIAL AIRLINE

Though TE and TM modes may propagate across coaxial cable, the TEM mode with no cut-off frequency remains the dominant mode due to its lack of cut-off frequency. As coaxial cable has no frequency constraints, it is a wide band waveguide. In addition, coaxial line, like rectangular waveguide, is insulated and may be employed at high frequencies. The geometry of coaxial lines and field lines is seen in Fig. 1.16.

1.7.3 ATTENUATION CONSTANT

The γ can be expressed using the well-known formula[111]:

$$\gamma = j\omega\sqrt{\mu\varepsilon} \tag{1.78}$$

Where, μ is the complex permeability and ε is the complex permittivity.

$$\mu = \mu_0(\mu' - i\mu'') \tag{1.79}$$

$$\varepsilon = \varepsilon_0(\varepsilon' - i\varepsilon'') \tag{1.80}$$

Where, ε', ε'' represent the real and imaginary components of complex permittivity, μ', μ'' represent the real and imaginary parts of the complex permeability, ε_0 and μ_0 reflect the free space permittivity and permeability respectively.
Putting these expressions of μ and ε in γ,

$$\gamma = j\omega\sqrt{\mu_0\varepsilon_0}[(\mu' - i\mu'')(\varepsilon' - i\varepsilon'')]^{1/2}$$

$$\gamma = j\omega\sqrt{\mu_0\varepsilon_0}[(\mu'\varepsilon' - \mu''\varepsilon'') - i(\mu'\varepsilon'' + \mu''\varepsilon')]^{1/2}$$

$$\gamma^2 = -\omega^2\mu_0\varepsilon_0[(\mu'\varepsilon' - \mu''\varepsilon'') - i(\mu'\varepsilon'' + \mu''\varepsilon')] \tag{1.81}$$

Replacing, $c^2 = \frac{1}{\sqrt{\mu_0\varepsilon_0}}$ in Eq. 1.81:

$$\gamma^2 = \frac{\omega^2}{c^2}[(\mu''\varepsilon'' - \mu'\varepsilon') + i(\mu'\varepsilon'' + \mu''\varepsilon')] \tag{1.82}$$

Replacing, $\gamma = \alpha + j\beta$ in Eq. 1.82:

$$\alpha^2 - \beta^2 + 2j\alpha\beta = \frac{\omega^2}{c^2}[(\mu''\varepsilon'' - \mu'\varepsilon') + i(\mu'\varepsilon'' + \mu''\varepsilon')] \tag{1.83}$$

Equating, real and imaginary parts from both sides of Eq. 1.83:

$$\alpha^2 - \beta^2 = \frac{\omega^2}{c^2}(\mu''\varepsilon'' - \mu'\varepsilon') \tag{1.84}$$

$$2\alpha\beta = \frac{\omega^2}{c^2}(\mu'\varepsilon'' + \mu''\varepsilon')$$

Or,

$$\beta = \frac{\omega^2}{2\alpha c^2}(\mu'\varepsilon'' + \mu''\varepsilon') \tag{1.85}$$

Replacing the expression of b in Eq. 1.84,

$$\alpha^2 - \frac{\omega^4}{4\alpha^2 c^4}(\mu'\varepsilon'' + \mu''\varepsilon')^2 = \frac{\omega^2}{c^2}(\mu''\varepsilon'' - \mu'\varepsilon')$$

$$\alpha^4 - \frac{\omega^4}{4c^4}(\mu'\varepsilon'' + \mu''\varepsilon')^2 = \frac{\omega^2}{c^2}\alpha^2(\mu''\varepsilon'' - \mu'\varepsilon')$$

$$\alpha^4 - \frac{\omega^2}{c^2}\alpha^2(\mu''\varepsilon'' - \mu'\varepsilon') = \frac{\omega^4}{4c^4}(\mu'\varepsilon'' + \mu''\varepsilon')^2$$

$$\alpha^4 - 2.\alpha^2.\frac{\omega^2}{2c^2}(\mu''\varepsilon'' - \mu'\varepsilon') = \frac{\omega^4}{4c^4}(\mu'\varepsilon'' + \mu''\varepsilon')^2$$

$$\alpha^4 - 2.\alpha^2.\frac{\omega^2}{2c^2}(\mu''\varepsilon'' - \mu'\varepsilon') + \frac{\omega^4}{4c^4}(\mu''\varepsilon'' - \mu'\varepsilon')^2 = \frac{\omega^4}{4c^4}(\mu'\varepsilon'' + \mu''\varepsilon')^2 + \frac{\omega^4}{4c^4}(\mu''\varepsilon'' - \mu'\varepsilon')^2$$

$$[\alpha^2 - \frac{\omega^2}{2c^2}(\mu''\varepsilon'' - \mu'\varepsilon')]^2 = \frac{\omega^4}{4c^4}[(\mu'\varepsilon'' + \mu''\varepsilon')^2 + (\mu''\varepsilon'' - \mu'\varepsilon')^2]$$

$$\alpha^2 - \frac{\omega^2}{2c^2}(\mu''\varepsilon'' - \mu'\varepsilon') = \frac{\omega^2}{2c^2}[(\mu'\varepsilon'' + \mu''\varepsilon')^2 + (\mu''\varepsilon'' - \mu'\varepsilon')^2]^{1/2}$$

$$\alpha^2 = \frac{\omega^2}{2c^2}(\mu''\varepsilon'' - \mu'\varepsilon') + \frac{\omega^2}{2c^2}[(\mu'\varepsilon'' + \mu''\varepsilon')^2 + (\mu''\varepsilon'' - \mu'\varepsilon')^2]^{1/2}$$

$$\alpha = \frac{\omega}{\sqrt{2}c}\sqrt{(\mu''\varepsilon'' - \mu'\varepsilon') + \sqrt{(\mu'\varepsilon'' + \mu''\varepsilon')^2 + (\mu''\varepsilon'' - \mu'\varepsilon')^2}} \tag{1.86}$$

Replacing, $\omega = 2\pi f$

$$\alpha = \frac{\sqrt{2}\pi f}{c}\sqrt{(\mu''\varepsilon'' - \mu'\varepsilon') + \sqrt{(\mu'\varepsilon'' + \mu''\varepsilon')^2 + (\mu''\varepsilon'' - \mu'\varepsilon')^2}} \tag{1.87}$$

1.7.4 EXPRESSION OF MAGNETIC TANGENT LOSS

The permeability μ, of a material, is defined as,

$$\vec{B} = \mu\vec{H} \tag{1.88}$$

where $\vec{B}$ is the flux density (T), $\vec{H}$ is the magnetic field intensity (A/m), and μ_0 is the permeability of free space (4π x 10^{-7} H/m).

Similarly, to how electric losses may be represented by a complex permeability, time-varying magnetic field losses can be characterized by a complex relative permeability

$$\mu = \mu' - i\mu'' \tag{1.89}$$

where μ' is the permeability and μ'' describes all the magnetic losses. An analogous magnetic loss tangent, $\tan\delta_\mu$ can also be defined,

$$\tan\delta_\mu = \frac{\mu''}{\mu'} \tag{1.90}$$

On the other hand, the power P, absorbed per unit volume (W/m^3) of the sample at a given instant in time can be given by[114],

$$P = 2\pi f\mu_0\mu''\left|\vec{H}\right|^2 = 2\pi f\mu_0\mu'\tan\delta_\mu\left|\vec{H}\right|^2 \tag{1.91}$$

The absorbed power may be shown to vary linearly with frequency, permeability, loss tangent and the square of the magnetic field.

The energy dissipation (W) due to eddy current varies with sample shape, but always rises with the square of the frequency (f), magnetic field ($\vec{B}$), sample dimension (d) and linearly with conductivity (σ) [114]–[116].

Thus,

$$W \propto \sigma f^2\left|\vec{B}\right|^2 d^2 = k\sigma f^2\left|\vec{B}\right|^2 d^2 \tag{1.92}$$

Where, k = proportionality constant.

If the total magnetic loss is only due to Eddy current loss, then,

$$\text{Total loss } (P) \sim k\sigma f^2\vec{B}^2 d^2 \tag{1.93}$$

Substituting the expression of total loss from Eq. (1.91) in Eq. (1.93), we obtain,

$$2\pi f\mu_0\mu'\tan\delta_\mu\left|\vec{H}\right|^2 \sim k\sigma f^2\left|\vec{B}\right|^2 d^2$$

Figure 1.17. Schematic representation of a 2-port network

$$2\pi f\mu_0\mu'\tan\delta_\mu\left|\vec{H}\right|^2 \sim k\sigma f^2{\mu_0}^2{\mu'}^2\left|\vec{H}\right|^2 d^2$$

$$\tan\delta_\mu \sim \frac{k}{2\pi}\sigma f\mu_0\mu' d^2$$

$$\frac{\mu''}{\mu'} \sim \left(\frac{k}{2\pi}\right)\mu_0\mu'(d^2\sigma)f \qquad (1.94)$$

The formula derived above is the approximate expression of magnetic tangent loss when the loss generates only due to eddy current.

1.7.5 SCATTERING PARAMETERS

Incorporating EM field theory and circuit analysis, microwave network analysis provides a more easy and practical approach. A terminal pair must be properly specified since measuring voltage or current at microwave frequencies is challenging. Typical terminal or port values include impedance, admittance, and scattering matrices from circuit theory. This sort of representation leads to the creation of comparable circuits for arbitrary networks, which will be of considerable aid in the design of passive components such as couplers and filters. For a network with several ports, the impedance, admittance, and scattering characteristics in matrix form are as follows:

$$[V] = [Z][I]$$

$$[I] = [Y][V]$$

$$[V^-] = [S][V^+]$$

Due to the absence of equipment to measure port current and voltage directly and the difficulties of achieving flawless opens/shorts, it is difficult to test Y or Z characteristics directly for transmission lines at high RF and microwave frequencies. Under these

circumstances, the scattering matrix gives direct measurements for incident, reflected, and transmitted waves. A certain component of the scattering matrix is distinguished as,

$$S_{ij} = \frac{V_i^-}{V_j^+}|_{V_k^+=0,\ k\neq j} \tag{1.95}$$

In words, Eq. 1.95 states that S_{ij} is the ratio of the reflected or transmitted wave amplitude V_i^- coming at port i to the incident wave at port j is voltage V_j^+. The two-port device has four S-parameters: S_{11}, S_{21}, S_{12}, and S_{22}. Fig. 1.17 is a schematic illustration of the S-parameters of a 2-port network. Here, S_{11} and S_{22} are the forward and reverse reflection coefficients, whereas S_{21} and S_{12} are the forward and reverse gains.

The expression for 2-port S-parameters is shown below,

$$\begin{bmatrix} b_1 \\ b_2 \end{bmatrix} = \begin{bmatrix} S_{11} & S_{12} \\ S_{21} & S_{22} \end{bmatrix} \begin{bmatrix} a_1 \\ a_2 \end{bmatrix} \tag{1.96}$$

1.7.6 NICHOLSON-ROSS-WEIR ALGORITHM

Fig. 1.18 depicts the reflection and transmission of incident waves in situations when a material under test (MUT) is enclosed inside a wave guide or coaxial cable. Transmission/Reflection line measurements entail placing a sample in a portion of waveguide or coaxial line and measuring the two-port complex scattering parameters using a vector network analyser (VNA). S-parameters are converted to complex permittivity and permeability by solving equations using different techniques. Nicholson-Ross-Weir (NRW) is the most used method for measuring the values of ferrite and other magnetic materials [117]. Typically, one solves a transcendental equation using the sample length, sample position, and reflection coefficient to find and values. The phases of the NRW approach are discussed in detail below.

The first step is to determine the relationships between μ and ε values with Γ. Some parameter expressions such as γ, k_c, η are recalled, $\gamma^2 = k_c^2 - k^2$, $k_c = {}^{2\pi}/_{\lambda_c}$ (λ_c = cut-off wavelength), $k = \omega\sqrt{\varepsilon\mu}$ and $\eta = {}^{j\omega\mu}/_{\gamma}$. Reflection co-efficient, Γ is written as,

$$\Gamma = \frac{\eta-\eta_0}{\eta+\eta_0} = \frac{\frac{\gamma_0}{\gamma}\mu-1}{\frac{\gamma_0}{\gamma}\mu+1} \tag{1.97}$$

Where, γ_0 is the complex propagation constant in the air. Solving for μ,

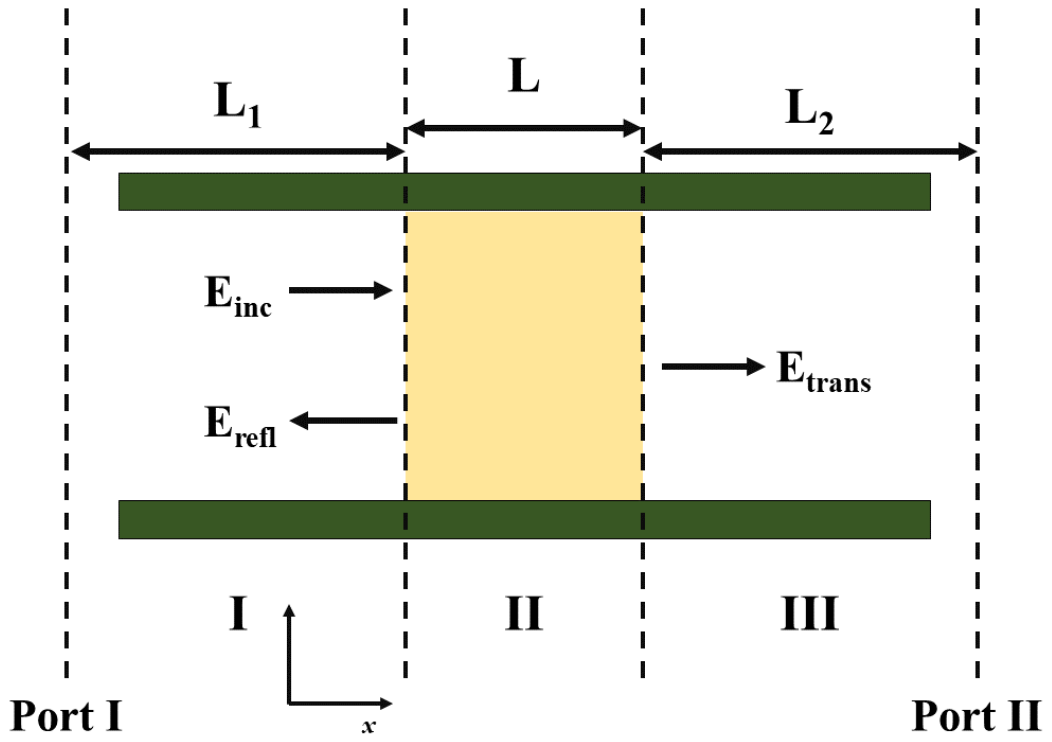

Figure 1.18. Electromagnetic waves transmitting and reflecting from a sample in a transmission line

$$\mu = \left(\frac{1+\Gamma}{1-\Gamma}\right)\frac{\gamma}{\gamma_0}$$

$$\frac{\gamma}{\gamma_0} = \frac{\sqrt{\frac{\omega^2\varepsilon\mu}{c^2} - \left(\frac{2\pi}{\lambda_c}\right)^2}}{j\sqrt{\left(\frac{\omega}{c}\right)^2 - \left(\frac{2\pi}{\lambda_c}\right)^2}} = \frac{\gamma}{j2\pi\sqrt{\frac{1}{\lambda_0^2} - \frac{1}{\lambda_c^2}}} \tag{1.98}$$

Defining $\frac{1}{\Lambda} = \frac{\gamma}{j2\pi}$ and from 1.97 and 1.98,

$$\mu = \left(\frac{1+\Gamma}{1-\Gamma}\right)\frac{1}{\Lambda\sqrt{\frac{1}{\lambda_0^2} - \frac{1}{\lambda_c^2}}} \tag{1.99}$$

From, $\gamma^2 = (2\pi)^2\left[\frac{1}{\lambda_0^2} - \frac{\mu\varepsilon}{\lambda_c^2}\right]$, solving for ε gives,

$$\varepsilon = \frac{\lambda_0^2\left[\frac{1}{\lambda_c^2} - \left(\frac{\gamma}{2\pi}\right)^2\right]}{\mu} = \frac{\lambda_0^2}{\mu}\left[\frac{1}{\lambda_c^2} + \frac{1}{\Lambda^2}\right] \tag{1.100}$$

As seen in Fig. 1.18, the following phase tries to elucidate the relationship between Γ, γ and the scattering matrix, which contains information about incident, reflected and transmitted waves. Assuming normal incidence in an isotropic medium ($S_{12} = S_{21}$), the total reflected fields (Γ_{in}) at the interface is given by,

$$\Gamma_{in} = \Gamma_{12} + T_{12}\Gamma_{in}T_{21}e^{-2\gamma L} + T_{12}\Gamma_{21}\Gamma_{23}^2T_{21}e^{-4\gamma L} + \cdots$$

$$\Gamma_{in} = \Gamma_{12} + \frac{T_{12}T_{21}\Gamma_{23}e^{-2\gamma L}}{1-\Gamma_{21}\Gamma_{23}e^{-2\gamma L}} \tag{1.101}$$

Here Γ_{ij} and T_{ij} represent the reflection coefficient and transmission coefficient of the wave propagating from material 'i' to material 'j', respectively. In the traditional arrangement, materials 1 and material 3 are air. On the basis of 1.95 and 1.96, we may conclude,

$$\Gamma_{12} = -\Gamma_{21} = -\Gamma_{23} \tag{1.102}$$

In addition, using the boundary condition of continuity for the tangential component of electric fields at the contact,

$$T_{12} = 1 + \Gamma_{21} \tag{1.103}$$

Defining $z = e^{-\gamma L}$ and $\Gamma = \Gamma_{12}$, we obtain from 1.101,

$$\frac{\sum E_{reflected}}{E_{incident}} = S_{11} = \frac{\Gamma(1-z^2)}{1-\Gamma^2z^2} \tag{1.104}$$

In a similar manner, the transmission co-efficient results in,

$$\frac{\sum E_{transmitted}}{E_{incident}} = \frac{T_{32}T_{21}e^{-\gamma L}}{1-\Gamma_{21}\Gamma_{23}e^{-2\gamma L}} = \frac{(1-\Gamma^2)z}{1-\Gamma^2z^2} = S_{21} \tag{1.105}$$

To obtain expression of Γ and z in terms of S_{11} and S_{21},

$$K = \frac{S_{11} - S_{21} + 1}{2S_{11}}$$

$$\Gamma^2 - 2\Gamma K + 1 = 0$$

$$\Gamma = K \pm \sqrt{K^2 - 1} \tag{1.106}$$

There are two solutions to the quadratic equation. The physical constraint $\Gamma < 1$ is used to identify the right solution for a passive medium. From 1.103, 1.104, and 1.105,

$$Z = \frac{S_{11}+S_{21}-\Gamma}{1-(S_{21}+S_{11})\Gamma} = e^{-\gamma L} \tag{1.107}$$

1.7.7 CORRECTIONS & POLYNOMIAL FIT MODEL

The fundamental issue with the NRW approach is its phase ambiguity, which renders the solution not totally analytic. With these transmission line approaches for magnetic materials, numerical singularities may occur at frequencies that are integral multiples of a half wave length ($\lambda/2$). The most popular solution to this issue is to utilize a very small sample size. Moreover, air gaps and over-modification are two important difficulties encountered while measuring transmission lines [118]. The defects may generate evanescent waves close to the sample-material contact, resulting in noise in the output. Among the numerous solutions, the downside of the two-sample strategy is that it requires two samples of different lengths simultaneously. Polynomial fitting is a more recent methodology that implies a functional connection between material attributes and measurement frequency. It is assumed that the functional connection is a polynomial of n^{th} order [119],

$$y_n = \sum_{n=0}^{n=\infty} a_n x^n \tag{1.108}$$

Here the a_i terms are constants; n is the order of the polynomial and the initial values and order of the polynomial are guessed before fitting.

External surfaces of the sample that are in touch with the sample holder may be coated with a conducting paste to close any gaps between the sample holder and sample. Air gaps between surfaces may be seen as capacitor layers [118]. This method implies that the gaps between the transmission line and the sample may be accurately approximated by a series of capacitors.

$$\frac{1}{C_m} = \frac{1}{C_1} + \frac{1}{C_2} + \frac{1}{C_3} \tag{1.109}$$

For a coaxial line,

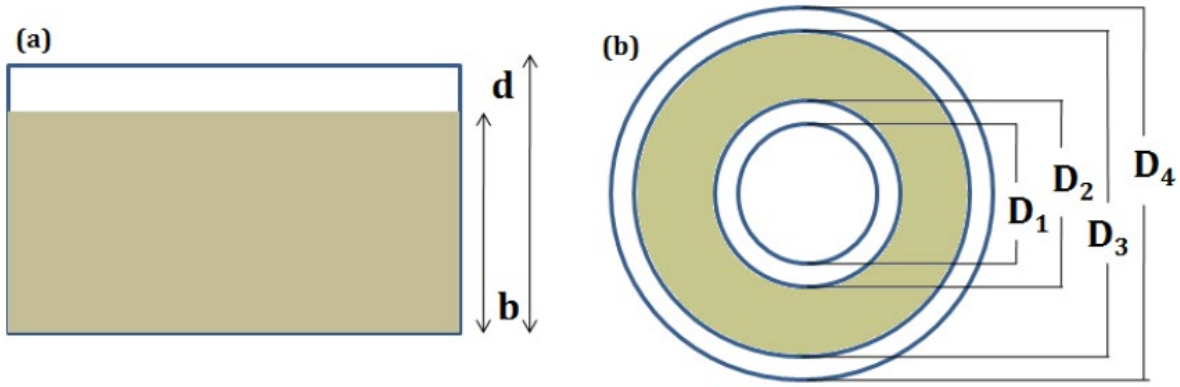

Figure 1.19. Air gaps after a sample inserted in a (a) rectangular waveguide and (b) coaxial line

$$C = \frac{2\pi\varepsilon l}{\ln\frac{R_2}{R_1}} \tag{1.110}$$

Solving for ε provides,

$$\varepsilon_c' = \varepsilon_m' \frac{L_2}{L_3 - \varepsilon_m' L_1} \tag{1.111}$$

$$\varepsilon_c'' = (\varepsilon_c' \times \frac{\varepsilon_m''}{\varepsilon_m'}) \frac{L_3}{L_3 - L_1 \varepsilon_m' (1 + [\frac{\varepsilon_m''}{\varepsilon_m'}]^2)} \tag{1.112}$$

Modelling transmission line as a series of inductors for the E-field gap,

$$L_c = L_m - L_{air}$$

where c, m, and air denote to corrected value, measured value and air space, respectively. For a coaxial line,

$$L = \frac{1}{2\pi}\mu' \ln\frac{D_3}{D_2} \tag{1.113}$$

Therefore, we can write for the corrected permeability,

$$\mu_c' = \mu_m' \frac{L_3 - L_1}{L_2} \tag{1.114}$$

$$\mu_c'' = \mu_m'' \frac{L_3}{L_2} \tag{1.115}$$

Where,

$$L_1 = \ln\frac{D_2}{D_1} + \ln\frac{D_4}{D_3} \tag{1.116}$$

$$L_2 = \ln\frac{D_3}{D_2} \tag{1.117}$$

$$L_3 = \ln\frac{D_4}{D_1} \tag{1.118}$$

These formulae for gap correction may be easily obtained from Maxwell's equations. At higher frequencies, this adjustment should contain a frequency-dependent term. Considering same models and H-field gap for rectangular waveguide, the revised values for μ and ε are,

$$\varepsilon_c' = \varepsilon_m' \frac{d}{b - (b-d)\varepsilon_m'} \tag{1.119}$$

$$\varepsilon_c'' = \varepsilon_c'\left(\frac{\varepsilon_m''}{\varepsilon_m'}\right)\frac{b}{b-(b-d)\varepsilon_m'} \quad (1.120)$$

$$\mu_c' = \mu_m'\left(\frac{b}{d}\right) - \left(\frac{b-d}{d}\right) \quad (1.121)$$

$$\mu_c'' = \mu_m''\frac{b}{d} \quad (1.122)$$

Fig. 1.19 depicts the possible placements of air gaps following insertion of a sample in a coaxial line and a rectangular waveguide, respectively.

1.7.8 EMI SHIELDING FOR SINGLE LAYER ABSORBER

Fig. 1.20 depicts the diagram of an electromagnetic wave ordinarily impinge on an absorber and probable material interactions. Shielding efficiency (SE) is a metric that estimates the amount of electromagnetic (EM) energy impeded by an absorbent material slab as it passes through. A regularly incoming electromagnetic wave (E_I) is typically partly reflected at the air-absorber interface, designated as E_R and detectable by $S_{11-OPEN}$, partially penetrating through the layer, denoted as E_T (S_{21}), and partially attenuated in the absorber, E_A. Consequently, three distinct processes, namely reflection, absorption, and multiple internal reflections, contribute to the overall attenuation, which corresponds to shielding effectiveness

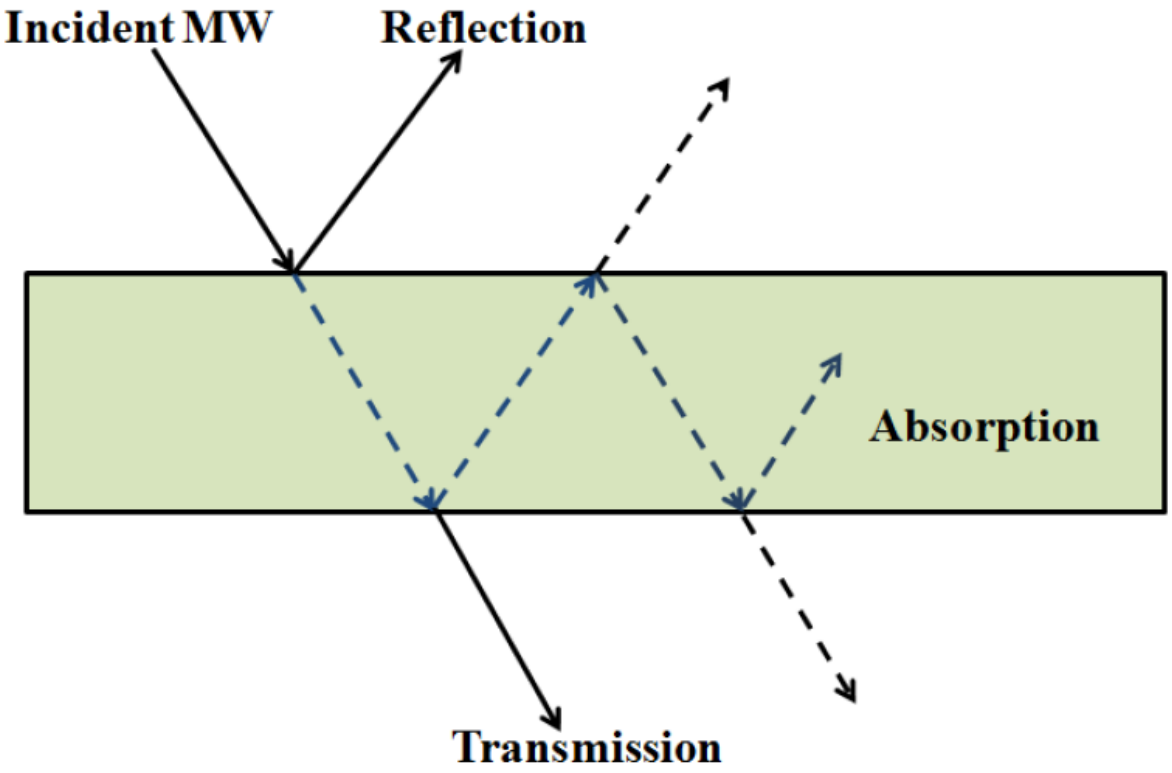

Figure 1.20. Schematic diagram of reflected and transmitted waves when an EM wave is incident on a material

SE_R, SE_A, and SE_M, respectively [39], [120]. Total shielding effectiveness (SE) may be represented as the total of contributions from reflection (SE_R), absorption (SE_A), and internal multiple reflections (SE_M).

$$SE\ (dB) = 10\log\left({P_t}/{P_I}\right) = SE_A + SE_R + SE_M \tag{1.123}$$

Here, P_t represents the transmitted power, and P_I represents the incident power of EM wave. The SE components are defined as follows,

$$SE_R\ (dB) = 10\log(1-R),\ [\text{where}, R = |S_{11}|^2] \tag{1.124}$$

And,

$$SE_A\ (dB) = 10\log\left(\frac{T}{1-R}\right),\ [\text{where}, T = |S_{21}|^2] \tag{1.125}$$

Neglecting minute effects from multiple reflections ($SE_M = 20\log\left(1-10^{\frac{SE_A}{10}}\right)$) in a slab and putting 1.64 in 1.63, total SE results in,

$$SE\ (dB) = 20\log|S_{21}| \tag{1.126}$$

SE_R is proportional to the relative impedance mismatch between the surface of the shielding material and the EM waves, while absorption loss is caused by ohmic losses and heating of the material as a consequence of currents created in the medium.

Absorber slab with a conducting metal backing follows Eq. 1.42 for impedance and rather than transmission; EM wave is completely reflected off absorber-metal surface. The RL characteristics may then be directly measured using $S_{11-\text{SHORT}}$, which coincides with the transmission line theory's [121] estimated value. At a thickness of a quarter wavelength, electromagnetic waves reflected from the first and second surfaces of the absorber are 180 degrees out of phase, causing destructive interference. This matching thickness (t_m) is essential for building the correct absorber thickness for maximal shielding, and it may be understood from the quarter wavelength ($\lambda/4$) model as follows:

$$t_m = \frac{nc}{4f_m\sqrt{\varepsilon_r\mu_r}}\ (n = 1, 3, 5, \dots) \tag{1.127}$$

where for odd values of n, waves reflected from two absorber interfaces go out of phase. Consequently, RL may be tailored for certain frequencies by improving the material characteristics and thickness.

1.7.9 BRIEF REVIEW ON AVAILABLE EMA

Recent developments in electromagnetic wave-absorbent materials demonstrate the transition from dielectric carbon-based compounds to complex ferrite-dielectric quaternary compounds. Over the years, materials such as carbons, metal powders, ferrites, oxides, and polymers have been merged, coated, and doped into one another to get the desired properties, and various synthesis techniques have been used to alter their distinctive attributes. For

Table 1.1 Microwave absorption properties of different possible EMA materials

Material	Thickness (mm)	RL_{min}(dB)	Peak frequency (GHz)
$BaCo_{0.9}Zn_{1.1}Fe_{16}O_{27}$ [122]	2.0	-33.6	12.0
FeSiAl [123]	4.0	-39.7	1.4
$SrZnCoFe_{16}O_{17}$ [124]	2.6	-33.4	10.4
rGO/MoS_2 [125]	2.0	-33.2	13.0
Fe_3O_4/C [126]	3.0	-34.7	11.6
PEO/Graphene [127]	2.5	-37.8	16.4
D1.43 µm Carbon Fibers [128]	3.0	-22.9	7.6
Ni/MWNT 5 wt.%[129]	4.0	-23.1	8.0
PPy/Fe_3O_4/PVDF [130]	2.5	-21.5	16.8
Porous Flower Like Fe_3O_4 [131]	2.0	-28.31	13.2
Fe nanowire/epoxy [132]	2.0	-47.0	9.4
FeNi@C [133]	2.0	-47.6	3.17
Fe_3O_4/SiO_2/PVDF Nanorod [134]	2.5	-28.6	8.1
Fe@$NiFe_2O_4$ [135]	1.5	-27.0	13
Fe nanoflake@SiO_2 [136]	3.6	-20.0	7.3
$NiFe_2O_4$ Nanohollowspheres [137]	2.0	-59.2	11.7
$MnFe_2O_4$ Nanohollowspheres [138]	5.1	-55.4	9.6

instance, Qiu et al. [45] examined microwave absorbing materials based on lightweight nano-porous carbon produced from walnut shells, obtaining a maximum reflection loss of 42.4 dB at 8.88 GHz due to dielectric relaxation loss. Liu et al. [82] investigated ZnO-coated Fe nanocapsules and determined that an *RL* of -57.1dB at 7.8 GHz is best. Table 1.1 summarizes the microwave absorption capabilities of several types of EMA materials is shown.

1.8 MOTIVE OF THE THESIS

Due to the fast growth of technology, electro-magnetic (EM) wave pollution has become hazardous to human health, necessitating the use of EM wave absorbers (EMA) to protect the undesirable waves. In this context, ferrites are preferable to conventional dielectrics such as carbon-based materials or magnetic ultrafine metal powders due to their synergistic magnetic and dielectric capabilities. The high density of ferrites makes them cumbersome and difficult to employ in practical applications, despite their many benefits. Nano-hollow spheres (NHS) are a recent trend among nano-structures, as a result of the preference for lightweight and space-efficient EMA materials. In addition, nano-structures have unique features compared to their bulk counterparts, which makes straightforward adjustment of their attributes crucial. This thesis introduces numerous strategies, including as chemical doping, hybridization of materials, morphology, and size control, to develop an effective broad-band EMA material.

1.9 THESIS ORGANIZATION

The entire thesis has been separated into seven chapters. The following is a brief summary of each chapter.

- *Chapter 1*: This chapter provides a brief introduction to ferrite nanostructures, including their crystal structure, magnetic, electric, and microwave absorption characteristics. We have also explored the surface alteration of NSs and its repercussions. This chapter describes the frequency dependency of magnetic and electric characteristics, their origins, and their applications. In addition, the motivation for the thesis study and a summary of the work completed are presented.

- *Chapter 2*: The second chapter focuses on procedures for synthesis, methodologies for characterisation, and measurements.

- *Chapter 3*: The third chapter covers the impact of coating manganese ferrite nanohollowspheres with silica and cobalt ferrite individually. Further research is conducted and reported on the optimization of layer thicknesses of the aforementioned material layers in order to acquire the most efficient microwave performance.

- *Chapter 4*: The fourth chapter discusses the alteration of sodium bismuth titanate (NBT) and strontium titanate (STO) to get a Curie temperature close to room temperature and high dielectric constants. Cobalt ferrite is coated to further improve microwave properties by introducing magnetic characteristics.

- *Chapter 5*: The fifth chapter explores the effective tuning of magnetic characteristics of soft magnetic material nickel nanoparticles by forming exchange-coupled core-shell structures using hard magnetic material, cobalt ferrite as the shell and enhancing the electromagnetic wave absorption properties as well.

- *Chapter 6*: In the sixth chapter, conclusions are drawn and the scope of future study is discussed.

REFERENCES

[1] R. T. Hitchcock, A. I. H. Association, and A. I. H. Association. N. R. Committee, *Radio-frequency and Microwave Radiation*. in Nonionizing radiation guide series. American Industrial Hygiene Association, 2004. [Online]. Available: https://books.google.co.in/books?id=0TUIQ9-Ap5cC

[2] P. R. Karmel, G. D. Colef, and R. L. Camisa, *Introduction to Electromagnetic and Microwave Engineering*. in Wiley Series in Microwave and Optical Engineering. Wiley, 1998. [Online]. Available: https://books.google.co.in/books?id=iruLnH941OEC

[3] M. L. Sisodia, *Microwaves : Introduction To Circuits,Devices And Antennas*. New Age International, 2007. [Online]. Available: https://books.google.co.in/books?id=iEvgmwH1esgC

[4] A. J. Cox, J. G. Louderback, S. E. Apsel, and L. A. Bloomfield, "Magnetism in 4d-transition metal clusters," *Phys Rev B*, vol. 49, no. 17, pp. 12295–12298, May 1994, doi: 10.1103/PhysRevB.49.12295.

[5] J. I. Martín, J. Nogués, K. Liu, J. L. Vicent, and I. K. Schuller, "Ordered magnetic nanostructures: fabrication and properties," *J Magn Magn Mater*, vol. 256, no. 1, pp. 449–501, 2003, doi: https://doi.org/10.1016/S0304-8853(02)00898-3.

[6] Y. Xu, K. Meehan, L. Guido, G. Lu, C. Wyatt, and N. Love, "Synthesis and Characterization of Silica Coated CdSe/CdS Core/Shell Quantum Dots," Dec. 2005.

[7] A. G. Kolhatkar, A. C. Jamison, D. Litvinov, R. C. Willson, and T. R. Lee, "Tuning the magnetic properties of nanoparticles," *International Journal of Molecular Sciences*, vol. 14, no. 8. pp. 15977–16009, 2013. doi: 10.3390/ijms140815977.

[8] C.-Y. Wen *et al.*, "Fluorescent/magnetic micro/nano-spheres based on quantum dots and/or magnetic nanoparticles: preparation, properties, and their applications in cancer studies," *Nanoscale*, vol. 8, no. 25, pp. 12406–12429, 2016, doi: 10.1039/C5NR08534A.

[9] G. Datt and A. C. Abhyankar, "Dopant driven tunability of dielectric relaxation in MxCo(1-x)Fe2O4 (M: Zn2+, Mn2+, Ni2+) nano-ferrites," *J Appl Phys*, vol. 122, no. 3, p. 034102, Jul. 2017, doi: 10.1063/1.4990275.

[10] C. V Ramana, Y. D. Kolekar, K. Kamala Bharathi, B. Sinha, and K. Ghosh, "Correlation between structural, magnetic, and dielectric properties of manganese substituted cobalt ferrite," *J Appl Phys*, vol. 114, no. 18, p. 183907, Nov. 2013, doi: 10.1063/1.4827416.

[11] S. Sun *et al.*, "Monodisperse MFe2O4 (M = Fe, Co, Mn) Nanoparticles," *J Am Chem Soc*, vol. 126, no. 1, pp. 273–279, Jan. 2004, doi: 10.1021/ja0380852.

[12] F. Wang *et al.*, "Template free synthesis and electromagnetic wave absorption properties of monodispersed hollow magnetite nano-spheres," *J Mater Chem*, vol. 21, no. 12, pp. 4314–4320, 2011, doi: 10.1039/C0JM02894K.

[13] B. Guo *et al.*, "Hollow Structured Micro/Nano MoS2 Spheres for High Electrocatalytic Activity Hydrogen Evolution Reaction," *ACS Appl Mater Interfaces*, vol. 8, no. 8, pp. 5517–5525, Mar. 2016, doi: 10.1021/acsami.5b10252.

[14] J. S. An, W. J. Han, and H. J. Choi, "Synthesis of hollow magnetite nanoparticles via self-assembly and their magnetorheological properties," *Colloids Surf A Physicochem Eng Asp*, vol. 535, pp. 16–23, 2017, doi: https://doi.org/10.1016/j.colsurfa.2017.09.019.

[15] P. Liu, M. Yang, S. Zhou, Y. Huang, and Y. Zhu, "Hierarchical shell-core structures of concave spherical NiO nanospines@carbon for high performance supercapacitor electrodes," *Electrochim Acta*, vol. 294, pp. 383–390, 2019, doi: https://doi.org/10.1016/j.electacta.2018.10.112.

[16] C. C. Li, Q. H. Li, L. B. Chen, and T. H. Wang, "A Facile Titanium Glycolate Precursor Route to Mesoporous Au/Li4Ti5O12 Spheres for High-Rate Lithium-Ion Batteries," *ACS Appl Mater Interfaces*, vol. 4, no. 3, pp. 1233–1238, Mar. 2012, doi: 10.1021/am2018145.

[17] J.-W. Yoon, Y. J. Hong, Y. Chan Kang, and J.-H. Lee, "High performance chemiresistive H2S sensors using Ag-loaded SnO2 yolk–shell nanostructures," *RSC Adv*, vol. 4, no. 31, pp. 16067–16074, 2014, doi: 10.1039/C4RA01364F.

[18] Z. Yang, Z. Li, Y. Yang, and Z. J. Xu, "Optimization of ZnxFe3–xO4 Hollow Spheres for Enhanced Microwave Attenuation," *ACS Appl Mater Interfaces*, vol. 6, no. 24, pp. 21911–21915, Dec. 2014, doi: 10.1021/am5075612.

[19] Z. Yang, Z. Li, Y. Yang, and Z. J. Xu, "Optimization of ZnxFe3–xO4 Hollow Spheres for Enhanced Microwave Attenuation," *ACS Appl Mater Interfaces*, vol. 6, no. 24, pp. 21911–21915, Dec. 2014, doi: 10.1021/am5075612.

[20] K. Karmakar, D. Maity, D. Pal, K. Mandal, and G. G. Khan, "Photo-Induced Exciton Dynamics and Broadband Light Harvesting in ZnO Nanorod-Templated Multilayered Two-Dimensional MoS2/MoO3 Photoanodes for Solar Fuel Generation," *ACS Appl Nano Mater*, vol. 3, no. 2, pp. 1223–1231, Feb. 2020, doi: 10.1021/acsanm.9b01972.

[21] P. Liu, Y. Zhang, J. Yan, Y. Huang, L. Xia, and Z. Guang, "Synthesis of lightweight N-doped graphene foams with open reticular structure for high-efficiency electromagnetic wave absorption," *Chemical Engineering Journal*, vol. 368, pp. 285–298, 2019, doi: https://doi.org/10.1016/j.cej.2019.02.193.

[22] A. Farajpour, M. H. Ghayesh, and H. Farokhi, "A review on the mechanics of nanostructures," *Int J Eng Sci*, vol. 133, pp. 231–263, 2018, doi: https://doi.org/10.1016/j.ijengsci.2018.09.006.

[23] V. B. Barbeta, R. F. Jardim, P. K. Kiyohara, F. B. Effenberger, and L. M. Rossi, "Magnetic properties of Fe3O4 nanoparticles coated with oleic and dodecanoic acids," *J Appl Phys*, vol. 107, no. 7, p. 073913, Apr. 2010, doi: 10.1063/1.3311611.

[24] A. G. Kolhatkar, A. C. Jamison, D. Litvinov, R. C. Willson, and T. R. Lee, "Tuning the magnetic properties of nanoparticles," *International Journal of Molecular Sciences*, vol. 14, no. 8. pp. 15977–16009, 2013. doi: 10.3390/ijms140815977.

[25] H. L. Andersen, M. Saura-Múzquiz, C. Granados-Miralles, E. Canévet, N. Lock, and M. Christensen, "Crystalline and magnetic structure-property relationship in spinel ferrite nanoparticles," *Nanoscale*, vol. 10, no. 31, pp. 14902–14914, Aug. 2018, doi: 10.1039/c8nr01534a.

[26] R. Rakshit, M. Mandal, M. Pal, and K. Mandal, "Tuning of magnetic properties of CoFe2O4 nanoparticles through charge transfer effect," *Appl Phys Lett*, vol. 104, no. 9, p. 092412, Mar. 2014, doi: 10.1063/1.4867706.

[27] S. Talukdar, D. Mandal, and K. Mandal, "Surface modification of Cobalt ferrite nano-hollowspheres for inherent multiple photoluminescence and enhanced photocatalytic activities," *Chem Phys Lett*, vol. 672, pp. 57–62, 2017, doi: https://doi.org/10.1016/j.cplett.2017.01.062.

[28] X. Song, G. Chen, L. Guan, H. Zhang, and J. Tao, "Interfacial engineering of MoS2/TiO2 hybrids for enhanced electrocatalytic hydrogen evolution reaction," *Applied Physics Express*, vol. 9, no. 9, p. 095801, 2016, doi: 10.7567/APEX.9.095801.

[29] X. Zhou *et al.*, "Synthesis of porous carbon embedded with NiCo/CoNiO2 hybrids composites for excellent electromagnetic wave absorption performance," *J Colloid Interface Sci*, vol. 575, pp. 130–139, 2020, doi: https://doi.org/10.1016/j.jcis.2020.04.099.

[30] Y. Yang, M. Li, Y. Wu, B. Zong, and J. Ding, "Size-dependent microwave absorption properties of Fe3O4 nanodiscs," *RSC Adv*, vol. 6, no. 30, pp. 25444–25448, 2016, doi: 10.1039/C5RA28035D.

[31] C. Dey, K. Baishya, A. Ghosh, M. M. Goswami, A. Ghosh, and K. Mandal, "Improvement of drug delivery by hyperthermia treatment using magnetic cubic cobalt ferrite nanoparticles," *J Magn Magn Mater*, vol. 427, pp. 168–174, 2017, doi: https://doi.org/10.1016/j.jmmm.2016.11.024.

[32] D. Maity, K. Karmakar, and K. Mandal, "N-N type core-shell heterojunction engineering with MoO3 over ZnO nanorod cores for enhanced solar energy harvesting application in a photoelectrochemical cell," *J Alloys Compd*, vol. 791, pp. 739–746, 2019, doi: https://doi.org/10.1016/j.jallcom.2019.03.292.

[33] J. Liu and D. Xue, "Thermal oxidation strategy towards porous metal oxide hollow architectures," *Advanced Materials*, vol. 20, no. 13, pp. 2622–2627, Jul. 2008, doi: 10.1002/adma.200800208.

[34] M. Alam, K. Mandal, and G. G. Khan, "Origin and tuning of room temperature ferromagnetism and ferroelectricity in double perovskite Y2NiMnO6 nanostructured thin films," *J Alloys Compd*, vol. 822, p. 153540, 2020, doi: https://doi.org/10.1016/j.jallcom.2019.153540.

[35] S. F. Soares, T. Fernandes, A. L. Daniel-da-Silva, and T. Trindade, "The controlled synthesis of complex hollow nanostructures and prospective applications†," *Proceedings of the Royal Society A: Mathematical, Physical and Engineering Sciences*, vol. 475, no. 2224, p. 20180677, Apr. 2019, doi: 10.1098/rspa.2018.0677.

[36] W. Ruan *et al.*, "Metal–organic framework derived cobalt phosphosulfide with ultrahigh microwave absorption properties," *Nanotechnology*, vol. 29, no. 40, p. 405703, 2018, doi: 10.1088/1361-6528/aad39b.

[37] P. Chen, B. Cui, X. Cui, W. Zhao, Y. Bu, and Y. Wang, "A microwave-triggered controllable drug delivery system based on hollow-mesoporous cobalt ferrite magnetic nanoparticles," *J Alloys Compd*, vol. 699, pp. 526–533, 2017, doi: https://doi.org/10.1016/j.jallcom.2016.12.304.

[38] Y. Li, N. Li, W. Pan, Z. Yu, L. Yang, and B. Tang, "Hollow Mesoporous Silica Nanoparticles with Tunable Structures for Controlled Drug Delivery," *ACS Appl Mater Interfaces*, vol. 9, no. 3, pp. 2123–2129, Jan. 2017, doi: 10.1021/acsami.6b13876.

[39] R. Panigrahi and S. K. Srivastava, "Trapping of microwave radiation in hollow polypyrrole microsphere through enhanced internal reflection: A novel approach," *Sci Rep*, vol. 5, no. 1, p. 7638, 2015, doi: 10.1038/srep07638.

[40] M. Mandal Goswami, "Synthesis of Micelles Guided Magnetite (Fe3O4) Hollow Spheres and their application for AC Magnetic Field Responsive Drug Release," *Sci Rep*, vol. 6, no. 1, p. 35721, 2016, doi: 10.1038/srep35721.

[41] S. Sutradhar, S. Saha, and S. Javed, "Shielding Effectiveness Study of Barium Hexaferrite-Incorporated, β-Phase-Improved Poly(vinylidene fluoride) Composite Film: A Metamaterial Useful for the Reduction of Electromagnetic Pollution," *ACS Appl Mater Interfaces*, vol. 11, no. 26, pp. 23701–23713, Jul. 2019, doi: 10.1021/acsami.9b05122.

[42] W. Hou *et al.*, "Nanodiamond–Manganese dual mode MRI contrast agents for enhanced liver tumor detection," *Nanomedicine*, vol. 13, no. 3, pp. 783–793, 2017, doi: https://doi.org/10.1016/j.nano.2016.12.013.

[43] D. Sarkar, M. Mandal, and K. Mandal, "Domain controlled magnetic and electric properties of variable sized magnetite nano-hollow spheres," *J Appl Phys*, vol. 112, no. 6, p. 064318, Sep. 2012, doi: 10.1063/1.4754018.

[44] X. Qiu, L. Wang, H. Zhu, Y. Guan, and Q. Zhang, "Lightweight and efficient microwave absorbing materials based on walnut shell-derived nano-porous carbon," *Nanoscale*, vol. 9, no. 22, pp. 7408–7418, Jun. 2017, doi: 10.1039/c7nr02628e.

[45] Y. Ding *et al.*, "Reduced Graphene Oxide Functionalized with Cobalt Ferrite Nanocomposites for Enhanced Efficient and Lightweight Electromagnetic Wave Absorption," *Sci Rep*, vol. 6, no. 1, p. 32381, 2016, doi: 10.1038/srep32381.

[46] F. Qin and C. Brosseau, "A review and analysis of microwave absorption in polymer composites filled with carbonaceous particles," *J Appl Phys*, vol. 111, no. 6, p. 061301, Mar. 2012, doi: 10.1063/1.3688435.

[47] K. Sakata and Y. Masuda, "Ferroelectric and Antiferroelectric Properties of (Na0.5 Bi0.5)TiO3-SrTiO3 Solid Solution Ceramics," *Ferroelectrics*, vol. 7, no. 1, pp. 347–349, Jan. 1974, doi: 10.1080/00150197408238042.

[48] B.-J. Chu, D.-R. Chen, G.-R. Li, and Q.-R. Yin, "Electrical properties of Na 1/2 Bi 1/2 TiO 3-BaTiO 3 ceramics." [Online]. Available: www.elsevier.com/locate/jeurceramsoc

[49] J. Suchanicz, J. Kusz, and H. Bö Hm, "Structural and electric characteristics of (Na 0.5 Bi 0.5) 0.50 Ba 0.50 TiO 3 and (Na 0.5 Bi 0.5) 0.20 Ba 0.80 TiO 3 ceramics." [Online]. Available: www.elsevier.com/locate/mseb

[50] X. Wang, H. Lai-Wa Chan, and C. Choy, "Piezoelectric and dielectric properties of CeO 2-added (Bi 0.5 Na 0.5) 0.94 Ba 0.06 TiO 3 lead-free ceramics." [Online]. Available: www.elsevier.com/locate/ssc

[51] O. Elkechai, M. Manier, and J. P. Mercurio, "Na0.5Bi0.5TiO3-K0.5Bi 0.5TiO3 (NBT-KBT) system: A structural and electrical study," *Physica Status Solidi A Appl Res*, vol. 157, no. 2, pp. 499–506, 1996, doi: 10.1002/pssa.2211570234.

[52] H. Yang *et al.*, "Lead-Free Piezoelectric Ceramics of (Bi 1/2 Na 1/2)TiO 3-KNbO 3-1/2(Bi 2 O 3 ·Sc 2 O 3) System You may also like Eight-year Simultaneous Monitoring Observations of H 2 O and SiO Masers toward V627 Cas Planar electro-optic deflector using KTa 1x Nb x O 3 for low-power-consumption operation Effect of Ni doping on the electro-optic property in K(Ta 0.6 Nb 0.4)O 3 films," 1998.

[53] A. Ali Khan *et al.*, "Dielectric and Piezoelectric Properties of (Bi 0.5 Na 0.5)TiO 3-(Bi 0.5 K 0.5)TiO 3 Systems Inorganic dielectric materials for energy storage applications: a review Anina Anju Balaraman and Soma Dutta-Dielectric and Piezoelectric Properties of (Bi 0.5 Na 0.5)TiO 3-(Bi 0.5 K 0.5)TiO 3 Systems," 1999.

[54] J. Yun Yi *et al.*, "Dielectric and Piezoelectric Properties of (A 0.5 Bi 0.5)TiO 3-ANbO 3 (A=Na, K) Systems You may also like Stabilized antiferroelectric phase in lanthanum-doped (Na Inorganic dielectric materials for energy storage applications: a review Anina Anju Balaraman and Soma Dutta-Dielectric and Piezoelectric Properties of (A 0.5 Bi 0.5)TiO 3-ANbO 3 (A = Na, K) Systems morphotropic phase boundary," 2001.

[55] K. Reichmann, A. Feteira, and M. Li, "Bismuth Sodium Titanate based materials for piezoelectric actuators," *Materials*, vol. 8, no. 12. MDPI AG, pp. 8467–8495, 2015. doi: 10.3390/ma8125469.

[56] J. Suchanicz, " Behaviour of Na 0.5 Bi 0.5 TiO 3 ceramics in the a.c. electric field ," *Ferroelectrics*, vol. 209, no. 1, pp. 561–568, Apr. 1998, doi: 10.1080/00150199808018070.

[57] "Soft Modes in Ferroelectrics and Antiferroelectrics." [Online]. Available: http://iopscience.iop.org/0031-9112/27/3/038

[58] R. A. Cowley, "Structural phase transitions I. Landau theory," *Adv Phys*, vol. 29, no. 1, pp. 1–110, Jan. 1980, doi: 10.1080/00018738000101346.

[59] M. Fischer, A. M. Lahmar Maglione, A. San Miguel, J. P. Itic, A. Polian, and F. Baudelet, "Local disorder studied in SrTi03 at low temperature by EXAFS spectroscopy," 1994.

[60] H. Unoki and T. Sakudo, "Electron Spin Resonance of Fe3+ in SrTiO3 with Special Reference to the 110°K Phase Transition," *J Physical Soc Japan*, vol. 23, no. 3, pp. 546–552, Sep. 1967, doi: 10.1143/JPSJ.23.546.

[61] A. Dutta, A. Gorai, D. Mandal, and K. Mandal, "Dielectric and microwave absorption properties of Na0.5Bi0.5TiO3–SrTiO3 system," *Ferroelectrics*, vol. 583, no. 1, pp. 252–263, 2021, doi: 10.1080/00150193.2021.1980324.

[62] H. Zeng, S. Sun, J. Li, Z. L. Wang, and J. P. Liu, "Tailoring magnetic properties of core⁄shell nanoparticles," *Appl Phys Lett*, vol. 85, no. 5, pp. 792–794, Jul. 2004, doi: 10.1063/1.1776632.

[63] H. Zeng, J. Li, Z. L. Wang, J. P. Liu, and S. Sun, "Bimagnetic Core/Shell FePt/Fe3O4 Nanoparticles," *Nano Lett*, vol. 4, no. 1, pp. 187–190, Jan. 2004, doi: 10.1021/nl035004r.

[64] R. Ghosh Chaudhuri and S. Paria, "Core/shell nanoparticles: Classes, properties, synthesis mechanisms, characterization, and applications," *Chemical Reviews*, vol. 112, no. 4. pp. 2373–2433, Apr. 11, 2012. doi: 10.1021/cr100449n.

[65] L. Gopal and T. Sudarshan, "Core shell particles," *Surface Engineering*, vol. 38, no. 7–9, pp. 675–679, Sep. 2022, doi: 10.1080/02670844.2022.2170550.

[66] K. S. Kumar, V. B. Kumar, and P. Paik, "Recent Advancement in Functional Core-Shell Nanoparticles of Polymers: Synthesis, Physical Properties, and Applications in Medical Biotechnology," *Journal of Nanoparticles*, vol. 2013, p. 672059, 2013, doi: 10.1155/2013/672059.

[67] R. Singh and R. Bhateria, "Core–shell nanostructures: a simplest two-component system with enhanced properties and multiple applications," *Environ Geochem Health*, vol. 43, no. 7, pp. 2459–2482, 2021, doi: 10.1007/s10653-020-00766-1.

[68] K. E. Sickafus, J. M. Wills, and N. W. Grimes, "Structure of Spinel," *Journal of the American Ceramic Society*, vol. 82, no. 12, pp. 3279–3292, Dec. 1999, doi: https://doi.org/10.1111/j.1151-2916.1999.tb02241.x.

[69] Z. Szotek, W. M. Temmerman, D. Ködderitzsch, A. Svane, L. Petit, and H. Winter, "Electronic structures of normal and inverse spinel ferrites from first principles," *Phys Rev B*, vol. 74, no. 17, p. 174431, Nov. 2006, doi: 10.1103/PhysRevB.74.174431.

[70] J. Liu, Y. Bin, and M. Matsuo, "Magnetic Behavior of Zn-Doped Fe3O4 Nanoparticles Estimated in Terms of Crystal Domain Size," *The Journal of Physical Chemistry C*, vol. 116, no. 1, pp. 134–143, Jan. 2012, doi: 10.1021/jp207354s.

[71] A. H. Morrish, *The Physical Principles of Magnetism*. 2001.

[72] S. Gangopadhyay *et al.*, "Magnetic properties of ultrafine iron particles," *Phys Rev B*, vol. 45, no. 17, pp. 9778–9787, May 1992, doi: 10.1103/PhysRevB.45.9778.

[73] D. Sarkar, M. Mandal, R. Das, and K. Mandal, "Fabrication of Biologically Functionalized, Electrically Conducting, and Aligned Magnetic Nanoparticles," *IEEE Trans Magn*, vol. 47, no. 10, pp. 3163–3166, 2011, doi: 10.1109/TMAG.2011.2147764.

[74] R. Skomski, *Simple models of magnetism*. Oxford university press, 2008.

[75] R. Day, M. Fuller, and V. A. Schmidt, "Hysteresis properties of titanomagnetites: Grain-size and compositional dependence," *Physics of the Earth and Planetary Interiors*, vol. 13, no. 4, pp. 260–267, 1977, doi: https://doi.org/10.1016/0031-9201(77)90108-X.

[76] C. Kittel, *Elementary Statistical Physics*. in Dover Books on Physics Series. Dover Publications, 2004. [Online]. Available: https://books.google.co.in/books?id=5sd9SAoRjgQC

[77] U. J. Fourier, *Magnetism: Fundamentals, Materials and Applications*. Springer New York, 2004.

[78] H. Zhang, D. Zeng, and Z. Liu, "The law of approach to saturation in ferromagnets originating from the magnetocrystalline anisotropy," *J Magn Magn Mater*, vol. 322, no. 16, pp. 2375–2380, 2010, doi: https://doi.org/10.1016/j.jmmm.2010.02.040.

[79] G. Xiong *et al.*, "Preparation and Magnetic Properties of CoCrFeO4 Nanocrystals," *Chemistry of Materials*, vol. 13, no. 6, pp. 1943–1945, Jun. 2001, doi: 10.1021/cm000854i.

[80] J. B. Weaver and E. Kuehlert, "Measurement of magnetic nanoparticle relaxation time," *Med Phys*, vol. 39, no. 5, pp. 2765–2770, May 2012, doi: https://doi.org/10.1118/1.3701775.

[81] R. Valenzuela, "Novel applications of ferrites," *Physics Research International*. 2012. doi: 10.1155/2012/591839.

[82] M. Lakshmanan, "The fascinating world of the Landau–Lifshitz–Gilbert equation: an overview," *Philosophical Transactions of the Royal Society A: Mathematical, Physical and Engineering Sciences*, vol. 369, no. 1939, pp. 1280–1300, Mar. 2011, doi: 10.1098/rsta.2010.0319.

[83] B. K. Das and P. Chaudhari, "On the dynamic susceptibility of the bulging domain wall model of polycrystalline magnetic oxides," *J Mater Sci*, vol. 13, no. 1, pp. 84–88, 1978, doi: 10.1007/BF00739277.

[84] R. Dorey, "Chapter 4 - Microstructure–property relationships: How the microstructure of the film affects its properties," in *Ceramic Thick Films for MEMS and Microdevices*, R. Dorey, Ed., Oxford: William Andrew Publishing, 2012, pp. 85–112. doi: https://doi.org/10.1016/B978-1-4377-7817-5.00004-3.

[85] G. Datt and A. C. Abhyankar, "Dopant driven tunability of dielectric relaxation in MxCo(1-x)Fe2O4 (M: Zn2+, Mn2+, Ni2+) nano-ferrites," *J Appl Phys*, vol. 122, no. 3, p. 034102, Jul. 2017, doi: 10.1063/1.4990275.

[86] C. v Ramana, Y. D. Kolekar, K. Kamala Bharathi, B. Sinha, and K. Ghosh, "Correlation between structural, magnetic, and dielectric properties of manganese substituted cobalt ferrite," *J Appl Phys*, vol. 114, no. 18, p. 183907, Nov. 2013, doi: 10.1063/1.4827416.

[87] N. Shukla, V. Kumar, and D. K. Dwivedi, "DEPENDENCE OF DIELECTRIC PARAMETERS AND A.C. CONDUCTIVITY ON FREQUENCY AND TEMPERATURE IN BULK Se 90 Cd 8 In 2 GLASSY ALLOY," 2016.

[88] Andrew K Jonscher, "Dielectric relaxation in solids," *J Phys D Appl Phys*, vol. 32, no. 14, p. R57, 1999, doi: 10.1088/0022-3727/32/14/201.

[89] A. K. Jonscher and R. Holloway, "Physics To cite this article: Andrew K Jonscher," 1999.

[90] K. Vasundhara, S. N. Achary, S. K. Deshpande, P. D. Babu, S. S. Meena, and A. K. Tyagi, "Size dependent magnetic and dielectric properties of nano CoFe2O4 prepared by a salt assisted gel-combustion method," *J Appl Phys*, vol. 113, no. 19, p. 194101, May 2013, doi: 10.1063/1.4804946.

[91] R. Tang *et al.*, "Dielectric relaxation, resonance and scaling behaviors in Sr3Co2Fe24O41 hexaferrite," *Sci Rep*, vol. 5, Aug. 2015, doi: 10.1038/srep13645.

[92] S. K. Pradhan and B. K. Roul, "Electrical behavior of high resistivity Ce-doped BiFeO 3 multiferroic," *Physica B Condens Matter*, vol. 407, no. 13, pp. 2527–2532, Jul. 2012, doi: 10.1016/j.physb.2012.03.061.

[93] C. G. Koops, "On the Dispersion of Resistivity and Dielectric Constant of Some Semiconductors at Audiofrequencies," *Physical Review*, vol. 83, no. 1, pp. 121–124, Jul. 1951, doi: 10.1103/PhysRev.83.121.

[94] N Ponpandian, P Balaya, and A Narayanasamy, "Electrical conductivity and dielectric behaviour of nanocrystalline NiFe2O4 spinel," *Journal of Physics: Condensed Matter*, vol. 14, no. 12, p. 3221, 2002, doi: 10.1088/0953-8984/14/12/311.

[95] A. K. Jonscher, "The 'universal' dielectric response," *Nature*, vol. 267, no. 5613, pp. 673–679, 1977, doi: 10.1038/267673a0.

[96] J. Liu *et al.*, "Microwave absorption enhancement of multifunctional composite microspheres with spinel Fe 3O 4 cores and anatase TiO 2 shells," *Small*, vol. 8, no. 8, pp. 1214–1221, Apr. 2012, doi: 10.1002/smll.201102245.

[97] Y. Yin, X. Liu, X. Wei, R. Yu, and J. Shui, "Porous CNTs/Co Composite Derived from Zeolitic Imidazolate Framework: A Lightweight, Ultrathin, and Highly Efficient Electromagnetic Wave Absorber," *ACS Appl Mater Interfaces*, vol. 8, no. 50, pp. 34686–34698, Dec. 2016, doi: 10.1021/acsami.6b12178.

[98] C.-Y. Wen *et al.*, "Fluorescent/magnetic micro/nano-spheres based on quantum dots and/or magnetic nanoparticles: preparation, properties, and their applications in cancer studies," *Nanoscale*, vol. 8, no. 25, pp. 12406–12429, 2016, doi: 10.1039/C5NR08534A.

[99] V. Shukla, "Review of electromagnetic interference shielding materials fabricated by iron ingredients," *Nanoscale Advances*, vol. 1, no. 5. Royal Society of Chemistry, pp. 1640–1671, 2019. doi: 10.1039/c9na00108e.

[100] R. Valenzuela, "Novel Applications of Ferrites," *Physics Research International*, vol. 2012, p. 591839, 2012, doi: 10.1155/2012/591839.

[101] M. Green and X. Chen, "Recent progress of nanomaterials for microwave absorption," *Journal of Materiomics*, vol. 5, no. 4. Chinese Ceramic Society, pp. 503–541, Dec. 01, 2019. doi: 10.1016/j.jmat.2019.07.003.

[102] M. Pardavi-Horvath and M. Pardavi-Horvath, "Microwave applications of soft ferrites," 2000. [Online]. Available: http://www.rec-usa.com/rmhor.htm

[103] F. Wang *et al.*, "Template free synthesis and electromagnetic wave absorption properties of monodispersed hollow magnetite nano-spheres," *J Mater Chem*, vol. 21, no. 12, pp. 4314–4320, Mar. 2011, doi: 10.1039/c0jm02894k.

[104] R. Panigrahi and S. K. Srivastava, "Trapping of microwave radiation in hollow polypyrrole microsphere through enhanced internal reflection: A novel approach," *Sci Rep*, vol. 5, Jan. 2015, doi: 10.1038/srep07638.

[105] X. Bai, Y. Zhai, and Y. Zhang, "Green approach to prepare graphene-based composites with high microwave absorption capacity," *Journal of Physical Chemistry C*, vol. 115, no. 23, pp. 11673–11677, Jun. 2011, doi: 10.1021/jp202475m.

[106] X. G. Liu, D. Y. Geng, H. Meng, P. J. Shang, and Z. D. Zhang, "Microwave-absorption properties of ZnO-coated iron nanocapsules," *Appl Phys Lett*, vol. 92, no. 17, p. 173117, Apr. 2008, doi: 10.1063/1.2919098.

[107] T. Tian *et al.*, "Graphene-based nanocomposite as an effective, multifunctional, and recyclable antibacterial agent," *ACS Appl Mater Interfaces*, vol. 6, no. 11, pp. 8542–8548, Jun. 2014, doi: 10.1021/am5022914.

[108] J. Baker-Jarvis, M. Janezic, J. G. Jr, and R. Geyer, "Transmission/Reflection and Short-Circuit Line Methods for Measuring Permittivity and Permeability." Technical Note (NIST TN), National Institute of Standards and Technology, Gaithersburg, MD, 1992.

[109] D. Zhang *et al.*, "Light-weight and low-cost electromagnetic wave absorbers with high performances based on biomass-derived reduced graphene oxides," *Nanotechnology*, vol. 30, no. 44, Aug. 2019, doi: 10.1088/1361-6528/ab35fa.

[110] J. Z. He, X. X. Wang, Y. L. Zhang, and M. S. Cao, "Small magnetic nanoparticles decorating reduced graphene oxides to tune the electromagnetic attenuation capacity," *J Mater Chem C Mater*, vol. 4, no. 29, pp. 7130–7140, 2016, doi: 10.1039/c6tc02020h.

[111] "Pozar_Microwave Engineering(2012)".

[112] R. E. Collin, "A C LA SSlC REISSUE Foundations for Microwave Engineering SECOND EDITION."

[113] D. J. Griffiths, *Introduction to Electrodynamics*, 4th ed. Cambridge: Cambridge University Press, 2017. doi: DOI: 10.1017/9781108333511.

[114] H. Mamiya and B. Jeyadevan, "Design Criteria of Thermal Seeds for Magnetic Fluid Hyperthermia - From Magnetic Physics Point of View," in *Nanomaterials for Magnetic and Optical Hyperthermia Applications*, Elsevier, 2018, pp. 13–39. doi: 10.1016/B978-0-12-813928-8.00001-6.

[115] J. Barranger, "N A S A T E C H N I C A L N O T E w-HYSTERESIS A N D A TRANSFORMER A N APPLICATION EDDY-CURRENT LOSSES OF LAMINATION VIEWED AS OF THE POYNTING THEOREM."

[116] S. Dobák, C. Beatrice, V. Tsakaloudi, and F. Fiorillo, "magnetochemistry Magnetic Losses in Soft Ferrites," 2022, doi: 10.3390/magnetochemistry.

[117] A. N. Vicente, G. M. I. Dip, and C. Junqueira, "The step by step development of NRW method," in *SBMO/IEEE MTT-S International Microwave and Optoelectronics Conference Proceedings*, 2011, pp. 738–742. doi: 10.1109/IMOC.2011.6169318.

[118] J. Baker-Jarvis, M. D. Janezic, J. H. Grosvenor, and R. G. Geyer, "NIST Technical Note 1355-R," *NIST, Boulder USA*, p. 20, 1993.

[119] P. G. Bartley and S. B. Begley, "A new technique for the determination of the complex permittivity and permeability of materials," in *2010 IEEE Instrumentation & Measurement Technology Conference Proceedings*, 2010, pp. 54–57. doi: 10.1109/IMTC.2010.5488184.

[120] V. Shukla, "Review of electromagnetic interference shielding materials fabricated by iron ingredients," *Nanoscale Advances*, vol. 1, no. 5. Royal Society of Chemistry, pp. 1640–1671, 2019. doi: 10.1039/c9na00108e.

[121] T. Wang, R. Han, G. Tan, J. Wei, L. Qiao, and F. Li, "Reflection loss mechanism of single layer absorber for flake-shaped carbonyl-iron particle composite," *J Appl Phys*, vol. 112, no. 10, p. 104903, Nov. 2012, doi: 10.1063/1.4767365.

[122] L. Deng, L. Ding, K. Zhou, S. Huang, Z. Hu, and B. Yang, "Electromagnetic properties and microwave absorption of W-type hexagonal ferrites doped with La3+," *J Magn Magn Mater*, vol. 323, no. 14, pp. 1895–1898, 2011, doi: https://doi.org/10.1016/j.jmmm.2011.02.034.

[123] Y. Feng, C. Tang, and T. Qiu, "Effect of ball milling and moderate surface oxidization on the microwave absorption properties of FeSiAl composites," *Materials Science and Engineering: B*, vol. 178, no. 16, pp. 1005–1011, 2013, doi: https://doi.org/10.1016/j.mseb.2013.06.004.

[124] P. Azizi, S. M. Masoudpanah, and S. Alamolhoda, "Magnetic and microwave absorption properties of SrZnCoFe16O27 powders synthesized by solution combustion method," *J Alloys Compd*, vol. 739, pp. 211–217, 2018, doi: https://doi.org/10.1016/j.jallcom.2017.12.179.

[125] Y. Wang, D. Chen, X. Yin, P. Xu, F. Wu, and M. He, "Hybrid of MoS2 and Reduced Graphene Oxide: A Lightweight and Broadband Electromagnetic Wave Absorber," *ACS Appl Mater Interfaces*, vol. 7, no. 47, pp. 26226–26234, Dec. 2015, doi: 10.1021/acsami.5b08410.

[126] X. Liu, H. Guo, Q. Xie, Q. Luo, L.-S. Wang, and D.-L. Peng, "Enhanced microwave absorption properties in GHz range of Fe3O4/C composite materials," *J Alloys Compd*, vol. 649, pp. 537–543, 2015, doi: https://doi.org/10.1016/j.jallcom.2015.07.084.

[127] X. Bai, Y. Zhai, and Y. Zhang, "Green Approach To Prepare Graphene-Based Composites with High Microwave Absorption Capacity," *The Journal of Physical Chemistry C*, vol. 115, no. 23, pp. 11673–11677, Jun. 2011, doi: 10.1021/jp202475m.

[128] Z. Chu, H. Cheng, W. Xie, and L. Sun, "Effects of diameter and hollow structure on the microwave absorption properties of short carbon fibers," *Ceram Int*, vol. 38, no. 6, pp. 4867–4873, 2012, doi: https://doi.org/10.1016/j.ceramint.2012.02.077.

[129] T. Zou, H. Li, N. Zhao, and C. Shi, "Electromagnetic and microwave absorbing properties of multi-walled carbon nanotubes filled with Ni nanowire," *J Alloys Compd*, vol. 496, no. 1, pp. L22–L24, 2010, doi: https://doi.org/10.1016/j.jallcom.2010.02.103.

[130] L.-S. Fu, J.-T. Jiang, C.-Y. Xu, and L. Zhen, "Synthesis of hexagonal Fe microflakes with excellent microwave absorption performance," *CrystEngComm*, vol. 14, no. 20, pp. 6827–6832, 2012, doi: 10.1039/C2CE25836F.

[131] X. Li, B. Zhang, C. Ju, X. Han, Y. Du, and P. Xu, "Morphology-Controlled Synthesis and Electromagnetic Properties of Porous Fe3O4 Nanostructures from Iron Alkoxide Precursors," *The Journal of Physical Chemistry C*, vol. 115, no. 25, pp. 12350–12357, Jun. 2011, doi: 10.1021/jp203147q.

[132] J. Liu, M. Itoh, M. Terada, T. Horikawa, and K. Machida, "Enhanced electromagnetic wave absorption properties of Fe nanowires in gigaherz range," *Appl Phys Lett*, vol. 91, no. 9, p. 093101, Aug. 2007, doi: 10.1063/1.2775804.

[133] C. Feng, X. Liu, Y. Sun, C. Jin, and Y. Lv, "Enhanced microwave absorption of flower-like FeNi@C nanocomposites by dual dielectric relaxation and multiple magnetic resonance," *RSC Adv.*, vol. 4, no. 43, pp. 22710–22715, 2014, doi: 10.1039/C4RA01437E.

[134] X. Liu, Y. Chen, X. Cui, M. Zeng, R. Yu, and G.-S. Wang, "Flexible nanocomposites with enhanced microwave absorption properties based on Fe3O4/SiO2 nanorods and polyvinylidene

fluoride," *J. Mater. Chem. A*, vol. 3, no. 23, pp. 12197–12204, 2015, doi: 10.1039/C5TA01924A.

[135] H. Lv, H. Zhang, G. Ji, and Z. J. Xu, "Interface Strategy To Achieve Tunable High Frequency Attenuation," *ACS Appl Mater Interfaces*, vol. 8, no. 10, pp. 6529–6538, Mar. 2016, doi: 10.1021/acsami.5b12662.

[136] L. Yan, J. Wang, X. Han, Y. Ren, Q. Liu, and F. Li, "Enhanced microwave absorption of Fe nanoflakes after coating with SiO2 nanoshell," *Nanotechnology*, vol. 21, no. 9, p. 095708, 2010, doi: 10.1088/0957-4484/21/9/095708.

[137] D. Mandal, A. Gorai, and K. Mandal, "Electromagnetic wave trapping in NiFe2O4 nano-hollow spheres: An efficient microwave absorber," *J Magn Magn Mater*, vol. 485, pp. 43–48, Sep. 2019, doi: 10.1016/j.jmmm.2019.04.033.

[138] D. Mandal and K. Mandal, "Enhancement of electromagnetic wave absorption in MnFe2O4 nano-hollow spheres," *J Appl Phys*, vol. 129, no. 7, p. 074902, Feb. 2021, doi: 10.1063/5.0039560.

CHAPTER 2

EXPERIMENTAL DETAILS

This chapter briefly outlines a number of sample preparation techniques employed for this thesis study, including bulk and nanostructure samples (such as nanoparticles, nano hollow spheres and core-shell structures). A number of characterization techniques are also presented here to investigate the structural, magnetic, electric, and microwave properties of the materials.

Chapter 2

2.1 PREAMBLE

In this chapter, an overview of various experimental approaches, including wet-chemical, co-precipitation and solvothermal processes, that are utilized to synthesize different nanostructures (NSs) of ferrites such as nano-hollowspheres and core-shells is presented. In addition, the following experimental techniques applied in order to characterize the synthesized materials are also illustrated briefly.

The structural phase and characteristics of the materials are investigated by powder X-ray diffraction (XRD) pattern using SmartLab automated multipurpose X-ray diffractometer and PANalytical X'Pert PRO equipped with Cu-K_α radiation. The size and morphology of nanostructures are studied using an FEI QUANTA FEG 250 field-emission scanning electron microscope (FESEM) (0.2–30 kV) and a FEG high-resolution transmission electron microscope (HRTEM) (80–200 kV). For elemental analysis of the materials, the Energy-dispersive X-ray (EDX) spectrum is captured. Differential Scanning Calorimetry (DSC) and thermal gravimetric analysis (TGA) measurements are done in the temperature range from room temperature to 500 °C using Q-2000 unit. All the relevant magnetic measurements are carried out using a Vibrating Sample Magnetometer (VSM) (Lakeshore Cryotronics-7407), Physical Property Measurement System (PPMS) (Quantum Design, DYNACOOL). AC dielectric properties of NHSs are investigated using LCR meter (Hioki-3532-50; Japan and NF ZM2376 by National Instruments). Microwave properties of the samples for the frequency range 1–20 GHz are measured using Anritsu MS46122B Vector Network Analyzer (VNA). Each composite sample is properly inserted in port-1 end of a coaxial airline (Maury Microwaves−8043S6) and set-up calibration is performed using TOSLKF50A-20 kit for the measurements. Further analysis from measured 2-port scattering (S)-parameters is executed with polynomial fit model of Nicholson-Ross-Weir (NRW) algorithm based on transmission line technique [1].

2.2 SYNTHESIS TECHNIQUES

There are several approaches developed to manufacture nanomaterials with distinct structures and, therefore, characteristics. Top-down (i.e., bulk to nanoparticle) and bottom-up (i.e., atom to nanoparticle) methodologies may be used to describe these techniques [2]. Imperfections in the surface structures of NSs, which may have a substantial impact on their physical characteristics and surface chemistry, are the greatest downside of the top-down method. The bottom-up strategy, on the other hand, increases the likelihood of producing NSs

with fewer flaws, more chemical composition uniformity, and greater control over the positioning of individual atoms.

Typically, nanostructures are generated in two steps: nucleation and growth (as seen in Fig. 2.1(a)) [3]. When nuclei develop consistently, homogeneous nucleation occurs, while heterogeneous nucleation happens when there is structural inhomogeneity. The parent phase condition for nucleation, known as supersaturation, may be attained by judicious management of reaction circumstances such as solvent, capping agents, and temperature, among others. In a chemical reaction, the minimum size of a stable particle is determined by the total free energy changes (ΔG) associated with the homogeneous nucleation process [4]. Eq. 2.1 relates the surface energy and the free energy of the bulk crystal ΔG_v, to the total free energy ΔG for a spherical particle of radius, r. The crystal free energy, ΔG_v, is dependent on the temperature (T), Boltzmann's constant (k_B), the supersaturation of the solution (S), and its molar volume (v), as shown in Eq. 2.2.

$$\Delta G = 4\pi r^2\gamma + \frac{4}{3}\pi r^3 \Delta G_v \tag{2.1}$$

$$\Delta G_v = -\frac{k_B T \ln(S)}{v} \tag{2.2}$$

Due to the surface free energy always being positive and the crystal free energy always being negative, as shown in Fig. 2.1(b), it is possible to determine the maximum free energy through which a nucleus will pass to form a stable nucleus by differentiating ΔG with respect to r and setting it to zero, $\frac{d\Delta G}{dr} = 0$. This gives a critical free energy and also a critical radius.

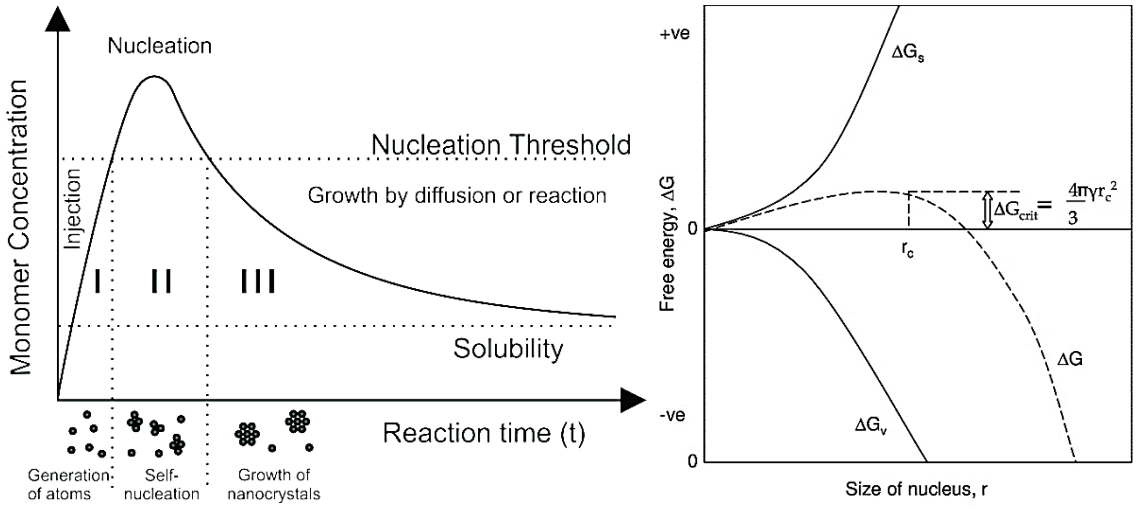

Figure 2.1. (a) Nucleation and growth step in a classical synthesis, (b) Free-energy diagram for nucleation process.

Therefore, beyond a certain critical radius, the particles will form and expand, whereas below this radius they will disperse. The development of nanoparticles (NPs) is based on the diffusion of tiny particles into a solution and onto the surface of other particles. This growth process of NPs is often known as Ostwald ripening, which occurs owing to the size-dependent change in solubility of NPs [5]. Due to the high solubility and surface energy of smaller particles in solution, they redissolve, hence allowing the growth of bigger particles. For shape control, the widely accepted Gibbs–Curie–Wulff theorem proposes that the form of a crystal is defined by the surface free energy of individual crystallographic faces and that the final crystal shape is established in such a manner as to minimize the overall free energy of the system [4].

2.2.1 WET CHEMICAL METHOD

Wet chemical approach is primarily a "bottom-up" methodology for synthesizing nanoparticles by chemical reduction of metal salts, electrochemical procedure, or controlled breakdown of various meta-stable organic and metallic compounds [3]. This technique utilizes aqueous or non-aqueous solutions. This simple, affordable, modular, and scalable approach may be utilized to manufacture even metal oxides in the micrometer range with more control over nanostructure.

This method can be used to grow a coating over some core materials. For coating, the already prepared core materials are needed to be dispersed in the solutions. The stoichiometry of the reagents in the solution and the shape, size and amount of the core materials are the important factors influencing the layer thickness over the core materials.

The coating of $CoFe_2O_4$ over $MnFe_2O_4$ from Chapter 3 and the Nickel nanoparticles from chapter 5, are synthesised using this method.

2.2.2 SOLVOTHERMAL METHOD

Solvothermal technique is a method for producing different nanostructures of metals, semiconductors, ceramics, and polymers from aqueous or non-aqueous media by manipulating pressure, temperature, surfactant concentration, and reaction time [2], [4]. This method uses various polar (such as water, ethanol, etc.) or non-polar (such as benzene, ethylene glycol, etc.) solvents under high pressure and temperature (generally above the boiling point of the solvent) to facilitate the interaction of various precursor molecules during the synthesis procedure. This technique is quite similar to the hydrothermal process, with the exception that the precursor solution is often non-aqueous.

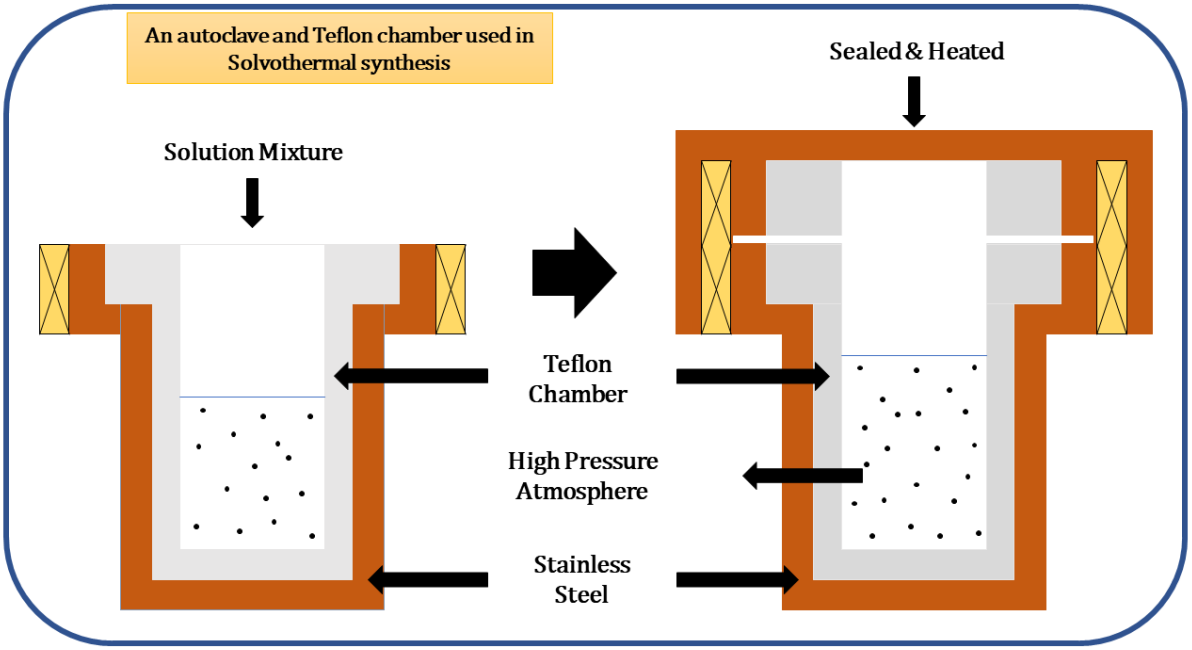

Figure 2.2. Schematic diagrams of an autoclave and a Teflon chamber used in solvothermal synthesis

In this process, a sealed reaction vessel is used, and at a temperature over the boiling point of the solvent, an autogenous (i.e., self-developing and not externally applied) pressure is generated [2], [6]. This pressure inside the sealed container rises with temperature and also relies on other experimental variables, including the percentage of the vessel that is filled, the number of dissolved salts, and the quantity of capping agents. Pressure and temperature have a significant effect on the mobility of ions, viscosity of solvent, and dielectric characteristics, and this component also alters the solubility and activity of the reactants. This method begins with the dissolving of precursor solutes in the solvent at room temperature through magnetic stirring. The mixture is then transported into an autoclave chamber coated with Teflon, as seen in Fig. 2.2. The precursor solution is added to fill the chamber to 70% capacity, and the autoclave is then shut and heated to a predetermined temperature. This technique may be used to create several nanostructures, including cubes, hollow spheres, wires, rods, single crystals, and many more. In addition, the nanostructures produced by this method may be readily manipulated by adjusting the solvent supersaturation, concentration, and kinetic control. This process may also be used to create thermodynamically stable or metastable states of new materials that are difficult to produce by conventional means. Formation of NSs by solvothermal approach is significantly impacted by several thermodynamic and crystallographic variables, such as directed attachment at phases, selective ligand adsorption, and molecular template mechanism, among others.

The following is the synthesis technique for Fe_3O_4 nano hollow spheres: In a solution of 40 ml Ethylene Glycol (EG) and 20 ml ethyl alcohol, 2.4 g of $FeCl_3$, $6H_2O$ is dissolved. The solution is stirred with a magnetic stirrer until the ferric chloride becomes completely miscible. Then, 1.06 grams of Urea and 2 ml oleylamine are added to the preceding solution in order to produce the particles. These solutions are stirred once more until they are fully transparent. The resulting solutions are then put in 80 ml teflon-lined stainless-steel autoclaves for the solvothermal procedure. The solvothermal treatment is carried out for 15 hours at 180 °C. After 15 hours, the resulting black solutions are repeatedly washed in alcohol and then dried overnight at 60 °C.

Here, the function of Ethylene Glycol (EG) is to partly convert Fe^{+3} ions to Fe^{+2} ions. Urea helps precipitate Fe^{+3} and Fe^{+2} to their corresponding hydroxides, where the hydroxyl group is derived from ammonium-hydroxide produced from urea and following heat treatment, both iron hydroxides forms Fe_3O_4 through removal of water. The possible chemical reaction is given below [7]:

$$2Fe^{3+} \xrightarrow{\text{Partial reduction by ethylene glycol}} Fe^{3+} + Fe^{2+}$$

$$CO(NH_2)_2 + H_2O \rightarrow 2NH_3 + CO_2$$

$$NH_3 + H_2O \rightarrow NH_4^+ + OH^-$$

$$Fe^{3+} + 3OH^- \rightarrow Fe(OH)_3$$

$$Fe^{2+} + 2OH^- \rightarrow Fe(OH)_2$$

$$2Fe(OH)_3 + Fe(OH)_2 \xrightarrow{\text{Prolonged Heating}} Fe_3O_4 + 4H_2O$$

Here, from chapter 3, the $MnFe_2O_4$ nano hollow spheres, from chapter 4, the coating of $CoFe_2O_4$ over $Sr_{0.5}Na_{0.25}Bi_{0.25}TiO_3$, and from chapter 5, the coating of $CoFe_2O_4$ over Nickel is synthesized by this particular method.

2.2.3 STÖBER PROCESS

The Stöber process is a sol-gel technique for the production of monodisperse (uniform) spherical silica (SiO_2) materials. The process affords microscopic particles of colloidal silica with diameters ranging from 50 to 2000 nm; particle sizes are fairly uniform with the distribution determined by the choice of conditions such as reactant concentrations, catalysts, and temperature. Larger particles are formed when the concentrations of water and ammonia are raised, but with a consequent broadening of the particle-size distribution. The initial

concentration of TEOS is inversely proportional to the size of the resulting particles; thus, higher concentrations on average lead to smaller particles due to the greater number of nucleation sites, but with a greater spread of sizes. Particles with irregular shapes can result when the initial precursor concentration is too high.

In this method, Silica precursor tetraethyl orthosilicate ($Si(OEt)_4$, TEOS) is hydrolyzed in alcohol (usually methanol or ethanol) using ammonium hydroxide as a catalyst [8], [9]:

$$Si(OEt)_4 + H_2O \rightarrow Si(OEt)_3OH + EtOH$$

$$Si(OEt)_4 + 2H_2O \rightarrow Si(OEt)_2(OH)_2 + 2EtOH$$

The process generates ethanol and a mixture of ethoxysilanols (such as $Si(OEt)_3OH$, $Si(OEt)_2(OH)_2$) which can subsequently condense with TEOS or another silanol with the loss of alcohol or water:

$$2Si(OEt)_3OH \rightarrow (EtO)_3Si - O - Si(OEt)_3 + H_2O$$

$$Si(OEt)_3OH + Si(OEt)_4 \rightarrow (EtO)_3Si - O - Si(OEt)_3 + EtOH$$

$$Si(OEt)_3OH + Si(OEt)_2(OH)_2 \rightarrow (EtO)_3Si - O - Si(OEt)_2OH + H_2O$$

Further hydrolysis of the ethoxy groups and subsequent condensation produces microscopic particles of colloidal SiO_2 by crosslinking process.

This technique may be used to develop a silica coating over certain core materials. For this, it is necessary to disperse the already-prepared core components in the precursor solution. Important parameters determining the layer thickness over the core materials include the stoichiometry of the reagents in the solution and the form, size, and quantity of the core material.

Using this approach, the SiO_2 coating over $MnFe_2O_4$ from Chapter 3 is applied.

2.2.4 SOLID STATE REACTION METHOD

The usual solid state reaction method requires calcining the mixture at a very high temperature to enable cations to migrate amongst one another and mix the correct metallic oxides and carbonates over the course of hours. Using this method, the exceedingly slow chemical reaction is carried out by ion diffusions in solid states. Due to the fact that the reaction in this synthesis process occurs when the chemicals come into contact, an equal distribution of

components and proper mixing are essential. The reactions begin rapidly due to the short diffusion routes, but as they advance, they progressively slow down. As a consequence of the inhomogeneity of the mixture, this method may encounter uneven particle shape and size, loss of stoichiometry, formation of undesirable phases, etc.

Sodium Bismuth Titanate-Strontium Titanate Solid Solution from chapter 4 is synthesized in this thesis using the conventional solid state reaction method.

2.3 FABRICATION OF SAMPLES FOR MEASUREMENTS

For various measurements, the as-synthesized powder ferrite samples should be given the relevant shapes and forms. For dielectric tests, powder samples are compressed into pellets and linked to wires using silver paste. For FTIR spectroscopy, where potassium bromide (KBr, spectroscopic grade) is generally employed as the window material, powder samples must also be pelletized. To pelletize the powder sample, about 25 MPa of pressure is applied using a Riken Pressure Gauge. For microwave measurements utilizing coaxial line and VNA, the material should have a toroidal form with an outside diameter of 3.5 mm and an inner diameter of 1.5 mm, per the coaxial line's dimensions. As seen in Fig. 2.3, composite samples for

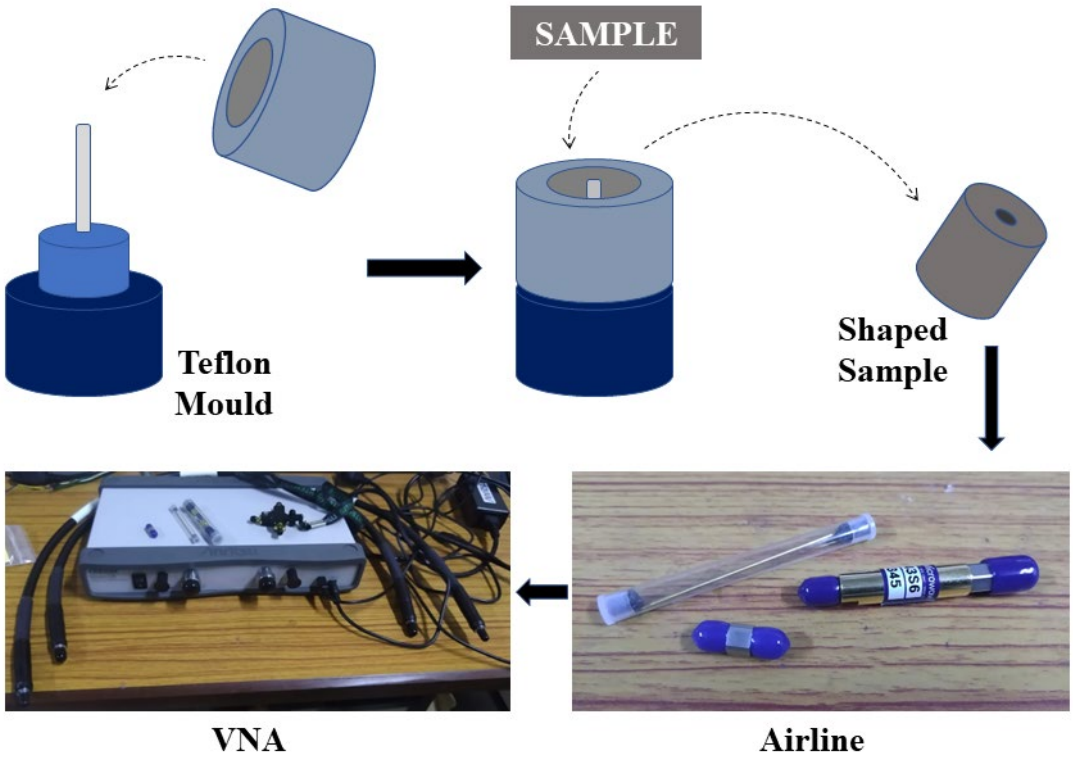

Figure 2.3. Teflon mould for sample preparation for study of Microwave properties

microwave measurements are formed by putting powder samples at various weight percents into an Epoxy Resin matrix and then molding this mixture in a precisely manufactured self-made Teflon mold.

2.4 CHARACTERIZATION TECHNIQUES

2.4.1 X-RAY DIFFRACTION (XRD)

X-ray diffraction (XRD) is a well-known method for analysing the crystal structures, phases, preferred crystal orientations, chemical compositions, and other structural properties of a material, such as the average grain size, lattice strain, and crystal defects. A cathode ray tube produces X-rays, which are then filtered to generate monochromatic radiation, collimated to concentrate, and directed towards the sample. When a monochromatic X-ray is impacted onto a material, the atoms in the material scatter the X-ray, as illustrated in Fig. 2.4, since the wavelength of X-rays is equivalent to the atomic size [10]. When Bragg's law is satisfied, these dispersed waves create constructive and destructive interferences.

$$2d_{hkl}sin\theta = n\lambda \tag{2.3}$$

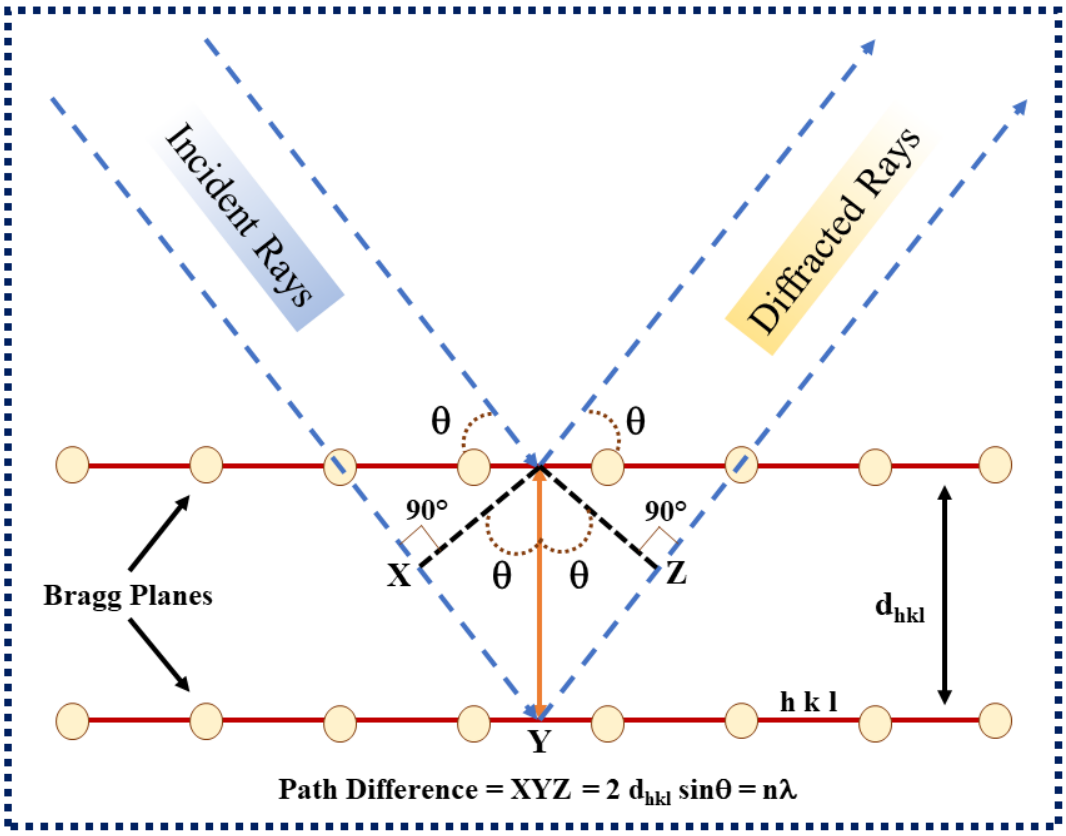

Figure 2.4. Schematic diagram of diffraction of X-rays by a crystal

Where d_{hkl} is the spacing between two planes, θ is the incident angle of X-Rays, n is any integer number, and λ is the wavelength of the X-Rays. The Bragg's law is portrayed in Figure 2.3.

X-ray powder diffraction (XRD) is a valuable analytical method frequently used for phase identification of crystalline materials. It may offer the following information on the investigated material: (a) Phase composition, (b) Crystallite size, (c) Quantitative phase analysis, (d) Unit cell lattice parameters, and (e) Micro-strain, etc.

The phase and structure of the all samples reported in this thesis are investigated by X-ray diffraction (XRD) recorded at room temperature with Panalytical X'Pert Pro diffractometer and SmartLab automated multipurpose X-ray diffractometer using the Cu-K_α line (λ = 1.54 Å).

2.4.2 FIELD EMISSION SCANNING ELECTRON MICROSCOPE (FESEM)

The Field Emission Scanning Electron Microscope (FESEM) is a microscope that takes topographical images of objects using a focused electron beam [11], [12]. A significant electrical field gradient is used in FESEM to concentrate and accelerate an electron beam. As the beam bombards the target region of the object, secondary electrons are released. Angle and velocity of secondary electron emission are related to the surface structure of the object. The secondary electrons that are emitted are detected, and the resulting data is processed further to produce a digital picture.

An FESEM mainly consists of parts discussed below [Fig. 2.5],

- Electron Gun: In a conventional electron microscope, electrons are primarily produced by heating a tungsten filament to around 2800 °C using an electric current. In a field emission (FE) scanning electron microscope, there is no heating involved in the electron beam emission process. Instead, a cathode consisting of a very thin and sharp tungsten needle (tip diameter 10^{-7} –10^{-8} m) is put in front of a main anode to create a voltage in the range of 0.5 to 30 kV. Since the electron beam generated by the FE source is 1,000 times smaller than that of a conventional microscope, the picture quality is significantly enhanced.

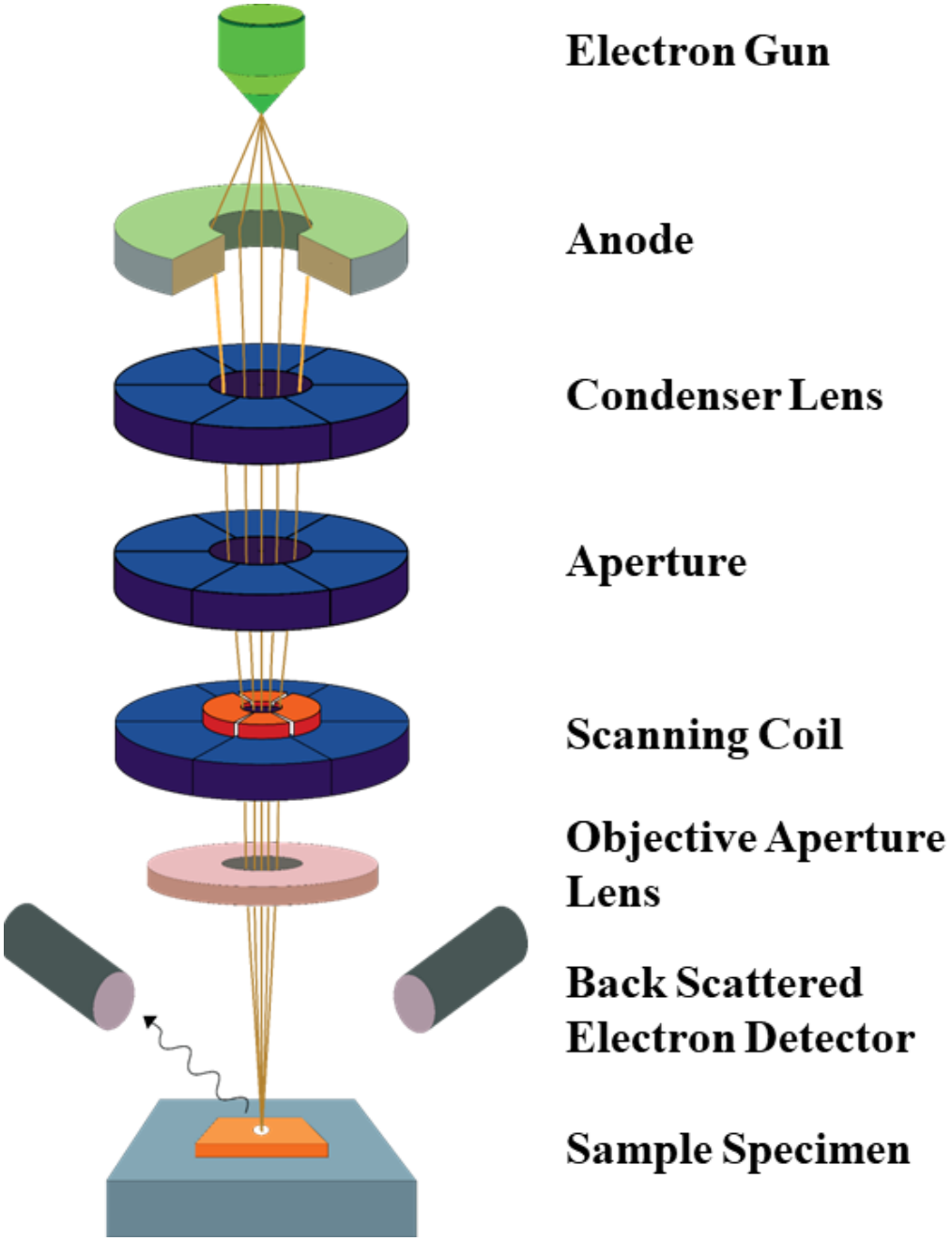

Figure 2.5. Schematic presentation of the fundamental process for both FESEM and EDX

- Condenser lens: The primary purpose of condenser lenses is to alter the beam diameter. Low current results in a small diameter but poor signal-to-noise ratio or resolution, while high current has the opposite effect.
- Scan coils: The scan coils direct the electron beam's deflection towards the item in a zigzag pattern. The scan movement and velocity influence the image's sharpness and refresh rate on the display.
- The objective lens: The electron beam is focused on the item via the objective lens. For an item located near to the objective lens to deflect the electron beam, it must provide a greater

force. However, because to the lowest beam diameter, the highest resolution is achieved at short working distances.

- Detector: The velocity of the secondary electrons released after the main probe bombards an item varies based on the level and angle of the object's surface from where they are emitted. The scintillators light up when the emitted secondary electrons collide with them. Depending on the characteristics of the secondary electrons, the lighting and its position vary. The signal is amplified and converted into a video signal in order to produce the digital picture.

When an electron beam strikes a substance, electrons are expelled from the atoms, even those on the surface. At this time, an electron from a higher energy shell fills the vacancy and produces X-ray that is distinctive of the material and contains information about its constituent components. This method is known as EDAX or energy dispersive X-ray analysis. EDAX is used to identify the chemical components present on the surface of a sample.

2.4.2.1 ENERGY DISPERSIVE X-RAY SPECTROSCOPY (EDX)

Energy dispersive analysis of X-ray (EDX) is a method for determining the elemental makeup of a substance. During this procedure, the sample is blasted with high-energy electrons, which interact with the sample's electrons. During this process, the electrons from the inner shell of the atoms might be excited to higher energy levels, or they can be expelled, resulting in an electron shortage in the inner shell (hole). Eventually, the hole is filled with electrons from the outer shell's higher energy levels. Consequently, the energy difference between these two energy levels is expelled from the material as X-rays. A Si (or Li) detector is often employed as an energy dispersive spectrometer to count the quantity of X-rays emitted. Fig. 2.5 depicts a schematic representation of the essential process for both FESEM and EDX. However, each element's atom emits X-rays with a distinct quantity of energy. Consequently, the elements included in the sample may be identified by calculating the amount of energy contained in the X-rays released by the sample. Typically, the peaks of an EDX spectrum correlate to the energy levels for which the most X-rays are received. These peaks are unique to an atom and so define a particular element. From the relative strengths of these peaks, the sample's atomic percentage may be calculated.

2.4.3 TRANSMISSION ELECTRON MICROSCOPE (TEM)

A transmission electron microscope (TEM) creates a picture by passing a high-energy electron beam through an extremely thin sample [13], [14]. Then, features such as particle size,

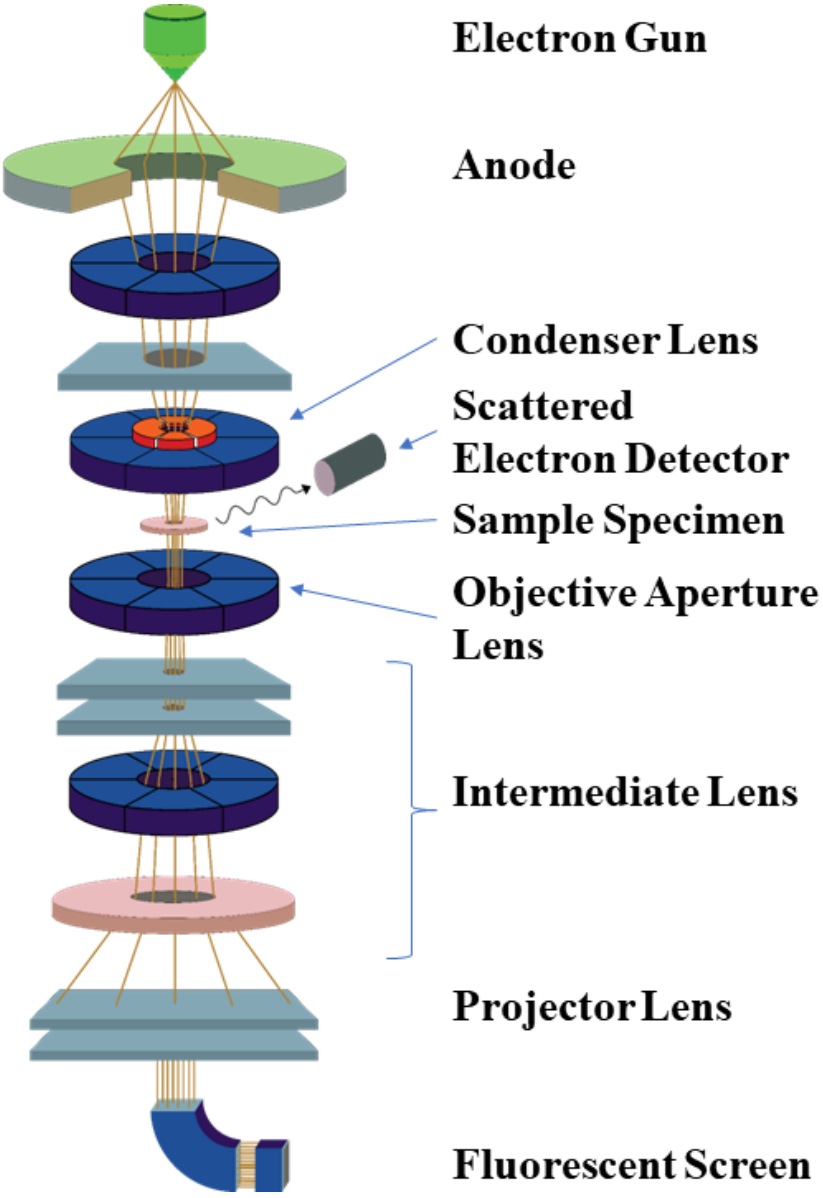

Figure 2.6. Schematic diagram of transmission electron microscope system

crystal structure, and chemical analysis are observed utilizing the electron-atom interactions. Transmission and scattering are the two primary interactions that occur when an electron beam touches a substance.

- Imaging: As illustrated in Fig. 2.6, in order to get an image, the electron beam emitted by the electron gun must travel through the condenser lens, which concentrates the beam into a narrow, thin, coherent beam. The beam then strikes the specimen, where portions of it pass through the specimen. To increase contrast by preventing high-angle diffracted electrons, the transmitted beam is passed via a lens with an objective aperture. The beam is then enlarged by passing it via an intermediate lens and a projector lens. As the picture

reaches the fluorescent screen, the image is visible to the user. The darker regions of the picture reflect regions of the sample through which fewer electrons may flow.

2.4.3.1 HIGH-ANGLE ANNULAR DARK-FIELD (HAADF)

In a scanning transmission electron microscope, annular dark-field imaging is a technique for mapping specimens (STEM). By capturing dispersed electrons using an annular dark-field detector, annular dark-field images are created. Conventional TEM dark-field imaging employs an objective aperture to gather only passing scattered electrons. In contrast, STEM dark-field imaging employs an annular detector to capture only the scattered electrons, as opposed to an aperture, to distinguish the scattered electrons from the main beam. As a result, the contrast processes between conventional dark field imaging and STEM dark field are distinct.

High-angle annular dark-field imaging (HAADF) is a STEM method that creates an annular dark field picture using Rutherford scattered electrons from the atomic nucleus, as opposed to Bragg scattered electrons. This method is very sensitive to fluctuations in the atomic number (Z) of atoms present in the sample. For elements with a higher Z, increased electrostatic interactions between the nucleus and electron beam scatter more electrons at larger angles. As a consequence, the HAADF detector detects a stronger signal from atoms with a higher Z, which causes them to seem brighter in the final picture. This significant dependency on Z (with contrast roughly proportional to Z^2) makes HAADF an effective method for identifying tiny portions of an element with a high Z in a matrix of material with a lower Z. Consequently, a typical use for HAADF is in heterogeneous catalysis research, where the assessment of the size and distribution of metal particles is crucial.

2.4.4 VIBRATING SAMPLE MAGNETOMETER (VSM)

The vibrating sample magnetometer (VSM) is often used to determine the magnetic characteristics of materials [15], [16]. It is capable of measuring magnetic moments as tiny as 10^{-5} emu. The sample is first put into a constant magnetic field (H). Next, the sample is vibrated sinusoidally to excite the pickup coils with the consequent fluctuation in magnetic flux. In accordance with Faraday's law of induction, an electromotive force (EMF) is created across the pickup coils with N identical loops and an area of cross-section, A. The EMF is produced by,

$$V = -NA\frac{dB}{dt} \tag{2.4}$$

If the coil is placed in a constant magnetic field (H), the magnetic flux (B) is given by,

$$B = \mu_0 H \tag{2.5}$$

Where μ_0 is the free space permeability.

If the sample possess a magnetization of M, then the magnetic flux around the vibrating sample is,

$$B = \mu_0 (H + M) \tag{2.6}$$

Therefore, the change in magnetic flux due to the presence of the sample is,

$$\Delta B = \mu_0 M \tag{2.7}$$

The induced force on the pick-up coil is therefore given by,

$$Vdt = -\mu_0 NAM \tag{2.8}$$

This output signal is recorded and used to calculate the magnetic moment of the sample.

The schematic diagram of a VSM unit is shown in Fig. 2.7. The parts that are used in VSM are,

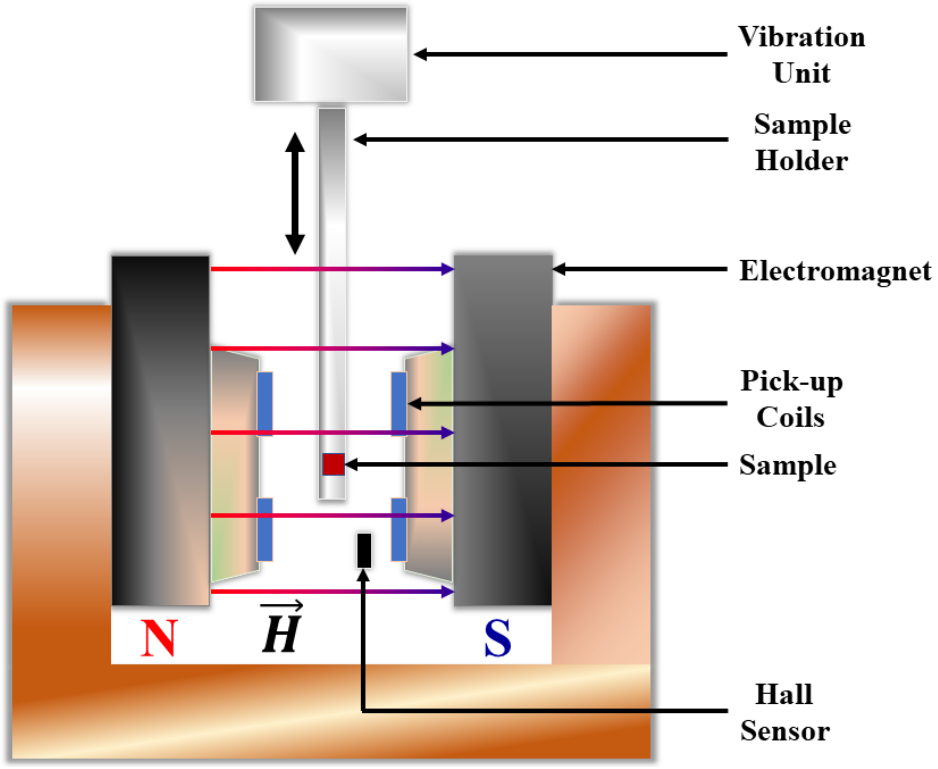

Figure 2.7. Schematic diagram of a vibrating sample magnetometer unit

- Water cooled electromagnet and power supply: In order to magnetize the sample, a water-cooled electromagnet and power supply are utilized to provide a steady magnetic field.
- Vibration unit and sample holder: The sample holding rod is coupled to the vibration exciter, and its end is positioned between the electromagnets in the middle area. The vibration unit moves the sample up and down at a particular frequency.
- Pick-up coils: The EMF force generated by the vibrating sample induces an alternating current in the pickup coils with the same frequency as the sample's vibration frequency. The produced signal comprises information on the magnetization of the sample.

A portion of the magnetic measurements presented in this dissertation are examined using a vibrating sample magnetometer (VSM, Lakeshore, model 7144). The model produces a maximum magnetic field of 1.6 T.

Quantum Design's DYNACOOL Physical Property Measurement System (PPMS) is also utilized as per needs. The VSM attached to this system provides following features:

- At 300K, noise levels of less than 6×10^{-7} emu at 300 K are reached by isolating the sample signal from external mechanical and electrical noise using a lock-in measurement technique. The magnetic sensitivity at 9 T is ±0.01% over 3 cm on axis. A superconducting magnet is used, oriented longitudinally which is reason behind strong magnetic field generated by the system.
- A temperature sensor integrated within the coil set provides local sample thermometry via exchange gas coupling. The temperature range is typically 1.8 to 400 K at vibration frequency of 60Hz. The temperature (T) stability of the system is $\pm0.1\%$ for T < 20 K and $\pm0.02\%$ for T > 20 K.
- The optional Large Bore Coil Set enables an even wider variety of sample holders with minimal loss of sensitivity.

2.4.6 DIELECTRIC MEASUREMENT

A capacitance analyser or an LCR meter (Inductance (L), Capacitance (C), and Resistance (R)) is a commonly used instrument for measuring the capacitance, inductance, and resistance of a sample. In this procedure, the inductance and capacitance of the material are not measured directly; rather, the material's impedance is measured and then translated into inductance and capacitance values. The LCR meter is used to measure impedance characteristics across a large frequency range, as well as the corresponding series resistance, capacitance, etc., and the Q factor of an inductive sample.

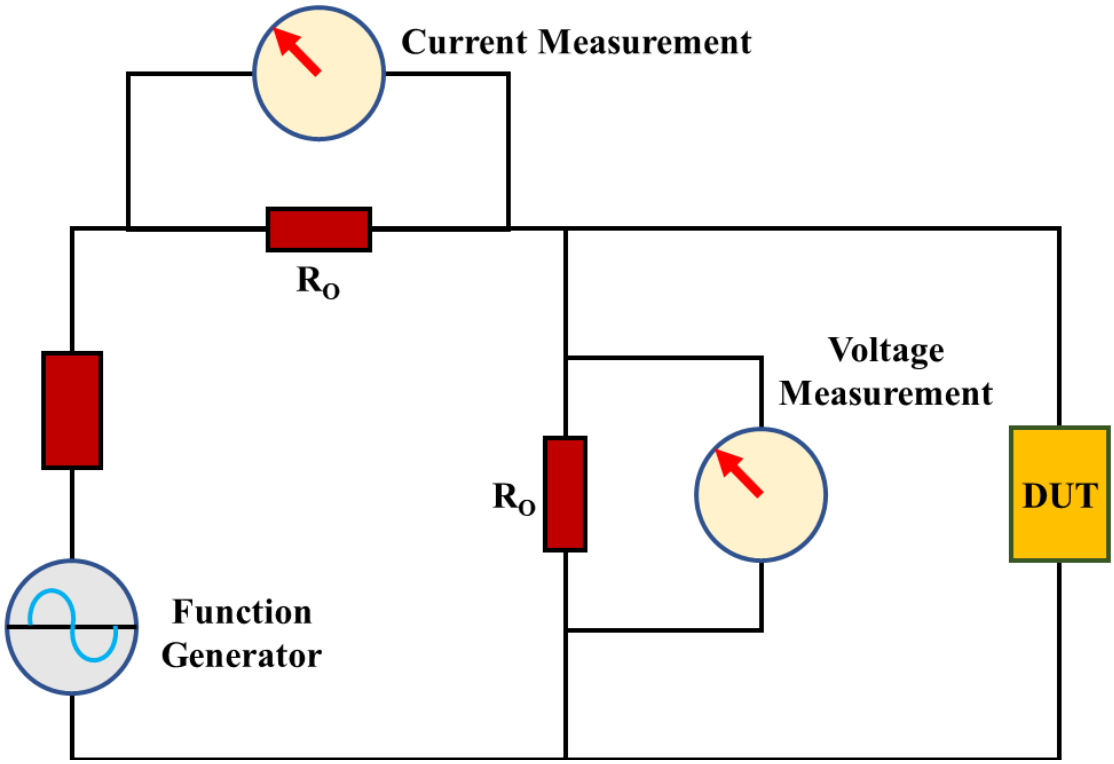

Figure 2.8. Schematic diagram of an LCR meter used to measure dielectric properties

The dielectric constant (ε_r) of a sample is calculated assuming a parallel plate capacitor setup, using the formula,

$$\varepsilon_r = \frac{\varepsilon}{\varepsilon_0} = \frac{Cd}{A\varepsilon_0} \tag{2.9}$$

Where C is the capacitance of the sample in Farad (F), d is the thickness of the sample in meter (m), A is the area of the electrode in square meter (m^2), ε_0 is the free space permittivity (8.854×10^{-12} F/m), and ε is the dielectric constant or relative permittivity of the sample.

The sample or device under test (DUT) is exposed to an *ac* voltage using the function generator, as seen in Fig. 2.8. The analyser then analyses the voltage and current across the DUT. The impedance is calculated by dividing the observed voltage by the measured current. The phase angle of voltage and current is computed using the sample's equivalent inductance or capacitance and resistance.

2.4.7 MICROWAVE MEASUREMENT TECHNIQUE - VECTOR NETWORK ANALYZER

The vector network analyser (VNA) is necessary for analysing the characteristics of electrical networks since it evaluates both amplitude and phase features. Reflection and

transmission of electrical networks are easy and precise to measure at high frequencies; hence, network analysers commonly monitor S-parameters. VNAs may be used on networks with any number of ports, however this article will focus on a two-port network system [17]. The VNA, which is an automated network analyser, is often used for radio frequency (RF) and microwave design applications and characterizations for both passive and active networks in terms of network scattering characteristics, i.e., *S* parameters.

Fig. 2.9 depicts a simplified block diagram of a vector network analyser. This figure depicts the standard components of a 2-port VNA. Ports 1 (P1) and 2 (P2) are the two ports of the device being evaluated (DUT). PC1 and PC2 are the precision cables linked to the P1 and P2 ports, respectively, of the VNA. The RF test frequency is created by a source with changeable frequencies, and its power level is adjusted by an attenuator with variable resistance. The direction of switch SW1 influences the test signal's route through the DUT. Consider first that SW1 is at position 1, such that the test signal is incident at P1 on the DUT, and in that case S11 and S21 can be measured. The test signal is routed to the common port of splitter 1, with the reference channel feeding a P1 reference receiver (REF1) and the test channel connecting to P1 via directional coupler DC1 and cable PC1. The third connection of DC1 connects the power reflected from P1 to the test receiver 1 through PC1 (TEST1). Similarly, P2 signals are routed through PC2 and DC2 prior to reaching TEST2. Coherent

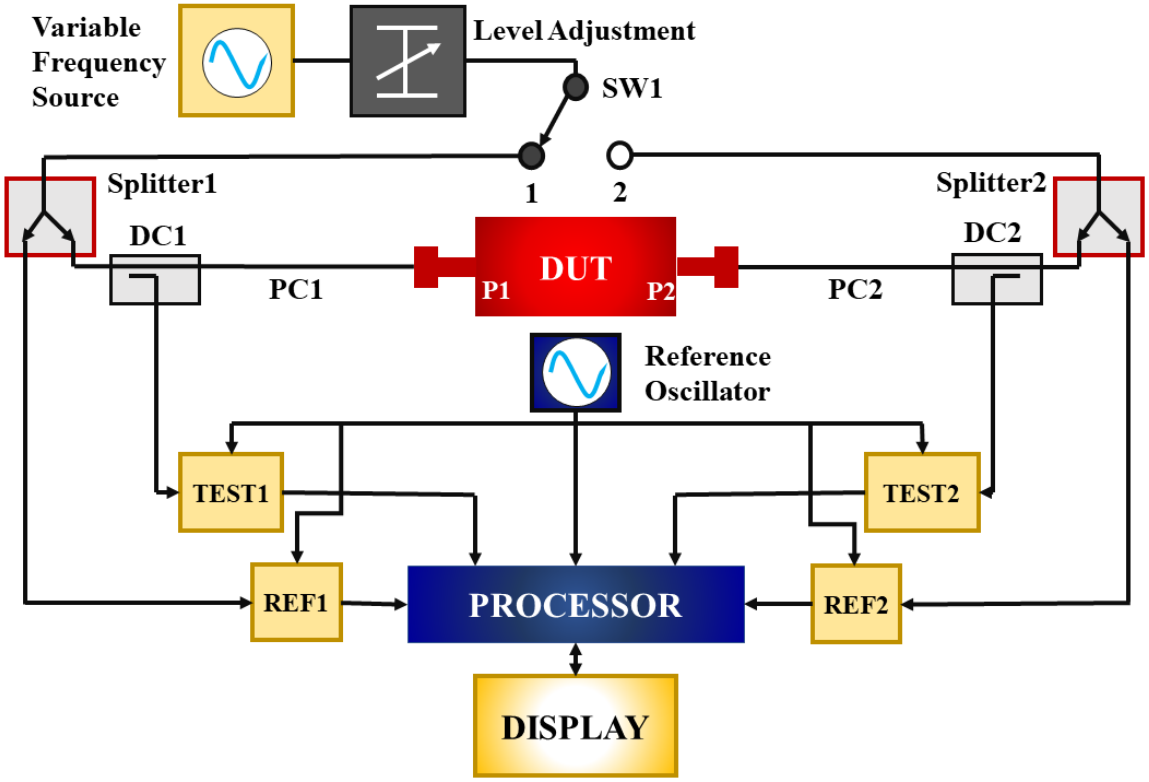

Figure 2.9. Simplified schematic presentation of a vector network analyser (VNA)

receivers are REF1, TEST1, TEST2, and TEST2 because they share the same reference oscillator and can measure the amplitude and phase of a test signal at a certain frequency. All complicated receiver output signals are routed to a processor, which executes the required mathematical calculations and displays the parameters and format specified by the user. Even though the instantaneous value of phase comprises both temporal and spatial components, the former is avoided by using two test channels, one as a reference and the other for measurement. This instrument can quickly detect parameters such as standing wave ratio (SWR), return loss, group delay, impedance, etc., as well as the network's time-domain response. A calibration technique corrects flaws resulting from mismatched directional couplers, poor directivity, cable loss, and changes in the analyser system's frequency response. The most straightforward for this objective is SOLT, which stands for Short, Open, Load, and Through. Modern network analysers save information pertaining to devices in a calibration kit.

REFERENCES

[1] O. Luukkonen, S. I. Maslovski, and S. A. Tretyakov, "A Stepwise Nicolson–Ross–Weir-Based Material Parameter Extraction Method," *IEEE Antennas Wirel Propag Lett*, vol. 10, pp. 1295–1298, 2011, doi: 10.1109/LAWP.2011.2175897.

[2] N. T. K. Thanh, N. Maclean, and S. Mahiddine, "Mechanisms of nucleation and growth of nanoparticles in solution," *Chemical Reviews*, vol. 114, no. 15. American Chemical Society, pp. 7610–7630, Aug. 13, 2014. doi: 10.1021/cr400544s.

[3] A. V. Nikam, B. L. V. Prasad, and A. A. Kulkarni, "Wet chemical synthesis of metal oxide nanoparticles: A review," *CrystEngComm*, vol. 20, no. 35, pp. 5091–5107, 2018, doi: 10.1039/C8CE00487K.

[4] S. Kumar and T. Nann, "Shape control of II-VI semiconductor nanomaterials," *Small*, vol. 2, no. 3, pp. 316–329, Mar. 2006, doi: 10.1002/smll.200500357.

[5] C. Burda, X. Chen, R. Narayanan, and M. A. El-Sayed, "Chemistry and properties of nanocrystals of different shapes," *Chemical Reviews*, vol. 105, no. 4. pp. 1025–1102, Apr. 2005. doi: 10.1021/cr030063a.

[6] D. Nunes *et al.*, "Metal Oxide Nanostructures for Sensor Applications."

[7] M. M. Goswami, C. Dey, A. Bandyopadhyay, D. Sarkar, and M. Ahir, "Micelles driven magnetite (Fe3O4) hollow spheres and a study on AC magnetic properties for hyperthermia application," *J Magn Magn Mater*, vol. 417, pp. 376–381, 2016, doi: https://doi.org/10.1016/j.jmmm.2016.05.069.

[8] W. Stöber, A. Fink, and E. Bohn, "Controlled growth of monodisperse silica spheres in the micron size range," *J Colloid Interface Sci*, vol. 26, no. 1, pp. 62–69, 1968, doi: https://doi.org/10.1016/0021-9797(68)90272-5.

[9] A. Van Blaaderen, J. Van Geest, and A. Vrij, "Monodisperse colloidal silica spheres from tetraalkoxysilanes: Particle formation and growth mechanism," *J Colloid Interface Sci*, vol. 154, no. 2, pp. 481–501, 1992, doi: https://doi.org/10.1016/0021-9797(92)90163-G.

[10] B. D. (Bernard D. Cullity, *Elements of x-ray diffraction*. Addison-Wesley Publishing Company, Inc, 1978.

[11] M. Abd Mutalib, M. A. Rahman, M. H. D. Othman, A. F. Ismail, and J. Jaafar, "Chapter 9 - Scanning Electron Microscopy (SEM) and Energy-Dispersive X-Ray (EDX) Spectroscopy," in *Membrane Characterization*, N. Hilal, A. F. Ismail, T. Matsuura, and D. Oatley-Radcliffe, Eds., Elsevier, 2017, pp. 161–179. doi: https://doi.org/10.1016/B978-0-444-63776-5.00009-7.

[12] K. Akhtar, S. A. Khan, S. B. Khan, and A. M. Asiri, "Scanning Electron Microscopy: Principle and Applications in Nanomaterials Characterization," in *Handbook of Materials Characterization*, S. K. Sharma, Ed., Cham: Springer International Publishing, 2018, pp. 113–145. doi: 10.1007/978-3-319-92955-2_4.

[13] B. Fultz and J. M. Howe, Eds., "The TEM and its Optics," in *Transmission Electron Microscopy and Diffractometry of Materials*, Berlin, Heidelberg: Springer Berlin Heidelberg, 2008, pp. 61–118. doi: 10.1007/978-3-540-73886-2_2.

[14] B. Fultz and J. M. Howe, Eds., "High-Resolution TEM Imaging," in *Transmission Electron Microscopy and Diffractometry of Materials*, Berlin, Heidelberg: Springer Berlin Heidelberg, 2008, pp. 517–582. doi: 10.1007/978-3-540-73886-2_10.

[15] V. Lopez-Dominguez *et al.*, "A simple vibrating sample magnetometer for macroscopic samples," *Review of Scientific Instruments*, vol. 89, no. 3, p. 034707, Mar. 2018, doi: 10.1063/1.5017708.

[16] W. Burgei, M. J. Pechan, and H. Jaeger, "A simple vibrating sample magnetometer for use in a materials physics course," *Am J Phys*, vol. 71, no. 8, pp. 825–828, Jul. 2003, doi: 10.1119/1.1572149.

[17] D. M. Pozar and J. Wiley, "Microwave Engineering Third Edition W WILEY."

CHAPTER 3

MAGNETIC AND NON-MAGNETIC BILAYER FORMATION OVER MANGANSE FERRITE NANOHOLLOWSPHERE AND OPTIMIZATION OF COATING THICKNESSES: AN EFFECTIVE METHOD TO OBTAIN ENHANCED ELECTROMAGNETIC WAVE ABSORPTION

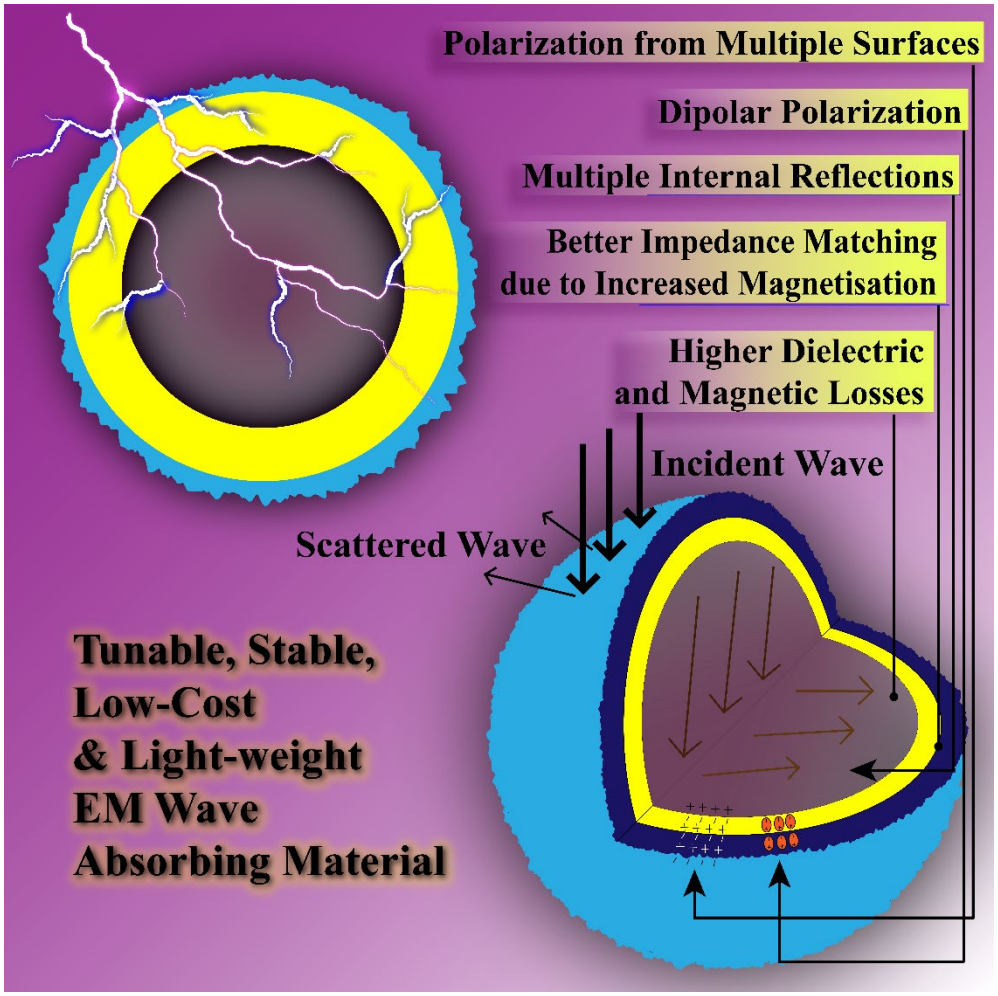

In this chapter, the manganese ferrite nano-hollowspheres reported in earlier research are coated with a dielectric silica layer and a magnetic cobalt ferrite layer for comparative analysis. Afterward, the layer thicknesses of each layer are further optimized to improve microwave absorption.

Chapter 3

3.1 Preamble

The quest for a material that is capable of effectively absorbing electromagnetic (EM) waves and has key characteristics such as low cost, thinness, lightweight, and high microwave absorption has captivated researchers.

Ferrite materials stand out as potentially favorable candidates in this scenario due to the magnetic and electric characteristics that they possess [1], [2]. In addition, changing the saturation magnetization (M_S), coercivity (H_C), permeability (μ), permittivity (ε), and conductivity (σ) of ferrites, among other properties of ferrites, can result in a wider effective bandwidth (BW_{eff}), improved impedance matching (i.e., $|Z_{in}/Z_0|\sim1$), and therefore increased minimum reflection loss (RL_{min}). For instance, Zhang et al. discovered that matching the EM parameters resulted in a considerable improvement in the amounts of EM energy that was absorbed [3].

Even though ferrites have many benefits, the high density of these materials brings down the overall mass efficiency of ferrite-based electromagnetic wave absorber (EMA) composites and limits how they may be employed in a practical application [4]. Utilization of ferrites featuring hollow morphologies is indeed a potential solution for this problem [4]–[6]. Its effectiveness as an EMA material is greater than that of its bulk or solid counterparts due to a lower density of nano-hollow spheres (NHSs), a higher dielectric loss due to dual interfacial area, a high surface-to-volume (STV) ratio, and a higher magnetic loss from its larger magnetic and surface anisotropy [7], [8]. All of these factors contribute to the material's ability to absorb more electromagnetic energy. In addition to this, multiple internal reflections of an electromagnetic wave from the hollow core of NHS and scattering from the outer surfaces both trap the wave, which increases its overall path length [7]–[9]. The transition metal-based spinel ferrite $MnFe_2O_4$ (MnFO) has the highest magnetization value of all the various spinel ferrites based on transition metals. This is because the manganese atom has the maximum number of unpaired electrons [10]–[12]. When the values of ε and μ in the NHS of MnFO are brought closer together, improved impedance matching can be achieved, resulting in better RL_{max} and a broader total effective bandwidth (BW_{eff}) [4], [13]. In addition, it is preferred to have high values of both ε and μ to reduce the required thickness of the absorbing material [14], [15]. Some of the most common strategies for achieving this purpose include shape and size control, chemical doping, and the hybridization of several types of materials [10], [14], [16], [17]. For instance, graphene oxide functionalization was performed on MnFO nanoparticles, and size

tuning of the MnFO NHS was performed to improve EM wave attenuation [4,10]. Wu et al. developed Fe_3O_4/C composite flowers for high-performance electromagnetic wave absorption [16].

In this study, the deposition of dielectric SiO_2 (MnFO@SiO) and magnetic $CoFe_2O_4$ (MnFO@CFO) on ~500 nm MnFO NHS has been conducted separately to enhance dielectric and magnetic loss, which in turn magnifies the EM wave attenuation capabilities. The better and close values of ε and μ in the $CoFe_2O_4$-coated MnFO sample, MnFO@CFO NHS, result in reflection loss as high as -66.48 dB (shielding > 99.999%) at 6.01 GHz at only 20 wt.% filler concentration in an epoxy matrix and for a composite length of only 4.46 mm. When compared to the attenuation constant of bare MnFO NHS, which is 191.3 Np/m, the attenuation constant of MnFO@CFO NHS is 457.8 Np/m, which represents a substantial improvement. In addition, silica-coated MnFO achieves a sufficiently high RL (-30.0 dB) at a thickness (t_m) of just 3 mm, which is a substantial reduction from that of MnFO NHS (t_m = 5.3 mm). This is because silica is an excellent dielectric material, which improves the composite material's overall dielectric permittivity. After that, the thicknesses of the SiO_2 and the CFO layers are individually adjusted to obtain optimum microwave absorption for each bi-layered material.

In addition, a composite absorber thickness-dependent study conducted on all sample sets demonstrates that the hybridization of NHS with each layer optimized is a viable method for enhancing electromagnetic wave interference (EMI) shielding. This was determined by comparing the outcomes of the study across all sample sets.

3.2 Experimental

3.2.1 Sample Preparation

3.2.1.1 Sample Preparation of MnFO NHS

The synthesis of MnFO NHSs is undertaken using a facile one-pot template-free solvothermal technique using polyvinylpyrrolidone (PVP) as a capping agent. As a precursor, the combination of $MnCl_2$, $6H_2O$, and $FeCl_3$, $6H_2O$, with a molar weight ratio of 1:2, is used. As solvents, ethylene glycol (EG) and ethyl alcohol (EtOH) are combined in a 2:1 ratio, and the reducing agent is urea. After combining all the ingredients in a 100 mm beaker and agitating the solution, 90 mg of PVP with a molecular weight of 29,000 is added to produce 500 nm NHS of MnFO. After 30 minutes of stirring, the produced clear and homogeneous solution is poured into a Teflon autoclave which is then enclosed in a stainless steel and transferred into a

hot air oven followed by a heating for 22 hours at a temperature of 180 °C. Subsequently, the as-prepared MnFO NHSs are treated with several washing in EtOH and distilled water, followed by magnetic separation and drying at 60 °C for approximately 30 minutes. The urea plays a role in the precipitation of Mn^{2+} and Fe^{3+} ions from their chloride salts to their respective hydroxides over the course of the reaction [18]. This is followed by the creation of the MnFO phase upon heating the material. The Ostwald ripening process progressively re-crystallizes smaller particles into bigger ones to reduce free surface energy. These clusters subsequently combine into hollow spheres in the presence of urea-formed gas bubbles under the influence of PVP to provide the maximum degree of stability feasible for the spheres [5], [19], [20].

3.2.1.2 Sample Preparation of Silica-Coated MnFO NHS

MnFO NHSs that have previously been produced are coated with SiO_2 using the Stöber technique [19]. During this step, 0.02 g of as-prepared MnFO NHSs are added to a solution containing 35 ml of ethyl alcohol, 3.5 ml of deionized water (DI), and 1.4 ml of NH_4OH at a concentration of 25 wt.%. The mixture is then stirred vigorously for 1 hour. After that, 0.5 ml of tetraethyl ortho-silicate (TEOS) is dripped drop-by-drop into the previously mentioned solution, and the mixture is agitated constantly for an additional 15 hours at room temperature. This is performed so that SiO_2 may be deposited onto the surface of MnFO NHS by hydrolysis and subsequent condensation of TEOS. After being repeatedly rinsed in DI and ethanol, the bi-layered NHSs that are generated are collected by magnetic separation. To optimize the coating thickness, three samples with SiO_2 thicknesses of 35 nm, 60 nm, and 75 nm are synthesized by varying the quantity of as-prepared MnFO NHS introduced during the Stöber procedure. The relevant samples are designated as MnFO@SiO-35, MnFO@SiO-60, and MnFO@SiO-75. The sample MnFO@SiO-75 is also commonly referred to as MnFO@SiO in this thesis since it is the first silica-coated MnFO NHS that has been produced to compare its microwave characteristics with bare MnFO NHS.

3.2.1.2 Sample Preparation of CFO-Coated MnFO NHS

CFO-coated bilayer MnFO NHSs are produced using a wet-chemical technique [21]. A solution containing pre-dispersed MnFO NHSs (0.05 g) and DI (20 ml) is heated at 80 °C for 30 minutes with the addition of 0.06 g $CoCl_2$, $6H_2O$ and 0.12 g $FeCl_3$, $6H_2O$ as raw materials. Then, a 20 ml solution of sodium hydroxide (NaOH) that has been separately heated is added drop-by-drop to the previous solution. At 80 °C, the solution is stirred for 1 hour with constant frequency. After 5 hours, the final sample is obtained by magnetic separation after numerous

DI and ethanol rinsing. In this method, the amount of MnFO NHSs in the precursor solution is adjusted to get the required CFO coating thickness over the MnFO NHSs. To optimize the coating thickness, three samples with CFO thicknesses of 20 nm, 35 nm, and 50 nm are synthesized and designated as MnFO@CFO-20, MnFO@CFO-35, and MnFO@CFO-50, respectively. In this dissertation, MnFO@CFO-50 is also referred to as MnFO@CFO since it is the first CFO-coated MnFO NHS sample that is synthesized to comparatively study the microwave properties with those of uncoated MnFO NHS. For the preparations described above, all of the ingredients are purchased from Sigma-Aldrich. These chemicals all have a purity level of at least 98%.

3.2.2 Characterization

In a Rigaku SmartLab equipped with Cu-K_α radiation, X-ray diffraction (XRD) is done to identify the phase of as-prepared materials. To determine the size and morphology of the samples, an FEI QUANTA FEG 250 field-emission scanning electron microscope (FESEM) with a voltage range of 0.2 to 30 kV and a FEG high-resolution transmission electron microscope (HRTEM) with a voltage range of 80 to 200 kV are used. The energy-dispersive X-ray (EDX) spectrum is captured to conduct the elemental analysis of materials-containing materials. At room temperature (about 300 K), magnetic measurements are obtained using a Lake Shore vibrating sample magnetometer (VSM) and a Quantum Design physical property measuring system (PPMS).

The microwave characteristics of the samples are analyzed within the frequency range of 1 GHz to 17 GHz using a coaxial cable (Maury Microwaves 8043S6) and an Anritsu MS46122B vector network analyzer (VNA). After loading 20 wt.% of powder samples into an epoxy resin matrix and correctly molding this mixture according to the desired dimension, the composite samples are produced for measurement in the microwave frequency spectrum of the VNA. The prepared composites are in the shape of hollow cylinders with an inner diameter of 1.5 mm and an outside diameter of 3.5 mm. For measurement, each composite sample is positioned with high precision at the "port one" end of the coaxial airplane. Using a polynomial fit model of the Nicholson-Ross-Weir (NRW) technique, further analysis of the resulting 2-port scattering (S)-parameters is performed using the transmission line approach [26].

3.3 Results and Discussion

3.3.1 Structure and Morphology

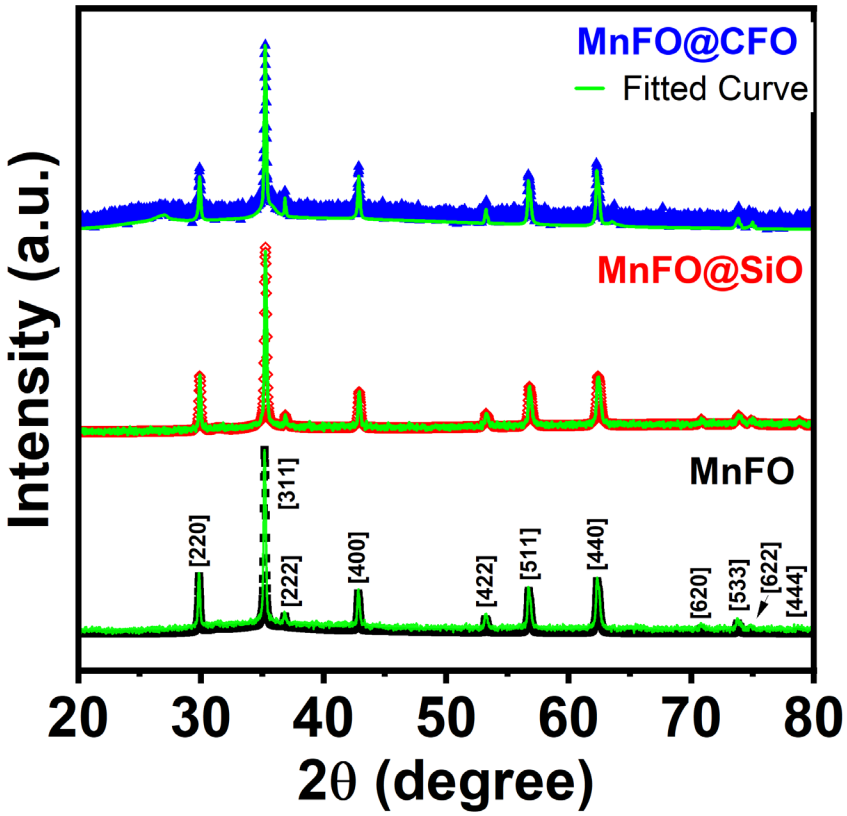

Figure 3.1. X-ray diffraction plots for MnFO, MnFO@SiO, and MnFO@CFO at ~ 300 K

Fig. 3.1 depicts the XRD patterns of MnFO nanohollowspheres and two bi-layered samples with silica and CFO. Similarly, Fig. 3.2 and Fig. 3.3 show the XRD patterns for the three various thicknesses of the SiO_2 and CFO layers individually over MnFO as well as the bare MnFO. As described in the scientific literature (JCPDS file no. 01-084-2781 for MnFO and 01-086-4437 for CFO), each pattern demonstrates the formation of a single-phase spinel face-centered cubic structure at room temperature. Due to the amorphous nature of silica, no peak can be attributed to silica observed in the XRD patterns of the silica-coated samples. The Smart Lab II is used to fit the XRD peaks, and the lattice parameters calculated from the greatest intensity peak corresponding to the [311] plane are listed in Table 3.1. The average crystallite sizes (D) and lattice strains (e) are calculated for each sample using the Debye-Scherrer formula and are also tabulated in Table 3.1. Compared to uncoated MnFO, SiO_2-coated MnFO core-shell NHSs have a greater D and a lower strain. The D and e values of 20 nm and 35 nm CFO-coated MnFO core-shell NHSs were greater than those of uncoated MnFO.

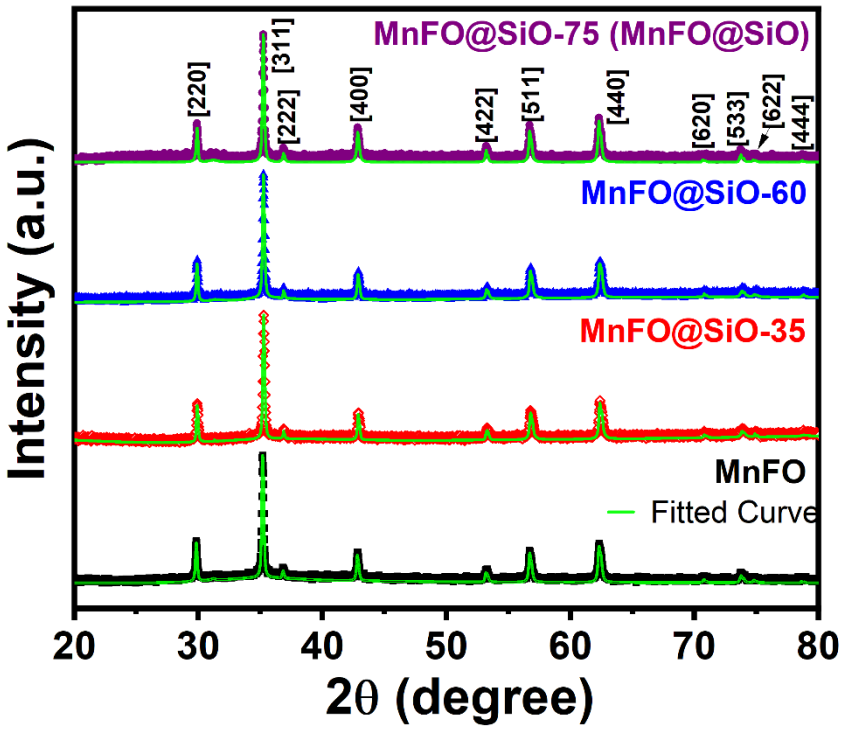

Figure 3.2. X-ray diffraction plots for MnFO, MnFO@SiO-35, MnFO@SiO-60, and MnFO@SiO-75 at ~ 300 K

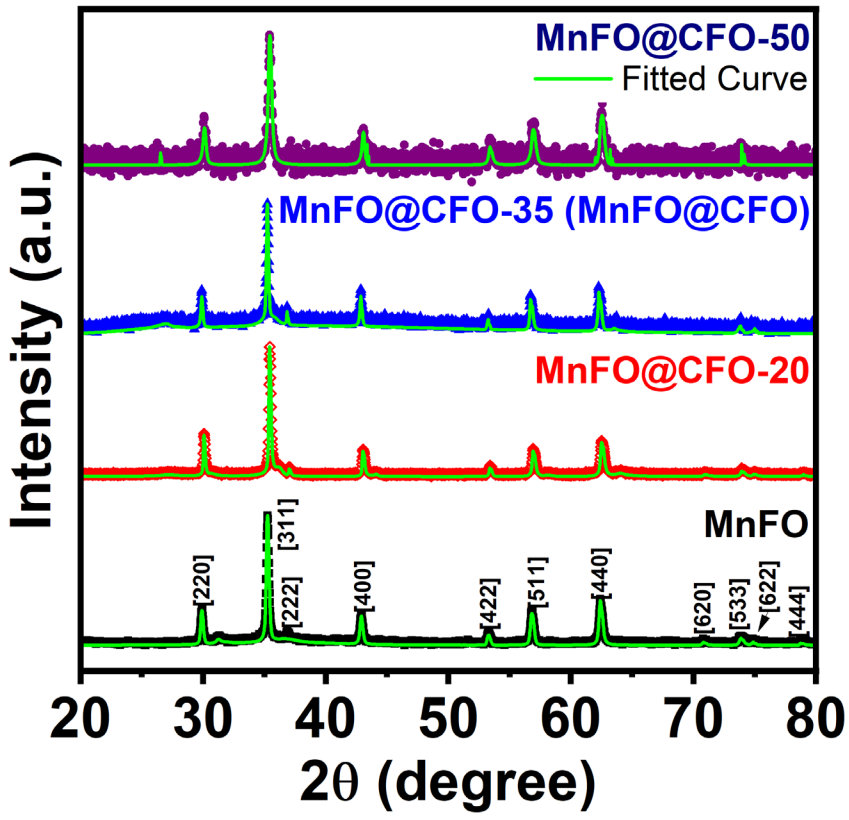

Figure 3.3. X-ray diffraction plots for MnFO, MnFO@CFO-20, MnFO@CFO-35, and MnFO@CFO-50 at ~ 300 K

Because the CFO shell and the MnFO shell have a thickness similar to the 50 nm CFO-coated MnFO, the D value decreases, which also increases the e value.

Figs. 3.4(g)–(i) represents the FESEM micrographs of MnFO NHS and its two-layer morphologies, i.e., MnFO@SiO-75 and MnFO@CFO-35. A similar study depicting the morphological structure of three different thicknesses of silica and CFO over MnFO NHS is illustrated in Figs. 3.4(h), (j), (k) and 3.4(i), (l), (p) accordingly. The interior hollow core of NHSs is visible in the relevant images for both uncoated and silica-coated samples. The average sizes of the samples are examined by plotting the size distribution curves, as seen in Figs. 3.4(a), (c), (e), (m-o), (q), and are listed in Table 3.1 along with the computed coating thicknesses for the various bi-layered samples. This comparative increase in size between MnFO@SiO-75 and MnFO@CFO-35 results in an increase in crystallite size and, therefore, a decrease in lattice strains. The EDX results are shown in Figs. 3.4(b), (d), (f) demonstrate the elemental presence of Mn, Fe, and O in all samples, as well as Co in the CFO-coated samples. The 'Co' element peak in the EDX spectrum of CFO-coated samples further verifies the effective deposition of the CFO layer on the surface of the MnFO NHS sample.

Table 3.1 Particle diameter, coating thickness, crystallite sizes (D), lattice strain (e), coercivities (H_C), and saturation magnetization (M_S) of bare MnFO, MnFO@SiO, and MnFO@CFO core-shell NHSs

Sample Name	Diameter (nm)	Coating Thickness (nm)	D (nm)	e	H_C (kOe)	M_S (emu/g)
MnFO	499.91 ± 20.19	-	39.89	0.00304	58.93	69.69
MnFO@SiO or MnFO@SiO-75	650.37 ± 22.69	75	60.73	0.00142	100.26	55.74
MnFO@CFO or MnFO@CFO-35	569.81 ± 13.09	35	60.44	0.00304	95.95	59.46
MnFO@SiO-35	570.30 ± 11.74	35	60.53	0.00150	77.05	35.74
MnFO@SiO-60	619.61 ± 16.90	60	58.36	0.00153	98.7	39.34
MnFO@CFO-20	539.90 ± 9.66	20	51.06	0.00171	76.71	36.67
MnFO@CFO-50	599.73 ± 15.94	50	32.64	0.00306	67.84	9.67

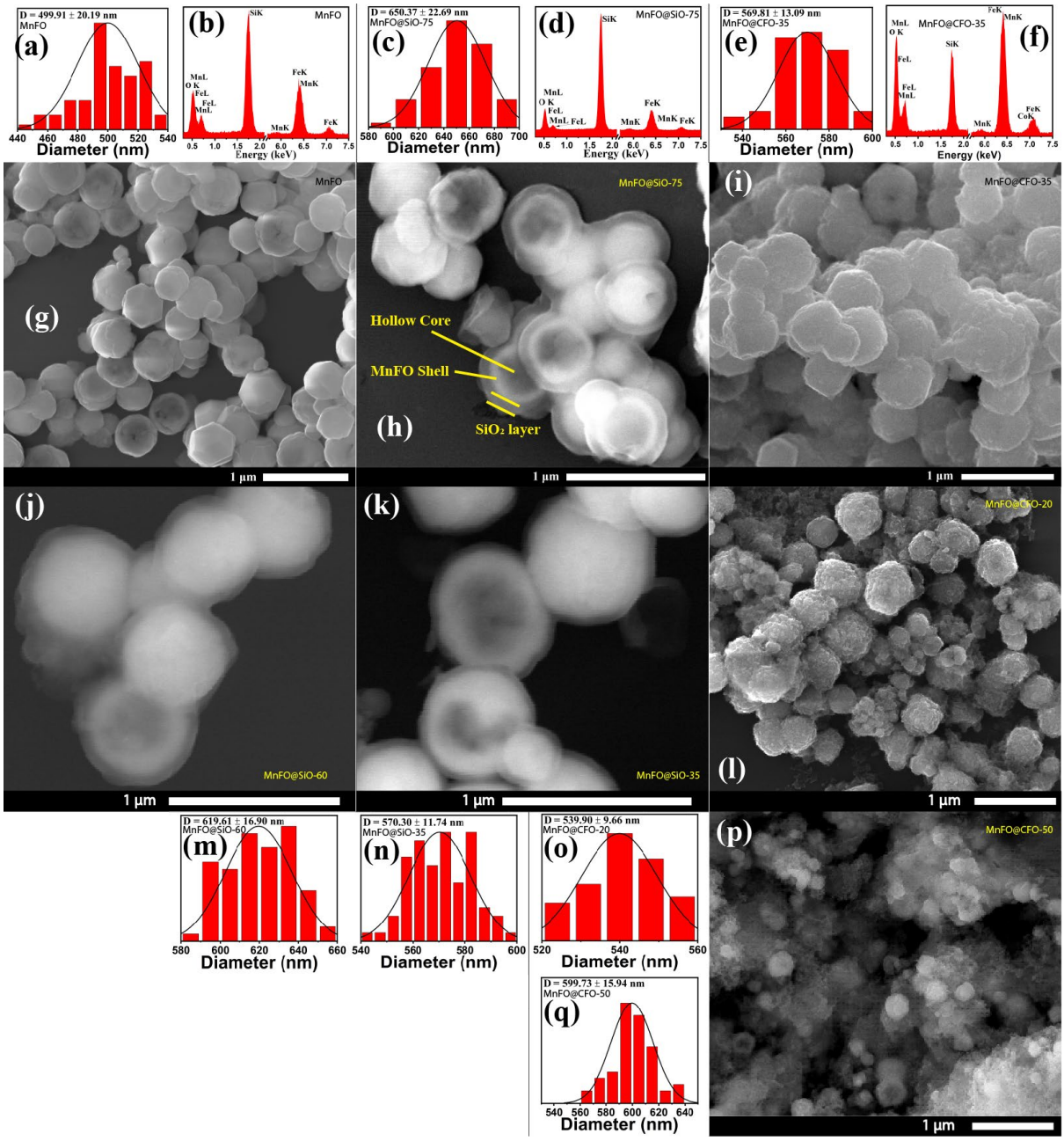

Figure 3.4. The size-distribution plots of (a) MnFO, (d) MnFO@SiO-75, (e) MnFO@CFO-35, (m) MnFO@SiO-60, (n) MnFO@SiO-35, (o) MnFO@CFO-20, and (q) MnFO@CFO-50. FESEM micrographs of (g) MnFO, (h) MnFO@SiO-75, (i) MnFO@CFO-35, (j) MnFO@SiO-60, (k) MnFO@SiO-35, (l) MnFO@CFO-20, and (p) MnFO@CFO-50. EDAX plots of (b) MnFO, (d) MnFO@SiO-75, (f) MnFO@CFO-35.

Figs. 3.5(a)-(c) show TEM micrographs of MnFO nanohollowspheres together with two bi-layered samples with silica and CFO. Alternatively, Figs. 3.6(a)-(c) and Figs. 3.7(a)-(c) show the TEM micrographs for the three various thicknesses of the SiO_2 and CFO-coated MnFO. In the case of bi-layered materials, the TEM micrographs show more pronounced views of the inner and outer portions of the NHSs, as well as surface changes. HRTEM micrographs of MnFO and MnFO@CFO-35 NHS are shown in Figs. 3.5(d) and (e), respectively. The distances measured between parallel diffraction planes in HRTEM micrographs correspond

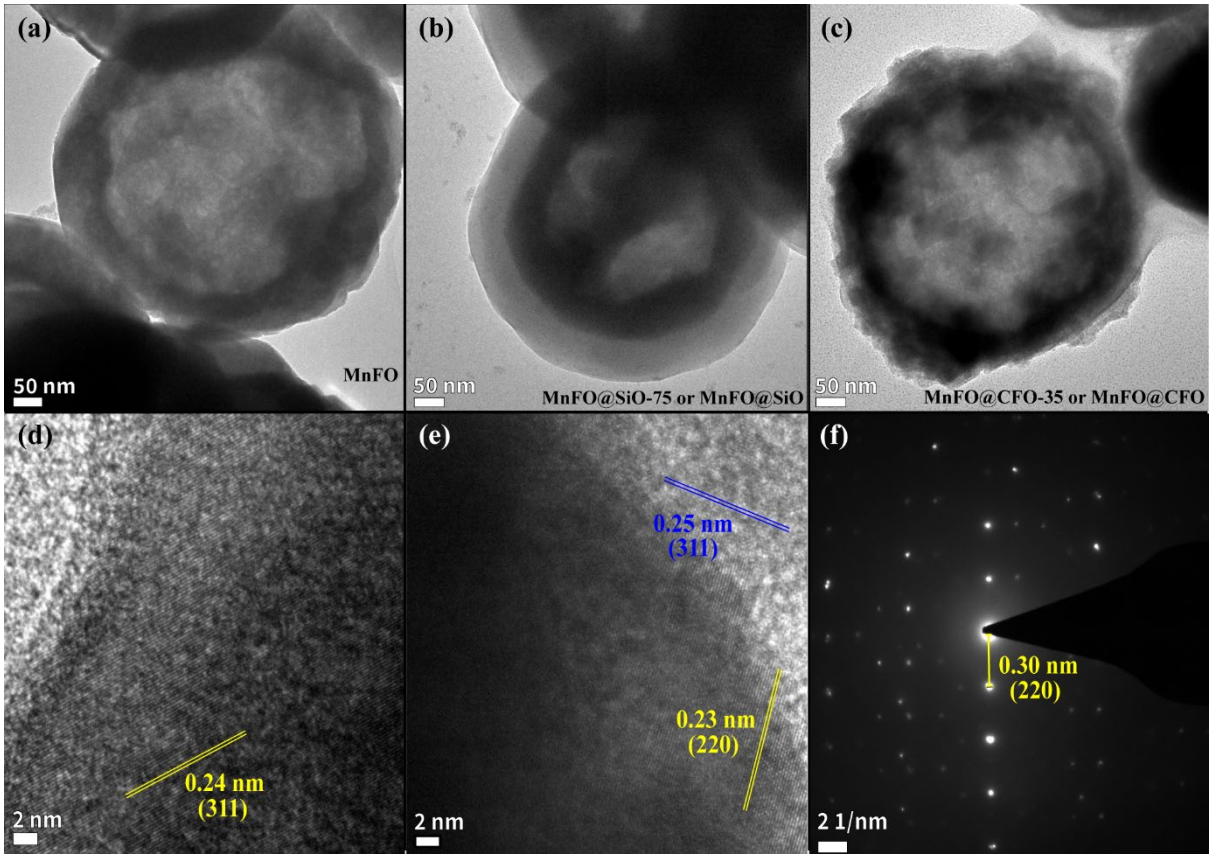

Figure 3.5. TEM micrographs for (a) MnFO NHS, (b) MnFO@SiO, (c) MnFO@CFO, HRTEM micrographs of (d) MnFO NHS; (e) MnFO@CFO-35, (f) SAED pattern for MnFO@SiO NHS.

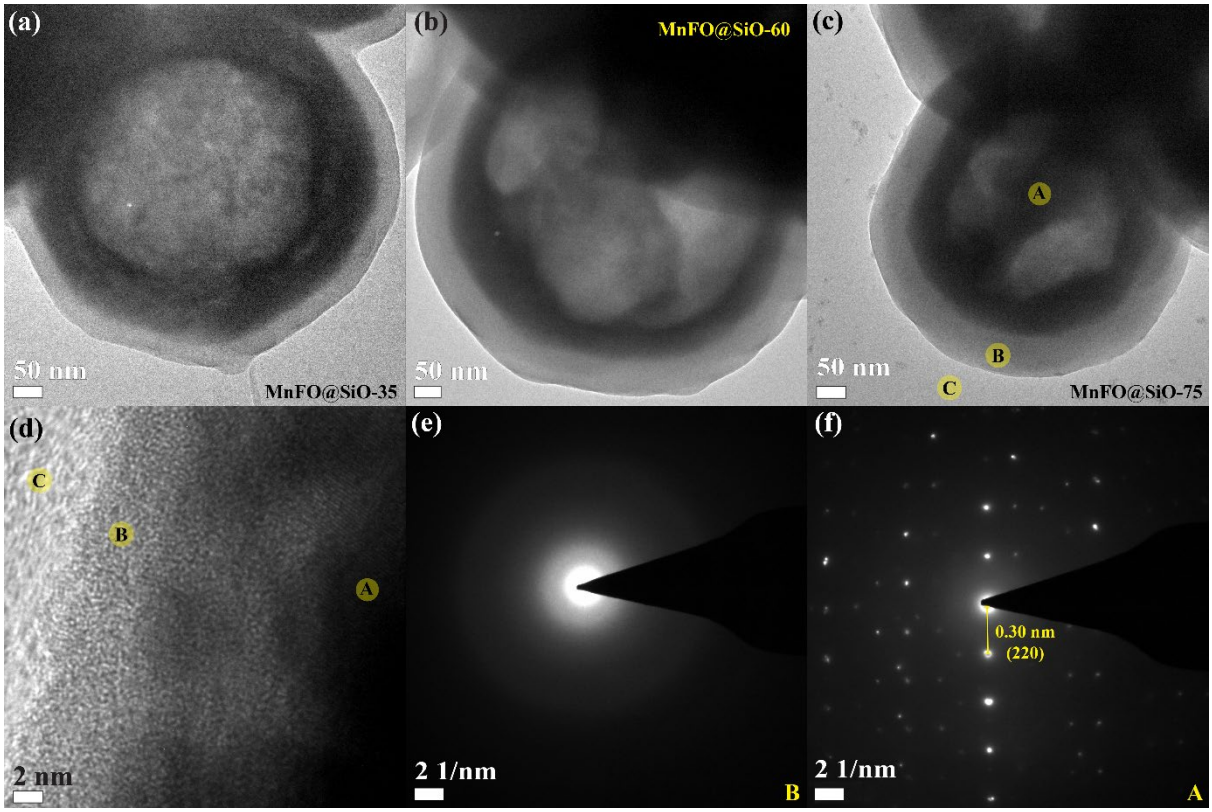

Figure 3.6. TEM micrographs for (a) MnFO/SiO-35, (b) MnFO/SiO-60, (c) MnFO/SiO-75, (d) HRTEM of MnFO@SiO-75, and SAED pattern for the same at (e) B site and (f) A site.

rather well with the values calculated from XRD data. These distances are 0.30 nm for (220), 0.25 nm for (311), and 0.23 nm for (222). In addition, HRTEM micrographs of MnFO@CFO-35 NHS exhibit cross-fringes, while no diffraction patterns are found at the boundary of NHS itself. The SAED pattern of MnFO@SiO is seen in Fig. 3.5(f). This pattern illustrates mainly the crystalline nature of NHS. In Fig. 3.6(d), at the HRTEM micrograph of MnFO/SiO-75, three locations, labeled A, B, and C sites, are selected and marked. A site is a point on the coated NHS, B site is the single SiO_2 coating section on the core-shell structure, and C site is the area of the TEM grid in the absence of any sample. Figs. 3.6(e) and (f) illustrate the SAED patterns for both locations B and A respectively. The SAED of site B reveals the amorphous character of SiO_2, while the SAED of site A reveals the crystalline nature of MnFO. The observed distance between the two bright spots of the SAED at site A is 0.30 nm, which corresponds to the [220] plane on MnFO. Again, three locations are selected and marked as A, B, and C sites for the MnFO@CFO-35 sample, depicted in Fig. 3.7(b). A site signifies the NHS shell as viewed through the CFO coating, B site denotes only CFO coating found outside the NHSs, and C site denotes the vacant space inside the TEM grid that does not include any samples. In the HRTEM micrograph of a MnFO@CFO-35 edge shown in Fig. 3.7(d), the contrast difference between the designated A, B, and C sites makes them stand out prominently.

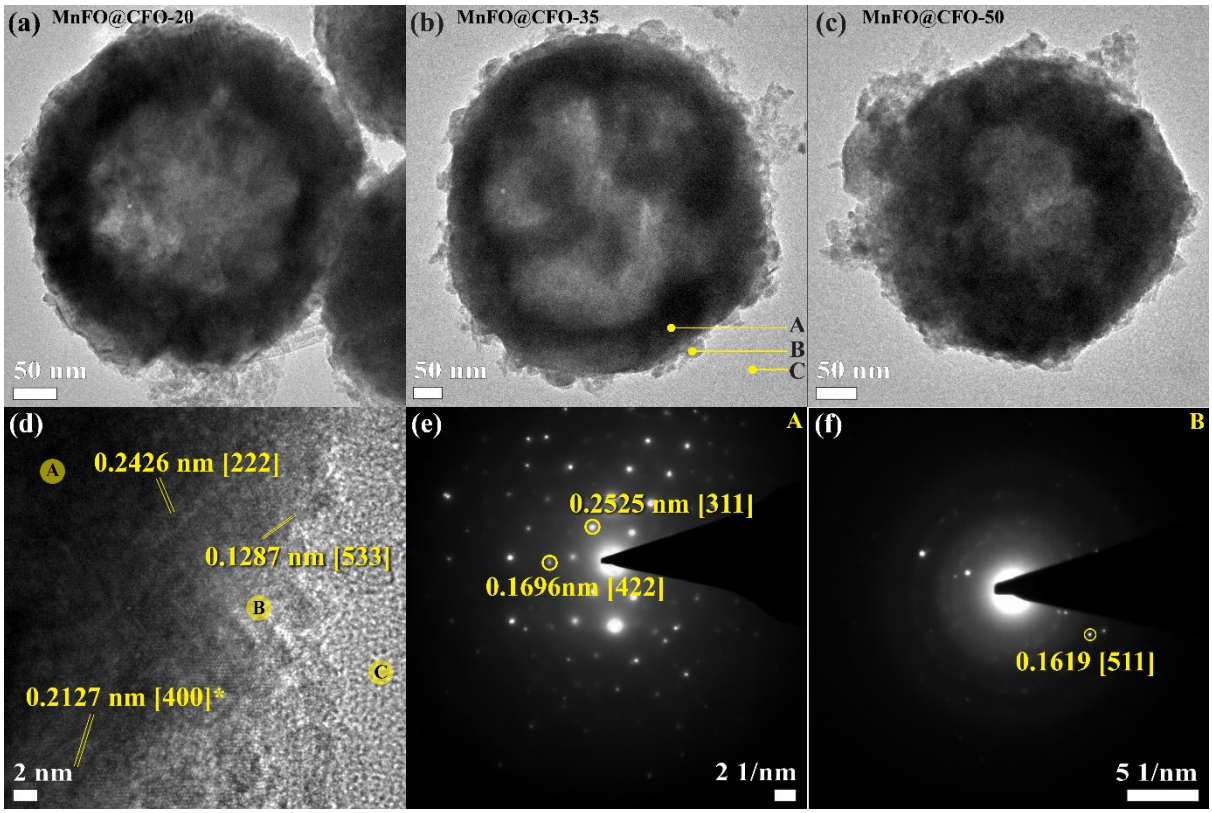

Figure 3.7. TEM micrographs for (a) MnFO@CFO-20, (b) MnFO@CFO-35, (c) MnFO@CFO-50, (d) HRTEM image of an edge of MnFO@CFO-35, SAED pattern for MnFO@CFO-35 at (e) A site; (f) B site

In addition, the diffraction fringes seen in this HRTEM image were measured based on the separation between parallel diffraction planes for a few sets at the A and B locations. Multiple cross fringes may be seen at site A. Here, the [222] and [400] planes of MnFO or CFO correspond to the 0.2426 nm and 0.2127 nm fringes, respectively. In contrast, the 0.1287 nm fringes at the B site correspond to the [533] plane of CFO. The SAED patterns for the A and B locations are shown in Figs. 3.7(e) and (f), respectively. The SAED at site A combines the crystalline characteristics of MnFO and CFO. The observed distances of 0.2525 nm and 0.1696 nm between the two brilliant spots of the SAED at the A site correspond to the [311] and [422] planes of MnFO or CFO. At the B site, the pattern becomes less dense with a spot of 0.1619 nm, and its parallel plane configurations correspond mostly to the [511] plane used by the CFO.

3.3.2 Electric and Magnetic Properties

Microwave absorption is highly connected to the complex permittivity and permeability, where the real portions ($\varepsilon'$and μ') represent the storage capacity and the imaginary parts (ε'' and μ'') reflect the loss capacity of electric and magnetic energy, respectively [22], [23]. Figs. 3.8(a) and (b) illustrate the frequency (f) dependence of the real (ε') and imaginary (ε'') components of the relative dielectric constants of the MnFO@SiO-75, MnFO@CFO-35, and bare MnFO NHS in the frequency range of 1–17 GHz. For MnFO and MnFO@SiO-75 NHS, ε' seems to decline with increasing frequency, whereas ε' for MnFO@CFO-35 maintains almost constant value over the whole region. Here, the dielectric constant derives mostly from interfacial and dipolar polarization contributions and follows Maxwell–Wagner grain–grain boundary models [24], [25] for ferrites. Fig. 3.9 depicts Cole-Cole plots for the sample composites MnFO NHS, MnFO@SiO-75, and MnFO@CFO-35. These data demonstrate the form of dielectric polarization described by Eq. 3.1 based on the Debye theory. The ε'' vs. ε' plots in the examined frequency domain for the samples consist of distorted asymmetric semicircular arcs, indicating modified Debye-type relaxation processes. These curves also indicate the existence of many types of dipolar relaxations in these heterogeneous systems and the charge carriers responsible for this.

$$(\varepsilon' - \frac{\epsilon_S + \epsilon_\infty}{2})^2 + \epsilon''^2 = (\frac{\epsilon_S + \epsilon_\infty}{2})^2 \quad (3.1)$$

Cole–Cole plots i.e., ε'' versus ε' curves for the samples, shown in Fig. 3.9, describe non-Debye type dielectric relaxation for the samples [26].

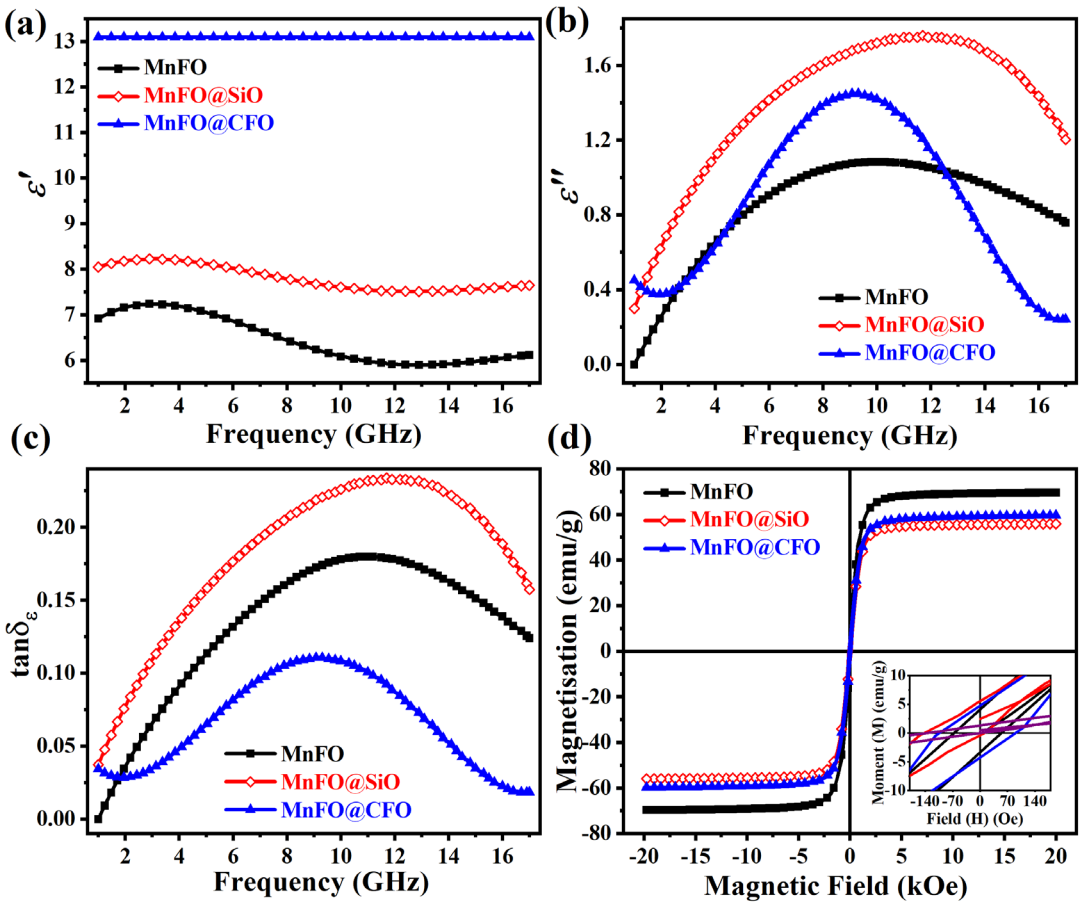

Figure 3.8. Frequency dependence (1–17 GHz) of (a) real (ε′), (b) imaginary (ε″) values of dielectric constant and (c) dielectric loss ($\tan\delta_\varepsilon$) (d)M–H plots at 300 K for all the samples.

As seen in Fig. 3.8, the rise in dielectric constants for the bi-layer morphologies is mostly attributable to the increasing quantity of charge carriers for surface polarization as the number of associated interfaces increases. Moreover, for MnFO@CFO-35, contribution in dipolar polarization from an additional dipole pair, Co^{2+}–Co^{3+} together with regular Fe^{2+}–Fe^{3+} and Mn^{2+}–Mn^{3+} in between tetrahedral (A) and octahedral (B) sites of MnFO, is responsible for the evident dramatic rise in ε'. As dielectric relaxation occurs with increasing frequency, ε' decays at high frequencies and these dipoles lag behind the field [17]. However, this dual contribution from MnFO and CFO also aids in maintaining the polarization of MnFO@CFO-35 over the frequency range. ε'' related to energy dissipation of accumulated charges, is found to grow for two-layered samples and to exhibit a broad hump at frequencies involving dielectric relaxation. Frequency dependence of dielectric loss, defined as $\tan\delta_\varepsilon = \varepsilon''/\varepsilon'$, is displayed in Fig. 3.8(c). Loss due to greater interfacial polarization in hybridized MnFO@SiO NHSs causes the $\tan\delta_\varepsilon$ to maximize, whereas less dielectric relaxation in MnFO@CFO-35 leads to a lower dielectric loss.

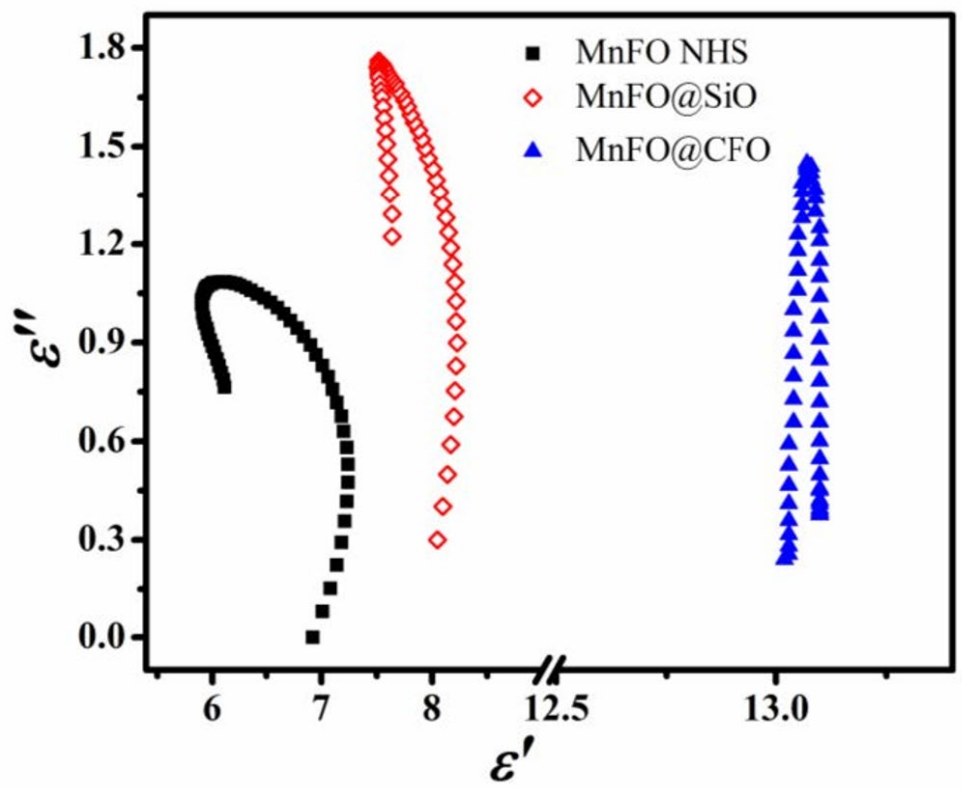

Figure 3.9. Cole-Cole plot for the studied samples

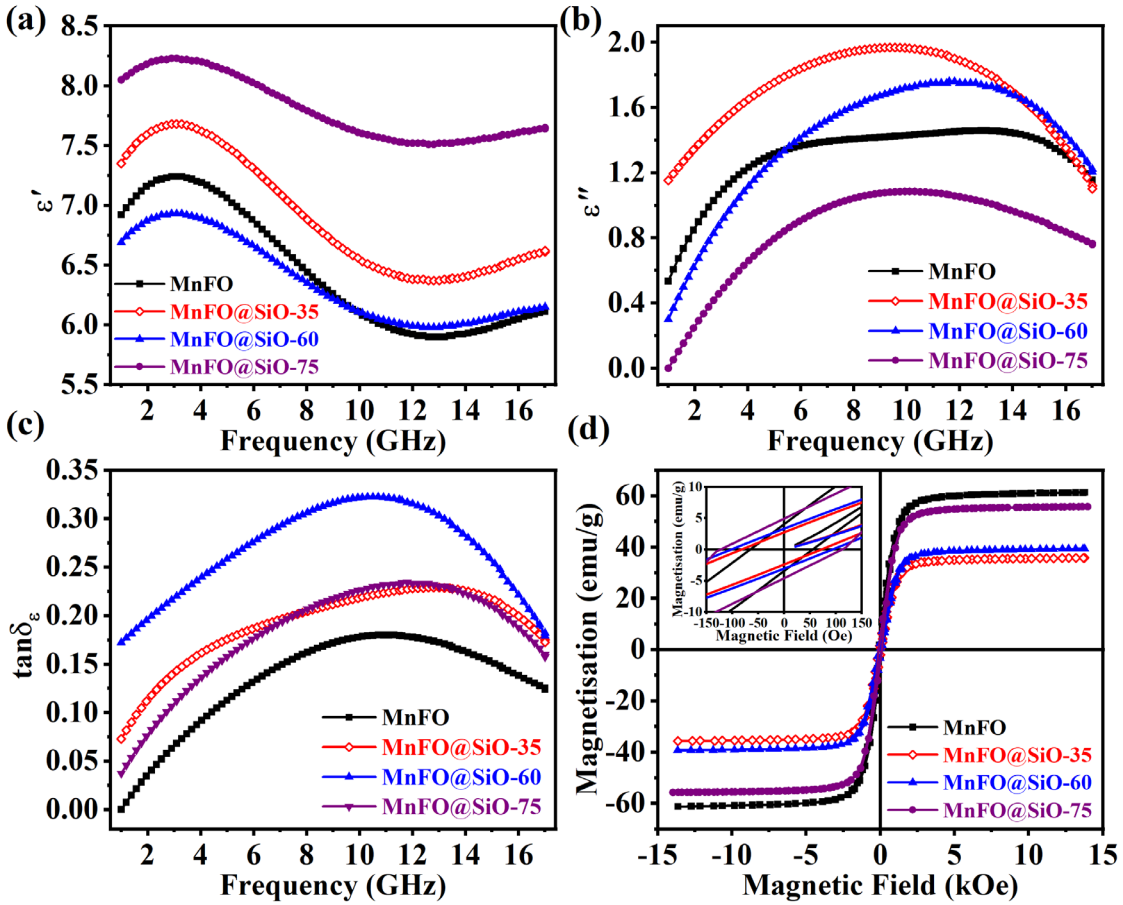

Figure 3.10. Frequency dependence (1–17 GHz) of (a) real (ε′), (b) imaginary (ε″) values of dielectric constant, (c) dielectric loss (tan δ_ε), and (d) M–H plots at 300 K for all the samples. Inset: the enlarged plot near the origin.

In Figs. 3.10(a) and (b), the frequency (1–17 GHz) dependence of ε' and ε'' for three SiO_2 coated samples of varying coating thicknesses and their bare counterpart are plotted. ε' decays with increasing frequency over all samples. Although ε' increases with the addition of a SiO_2 layer, the MnFO@SiO-60 sample exhibits an abnormal decrease that is close to that of the bare MnFO. The change in ε' observed in Fig. 3.10(a) can be attributed to the three most relevant factors according to our system. First, the higher number of associated interfaces in bi-layered morphologies as compared to bare MnFO induces an increased amount of charge carriers owing to surface polarization, hence enhancing ε' [19]. Second, for the bi-layered system, an increment in layer thickness decreases the STV ratio, which in turn decreases the bound charge per volume, hence lowering ε'. In contrast, a reduction in leakage current as layer thickness increases is the third factor influencing the change in ε' [27], [28]. The competing effect of the second and third factors determines the value of ε' at the bi-layered samples. The MnFO@SiO-35 and MnFO@SiO-75 show a gradual increase of ε' from the bare MnFO for the dominance of the first and third factors, respectively. However, for MnFO@SiO-60, the anomalous decrease in ε' is due to the dominance of the second factor. At high frequencies, ε' decays as dielectric relaxation occurs with increasing frequency, and dipoles lag behind the field [13]. The ε'' is related to energy dissipation of accumulated charges, which is directly proportional to the surface-to-volume (STV) ratio of the samples and is found to increase for the sample with the thinnest layer (MnFO@SiO-35) for having the highest STV ratio and decreases as the layer thickness increases. Also visible is a broad hump at frequencies containing dielectric relaxation. For MnFO@SiO-75, the thickness of the SiO_2 layer is sufficient to reduce the STV ratio, reducing ε'' even more than that of bare MnFO. The frequency dependence of dielectric loss, $\tan\delta_\varepsilon$, is displayed in Fig. 3.10(c). Loss from larger interfacial polarization in hybridized MnFO@SiO NHSs causes the $\tan\delta_\varepsilon$ maximum, but for MnFO@SiO-75, the lowered STV ratio comes into play, reducing it relative to other silica-coated core-shell NHSs.

The frequency dependency of ε' and ε'' of the three CFO-coated samples of varying coating thicknesses and their bare counterpart are plotted in Figs. 3.11(a) and (b). ε' of all the samples, except MnFO@CFO-35, grows steadily before declining with increasing frequency, whereas ε' of MnFO and MnFO@CFO-20 increases slightly above 12 GHz. Nonetheless, the ε' of MnFO@CFO-35 remains consistently high throughout the region. ε' increases as a result of the addition of the CFO layer, however, the MnFO@CFO-35 sample has some atypically high values. The four most important factors can be used to explain the change in ε' in our

system. Firstly, the existence of more associated interfaces in bi-layer morphologies than in bare MnFO results in an increase in charge carriers caused by surface polarization, which enhances ε' [29]. Second, the increase in ε' is caused by a contribution in dipolar polarisation from additional dipole pair Co^{2+}-Co^{3+} in addition to conventional Fe^{2+}-Fe^{3+} and Mn^{2+}-Mn^{3+} in the region between the tetrahedral and octahedral sites of MnFO. Thirdly, in a bi-layered system, an increase in layer thickness leads to a decrease in the STV ratio, which in turn reduces the bound charge per volume and ε'. Finally, the fourth element driving the change in ε' is a decrease in leakage current as the layer thickness increases [30]. The ε' of the bi-layered samples is determined by the competing effects of the third and fourth factors. For the dominance of the first, second, and third factors, the MnFO@CFO-20 exhibits a modest increase in ε' compared to the bare MnFO. The reason for the high ε' for MnFO@CFO-35 is the optimum synergistic effect of the first, second, and fourth factors in opposition to the third factor. However, with MnFO@CFO-50, the dominant third factor is responsible for the greater

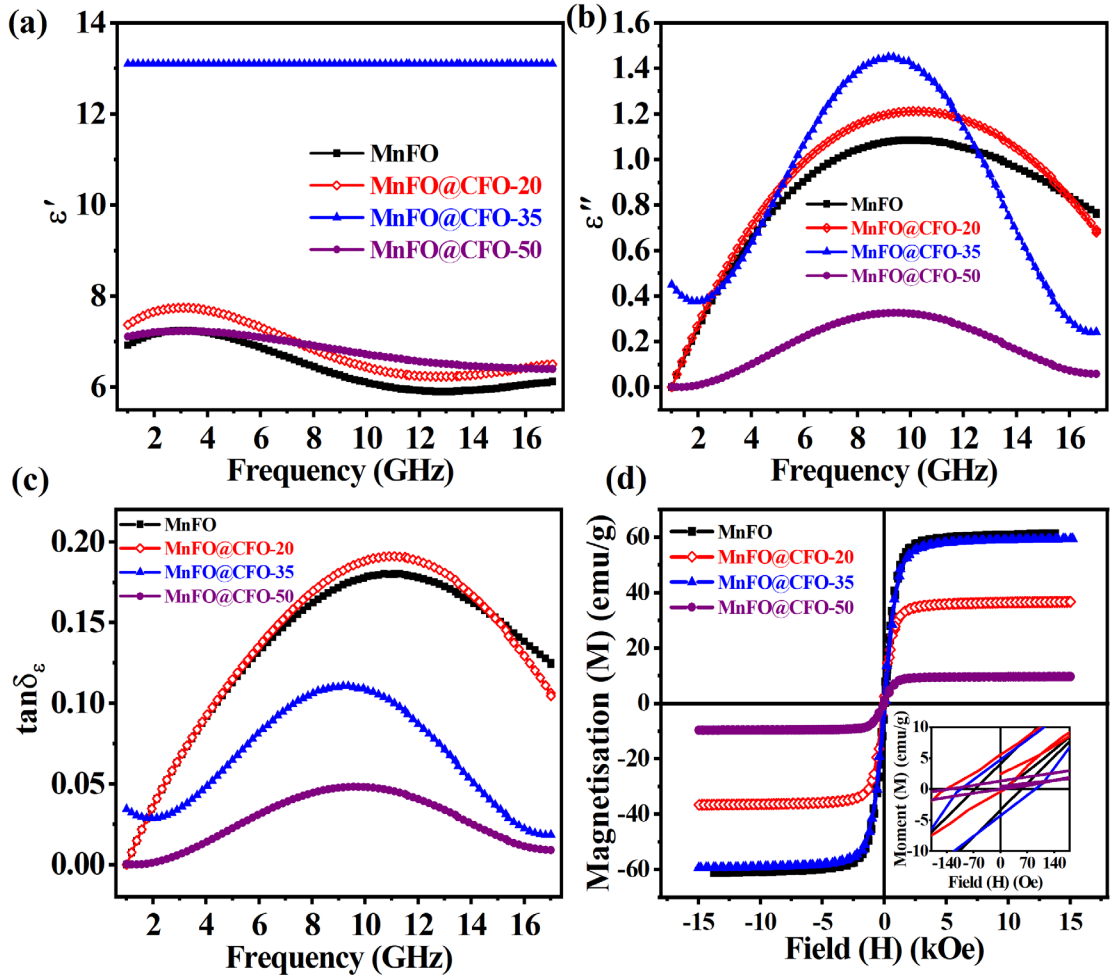

Figure 3.11. Frequency dependence (1 - 17 GHz) of (a) real (ε′), (b) imaginary (ε″) values of dielectric constant, (c) dielectric loss (tan δ_ε), (d) M-H plots at 300 K for all the samples; inset: the enlarged plot near the origin.

decrease in ε' compared to MnFO@CFO-35. At high frequencies, ε' decays as dielectric relaxation occurs with increasing frequency, and the dipoles lag behind the field.

The ε'' associated with the energy dissipation of accumulated charges is directly proportional to the STV ratio of the samples and drops for the sample with the thickest layer (MnFO@CFO-50) with the lowest STV ratio and increases with decreasing layer thickness. The dielectric relaxation frequencies exhibit a broad hump. NHSs with magnetic layers gather charges and subsequently release them, resulting in greater ε'' than bare ones. A large STV ratio of MnFO@CFO-50 reduces the accumulated charge per unit volume below that of bare MnFO. MnFO@CFO-20 has a lower ε'' than MnFO@CFO-35 because the CFO layer is too thin to gather charges for dissipation.

The frequency dependence of dielectric loss, $\tan\delta_\varepsilon$ is seen in Fig. 3.11(c). Due to the dielectric characteristics of the CFO, the inclusion of a CFO layer over the NHSs induces a modest increase in dielectric loss at the MnFO@CFO-20 compared to the bare MnFO. However, dielectric loss rapidly decreases with increasing layer thickness. The lower STV ratio in the samples with thicker layers reduces dielectric loss.

Fig. 3.8(d) depicts DC magnetic field-dependent magnetization curves at 300 K for MnFO nanohollowspheres and two bi-layered samples with silica and CFO. Likewise, Figs. 3.10(d) and 3.11(d) respectively show similar plots for the three different thicknesses of the SiO_2 and CFO layers individually over MnFO in addition to the bare MnFO. In the insets of each figure, the coercivities of the corresponding set are displayed on an enlarged scale close to the origin. Each curve exhibits a soft ferrimagnetic behavior. Table 3.1 displays the coercivity (H_C) and saturation magnetization (M_S) values determined from these plots. M_S decreases in the bi-layered composites compared to the bare MnFO NHS ($M_S \sim 69.69$ emu.g^{-1}) due to the pinning of spins on the surface, but H_C rises in the hybridized structures. Due to the existence of a non-magnetic layer of silica on the sample, the magnetic moment per gram of silica-coated NHSs is less than that of bare MnFO. The silica-coated core-shell NHSs with larger diameters possess larger D values which in turn enhances their M_S [14]. The increase in coercivity of silica-coated bi-layered samples originates from the increased magnetic anisotropy due to the presence of a non-magnetic second layer [5], [31]. Greater anisotropy increases magnetic loss which affects EM wave absorption and the conversion of EM wave energy into heat energy. In hybridized structures, the CFO layer generates pinning centers on the MnFO NHS surface. Consequently, H_C increases and M_S decreases again. The surface-

pinned spins at the outer surface of CFO expand as the CFO layer thickness increases from 20 nm to 35 nm, resulting in an increase in H_C and M_S as the D values of the system rise. In contrast, with the 50 nm CFO layer, the STV ratio rises substantially to lower H_C more than other CFO-coated hybridized structures, which is consistent with the decreased D value of the system. Here, the thickness of the CFO layer becomes similar to the thickness of the MnFO shell. Because the Mn-atom has more unpaired electrons than the Co atom, the M_S of MnFO@CFO-50 is much lower than that of bare MnFO.

In Fig. 3.12(a) and (b), the real (μ') and imaginary (μ'') components of relative permeability of MnFO nanohollowspheres and two bi-layered samples with silica and CFO are displayed as a function of frequency from 1 to 17 GHz. Figs. 3.13 and 3.14 show similar graphs for the three various thicknesses of the SiO_2 and CFO layers individually over MnFO as well as the bare MnFO. For both bare and bi-layered NHSs, μ' values are seen to decline up to a certain frequency for all samples, after which they remain almost constant. According to the Landau–Lifshitz–Gilbert equation [30], [32], [33], the dynamic magnetic characteristics of ferrimagnets are deeply associated with DC magnetic parameters such as magnetic anisotropy and magnetic susceptibility. Since silica is a non-magnetic substance, it contributes nothing to the total magnetic properties of a material that has been coated with it. As a consequence, no change is seen in the magnetic properties of samples coated with silica. μ'' displays characteristic resonance peaks of MnFO at 6 GHz for bare, all silica-coated, and 20 nm CFO-coated NHSs. For the 20 nm CFO-coated sample, the overall μ' decreases to a certain degree due to its lower Ms, while the overall μ'' increases due to the short-range exchange resonance between the MnFO and CFO spins at the interfaces. Throughout the measured frequency range, the overall plots have the same characteristics as bare MnFO. At MnFO@CFO-35, when a 35 nm CFO layer is present, the resonance peak of MnFO changes to a higher frequency of 3 GHz for μ', and the total values rise dramatically. Interfacial spin-spin interaction in CFO-coated samples may account for the large resonance peak seen in the μ'' plot. Due to the same thickness of the CFO layer and the MnFO shell in MnFO@CFO-50, a competitive effect is created within the material. Consequently, the μ' obtains a constant value between that of MnFO and MnFO@CFO-35 throughout the measured frequency range. Here, the μ'' follows a similar behavior to that of MnFO@CFO-35, but with a substantially decreased value because the magnetic loss contribution in MnFO NHS is dominated by the CFO, which inhibits resonance.

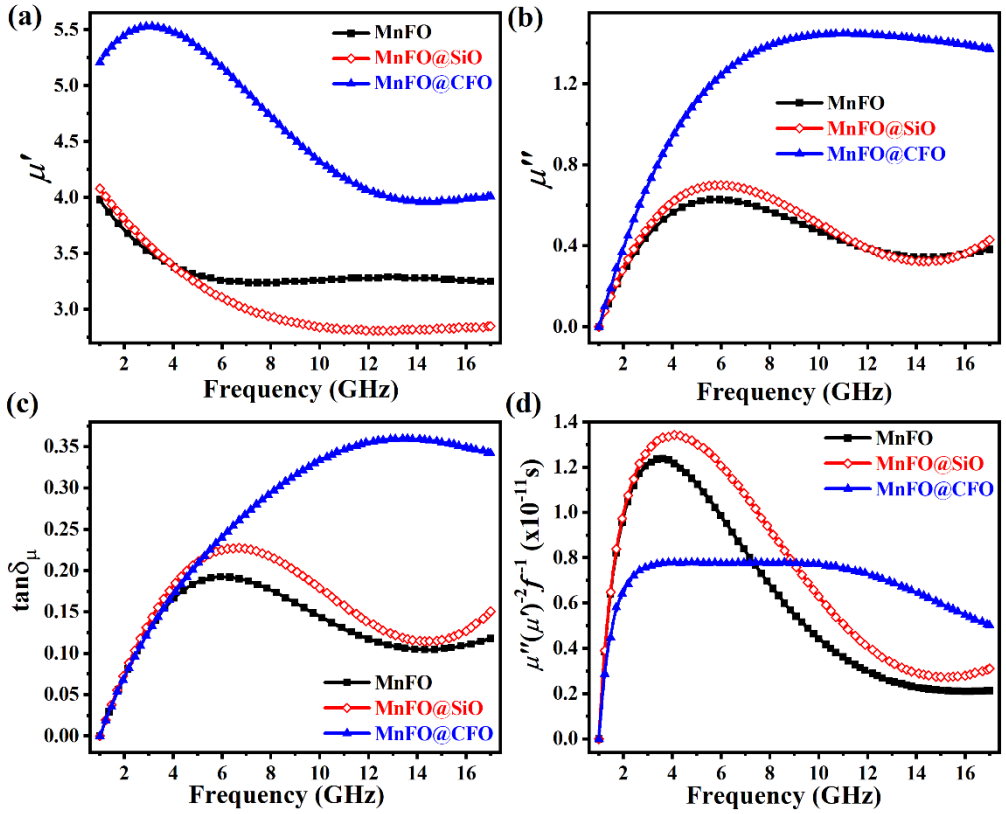

Figure 3.12. Frequency dependence (1–17 GHz) of (a) real (μ′), (b) imaginary (μ″) values of permeability, (c) magnetic loss (tan δ_μ) and(d) $\mu''(\mu')^{-2}f^{-1}$

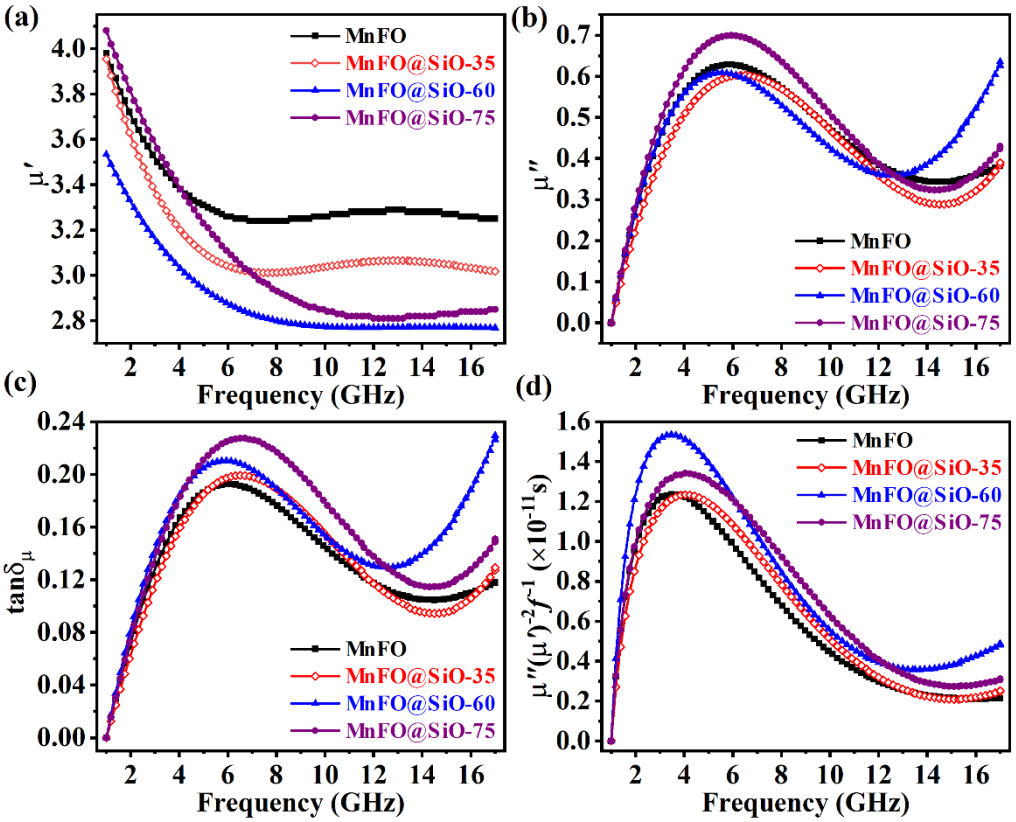

Figure 3.13. Frequency dependence (1–17 GHz) of (a) real (μ′), (b) imaginary (μ″) values of permeability, (c) magnetic loss (tan δ_μ) and(d) $\mu''(\mu')^{-2}f^{-1}$

Fig. 3.12(c) illustrates the variation of magnetic loss tangent with frequency for bare MnFO, 75 nm silica, and 35 nm CFO-coated NHSs. Fig. 3.13(c) and Fig. 3.14(c) show identical graphs for the three different thicknesses of silica and CFO-coated MnFO NHS. These curves are almost identical to the related μ'' versus f curves. Dynamic magnetic loss is well-known to originate primarily from magnetic hysteresis, domain wall resonance, eddy current effects, and natural and exchange resonance. Due to the reduced field intensity, the first two contributions are less effective for samples in the high-frequency range [34]. From the natural magnetic resonance equation [6], [35], $2\pi f_r = 4\gamma K/3\mu_0 M_S$, where γ is the gyromagnetic ratio (2.8 GHz/kOe for ferrites), resonance frequency (f_r) is determined to be approximately 4 GHz for $MnFe_2O_4$ NHSs, indicating substantial EM wave absorption through magnetic loss in this region.

Fig. 3.14(c) demonstrates that the interfacial spin-spin interaction in MnFO@CFO-35 may be accountable for a large resonance peak in the higher frequency range; thus, the magnetic loss of MnFO@CFO is greater than that of all other samples. Moreover, the eddy current loss contribution to μ'' may be written as $\mu''{\sim}2\pi\mu_0{\mu'}^2(d^2\sigma)f$ [30], [36], where d is the sample thickness, σ is the electrical conductivity, and μ_0 is the permeability of free space. If μ'' (or

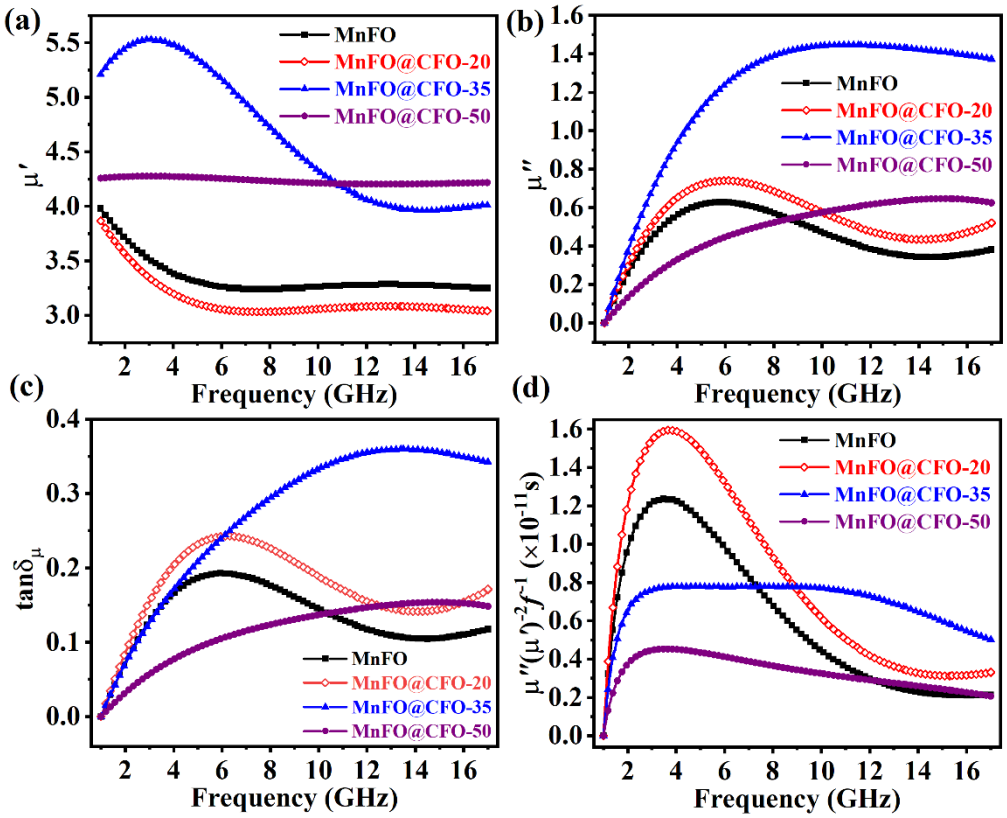

Figure 3.14. Frequency dependence (1–17 GHz) of (a) real (μ'), (b) imaginary (μ'') values of permeability, (c) magnetic loss ($\tan\delta_\mu$) and(d) $\mu''(\mu')^{-2}f^{-1}$

tan δ_μ) arises from eddy current loss, according to this equation the $\mu''(\mu')^{-2}f^{-1}$ curves will be constant with frequency [17].

To comprehend the likely causes of magnetic loss, the frequency dependence of $\mu''(\mu')^{-2}f^{-1}$ for MnFO, MnFO@SiO-75, and MnFO@CFO-35 is shown in Fig. 3.12(d). Fig. 3.13(d) and Fig. 3.14(d) show a similar plot for the three various thicknesses of the SiO_2 and CFO layers over MnFO, respectively. Around 4 GHz, a strong surge is seen for uncoated, all silica-coated, and 20 nm CFO-coated NHSs due to magnetic resonance in the system, and the value is almost constant afterward. The magnetic loss of these samples may be ascribed to resonance at low frequencies and eddy current loss at higher frequencies. For 35 nm and 50 nm CFO-coated samples, the curves are essentially consistent across the observed frequency range, indicating that eddy current loss predominates over magnetic loss over the entire frequency range under study.

3.3.3 Microwave Absorption Properties

The electromagnetic wave absorption qualities of a material are intimately connected with its magnetic and electric properties. Among these features, RL provides information about the material's ability to reduce reflected waves. This may occur through wave absorption, i.e., the transformation of EM waves into other energy, or the transmission of EM waves. Proper impedance matching is required for optimal EM wave propagation. Here, RL is computed using the following equations [37]:

$$Z_{in} = Z_0\sqrt{\frac{\mu_r}{\varepsilon_r}}\tanh\left[j\left(\frac{2\pi tf}{c}\right)(\mu_r\varepsilon_r)^{1/2}\right] \tag{3.2}$$

$$RL = 20\log\left|\frac{(Z_{in}-Z_0)}{(Z_{in}+Z_0)}\right| \tag{3.3}$$

where $\mu_r = \mu' - i\mu''$ and $\varepsilon_r = \varepsilon' - i\varepsilon''$ are relative permeability and permittivity of the material, c, the velocity of light in vacuum, t, the thickness of the composite absorber, Z_0 and Z_{in} are the impedance of free space and input impedance of absorber respectively.

For the optimum thickness design of ferrite-filled epoxy composites needed for practical applications, thickness-dependent research on EM wave absorption is conducted for NHSs. In Figs. 3.15(a)–(c), frequency-dependent RL is displayed for various thicknesses of 20 wt.% powder sample loaded epoxy resin composites for uncoated, 75 nm silica, and 35 nm

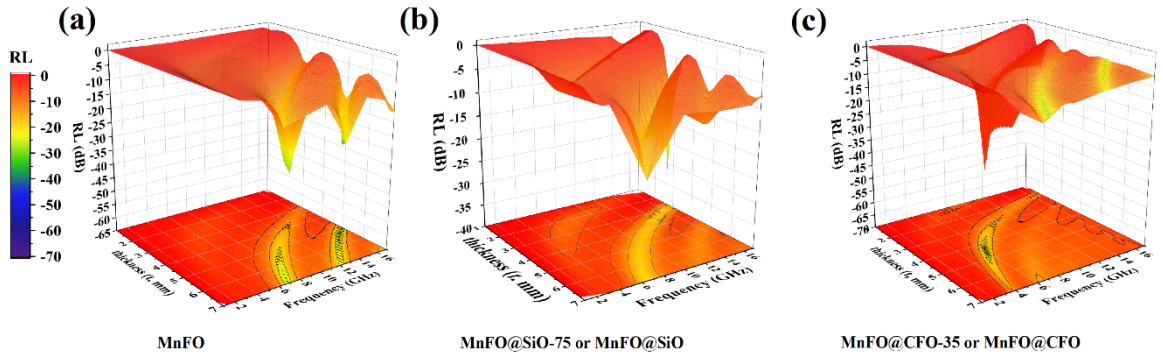

Figure 3.15. 3D plots of reflection loss (RL) of (a) MnFO NHS, (b) MnFO@SiO, (c) MnFO@CFO versus frequency and thickness

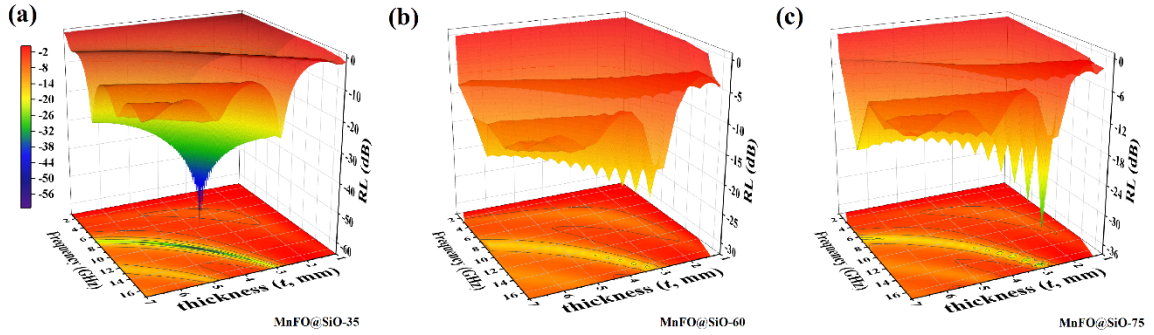

Figure 3.16. 3D plots of reflection loss (RL) of (a) MnFO@SiO-35, (b) MnFO@SiO-60, (c) MnFO@SiO-75 versus frequency and thickness,

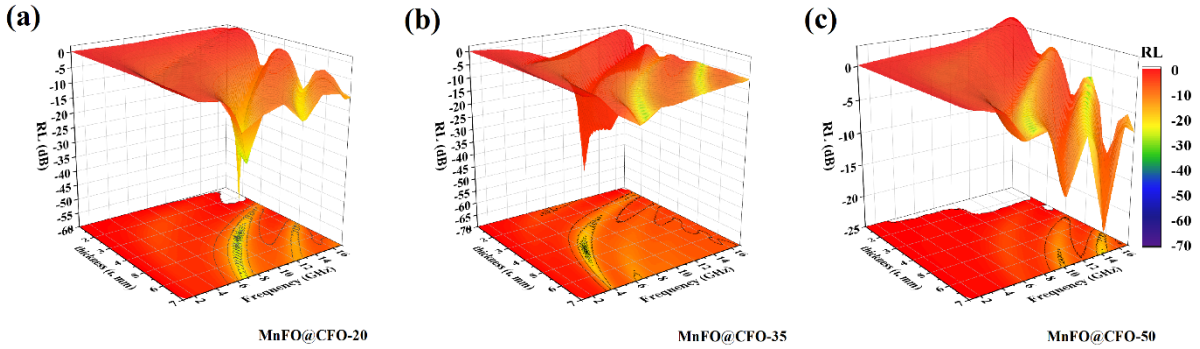

Figure 3.17. 3D plots of reflection loss (RL) of (a) MnFO@CFO-20, (b) MnFO@CFO-35, (c) MnFO@CFO-50 versus frequency and thickness

CFO-coated MnFO. Figs. 3.16(a)-(c) and 3.17(a)-(c) show identical 3D graphs for the three varied thicknesses of the SiO_2 and CFO layers over MnFO, respectively. In Table 3.2, the minimum reflection loss (RL_{min}) determined for all samples for each composite absorber composite absorber thickness (t_m) and frequency (f_m) as well as the total effective bandwidth (BW_{eff}) with RL < -10 dB for that t_m in the observed frequency range of 1-17 GHz are listed.

Fig. 3.18(a) compares the bare MnFO NHS with 75 nm silica-coated and 35 nm CFO-coated bi-layered samples at t_m = 4.46 mm. The MnFO@CFO-35 NHS exhibits an ideal RL of -66.48 dB at 6.01 GHz. $|Z_{in}/Z_0|$ vs. frequency plot in Fig. 3.18(c) indicates that the optimal impedance matching is reached, i.e., $|Z_{in}/Z_0|$ = 1.00, for the MnFO@CFO-35 sample at an

appropriate f_m. This result demonstrates that, in addition to adequate dielectric and magnetic losses, the optimal impedance matching in CFO-coated MnFO NHS is responsible for its superior EM wave absorption. In addition, silica-coated MnFO achieves a sufficiently high RL (-30 dB) at a thickness of just 3 mm, which is much smaller than MnFO NHS (t_m = 5.3 mm).

Fig. 3.19(a) compares the three various thicknesses of silica layer over MnFO as well as bare MnFO NHS at t_m = 4.40 mm, and an RL of -61.02 dB is obtained for MnFO/SiO-35 NHS at about 11.7 GHz. This measured BW for RL < -10 dB is 3.10 GHz. In Fig. 3.19(c), graphs of $|Z_{in}/Z_0|$ versus frequency reveal that the best impedance matching is attained, i.e., $|Z_{in}/Z_0|$ = 1.00 for the MnFO@SiO-35 sample at f_m = 11.7 GHz. This result demonstrates that, in addition to adequate dielectric and magnetic losses, the best impedance matching in MnFO NHS with the thinnest SiO_2 layer is responsible for its exceptional EM wave absorption.

Fig. 3.20(a) compares the three different thicknesses of the CFO layer over MnFO along with bare MnFO NHS at their respective t_m and an RL_{min} of -66.48 dB is found at around 6.01 GHz for MnFO@CFO-35 NHS. The BW_{eff} for RL < -10 dB observed for this sample, is 1.88 GHz. In Fig. 3.20(c), the $|Z_{in}/Z_0|$ vs. f plots show the best impedance matching is achieved i.e., $|Z_{in}/Z_0| \cong 1.00$ for MnFO@CFO-35 at corresponding f_m = 6.01 GHz. This finding demonstrates that the best impedance matching in MnFO NHS with a 35 nm CFO layer,

Table 3.2 Minimum reflection loss (RL_{min}), absorber thickness (t_m), frequency (f_m), and effective bandwidth (BW_{eff})

Sample Name	RL_{min}(dB)	t_m(mm)	f_m(GHz)	BW_{eff}(GHz)
MnFO	-36.13	4.95	17.0	4.43
MnFO@SiO or MnFO@SiO-75	-35.75	2.84	17.0	1.10
MnFO@CFO or MnFO@CFO-35	-66.48	4.46	6.01	1.88
MnFO@SiO-35	-61.02	4.40	11.7	3.10
MnFO@SiO-60	-21.39	3.17	17.0	2.32
MnFO@CFO-20	-58.99	4.70	10.9	2.89
MnFO@CFO-50	-22.98	7.00	14.2	3.90

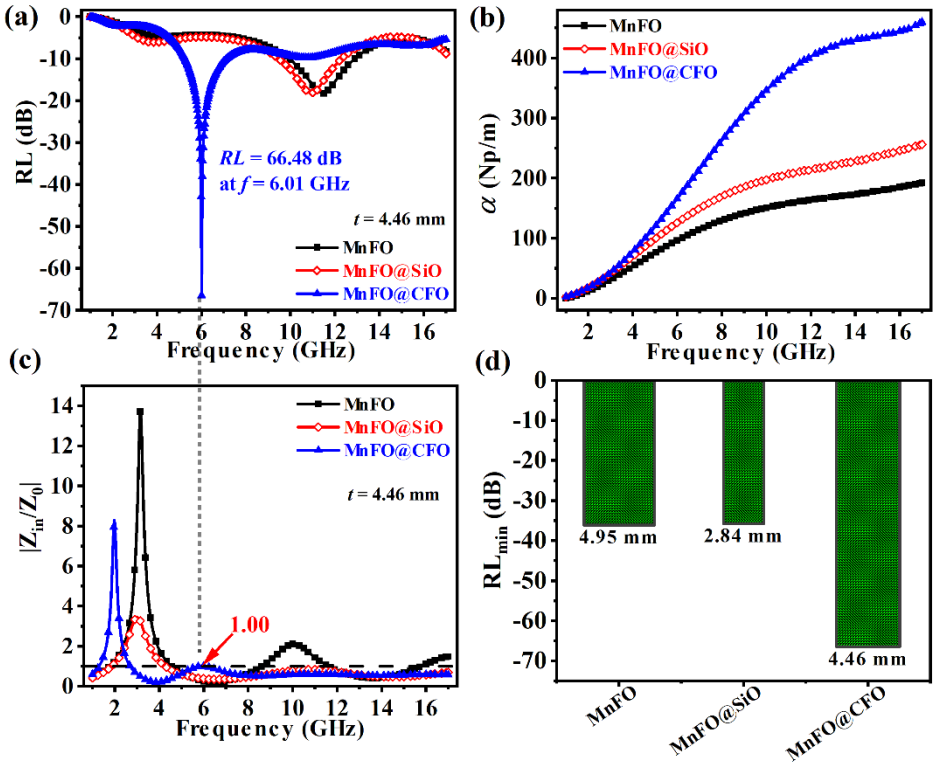

Figure 3.18. (a) Comparative RL versus f plot for the three samples; (b) Frequency dependent attenuation constant (∝), (c) $|Z_{in}/Z_0|$ ratio versus frequency,(d) RL_{min} values at t_m for all samples

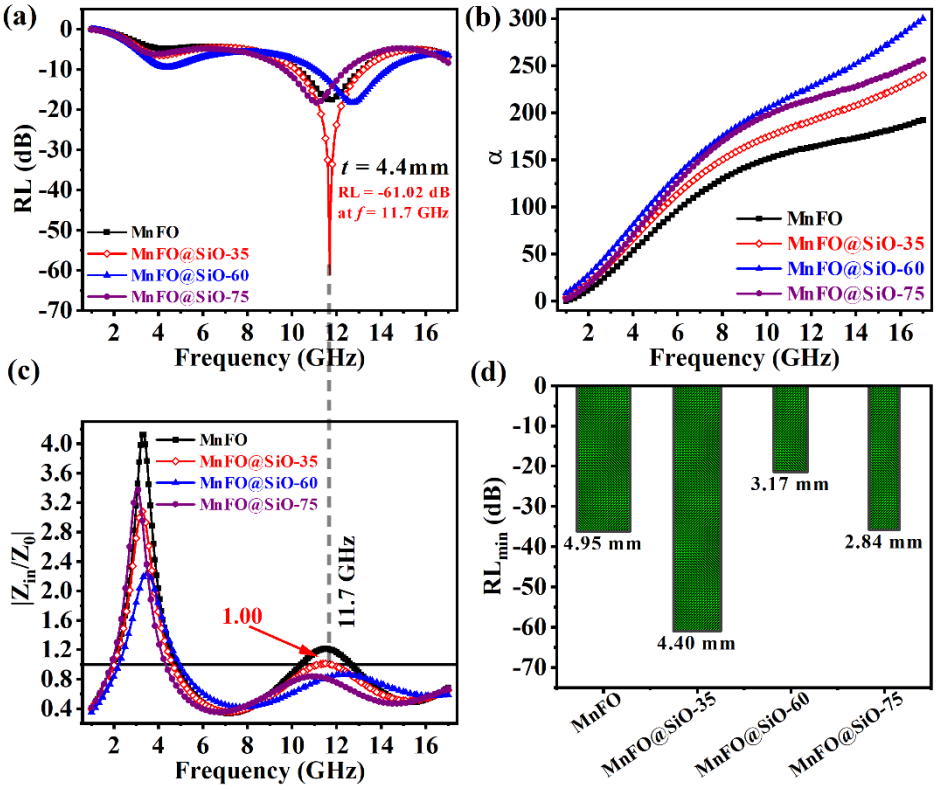

Figure 3.19. (a) Comparative RL versus f plot for the three samples; (b) Frequency dependent attenuation constant (∝), (c) $|Z_{in}/Z_0|$ ratio versus frequency,(d) RL_{min} values at t_m for all samples

together with adequate dielectric and magnetic losses, account for its superior EM wave absorption.

The attenuation constant (α) indicates the ability of the material to attenuate EM waves internally and can be calculated by the following equation:

$$\alpha = \frac{\sqrt{2}\pi f}{c}\sqrt{(\mu''\varepsilon'' - \mu'\varepsilon') + \sqrt{(\mu''\varepsilon'' - \mu'\varepsilon')^2 + (\mu''\varepsilon' + \mu'\varepsilon'')^2}} \qquad (3.4)$$

The values for MnFO NHS, 75 nm silica, and 20 nm CFO-coated samples are calculated and shown in Fig. 3.18(b). The same three various thicknesses of silica and CFO layer independently coated on MnFO NHS are shown in Fig. 3.19(b) and Fig. 3.20(b), respectively. α increases with frequency for all samples, and with higher values of ε_r and μ_r, rises for bi-layered NHSs. Due to the large STV ratio, the slope of α in Fig. 3.20(b) for MnFO@CFO-50 is even smaller than that of MnFO alone. MnFO@CFO-35 has the greatest growth.

A schematic approach, shown in Fig. 3.21, highlights the potential causes for the efficacy of bi-layered NHSs, which renders them highly suited and effective as a microwave absorber.

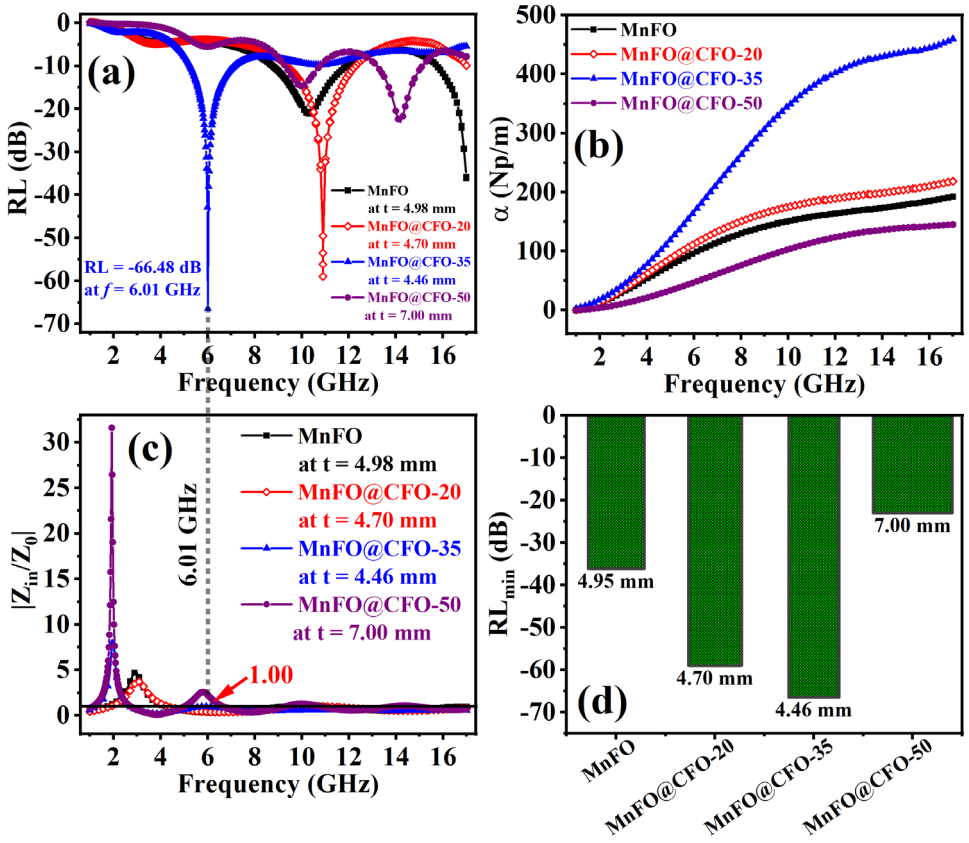

Figure 3.20. (a) Comparative RL versus f plot for the three samples; (b) Frequency dependent attenuation constant (α), (c) $|Z_{in}/Z_0|$ ratio versus frequency,(d) RL_{min} values at t_m for all samples

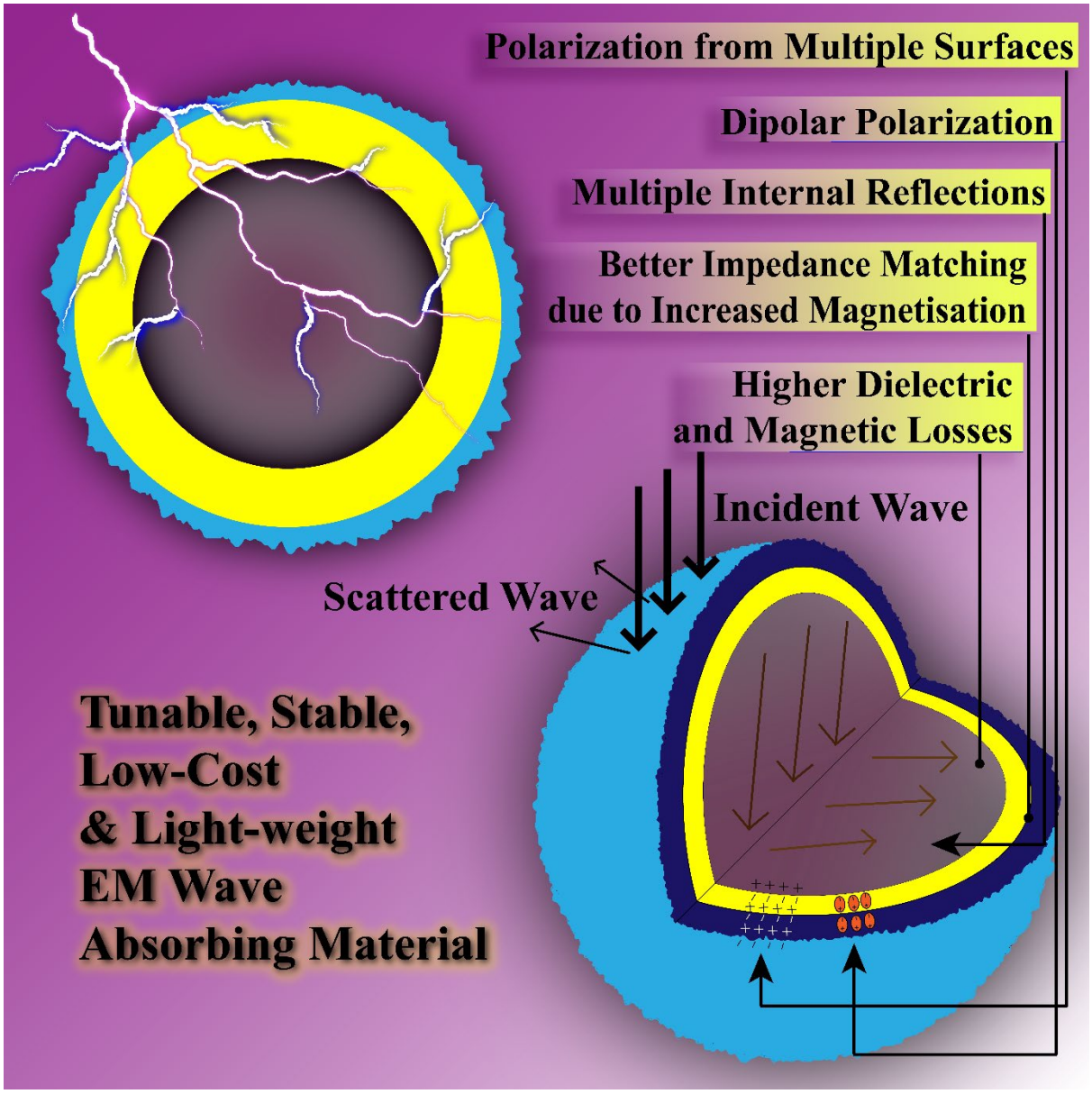

Figure 3.21. A schematic approach to highlight the potential causes for the efficacy of bi-layered NHSs, which renders them highly suited and effective as a microwave absorber.

Fig. 3.22(a) describes RL as a function of frequency for different thicknesses from 1 to 6 mm and Fig. 3.22(b) illustrates a comparison between simulated and experimental results for 35 nm CFO-coated MnFO NHS. With increasing t, RL rises till composite absorber thickness of t_m with a minimum reflection loss RL_{min}, then decreases again. RL peak frequency (f_m) and matching thickness (t_m) are related as [24], [34]:

$$t_m = \frac{nc}{4f_m\sqrt{|\mu_r\varepsilon_r|}} \ (n = 1, 3, 5, \ldots.) \tag{3.5}$$

where from the quarter-wavelength ($\lambda/4$) model, for odd values of n, reflected waves from two interfaces of the absorber become out of phase. A good agreement between experimental and simulated t_m can be noticed in Fig. 3.22(b). Higher matching modes and hence more peaks are

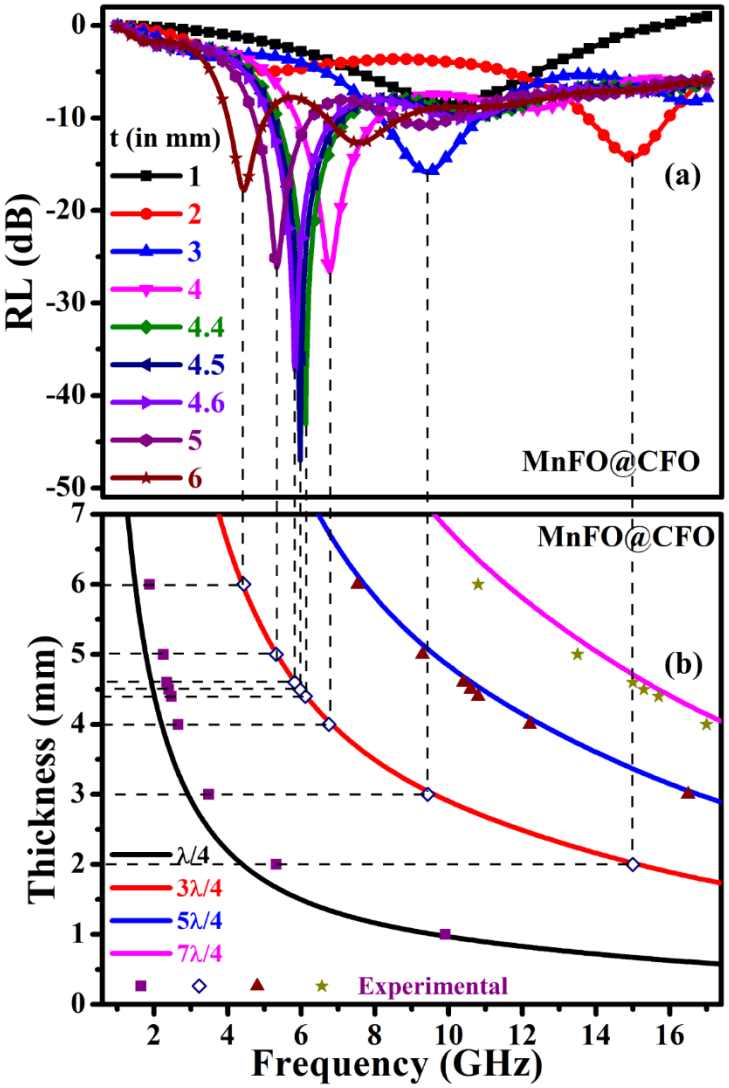

Figure 3.22. Comparison between simulated and experimental results

visible for thicker samples and the peak frequencies shift towards lower frequencies with increasing t of the samples [17], [34].

3.4 Conclusion

In conclusion, three different thicknesses of dielectric SiO_2 and magnetic $CoFe_2O_4$ have been successfully coated over MnFO NHSs, and the electromagnetic wave absorption properties within the widely used frequency range of 1–17 GHz have been thoroughly examined for both the uncoated and hybridized samples. Bi-layered morphologies with an increased number of related surfaces and dipoles for electric polarization and an increase in magnetic anisotropy boost dielectric and magnetic loss, which in turn enhances EM wave attenuation qualities. This typical shape is preferred as practical EMA materials because of scattering and internal reflections from NHSs and its lower density. The CFO-coated MnFO NHSs have increased numbers of linked interfaces and, consequently, spins owing to magnetic polarisation, exchange contacts between them, and a synergistic effect generated by many resonance centers. These characteristics enhance dielectric and magnetic loss, which increases the absorption of electromagnetic waves. The sample MnFO@CFO-35 exhibits RL as high as -66.48 dB (shielding > 99.99%) at 6.01 GHz with just 20 wt.% filler concentration in an epoxy matrix and a composite length of 4.46 mm for a 35 nm (out of 15 nm, 35 nm, and 50 nm) layer of CFO over MnFO NHS. The MnFO@CFO-35 NHS has a total effective bandwidth of about 1.88 GHz (RL -10 dB). Sample MnFO/SiO-35 demonstrates RL as high as -61.02 dB (shielding > 99.999%) at 11.7 GHz with just 20 wt.% filler concentration in an epoxy matrix and a

composite length of 4.40 mm. MnFO/SiO-35 NHS has a total effective BW (RL < -10 dB) of about 3.10 GHz. Consequently, an optimized layer of CFO on MnFO NHS displays improved EM wave absorption properties, making it a mass-efficient and economically advantageous EMA material for several high-frequency applications.

The minimum RL obtained here is comparable to other promising ferrite-based microwave absorbers as presented in Table 3.3.

Table 3.3 Optimal reflection loss (RL) and bandwidth (BW) of ferrite based promising microwave absorbers

Material	**Matrix**	**Filler Content (wt.%)**	$d_{out}: d_{in}: t$ **(mm)**	RL_{min}**(dB)**	BW_{eff}**(GHz)**
$CoFe_2O_4$@rGO nano-composites [1]	Paraffin	5	7.0:3.04:2.3	-25.7	4.67
ZnO/Fe_3O_4 nanoflowers [38]	Wax	60	7.0:3.04:2.7	-36.2	4.02
$MnFe_2O_4$@rGO nano-composites [10]	PVDF	5	7.0:3.04:3.0	-29.0	4.88
Fe_3O_4/SiO_2 nanorods [39]	PVDF	40	7.0:3.04:2.5	-28.6	2
$NiFe_2O_4$ nanoparticles [33]	Epoxy	70	21.7:10:2.5	-35.0	0.4
MnFO@CFO NHS	Epoxy	20	3.5:1.5:4.5	-47.0	2.2

References

[1] Y. Ding *et al.*, "Reduced Graphene Oxide Functionalized with Cobalt Ferrite Nanocomposites for Enhanced Efficient and Lightweight Electromagnetic Wave Absorption," *Sci Rep*, vol. 6, no. 1, p. 32381, 2016, doi: 10.1038/srep32381.

[2] Z. Yang, Z. Li, Y. Yang, and Z. J. Xu, "Optimization of ZnxFe3–xO4 Hollow Spheres for Enhanced Microwave Attenuation," *ACS Appl Mater Interfaces*, vol. 6, no. 24, pp. 21911–21915, Dec. 2014, doi: 10.1021/am5075612.

[3] M. Zhang *et al.*, "Cobalt doping of bismuth ferrite for matched dielectric and magnetic loss," *Appl Phys Lett*, vol. 115, no. 21, Nov. 2019, doi: 10.1063/1.5134741.

[4] Z. Yang, Z. Li, Y. Yang, and Z. J. Xu, "Optimization of ZnxFe3–xO4 Hollow Spheres for Enhanced Microwave Attenuation," *ACS Appl Mater Interfaces*, vol. 6, no. 24, pp. 21911–21915, Dec. 2014, doi: 10.1021/am5075612.

[5] F. Wang *et al.*, "Template free synthesis and electromagnetic wave absorption properties of monodispersed hollow magnetite nano-spheres," *J Mater Chem*, vol. 21, no. 12, pp. 4314–4320, 2011, doi: 10.1039/C0JM02894K.

[6] X. G. Liu, D. Y. Geng, H. Meng, P. J. Shang, and Z. D. Zhang, "Microwave-absorption properties of ZnO-coated iron nanocapsules," *Appl Phys Lett*, vol. 92, no. 17, p. 173117, Apr. 2008, doi: 10.1063/1.2919098.

[7] M. Han *et al.*, "Graphene-wrapped ZnO hollow spheres with enhanced electromagnetic wave absorption properties," *J Mater Chem A Mater*, vol. 2, no. 39, pp. 16403–16409, Oct. 2014, doi: 10.1039/c4ta03033h.

[8] R. Panigrahi and S. K. Srivastava, "Trapping of microwave radiation in hollow polypyrrole microsphere through enhanced internal reflection: A novel approach," *Sci Rep*, vol. 5, no. 1, p. 7638, 2015, doi: 10.1038/srep07638.

[9] D. Mandal, A. Gorai, and K. Mandal, "Electromagnetic wave trapping in NiFe 2 O 4 nano-hollow spheres: An efficient microwave absorber."

[10] X. J. Zhang *et al.*, "Enhanced microwave absorption property of reduced graphene oxide (RGO)-MnFe2O4 nanocomposites and polyvinylidene fluoride," *ACS Appl Mater Interfaces*, vol. 6, no. 10, pp. 7471–7478, May 2014, doi: 10.1021/am500862g.

[11] "citations-20231013T075754".

[12] K. Vamvakidis, M. Katsikini, D. Sakellari, E. C. Paloura, O. Kalogirou, and C. Dendrinou-Samara, "Reducing the inversion degree of MnFe2O4 nanoparticles through synthesis to enhance magnetization: evaluation of their 1H NMR relaxation and heating efficiency," *Dalton Transactions*, vol. 43, no. 33, pp. 12754–12765, 2014, doi: 10.1039/C4DT00162A.

[13] X. Zhou *et al.*, "Synthesis of porous carbon embedded with NiCo/CoNiO2 hybrids composites for excellent electromagnetic wave absorption performance," *J Colloid Interface Sci*, vol. 575, pp. 130–139, 2020, doi: https://doi.org/10.1016/j.jcis.2020.04.099.

[14] D. Mandal and K. Mandal, "Enhancement of electromagnetic wave absorption in MnFe2O4 nano-hollow spheres," *J Appl Phys*, vol. 129, no. 7, p. 074902, Feb. 2021, doi: 10.1063/5.0039560.

[15] J. Liu, Z. Yang, M. Li, L. Yang, T. Xue, and G. Xu, "Controllable synthesis of Fe3O4-based magneto-dielectric ternary nanocomposites and their enhanced microwave absorption properties," *Nanotechnology*, vol. 32, no. 1, p. 015707, 2021, doi: 10.1088/1361-6528/abb7b3.

[16] N. Wu *et al.*, "Enhanced Electromagnetic Wave Absorption of Three-Dimensional Porous Fe3O4/C Composite Flowers," *ACS Sustain Chem Eng*, vol. 6, no. 9, pp. 12471–12480, Sep. 2018, doi: 10.1021/ACSSUSCHEMENG.8B03097/ASSET/IMAGES/ACSSUSCHEMENG.8B03097.SOCIAL.JPEG_V03.

[17] Y. Zhang, H. Bin Zhang, X. Wu, Z. Deng, E. Zhou, and Z. Z. Yu, "Nanolayered Cobalt@Carbon Hybrids Derived from Metal-Organic Frameworks for Microwave Absorption," *ACS Appl Nano Mater*, vol. 2, no. 4, pp. 2325–2335, Apr. 2019, doi: 10.1021/acsanm.9b00226.

[18] W. Ruan *et al.*, "Metal–organic framework derived cobalt phosphosulfide with ultrahigh microwave absorption properties," *Nanotechnology*, vol. 29, no. 40, p. 405703, 2018, doi: 10.1088/1361-6528/aad39b.

[19] M. Qin, L. Zhang, X. Zhao, and H. Wu, "Defect Induced Polarization Loss in Multi-Shelled Spinel Hollow Spheres for Electromagnetic Wave Absorption Application," *Advanced Science*, vol. 8, no. 8, p. 2004640, Apr. 2021, doi: https://doi.org/10.1002/advs.202004640.

[20] M. Mandal Goswami, "Synthesis of Micelles Guided Magnetite (Fe3O4) Hollow Spheres and their application for AC Magnetic Field Responsive Drug Release," *Sci Rep*, vol. 6, no. 1, p. 35721, 2016, doi: 10.1038/srep35721.

[21] R. Rakshit, M. Pal, A. Chaudhuri, M. Mandal, and K. Mandal, "Research Update: Facile synthesis of CoFe2O4 nano-hollow spheres for efficient bilirubin adsorption," *APL Mater*, vol. 3, no. 11, p. 110701, Nov. 2015, doi: 10.1063/1.4935311.

[22] S. F. Soares, T. Fernandes, A. L. Daniel-da-Silva, and T. Trindade, "The controlled synthesis of complex hollow nanostructures and prospective applications†," *Proceedings of the Royal Society A: Mathematical, Physical and Engineering Sciences*, vol. 475, no. 2224, p. 20180677, Apr. 2019, doi: 10.1098/rspa.2018.0677.

[23] M. Alam, S. Talukdar, and K. Mandal, "Multiferroic properties of bilayered BiFeO3/CoFe2O4 nano-hollowspheres," *Mater Lett*, vol. 210, pp. 80–83, 2018, doi: https://doi.org/10.1016/j.matlet.2017.08.097.

[24] J.-Z. He, X.-X. Wang, Y.-L. Zhang, and M.-S. Cao, "Small magnetic nanoparticles decorating reduced graphene oxides to tune the electromagnetic attenuation capacity," *J Mater Chem C Mater*, vol. 4, no. 29, pp. 7130–7140, 2016, doi: 10.1039/C6TC02020H.

[25] D. Mandal and K. Mandal, "Tuning of structural, magnetic and dielectric properties of TFe2O4 (T = Mn, Fe, Co, Ni, Cu, and Zn) Nano-Hollow Spheres: Effect of cation substitution," *J Alloys Compd*, vol. 851, p. 156898, 2021, doi: https://doi.org/10.1016/j.jallcom.2020.156898.

[26] Y. Cheng *et al.*, "Engineering morphology configurations of hierarchical flower-like MoSe2 spheres enable excellent low-frequency and selective microwave response properties," *Chemical Engineering Journal*, vol. 372, pp. 390–398, Sep. 2019, doi: 10.1016/J.CEJ.2019.04.174.

[27] A. N. Vicente, G. M. Dip, and C. Junqueira, "The step by step development of NRW method," in *2011 SBMO/IEEE MTT-S International Microwave and Optoelectronics Conference (IMOC 2011)*, 2011, pp. 738–742. doi: 10.1109/IMOC.2011.6169318.

[28] X. Liu, H. Guo, Q. Xie, Q. Luo, L.-S. Wang, and D.-L. Peng, "Enhanced microwave absorption properties in GHz range of Fe3O4/C composite materials," *J Alloys Compd*, vol. 649, pp. 537–543, 2015, doi: https://doi.org/10.1016/j.jallcom.2015.07.084.

[29] Z. W. Li and Z. H. Yang, "Microwave absorption properties and mechanism for hollow Fe3O4 nanosphere composites," *J Magn Magn Mater*, vol. 387, pp. 131–138, 2015, doi: https://doi.org/10.1016/j.jmmm.2015.03.087.

[30] D. Mandal, A. Gorai, and K. Mandal, "Electromagnetic wave trapping in NiFe2O4 nano-hollow spheres: An efficient microwave absorber," *J Magn Magn Mater*, vol. 485, pp. 43–48, Sep. 2019, doi: 10.1016/j.jmmm.2019.04.033.

[31] Y. Huang *et al.*, "Preparation and microwave absorption properties of the hollow ZnFe2O4@C composites with core-shell structure," *J Magn Magn Mater*, vol. 502, May 2020, doi: 10.1016/j.jmmm.2020.166543.

[32] T. L. Gilbert, "A phenomenological theory of damping in ferromagnetic materials," *IEEE Trans Magn*, vol. 40, no. 6, pp. 3443–3449, 2004, doi: 10.1109/TMAG.2004.836740.

[33] M. Mehdipour and H. Shokrollahi, "Comparison of microwave absorption properties of SrFe12O19, SrFe12O19/NiFe2O4, and NiFe2O4 particles," *J Appl Phys*, vol. 114, no. 4, p. 043906, Jul. 2013, doi: 10.1063/1.4816089.

[34] P. Liu, Y. Huang, J. Yan, and Y. Zhao, "Magnetic graphene@PANI@porous TiO2 ternary composites for high-performance electromagnetic wave absorption," *J Mater Chem C Mater*, vol. 4, no. 26, pp. 6362–6370, 2016, doi: 10.1039/c6tc01718e.

[35] X. Liu, Y. Chen, X. Cui, M. Zeng, R. Yu, and G. S. Wang, "Flexible nanocomposites with enhanced microwave absorption properties based on Fe3O4/SiO2 nanorods and polyvinylidene fluoride," *J Mater Chem A Mater*, vol. 3, no. 23, pp. 12197–12204, Jun. 2015, doi: 10.1039/C5TA01924A.

[36] Y. Zhang *et al.*, "A facile self-template strategy for synthesizing 1D porous Ni@C nanorods towards efficient microwave absorption," *Nanotechnology*, vol. 28, no. 11, Feb. 2017, doi: 10.1088/1361-6528/aa5d6f.

[37] S. Hait, A. Gorai, and K. Mandal, "Origin of different microwave absorption in multiferroic Bismuth and Gallium Ferrite," *Mater Lett*, vol. 331, Jan. 2023, doi: 10.1016/j.matlet.2022.133520.

[38] W. Ma, R. Yang, and T. Wang, "ZnO Nanorod-Based Microflowers Decorated with Fe3O4 Nanoparticles for Electromagnetic Wave Absorption," *ACS Appl Nano Mater*, vol. 3, no. 8, pp. 8319–8327, Aug. 2020, doi: 10.1021/acsanm.0c01728.

[39] X. Liu, Y. Chen, X. Cui, M. Zeng, R. Yu, and G.-S. Wang, "Flexible nanocomposites with enhanced microwave absorption properties based on Fe3O4/SiO2 nanorods and polyvinylidene fluoride," *J. Mater. Chem. A*, vol. 3, no. 23, pp. 12197–12204, 2015, doi: 10.1039/C5TA01924A.

CHAPTER 4

TUNING OF ELECTROMAGNETIC PARAMETERS OF HIGHLY DIELECTRIC SODIUM BISMUTH TITANATE WITH VARYING DOPING CONCENTRATION OF STRONTIUM AND INCORPORATION OF MAGNETIC PARAMETERS BY COATING WITH COBALT FERRITE

In this chapter, the structural, dielectric, and microwave properties of $Sr_x(Na_{0.5}Bi_{0.5})_{1-x}TiO_3$ [SNBT(x*100)] samples with x = 0.25, 0.50, and 0.75 were investigated. Coating the most suited sample with cobalt ferrite enabled efficient microwave absorption.

4.1 Preamble

It is well known that microwave radiation is weakened when it travels through the electric, magnetic, and dielectric loss medium of microwave-absorbing materials (MAMs). Depending on the filler type, the dielectric (permittivity) and magnetic (permeability) properties have a significant impact in the microwave absorption performance [1], [2]. Fillers comprised of ceramic, metallic, and ionic components with a high dielectric constant may be used to increase the dielectric constant of microwave-absorbing materials. Barium titanate ($BaTiO_3$) with a perovskite structure is one of the most intriguing dielectric filler options for microwave absorption materials [3] due to its high dielectric constant and ferroelectric response.

Because of its robust ferroelectricity, high Curie temperature (T_C ~ 320 ºC), and wide range of possible dielectric property modifications, bismuth sodium titanate ($Na_{0.5}Bi_{0.5}TiO_3$, or NBT), a unique Ti-based ferroelectric perovskite oxide, has attracted a lot of interest. A negligible amount of relaxors known as NBT are implemented at the A-sites of the perovskite. The disorganized distribution of Na^{1+} and Bi^{3+} ions in the A-site sub-lattice of NBT is the root cause of the weak relaxor behavior seen in this compound. The crystal structure of NBT at room temperature is rhombohedral and belongs to the $R3c$ space group; however, at 225 ºC, the structure changes to tetragonal. The large maximum of electric permittivity in NBT may be the result of electromechanical interactions between the polar regions (rhombohedral phase) and the non-polar matrix (tetragonal phase), despite the fact that there is no phase change associated with this maximum [4]. The solid solution of NBT with a variety of perovskite oxides has been the subject of much research [5]–[12], with the goal of achieving the optimal characteristics required for technological applications. Owing to the high T_C of NBT and the other materials often employed to generate the solid solutions, the ferroelectric transition temperature in the majority of these scenarios is significantly higher than the room temperature. As a result, researchers are looking for a material that can lower the critical temperature (T_C) closer to room temperature while maintaining structural stability in a solid NBT solution.

In this regard, strontium titanate ($SrTiO_3$, ST) is an additional Ti-based perovskite oxide that demonstrates a phase transition at a temperature (105 K) below T_C [13]–[15]. It is generally recognized that the structural phase transition that occurs below T_C is of the displacement type, and it is also common knowledge that the crystalline lattice of the ST transforms from cubic to tetrahedral symmetry below T_C. Since the ionic radius of the Sr^{2+} ion (1.44 Å) lies between that

of the Bi^{3+} and the Na^{1+} ions, it is conceivable for the Sr^{2+} ion to go to the Na/Bi-site in the solid solution of ST-NBT. This movement may affect the crystal structure of the parent materials at room temperature. Altering the crystal symmetry in order to reduce the T_C and move it closer to room temperature is therefore desired from a scientific point of view.

These materials, on the other hand, are barely capable of satisfying all of the requirements for approved MAMs. As an alternative to the use of a single component substance, the construction of a one-of-a-kind composite made up of numerous components and a predetermined structure is an effective method for improving the microwave absorption capabilities of a material. Recently, there has been a lot of interest in the core/shell nanostructured materials consisting of magnetic and dielectric components. This is due to the fact that their superior physical and chemical characteristics compared to those of their single-component counterparts [8] have garnered considerable interest. An additional wave loss mechanism may be introduced in these materials via the cross-coupling effect [9] as a result of the near values of permeability in magnetic and permittivity in dielectric materials. These near values make the cross-coupling effect possible. Therefore, the utilization of these materials as a structural paradigm for the production of functional MAMs is advantageous.

4.2 Experimental

4.2.1 Sample Preparation

4.2.1.1 Sample Preparation of SNBTx

Using the solid state reaction method, the compounds with composition $Sr_x(Na_{0.5}Bi_{0.5})_{1-x}TiO_3$ (x = 0.25, 0.50, 0.75) [SNBT25, SNBT50, and SNBT75] were synthesized. Using an agate mortar and pestle, the stoichiometric amounts of high purity Bi_2O_3 (99% pure, Loba Chemie), TiO_2 (98%, Loba Chemie), Na_2CO_3 (99.5%, Loba Chemie), and $SrCO_3$ (reagent grade, Loba Chemie) are thoroughly mixed in the acetone medium for 12 hours. The mixtures are calcined in an alumina crucible at temperatures ranging from 1173 to 1373 °C for 8 to 12 hours in air, and then they are cooled at a rate of 80 °C per hour until they reach room temperature. Using a binder consisting of polyvinyl alcohol at a concentration of 2%, the calcined samples are pelletized into a disc with a diameter of approximately 7.6 mm. In order to prevent the loss of bismuth, the discs are finally cooled to room temperature at a rate of one kelvin per minute after being sintered at a temperature of 1423 K for 4 hours in crucibles constructed of sealed alumina.

4.2.1.2 Coating of SNBT50

For the purpose of coating the SNBT50 samples with CFO in their prepared state, the solvothermal method is utilized [16]. In the following process, a pre-dispersed SNBT50 sample (0.05 g) is placed in a solution consisting of 10 ml ethanol and 0.53 g urea. This solution is then subjected to the addition of 0.36 g $CoCl_2$, $6H_2O$, 0.89 g $FeCl_3$, $6H_2O$, and 20 ml Ethylene Glycol (EG). After the liquid has been well stirred, oleylamine is added as a surfactant. After that, the mixture is placed inside an autoclave made of stainless steel, and it is then heated to a temperature of 200 °C for a period of 24 hours. After many rounds of washing with ethanol and distilled water, the SNBT50@CFO samples are finally collected through magnetic separation. For the formulations described above, all of the ingredients required are purchased from Sigma-Aldrich. These compounds have a purity level of at least 99 percent.

4.2.2 Characterization

X-ray diffraction (XRD) is carried out in a Rigaku SmartLab equipped with Cu-K_α radiation in order to ascertain the phases of the synthesized samples. The Rietveld refinement of the XRD patterns for the SNBTx samples are done using the FullProf software [17] in order to determine the crystalline phase of the synthesized materials and to obtain the lattice parameters. During the Rietveld analysis, the background is provided with a polynomial function that has six coefficients, and pseudo-Voigt profiles are utilized in order to establish the shape of the peaks. An FEI QUANTA FEG 250 field-emission scanning electron microscope (FESEM) with a voltage range of 0.2 to 30 kV and a FEG high-resolution transmission electron microscope (HRTEM) with a voltage range of 80 to 200 kV are used in order to obtain information regarding the size of the samples as well as their morphology. This is done in order to learn more about the samples. First, an energy-dispersive X-ray (EDX) spectrum is obtained so that the elemental analysis of the CFO-coated SNBT50 sample can be determined. Using a vibrating sample magnetometer (VSM), the magnetic measurements are carried out in an applied field that is at its maximum 14 kOe strength at room temperature (~ 300 K) (Lake Shore).

A Vector Network Analyzer (VNA) made by Anritsu with the model number MS46122B and a coaxial airline made by Maury Microwaves with the model number 8043S6 are used in order to evaluate the microwave properties of the samples. This examination covers a frequency spectrum between 1 GHz and 17 GHz. After loading the powder samples into an epoxy resin matrix at a weight percentage of 20 wt.% for microwave measurements, the

mixtures are then moulded into a hollow cylindrical shape with an inner diameter (d_{in}) = 1.5 mm and an outer diameter (d_{out}) = 3.5 mm. This shape is used in order to ensure that the composites are correctly prepared in accordance with the dimension of the airline. After the composite samples have been correctly placed at the 'port 1' end of the coaxial airline, the VNA is used to measure the 2-port scattering (S)-parameters. This is done to determine the degree of scattering of electromagnetic wave occurred from the samples in both directions. The polynomial fit model of the Nicholson-Ross-Weir (NRW) technique based on the transmission line approach is utilized [18] to perform further study on the reported S-parameters.

4.3 Results and Discussion

4.3.1 Structure and Morphology

The Rietveld refinements of the room temperature XRD patterns of SNBT25, SNBT50, and SNBT75, respectively, are depicted in Figs. 4.1(a–c). According to the refined XRD patterns, which are shown in Fig. 4.1 by the solid red lines, all of the materials were synthesized in the cubic phase with *Pm*3*m* space group. The absence of any unidentified peak confirms the single-phase formation of the materials. In Table 4.1, the values for both the lattice parameters and the quality of fitting parameters are provided. Because the average ionic radius of Na^{1+} and Bi^{3+} (1.385 Å) and the ionic radius of Sr^{2+} (1.44 Å) are so close to one another, no substantial change in either the lattice parameters or the shifting of the XRD peaks with the increase in Sr concentration could be determined. In Fig. 4.2, the XRD pattern of SNBT50, CFO, and SNBT50@CFO are depicted.

CFO nanoparticles exhibit the same pattern as reported in the literature, which is consistent with a single-phase spinel face-centered cubic structure at room temperature (ICDD database no. 00-022-1086). In the pattern of SNBT50@CFO, the peaks from both the core

Table 4.1. Lattice parameter and refinement parameters obtained from Rietveld refinement of XRD data.

Materials	Lattice Parameters (Å)	χ^2	R_p	R_{wp}	R_{exp}
SNBT25	3.8958 (5)	2.07	4.32	6.06	3.71
SNBT50	3.8965 (4)	1.95	4.62	6.13	3.65
SNBT75	3.8971 (7)	2.11	4.54	6.05	3.57

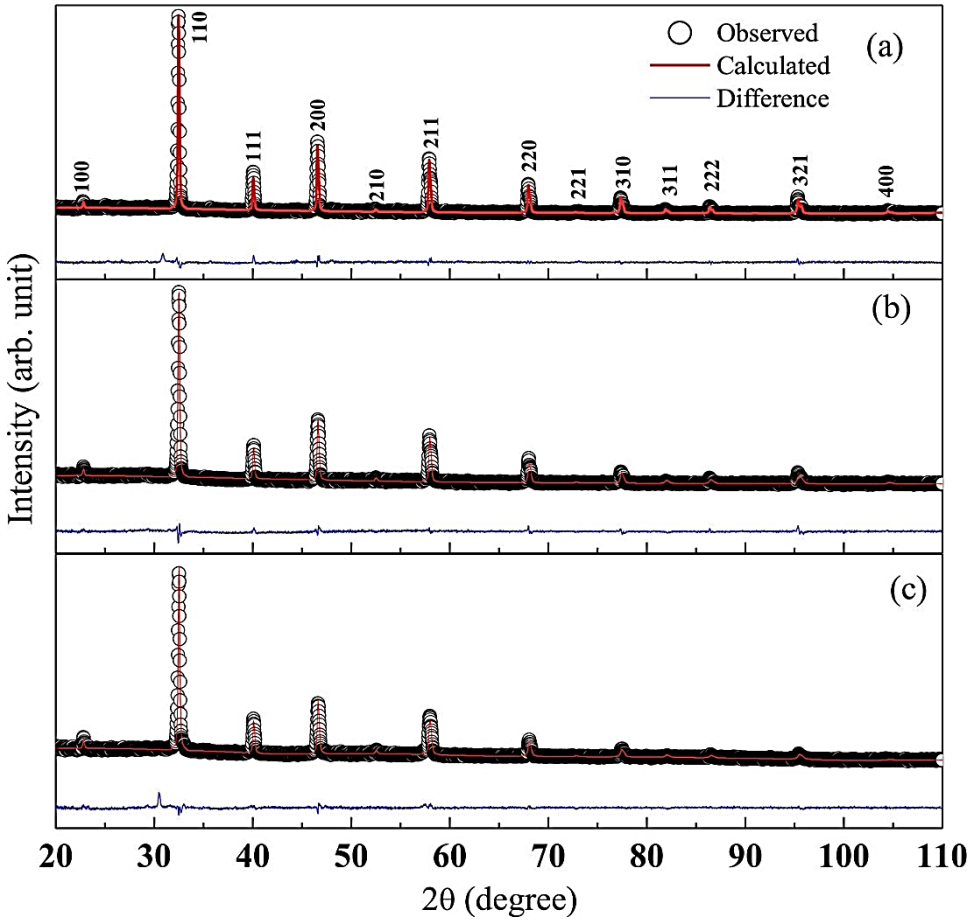

Figure 4.1. Rietveld refinement of the X-ray diffraction patterns of (a) SNBT25, (b) SNBT50 and (c) SNBT75. The symbols represent the experimental data and the lines the Full-Prof simulated patterns.

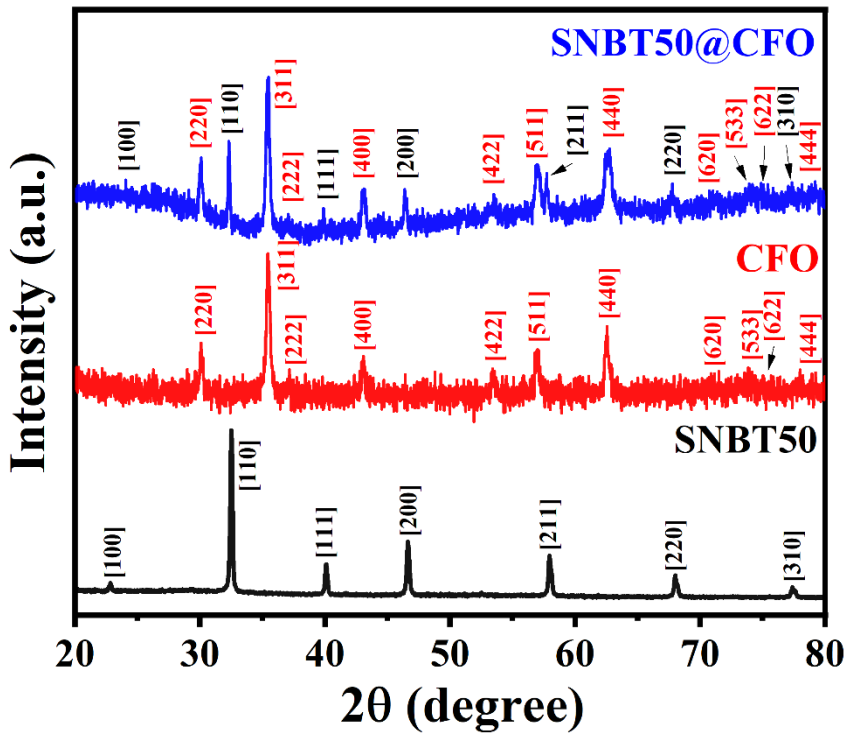

Figure 4.2. X-Ray Diffraction patterns of the samples obtained at room temperature

(SNBT50) and shell (CFO) material could be clearly observed. The composite is formed from a single phase of both materials, as evidenced by the lack of any unrecognized peaks.

The SEM images of the materials are shown in Fig. 4.3. All the SEM images show uniform distribution of the grains of different shapes and sizes. The average grain size obtained from SEM images is found to be 0.7, 0.72, and 0.69 μm, respectively for SNBT25, SNBT50, and SNBT75. It is observed from SEM images that the pellets are free of agglomeration and pores which suggests that the pellets are well-sintered.

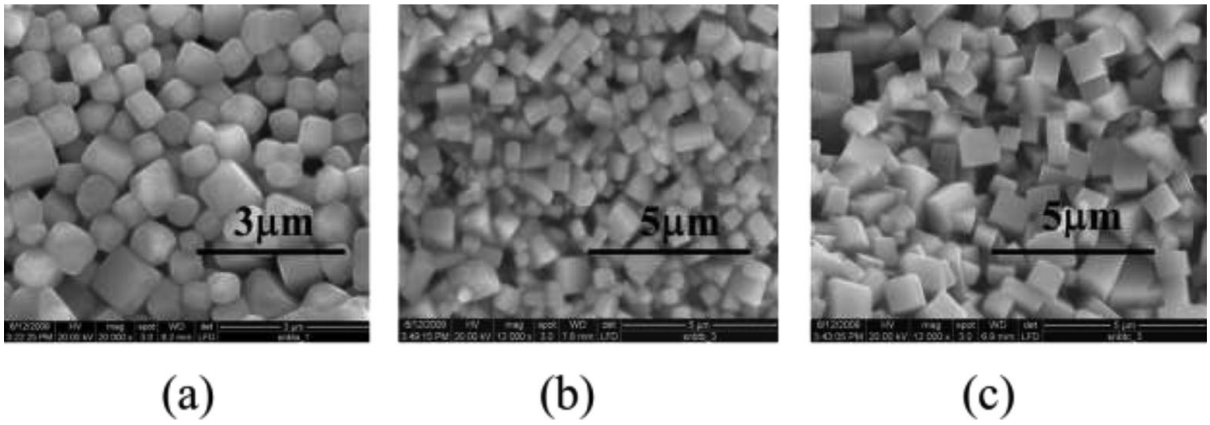

Figure 4.3. Scanning electron micrographs of SNBT25 (a), SNBT50 (b), and SNBT75 (c)

SEM and TEM analyses were performed in order to look into the morphology and microstructure of the SNBT50@CFO composites (Fig. 4.4). In accordance with Fig. 4.4(b), it can be depicted that SNBT50 has a coating of CFO shell surrounding it. It is also evident from Fig. 4.4(a) that the sample possess a smooth surface. On the surface of the SNBT50 particles, it is possible to observe a thin coating of CFO developed with a thickness between 5 and 15 nanometers. The nanocomposites are discerned to have an almost spherical form, and their diameter distribution lies between 200 and 300 nm, which is compatible with the SEM picture shown in Fig. 4.4(a). The high-resolution transmission electron microscopy (HRTEM) image, illustrated in Fig. 4.4(c), demonstrates a core-shell structured SNBT50@CFO composite having well-resolved lattice fringes of both materials. In Fig. 4.4(c), the (100) and (311) planes of the SNBT50 core and the CFO shell, respectively, are each indicated. The diffraction spots for both CFO and SNBT50 are displayed in the selected area electron diffraction (SAED) pattern shown in Fig. 4.4(d), which validates the crystalline structures of both CFO and SNBT50. The well-defined locations in the SAED pattern coincide with the allowable Bragg diffraction of (110) and (400) for the cubic phase of SNBT50 and CFO, respectively. The findings of the SEM and TEM analysis make it abundantly evident that the nanocomposites have a structure resembling a core-shell type, and that the inner SNBT50 cores have been effectively coated with the uniform CFO shells.

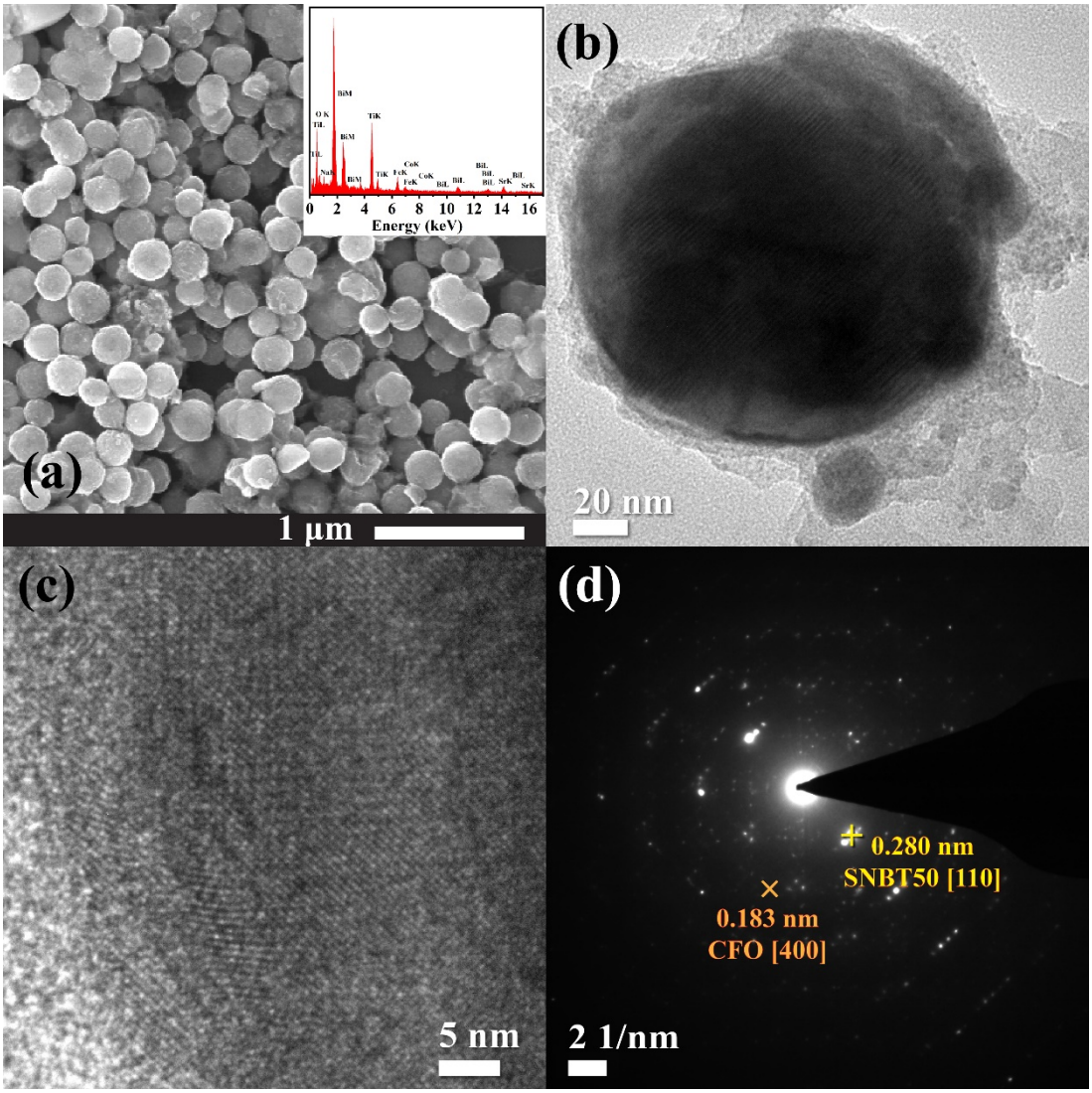

Figure 4.4. (a) SEM micrograph; (inset) EDAX spectrum, (b) TEM micrograph, (c)HRTEM and (d) SAED pattern of SNBT50@CFO core-shell composites

4.3.2 Dielectric Properties at Low Frequency Region

The temperature dependence of the dielectric constant (ε') and the loss tangent ($\tan\delta$) of the materials at a range of frequencies is depicted in Fig. 4.5(a–c). Because of the diffuse character of the dielectric peaks, it is likely that different local Curie points are present along with microscopic heterogeneity in each of the materials. It has been found that the peak value of the dielectric constant, ε'_m, decreases with increasing frequency, which is a characteristic feature of relaxor activity [19]. It can be seen from Fig. 4.5 that the value of the temperature, T_m, as well as the value of ε'_m are dependent on the percentage of Sr doping. At a frequency of 100 kHz, it was discovered that the value of T_m for SNBT25, SNBT50, and SNBT75, respectively, were 462.8, 325.5, and 218.3 K. Since the Sr doping does not have a substantial

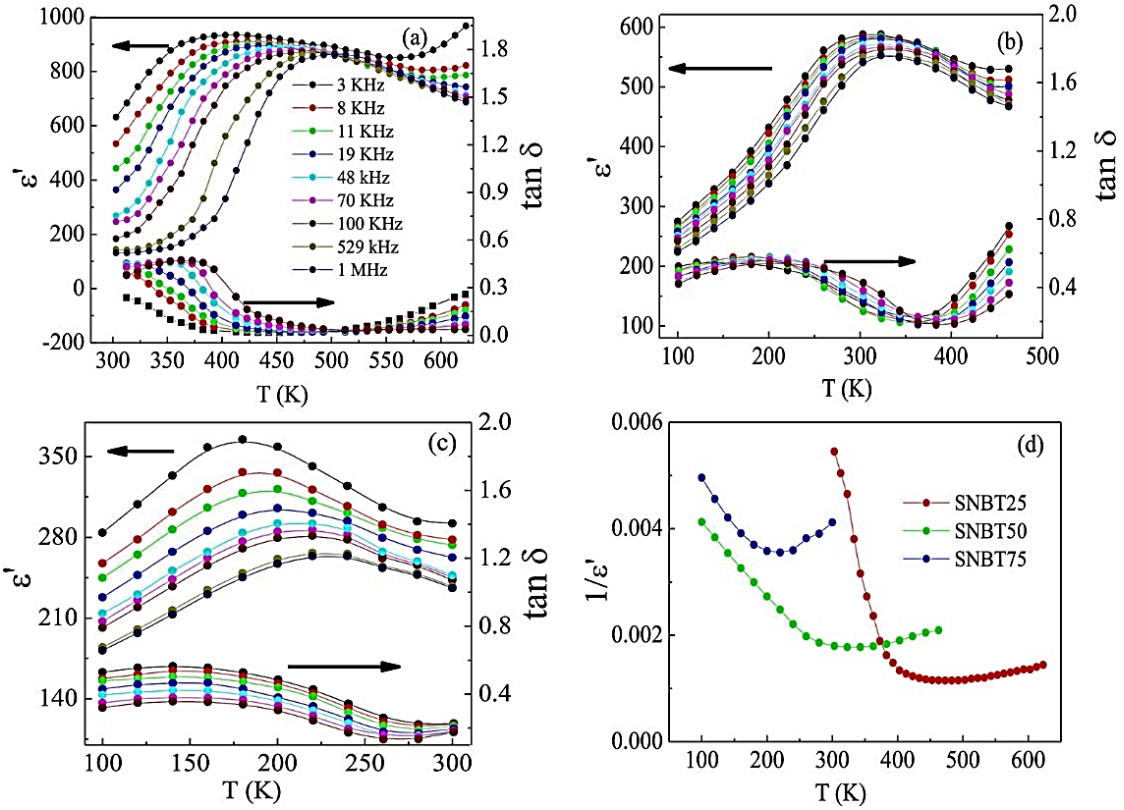

Figure 4.5. Temperature variation of dielectric constant (ε') and tan δ of SNBT25 (a), SNBT50 (b) and SNBT75 (c) at various frequencies. The inverse dielectric constant (1/ε') as a function of temperature at 100 kHz for $Sr_x(Na_{0.5}Bi_{0.5})_{1-x}TiO_3$ [x = 0.25, 0.50 and 0.75]

impact on the crystal structure of the materials, the change in dielectric characteristics with increasing Sr concentration may be explained as follows. Owing to the existence of the lone-pair in Bi^{3+} cation, the divalent pseudo-cation $(Na, Bi)^{2+}$ has a substantially higher degree of polarizability than Sr^{2+} does. Therefore, the value of ε'_m will decrease as the amount of Sr present in the materials increases. On the other hand, the weakening of the ferroelectric coupling between these micro-regi ons can be attributed to the reduction in the size of bismuth-rich areas that occurs as a result of the gradual breakup of relatively large bismuth-rich micro-regions into smaller regions [20]. As a consequence of this, the value of T_m drops as the number of Sr-ions increases. It can be shown from the inverse of ε'as a function of temperature at a frequency of 100 kHz, which is illustrated in Fig. 4.5(d), that these materials are unable to follow Curie-Weiss behavior. A significant deviation from the Curie–Weiss behavior is consistent with the fact that the SNBT systems are relaxors in nature. It can be further depicted from Fig. 4.5 that there is no significant change in the value of $\tan\delta$ with increasing Sr concentration. The peaks of the relaxation process can be interpreted from the $\tan\delta$ vs T plots. These plots show that the relaxation peaks shift to the higher temperature side as the frequency increases, which suggests that the relaxation process is temperature dependent.

For SNBT relaxor in the temperature region $T > T_m$ using the following modified Curie–Weiss law [21], the degree of diffuseness of the temperature dependence of ε' is estimated using the following equation,

$$\frac{1}{\varepsilon'} - \frac{1}{\varepsilon'_m} = \frac{(T-T_m)^\gamma}{c} \tag{4.1}$$

where c is the Curie constant. The value of exponent is 1 for normal ferroelectric phase and 2 for an ideal relaxor nature. The high values of γ in these samples, indicate the strong relaxor behavior of the materials [22]. Fig. 4.6 shows the logarithmic plots between $(1/\varepsilon' - 1/\varepsilon'_m)$ versus $(T - T_m)$ at two different frequencies for all the compositions. The value of γ is obtained from the slope of the curves in Fig. 4.5. The values of γ at 19(528) kHz are found to be 1.75(1.82), 1.87(1.89), and 1.88(1.76), respectively for SNBT25, SNBT50, and SNBT75. The observed values of γ confirms the relaxor behavior of the materials.

It is widely documented that the frequency dependence of T_m in relaxor materials cannot be characterized using an Arrhenius equation, as would be anticipated for a Debye relaxation process. The frequency dispersion of the maximum temperature of the dielectric constant in relaxor materials has been related to the distribution of relaxation times of the

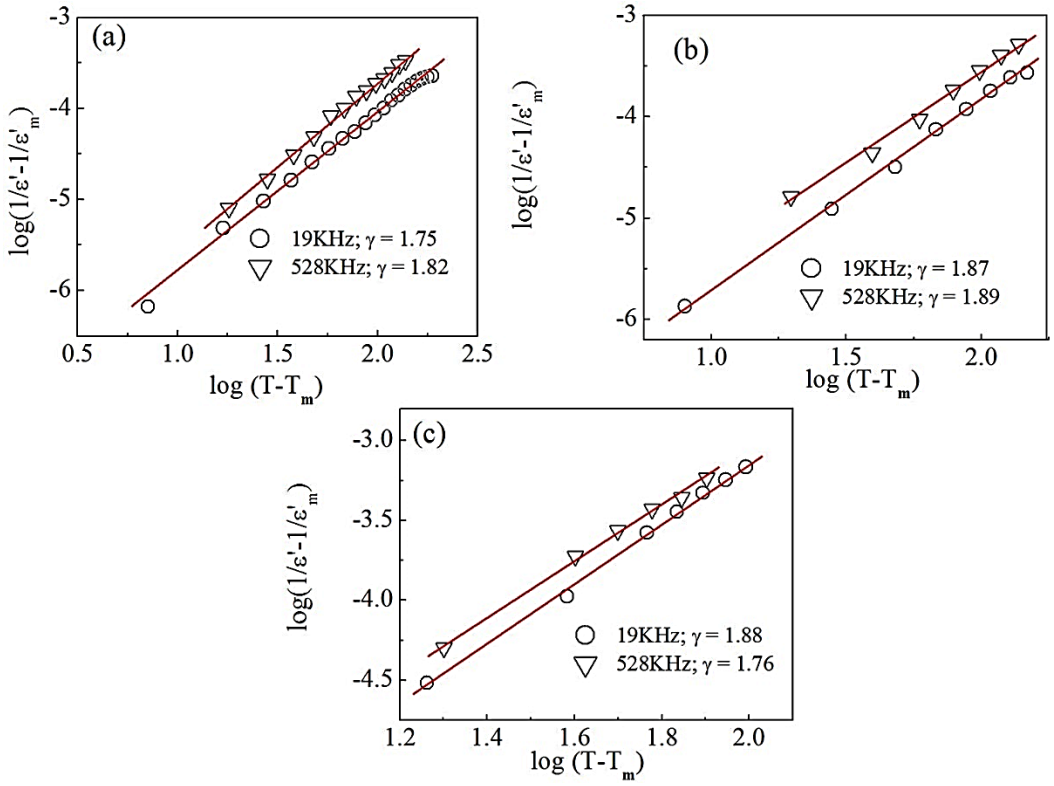

Figure 4.6. log ($1/\varepsilon' - 1/\varepsilon'_m$) versus log ($T-T_m$) plot for SNBT25 (a), SNBT50 (b) and SNBT75 (c). The symbols represent the experimental data points and the solid lines show a linear fit to the data points.

relaxors. Several theories have been developed to explain the diffuseness of the dielectric phase transition and the frequency dispersion of T_m. Due to the divergent character of the relaxation time below a specific temperature, the Vogel–Fulcher relation is regarded as the most effectively applied mathematical representation among the several theoretical models. The Vogel–Fulcher empirical relationship [18], [23] describes the frequency dependence of the temperature of the permittivity maximum (T_m) for the majority of relaxor ferroelectrics, defined as,

$$\nu_m = \nu_0 \, exp\left[-\frac{E_a}{k_B(T_m - T_f)}\right] \tag{4.2}$$

ν_0 represents the attempt frequency, k_B represents the Boltzmann constant, T_f represents the freezing temperature, and E_a represents the activation energy. The temperature dependence of relaxation frequency is shown in Fig. 4.7 by plotting T against $\ln \nu_m$. The solid line in Fig. 4.7 illustrates the best fit of Eq. (2) to the experimental data, and the calculated values of ν_0 and E_a are shown in Table 4.2.

Relaxor behavior in mixed oxide systems is known to be caused by a number of factors, including microscopic composition fluctuations, the merging of micro-polar areas, and a

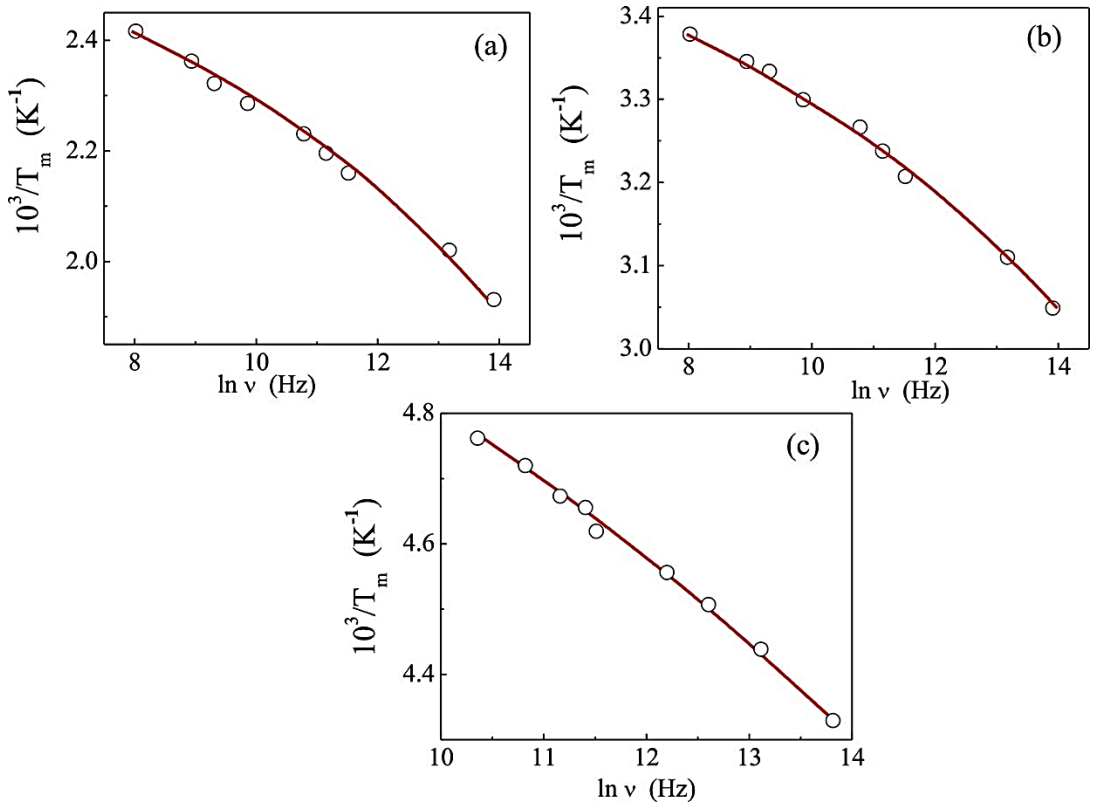

Figure 4.7. Frequency dependence of T_m for SNBT25 (a), SNBT50 (b) and SNBT75 (c). The symbols indicate the experimental data points and the solid line is the fit to Vogel–Fulcher relationship

linkage of order parameter and local disorder mode through local strain. Randomly distributed electrical strain fields are the primary driver of relaxor behavior in a mixed oxide system [24]. Here, SNBT is a mixed oxide system in which ferro-electrically active Sr^{2+}, Na^{1+}, and Bi^{3+} ions occupy the A-sites of the perovskite structure.

Table 4.2. Various parameters obtained from the analysis of relaxor behaviour of SNBT

Materials	ν_0 (Hz)	E_a (eV)
SNBT25	3.42×10^8	0.12
SNBT50	6.8×10^9	0.18
SNBT75	8.8×10^{10}	0.14

Let us compare the dielectric characteristics of SNBT with other doped $Na_{0.5}Bi_{0.5}TiO_3$ (NBT) materials. In the majority of investigations, NBT is doped with additional high dielectric constant minerals such as $BaTiO_3$ (BT) [25], $Ba_{0.5}Sr_{0.5}TiO_3$ (BST) [26], and $BiCrO_3$ (BCO) [27]; hence, the dielectric constant of these solid-solutions is relatively high compared to SNBT systems. However, the transition temperature for BT, BST, and BCO-doped NBT materials is much greater than ambient temperature, rendering these materials unsuitable for technological applications. In contrast, the transition temperature of one of the examined materials, SNBT50, is very near to ambient temperature (300 K at 3 kHz) and has a dielectric constant of 580.

4.3.3 Electric and magnetic properties in high frequency region

The frequency dependence of the real permittivity (ε') and $\tan\delta_\varepsilon$ spectra of the materials are shown in Fig. 4.8(a, b). All of the samples exhibit polarization relaxation in response to the electromagnetic wave. Multiple relaxation characteristics are shown in Fig. 4.8(c). The decrease in ε', followed by a modest increase as the frequency increases, is caused mostly by the polarizabilities (electronic, ionic, space charge, and dipole orientation) and electric displacement of dielectric materials. The ionic and electronic polarizations have an influence at frequencies of THz and PHz, respectively. For metal-based composites, the space charge polarization and dipole polarization processes might be utilized to explain the absorption of electromagnetic radiation, which may affect the permittivity as a function of frequency [28]. In this instance, the ups and downs in ε' spectra may be caused by the displacement current lag and the AC loss. SNBT50 has a much greater dielectric constant than

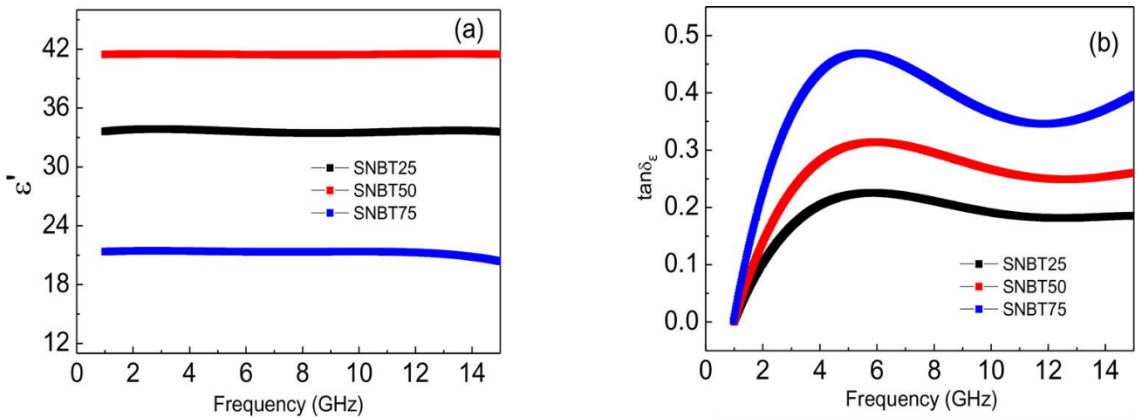

Figure 4.8. Frequency dependence of dielectric constant (ε′) (a), tan δε (b).

all other samples. Polarization is a significant contributor to the microwave absorptions of these substances. Fig. 4.5 also shows that when the concentration of Sr atoms increases, the maximum of polarization shifts from high temperature to low temperature at the same frequency. SNBT50 simultaneously obtains its maximum polarization close to room temperature. In the GHz band, SNBT50 has a greater dielectric constant than comparable materials at ambient temperature. The nature of repeated absorption may also be seen in the frequency dependence of $\tan \delta_\varepsilon$ in Fig. 4.8(b). At relatively low frequencies, the dielectric loss in perovskite materials is described by the leak conductance, but at relatively high frequencies, the relaxation polarization and the electric conductance contribute to dielectric loss. The dielectric polarization and related relaxation processes are regarded as the primary source of the loss mechanisms in SNBT substances. SNBT75 and SNBT25 have the highest and lowest values of $\tan \delta_\varepsilon$, respectively. Although SNBT50 has a greater $\tan \delta_\varepsilon$ than SNBT25, its dielectric constant at room temperature is superior to that of other materials, making it a potential microwave material for applications in many technological domains.

Figs. 4.9(a) and (b) depict the real (ε') and imaginary (ε'') portions of the permittivity, respectively. ε' value of SNBT50 ranges from 5.14 to 5.50 GHz and does not vary significantly between the studied frequency range, while ε' of CFO ranges from 5.97 to 6.52 GHz and exhibits the same frequency-dependent behavior as SNBT50. After coating with the CFO layer, the ε' of SNBT50@CFO core-shell composites rise to around 8.78 at lower frequencies, then drops with the increase in frequency up to 11.5 GHz and stays almost constant at 6.8 beyond that frequency. According to Maxwell-Wagner grain-grain boundary models for ferrites, the interfacial and dipolar polarization mostly contribute to the dielectric constant. At higher frequencies, ε' decays in Fig. 4.9(a) for core-shell composites, where dipoles lag behind the field, inducing dielectric relaxation. Again, for SNBT50, ε'' shows a nearly constant value of

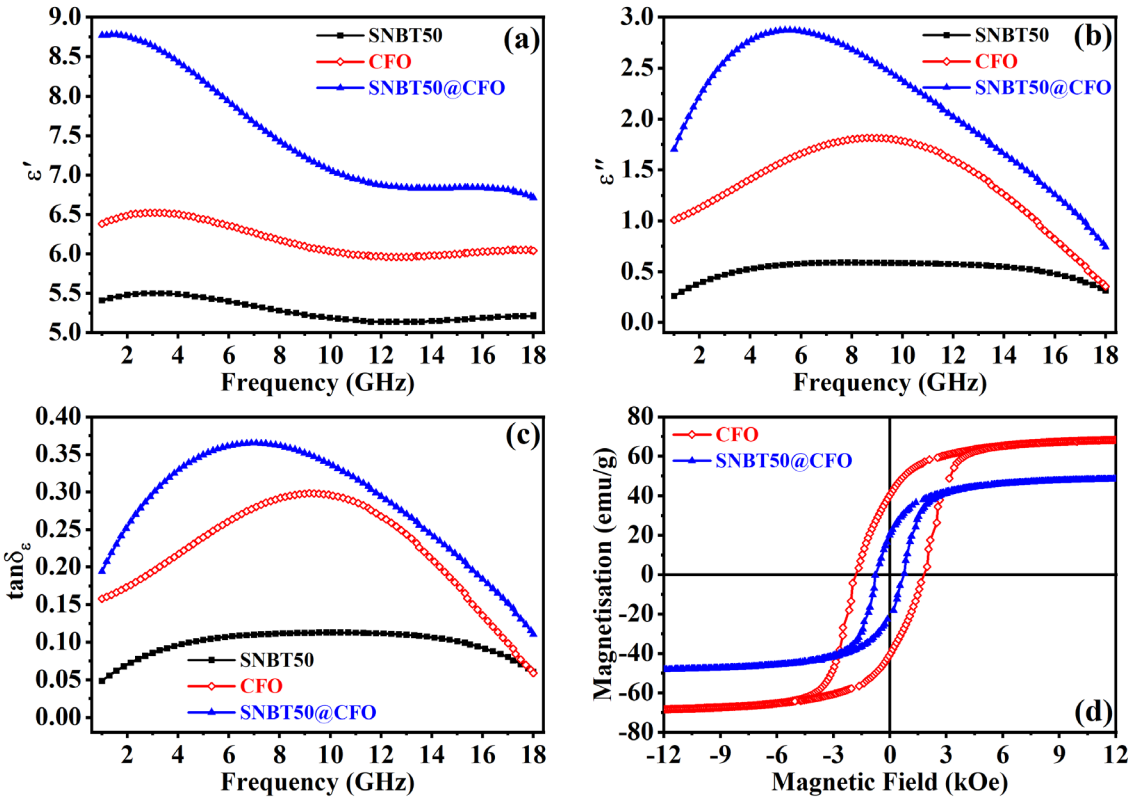

Figure 4.9. Frequency dependence of (a) real (ε'), (b) imaginary(ε") values of dielectric constant, (c) dielectric loss (tan δε), and (d) M–H plots at 300 K for all the samples

0.5 over the studied frequency band, but ε'' of CFO demonstrates a general rise in value with a substantial resonant peak value of 1.8 at 9 GHz. For SNBT50@CFO core-shell composites, the ε'' displays similar frequency-dependent behaviour as that of CFO but with overall larger values. Core-shell composites move the resonance peak to a lower frequency (5.42 GHz) with a greater value of 2.87.

Fig. 4.9(c) depicts the frequency dependence of dielectric loss, defined as $\tan\delta_\varepsilon = \varepsilon''/\varepsilon'$, which follows the same pattern as ε'' for all samples. The greater dielectric loss of SNBT50@CFO core-shell composites compared to SNBT50 and CFO nanoparticles adds considerably to the composite material's enhanced EM wave absorption. Polarization is known to be associated with dielectric loss. Since they occur between 10^3 and 10^6 Hz, electronic and ionic polarizations may be omitted from our experimental range. Due to the unequal distribution of space charge, however, interfacial polarization is possible between SNBT50 and the CFO shell. Since dipolar polarization also produces dielectric loss in the GHz frequency band, the interfacial polarization and dipolar polarization contribute to the dielectric loss in the examined systems.

Fig. 4.9(d) illustrates the DC magnetic field-dependent magnetization curves at 300 K for CFO and SNBT50@CFO, which display soft ferrimagnetic behavior. Table 4.3 contains the coercivity (H_C) and saturation magnetization (M_S) values derived from Fig. 4.9(d). The surface-to-volume ratio of CFO nanoparticles exceeds that of the CFO shell coated over the composites. Higher nanoparticle surface anisotropy results in higher H_C. Due to the presence of non-magnetic SNBT50 core, M_S values are lowered in the core-shell composites than that of the CFO nanoparticles.

Table 4.3 Magnetic parameters of CFO and SNBT50@CFO samples

Sample	H_C (kOe)	M_S (emu/g)
CFO nanoparticles	1.806	70.323
SNBT50@CFO core-shell composites	0.763	50.216

In Fig. 4.10(a) and (b), the real (μ') and imaginary (μ'') components of the relative permeability of the samples are displayed as a function of frequency. μ' is observed to decrease up to a specific frequency, after which it maintains a nearly constant value in all samples. The values of μ' for CFO are much greater than those of SNBT50. However, the μ' of the composite of SNBT50 and CFO is greater than that of the nanoparticles of SNBT50 alone. Fig. 4.10(b) indicates a resonance peak for CFO at about 8.81 GHz. For the bare and coated SNBT50 samples, μ'' values are found to grow identically with frequency up to a frequency of about ~7.6 GHz, beyond which it continues to increase for the coated SNBT50 whereas it stays almost constant for its bare counterparts.

The fluctuation of magnetic loss tangent ($\tan\delta_\mu = \mu''/\mu'$) with frequency ($f$) is shown in Fig. 4.10(c), which follows a nearly same trend as the μ'' versus f curve. Dynamic magnetic loss is well-known to result primarily from magnetic hysteresis, domain wall resonance, eddy current effects, and natural and exchange resonance. The effectiveness of the first two contributions is diminished for samples in the gigahertz frequency range and at very low fields. According to the natural magnetic resonance equation, $2\pi f_r = \frac{4\gamma K}{3\mu_0 M_S}$ where γ is the gyromagnetic ratio (2.8 GHz/kOe), the resonance frequency (f_r) for CFO nanoparticles is less than 1 GHz. The contribution of eddy current loss to μ'' may be written as $\mu'' \sim 2\pi\mu_0\mu'^2(d^2\sigma)$, where d is the sample thickness, σ is the electrical conductivity, and μ_0 is the permeability of

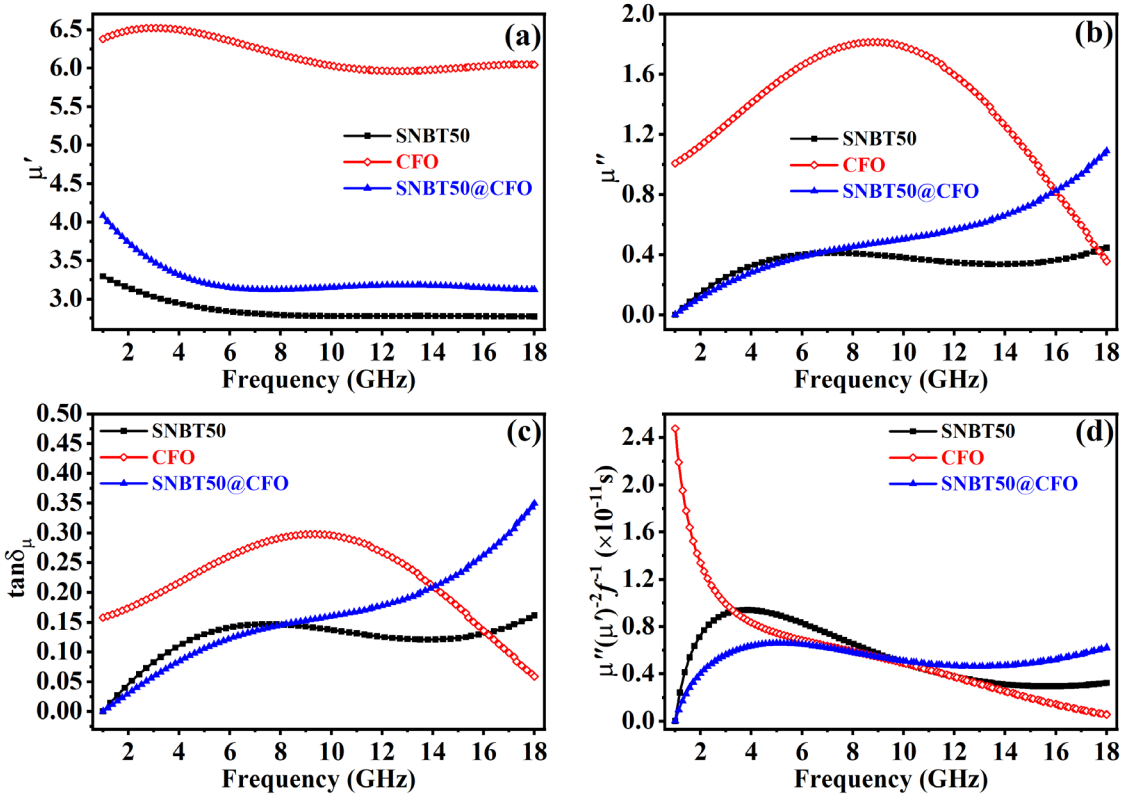

Figure 4.10. Frequency dependence (1–18 GHz) of (a) real (μ'), (b) imaginary (μ") values of magnetic permeability, (c) magnetic loss (tan δμ), and (d) μ"(μ')$^{-2}f^{-1}$ at 300 K for all the samples

empty space. If μ'' (or $\tan\delta_\mu$) arises from eddy current loss, then the $\mu''(\mu')^{-2}f^{-1}$ curves will be constant with frequency, according to this equation. Fig. 4.10(d) illustrates the frequency dependency of $\mu''(\mu')^{-2}f^{-1}$ in order to comprehend the potential causes of magnetic loss. For both uncoated and coated SNBT50 samples, the figure indicates that eddy current loss predominates over the entire frequency range. For CFO, the resonance peak is below our observed frequency range and thereafter drops and maintains fairly constant values which imply natural and exchange resonance at low frequency and dominance of eddy current loss afterwards.

4.3.4 Microwave absorption properties

Absorption of electromagnetic waves is highly dependent on the magnetic and electric characteristics of a substance. Among these qualities, reflection loss (RL) offers insights into the material's effectiveness in reducing the reflected waves. This may occur by either wave absorption, i.e., the transformation of EM waves into other energy, or EM wave transmission. Improper impedance matching is required for optimal EM wave propagation. Here, RL is computed using the following equations:

$$Z_{in} = Z_0(\frac{\mu_r}{\varepsilon_r})^{1/2}\tanh\left[j\left(\frac{2\pi tf}{c}\right)(\mu_r\varepsilon_r)^{\frac{1}{2}}\right] \quad (4.3)$$

$$RL = 20\log|(Z_{in} - Z_0)/(Z_{in} + Z_0)| \quad (4.4)$$

where $\mu_r = \mu' - i\mu''$ and $\varepsilon_r = \varepsilon' - i\varepsilon''$ are the relative permeability and permittivity of the material, c is the velocity of light in a vacuum, t is the thickness of the composite absorber, and Z_0 and Z_{in} are the impedance of free space and input impedance of the absorber, respectively.

Fig. 4.11 illustrates the variation of RL of SNBT materials with changing frequency. At 4 GHz, a maximum *RL* of -22 dB is reported for SNBT25 and SNBT50 suggesting that these materials have excellent microwave absorption characteristics within the studied frequency range. In contrast, the maximum *RL* of the SNBT75 is only -11 dB observed at 3.8 GHz. The absorption bandwidth having *RL* < -10 dB for SNBT25 and SNBT50 is 0.6 and 1

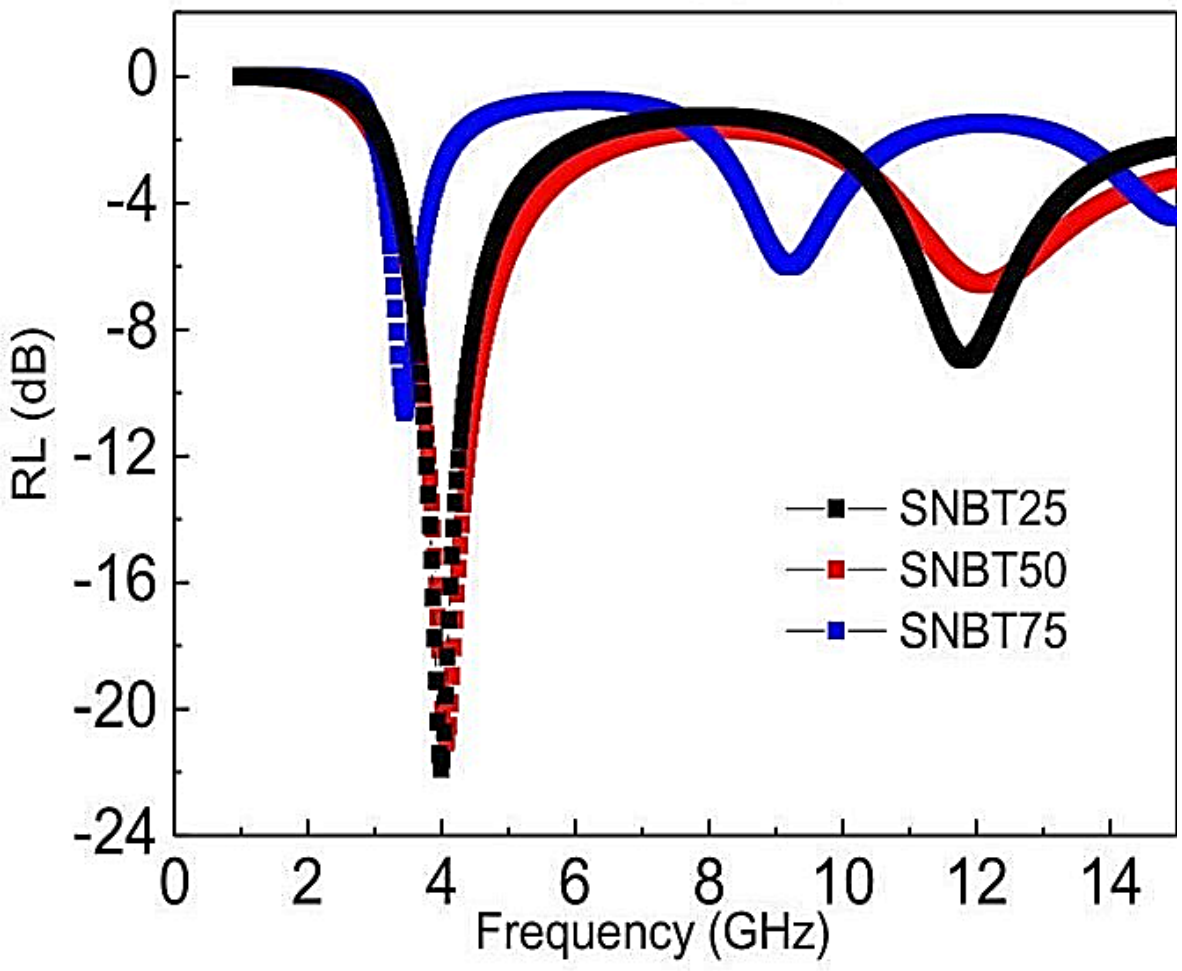

Figure 4.11. Reflection loss (RL) of SNBT materials in the frequency range 1 to 15 GHz.

GHz, respectively. All of these materials contribute significantly to the S-band area between 8 and 12 GHz (Fig. 4.11), despite the fact that the *RL* value of this microwave absorption peak is low. The aforementioned findings show that, among the three SNBT materials, SNBT50 has the most promising microwave characteristics.

Fig. 4.12(a) illustrates the frequency dependence of *RL* for all samples prepared by adding 20 wt.% powder in epoxy resin machined to a thickness of 4 mm. Here, we see that the EM absorption of SNBT50@CFO is more than that of its core equivalent. A thickness-dependent study on EM wave absorption is required for the proper design of an absorber for practical applications. In Fig. 4.12(d), the predicted *RL* for various thicknesses within the examined frequency range were compared. From this study, an optimal *RL* of -20.19 dB is found for thickness, t = 2.7mm at 17.5 GHz with an effective absorbance bandwidth of 4.56 GHz having *RL* < -10 dB. The frequency versus $|Z_{in}/Z_0|$ graphs in Fig. 4.12(c) reveal that the closer value of $|Z_{in}/Z_0|$ to 1 represents the better absorption characteristics of the materials.

The attenuation constant reveals the material's capacity to internally attenuate EM waves and can be computed using the following equation,

$$\alpha = \frac{\sqrt{2}\pi f}{c}\sqrt{(\mu''\varepsilon'' - \mu'\varepsilon') + \sqrt{(\mu''\varepsilon'' - \mu'\varepsilon')^2 + (\mu''\varepsilon' + \mu'\varepsilon'')^2}} \qquad (4.5)$$

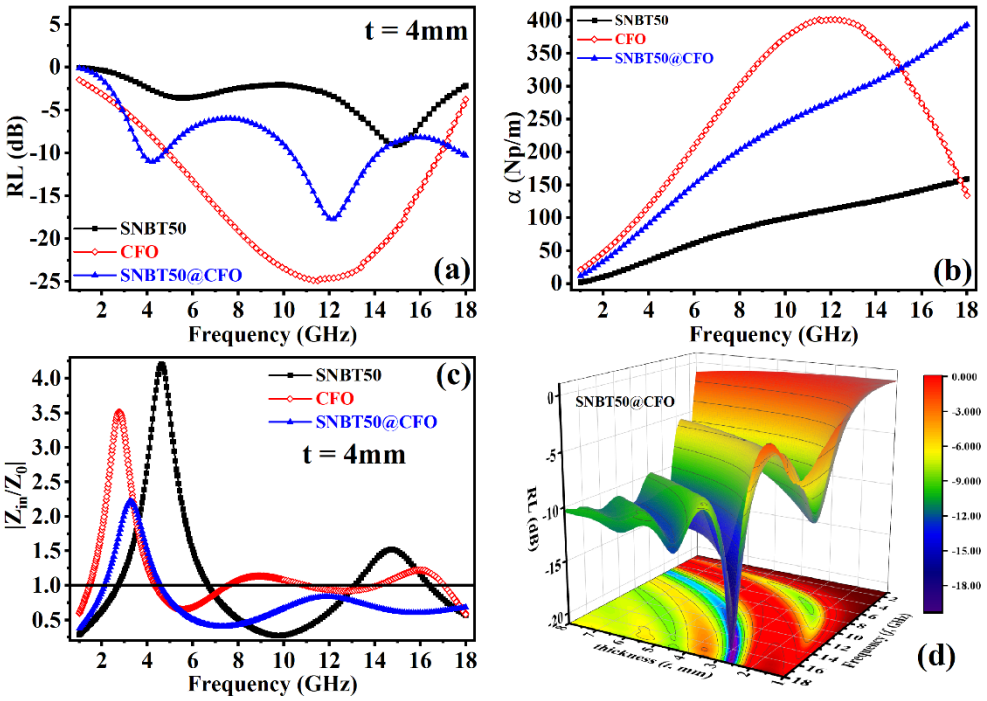

Figure 4.12. Frequency dependence of (a) RL at composite absorber thickness of 4mm, (b) Attenuation constant, (c) Impedance ratios at t = 4mm for all the samples, and (d) frequency and thickness dependence 3D-plot of SNBT50@CFO

Clearly, Fig. 4.12(b) demonstrates that SNBT50@CFO core-shell composites display a greater attenuation constant than bare SNBT50 over the studied frequency range, since the SNBT50@CFO core-shell composites exhibit both magnetic loss and dielectric loss followed by CFO coating. For the SNBT50@CFO composites, the better attenuation constant and the superior impedance matching are responsible for the improved microwave absorption capabilities and, therefore, for the larger reflection loss exhibited in Fig. 4.12(a).

The interface between SNBT50 cores and CFO shells leads to additional interfacial polarization, which may enhance the dielectric loss of the core-shell composites. On the basis of the synergistic effect of the SNBT50 core and the CFO shell, the effective complementarity between complex permittivity and permeability may be the determining factor in microwave absorption. Therefore, the development of magnetic-dielectric core-shell composites should be a viable way for creating microwave-absorbing materials with excellent performance.

4.4 Conclusions

The structural, dielectric and microwave properties of $Sr_x(Na_{0.5}Bi_{0.5})_{1-x}TiO_3$ ($0.25 \leq x \leq 0.75$) prepared using the solid-state reaction technique have been investigated. Similar studied are performed for cobalt ferrite coated SNBT50 (SNBT50@CFO) composites which exhibits both dielectric and magnetic properties. The Rietveld refinement of the X-ray diffraction pattern at room temperature suggests single-phase structure remained consistent with increasing Sr doping concentration in all the SNBT materials having a *Pm*3*m* crystal symmetry. The composites displayed peaks from both materials with no trace of any unidentified peak, which confirms that the composing materials have been successfully formed into single phase nature. The low-frequency dielectric properties of the SNBT materials are investigated using alternate current impedance spectroscopy in the frequency range from 50 to 1MHz in order to comprehend the effect of Sr doping on the dielectric properties of the materials. The temperature dependence of the dielectric constant at different frequencies gives diffuse peaks which have been attributed to the occurrence of relaxor behavior in these materials. The magnitudes of ε'_m, the maximum value of dielectric constant and T_m, the temperature corresponding to ε'_m are decreased with an increase of Sr^{2+} ion in the materials. There is evidence of Vogel–Fulcher type relaxational freezing in the samples. The microwave absorption properties of the materials have also been studied in the frequency range from 1 to 15 GHz. A maximum reflection loss of -22 dB at 4 GHz is observed for SNBT25 and SNBT50.

It is concluded from the above studies that SNBT50 is more promising material for microwave applications with respect to other two SNBT materials having high ferroelectricity at room temperature and a decent permittivity value. On the other hand, CFO itself being an excellent MAM due to its optimised permittivity and permeability values, the CFO coating significantly increases the permittivity of SNBT50@CFO composites as well as introduces permeability. Due to interfacial polarization, synergistic effect between the core and shell and introduction of magnetic loss in the sample, the enhancement of electromagnetic absorption properties occurs in terms of RL up to -20.19 dB with an increased effective absorption bandwidth of 4.56 GHz at a composite absorber length of as small as 2.7 mm. It also exhibits steadily increasing attenuation constant throughout the observed frequency region. Therefore, the improvement of EM wave absorption properties along with high ferroelectricity at room temperature makes SNBT50@CFO a highly promising candidate towards high-frequency multi-disciplinary applications.

References

[1] J. Hongxia, L. Qiaoling, Y. Yun, G. Zhiwu, and Y. Xiaofeng, "Preparation and microwave adsorption properties of core-shell structured barium titanate/polyaniline composite," *J Magn Magn Mater*, vol. 332, pp. 10–14, Apr. 2013, doi: 10.1016/j.jmmm.2012.11.010.

[2] N. Zhang, Y. Huang, and M. Wang, "3D ferromagnetic graphene nanocomposites with ZnO nanorods and Fe3O4 nanoparticles co-decorated for efficient electromagnetic wave absorption," *Compos B Eng*, vol. 136, pp. 135–142, 2018, doi: https://doi.org/10.1016/j.compositesb.2017.10.029.

[3] J. Su and J. Zhang, "Improvement of mechanical and dielectrical properties of ethylene propylene diene monomer (EPDM)/barium titanate (BaTiO3) by layered mica and graphite flakes," *Compos B Eng*, vol. 112, pp. 148–157, 2017, doi: https://doi.org/10.1016/j.compositesb.2017.01.002.

[4] J. Suchanicz, "Behaviour of Na0.5Bi0.5TiO3 ceramics in the a.c. electric field," *Ferroelectrics*, vol. 209, no. 1, pp. 561–568, Apr. 1998, doi: 10.1080/00150199808018070.

[5] K. Sakata and Y. Masuda, "Ferroelectric and antiferroelectric properties of (Na 0.5Bi 0.5)TiO3-SrTiO3 solid solution ceramics," *Ferroelectrics*, vol. 7, no. 1, pp. 347–349, Jan. 1974, doi: 10.1080/00150197408238042.

[6] B.-J. Chu, D.-R. Chen, G.-R. Li, and Q.-R. Yin, "Electrical properties of Na1/2Bi1/2TiO3–BaTiO3 ceramics," *J Eur Ceram Soc*, vol. 22, no. 13, pp. 2115–2121, 2002, doi: https://doi.org/10.1016/S0955-2219(02)00027-4.

[7] J. Suchanicz, J. Kusz, and H. Böhm, "Structural and electric characteristics of (Na0.5Bi0.5)0.50Ba0.50TiO3 and (Na0.5Bi0.5)0.20Ba0.80TiO3 ceramics," *Materials Science and Engineering: B*, vol. 97, no. 2, pp. 154–159, 2003, doi: https://doi.org/10.1016/S0921-5107(02)00577-9.

[8] X. Wang, H. Lai-Wa Chan, and C. Choy, "Piezoelectric and dielectric properties of CeO 2-added (Bi 0.5 Na 0.5) 0.94 Ba 0.06 TiO 3 lead-free ceramics." [Online]. Available: www.elsevier.com/locate/ssc

[9] O. Elkechai, M. Manier, and J. P. Mercurio, "Na0.5Bi0.5TiO3-K0.5Bi 0.5TiO3 (NBT-KBT) system: A structural and electrical study," *Physica Status Solidi A Appl Res*, vol. 157, no. 2, pp. 499–506, 1996, doi: 10.1002/pssa.2211570234.

[10] A. Sasaki, T. Chiba, Y. Mamiya, and E. Otsuki, "Dielectric and Piezoelectric Properties of (Bi 0.5 Na 0.5)TiO 3-(Bi 0.5 K 0.5)TiO 3 Systems," 1999.

[11] H. Yang *et al.*, "Lead-Free Piezoelectric Ceramics of (Bi 1/2 Na 1/2)TiO 3-KNbO 3-1/2(Bi 2 O 3 ·Sc 2 O 3) System You may also like Eight-year Simultaneous Monitoring Observations of H 2 O and SiO Masers toward V627 Cas Planar electro-optic deflector using KTa 1x Nb x O 3 for low-power-consumption operation Effect of Ni doping on the electro-optic property in K(Ta 0.6 Nb 0.4)O 3 films," 1998.

[12] T. Wada, K. Toyoike, Y. Imanaka, and Y. Matsuo, "Dielectric and Piezoelectric Properties of (A 0.5 Bi 0.5)TiO 3-ANbO 3 (A = Na, K) Systems morphotropic phase boundary," 2001.

[13] R. A. Cowley, "Structural phase transitions I. Landau theory," *Adv Phys*, vol. 29, no. 1, pp. 1–110, Jan. 1980, doi: 10.1080/00018738000101346.

[14] M. Fischer, A. M. Lahmar Maglione, A. San Miguel, J. P. Itic, A. Polian, and F. Baudelet, "Local disorder studied in SrTi03 at low temperature by EXAFS spectroscopy," 1994.

[15] H. Unoki and T. Sakudo, "Electron Spin Resonance of Fe3+ in SrTiO3 with Special Reference to the 110°K Phase Transition," *J Physical Soc Japan*, vol. 23, no. 3, pp. 546–552, Sep. 1967, doi: 10.1143/JPSJ.23.546.

[16] G. A. Smolenskii and A. I. Agranovskaya, "Dielectric polarization and losses of some complex compounds," *Zhur. Tekh. Fiz.*, vol. 28, 1958.

[17] J. Rodriguez-Carvajal, "PHYSICA Recent advances in magnetic structure determination neutron powder diffraction," 1993.

[18] G. S. Fulcher, "ANALYSIS OF RECENT MEASUREMENTS OF THE VISCOSITY OF GLASSES," *Journal of the American Ceramic Society*, vol. 8, no. 6, pp. 339–355, 1925, doi: https://doi.org/10.1111/j.1151-2916.1925.tb16731.x.

[19] S. Anwar, P. R. Sagdeo, and N. P. Lalla, "Ferroelectric relaxor behavior in hafnium doped barium-titanate ceramic," *Solid State Commun*, vol. 138, no. 7, pp. 331–336, 2006, doi: 10.1016/j.ssc.2006.03.018.

[20] N. W. Thomas, "A new framework for understanding relaxor ferroelectrics," *Journal of Physics and Chemistry of Solids*, vol. 51, no. 12, pp. 1419–1431, 1990, doi: https://doi.org/10.1016/0022-3697(90)90025-B.

[21] K. Uchino and S. Nomura, "Critical exponents of the dielectric constants in diffused-phase-transition crystals," *Ferroelectrics*, vol. 44, no. 1, pp. 55–61, Apr. 1982, doi: 10.1080/00150198208260644.

[22] G. A. Smolenskii and A. I. Agranovskaya, "Dielectric polarization and losses of some complex compounds," *Zhur. Tekh. Fiz.*, vol. 28, 1958.

[23] H. VOGEL, "Das Temperaturabhangigkeitsgesetz der Viskositat von Flussigkeiten," *Phys. Z.*, vol. 22, pp. 645–646, 1921, [Online]. Available: https://cir.nii.ac.jp/crid/1573668924039979008

[24] B. E. Vugmeister and M. D. Glinchuk, "Dipole glass and ferroelectricity in random-site electric dipole systems," *Rev Mod Phys*, vol. 62, no. 4, pp. 993–1026, Oct. 1990, doi: 10.1103/RevModPhys.62.993.

[25] C. Jiang *et al.*, "Grain oriented Na0.5Bi0.5TiO3-BaTiO3 ceramics with giant strain response derived from single-crystalline Na0.5Bi0.5TiO3-BaTiO3 templates," *J Eur Ceram Soc*, vol. 36, no. 6, pp. 1377–1383, 2016, doi: https://doi.org/10.1016/j.jeurceramsoc.2015.12.025.

[26] G. Xue *et al.*, "The dielectric and ferroelectric properties of (Ba0.5Sr0.5)TiO3-doped (Bi0.5Na0.5)TiO3 lead-free ceramics," *J Adv Dielectr*, vol. 07, no. 04, p. 1750028, Aug. 2017, doi: 10.1142/S2010135X1750028X.

[27] R. Selvamani, G. Singh, V. Sathe, V. S. Tiwari, and P. K. Gupta, "Dielectric, structural and Raman studies on (Na0.5Bi0.5TiO3)(1 − x)(BiCrO3)x ceramic," *Journal of Physics: Condensed Matter*, vol. 23, no. 5, p. 55901, Jan. 2011, doi: 10.1088/0953-8984/23/5/055901.

[28] A. Tiwari and K. P. P. Rajeev, "Electrical transport in LaNiO 3−δ (0 δ 0.14)," 1999.

CHAPTER 5

FORMATION OF URCHIN-LIKE NICKEL NANOPARTICLE@COBALT FERRITE CORE@SHELL NANOSTRUCTURE TO IMPLEMENT EXCHANGE INTERACTION AND ENHANCE ELECTROMAGNETIC WAVE ABSORPTION

In this chapter, we have prepared a core-shell structure with Nickel nanoparticle as core and Cobalt Ferrite as shell as a soft/hard magnetic nanostructure to tune the magnetic properties and enhance microwave properties as well.

5.1 Preamble

Nanoscale magnetism has stimulated considerable attention due to its usefulness in mapping the scaling limits of magnetic information storage technology, understanding spin dependent transport phenomena and tuning magnetic properties[1]–[5]. Recent advancements in the production of nearly monodisperse magnetic nanoparticles from metallic Fe, Co, and Ni, to iron oxides, TFe_2O_4 (T → transition metals) and Fe and Co intermetallic compounds, provides a variety of systems suitable for nanomagnetic studies[6]–[13]. It is well known that conductors of dimensions on the order of the skin depth are lossy at microwave frequencies due to eddy current effects [14]–[17]. An assembly of monodisperse magnetic nanoparticles with regulated interparticle spacing will allow in-depth investigations on magnetization, anisotropy, as well as magnetization reversal processes and interparticle interactions of the particles with varying sizes and surface properties. An intriguing magnetic nanoparticle system consists of core-shell structured nanoparticles having a magnetic core covered with a layer of a nonmagnetic, antiferromagnetic, or ferro/ferri-magnetic shell[7], [18]–[30]. A nonmagnetic coating is used routinely for magnetic core stabilization and surface functionalization in fields related to biomedical applications. A ferromagnetic core coated with an antiferromagnetic material generates exchange bias (a shift of the hysteresis loop along the field axis) and enhanced thermal stability of the core. Compared with these two different types of core-shell systems, a bimagnetic core-shell, where both core and shell are highly magnetic (ferro- or ferri-magnetic) is less explored yet more interesting owing to its potential in electromagnetic and permanent magnetic applications[25]. In such a system, the close proximity of the core and the shell results in effective exchange coupling and, therefore, cooperative magnetic switching, thus facilitating the fabrication of nanostructured magnetic materials with tuneable characteristics[7], [27], [31]–[33].

In this study, metallic nickel (Ni) nanoparticle, a soft magnetic material, is synthesized and will serve as the core in the core-shell system. Then it is coated with $CoFe_2O_4$ (CFO), a hard magnetic material which serves as the shell. As a result of exchange coupling at the interface between nickel and cobalt, the magnetic properties of Ni@CFO core-shell nanostructures are tuned to achieve increased remanence and saturation magnetisation, hence enhancing its microwave absorption capabilities. Moreover, a composite absorber thickness-dependent investigation on core-shell nanostructures reveals that exchange coupling between soft and hard magnetic material is a promising technique for enhancing electromagnetic interference (EMI) shielding.

5.2 Experimental

5.2.1 Sample Preparation

5.2.1.1 Sample Preparation of Nickel Nanoparticles

The hexahydrate form of nickel chloride ($NiCl_3$, $6H_2O$) is used to synthesize nickel nanoparticles. 2.665 g of $NiCl_3$, $6H_2O$ is added to 25 ml of the solvent, Ethylene glycol (EG). This solution is stirred with a magnetic stirrer until a clear solution is obtained. The pH of this solution is then adjusted to 9 with controlled addition of sodium hydroxide (NaOH) solution. This solution is then heated to 80 °C. A separate solution is next prepared by dissolving 6 ml of hydrazine hydrate in 24 ml of distilled water. Next, this solution is added drop-by-drop to the previous solution, which is kept at 80 °C. Subsequently, the color of this solution turns from green to black and then to grey. Using a magnetic stirrer cum heater, the mixture is further stirred for an hour while maintaining a temperature of roughly 80 °C. Finally, the solution becomes transparent due to the precipitation of black nickel (Ni) particles covering the magnetic bead. After cooling it to room temperature, the particles are washed several times with Ethanol and dried to collect the as-prepared Ni nanoparticles, which constitute the core.

5.2.1.2 Sample Preparation of CFO Nanoparticles

Cobalt chloride hexahydrate ($CoCl_2$, $6H_2O$) and Ferric chloride hexahydrate ($FeCl_3$, $6H_2O$) is used to prepare cobalt ferrite ($CoFe_2O_4$, CFO) nanoparticles. 0.360g $CoCl_2$, $6H_2O$ and 0.819g $FeCl_3$, $6H_2O$ is added to 20 ml of Ethylene glycol (EG) which is the solvent used for the synthesis. This solution is mixed using magnetic stirrer until a clear solution is obtained. Another solution is separately prepared by dissolving 0.53 g urea in 10 ml of distilled water. The previously prepared solution is now added in this solution and stirred until clear solution is acquired. Next, 3 ml of oleylamine is added drop-by-drop to it and stirred for a certain amount of time. The amount of oleylamine determines the size of the prepared nanoparticles. Increasing the amount of oleylamine results in the decrease of the size of the nanoparticles. After this, the mixture is transferred to a teflon flask which is then enclosed inside a stainless-steel autoclave. This autoclave is transferred into a hot air oven which is then kept at a temperature of 200 °C at kept for 20 hours. After 20 hours, the autoclave is cooled down to room temperature, and the particles are found precipitated at the bottom of the teflon flask. The precipitation is collected after washing several times using Ethanol and finally dried to collect the as-prepared $CoFe_2O_4$ nanoparticles.

5.2.1.3 Sample Preparation of Ni@CFO Core-Shell Nanostructures

To create Ni@$CoFe_2O_4$ (core@shell) core-shell nanostructures, the method for preparing $CoFe_2O_4$ nanoparticles is continued until the mixture is transferred to a teflon flask. Then, 0.05g of produced Ni nanoparticles are added to the liquid in the teflon flask, and it is well stirred using a sonicator. Now, the teflon flask is placed in an autoclave made of stainless steel, and the process continues as before. The particles precipitated at the bottom of the teflon flask are rinsed many times with ethanol and subsequently dried to collect the Ni@$CoFe_2O_4$ core-shell nanostructures.

5.2.2 Characterization

In a Rigaku SmartLab equipped with Cu-K_α radiation, X-ray diffraction, commonly known as XRD, is used to identify the phase of as-prepared materials. To determine the size and morphology of the samples, an FEI QUANTA FEG 250 field-emission scanning electron microscope (FESEM) with a voltage range of 0.2 to 30 kV and a FEG transmission electron microscope (TEM) with a voltage range of 80 to 200 kV are used. To get a clear idea of the core-shell material, high-angle annular dark-field (HAADF) imaging is performed using scanning transmission electron microscopy (STEM). The Energy-dispersive X-ray (EDX) spectrum is collected for elemental analysis of the materials. Using a vibrating sample magnetometer (Lake Shore VSM) at room temperature (about 300 K) and a maximum applied field of 14 kOe, magnetic measurements are obtained.

Using a coaxial cable (Maury Microwaves 8043S6) and an Anritsu MS46122B Vector Network Analyzer (VNA), the microwave properties of samples within the frequency range of 1 GHz to 17 GHz are analyzed. After loading 20 wt.% of powder samples into an epoxy resin matrix and properly moulding this mixture according to the required dimension, the composite samples are made ready for measurement in the microwave frequency spectrum of the VNA. The composites that are produced are hollow cylinders with an inner diameter (d_{in}) of 1.5 mm and an outer diameter (d_{out}) of 3.5 mm. Each composite sample is positioned inside the coaxial airline's 'port one' end. Using a polynomial fit model of the Nicholson-Ross-Weir (NRW) technique, additional analysis of the resulting 2-port scattering (S)-parameters is performed using the transmission line approach [34].

5.3 Results and Discussion

5.3.1 Structure and Morphology

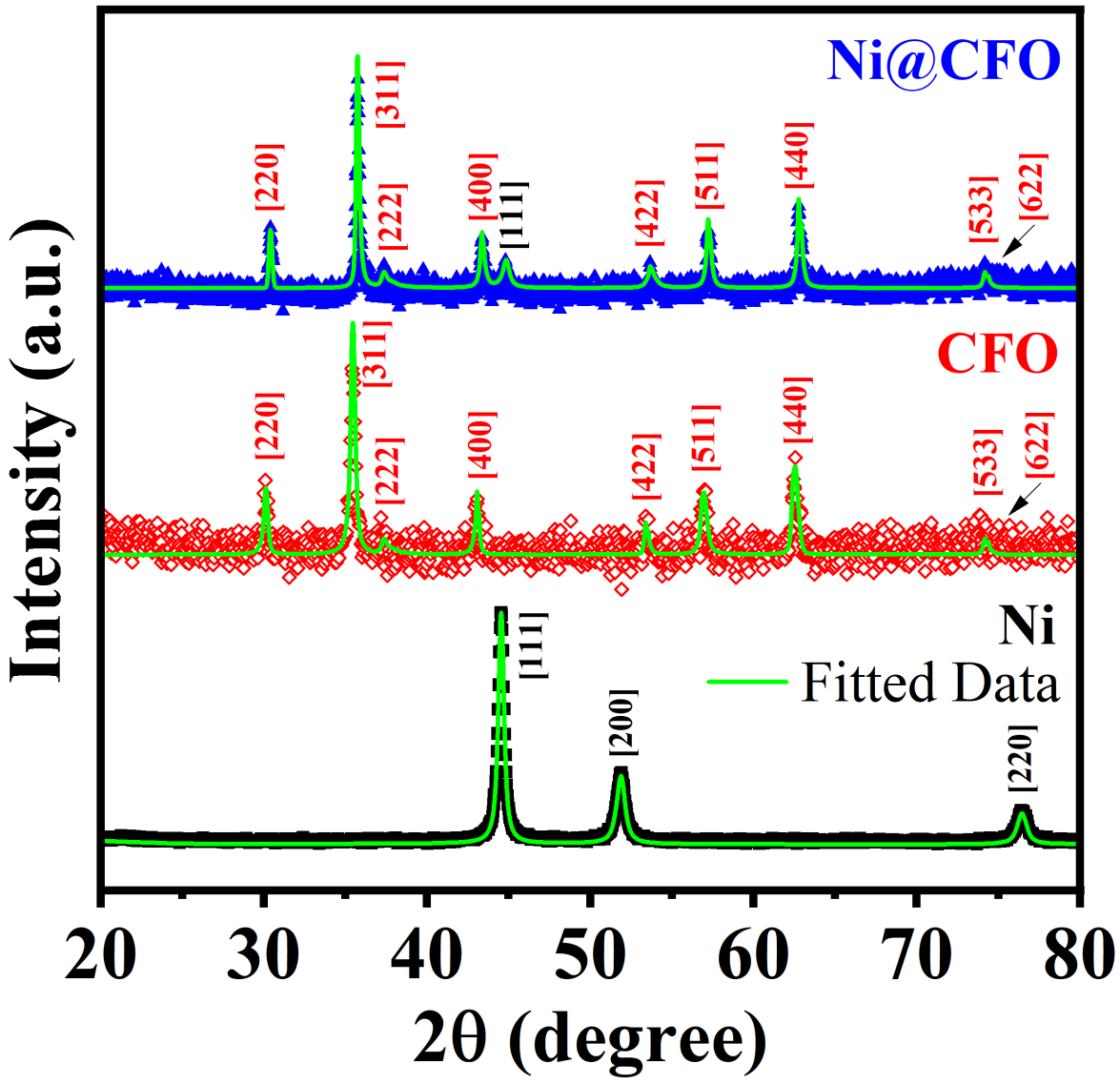

Figure 5.1. X-ray diffraction plots for Ni, CFO, and Ni@CFO at ~ 300 K

The XRD patterns of Ni@CFO CS along Ni and CFO nanoparticles are depicted in Fig. 5.2. The existence of a single-phase spinel face-centered cubic structure at room temperature is demonstrated by each of the patterns, as was previously described in the scientific literature (JCPDS file no. 00-004-0850 for Ni and 01-086-4437 for CFO). The XRD peaks are fitted using the Smart Lab II and the lattice parameters for the maximum intensity peak at the [111] and [311] plane for Ni and CFO respectively is noted in Table 5.1. Average crystallite sizes (D), as well as lattice strains (e), are estimated using the Debye-Scherrer formula for all the samples and are also listed in Table 5.1. At the XRD pattern of Ni@CFO, the highest peak for Ni nanoparticles, i.e., [111] exists but with reduced intensity due to the CFO shell over it.

Table 5.1 Particle diameter, shell thickness, crystallite sizes (D), lattice strain (e), coercivities (H_C), remnant magnetization (M_R), and saturation magnetization (M_S) of Ni, CFO, and Ni@CFO.

Sample Name	Diameter (nm)	Shell Thick-ness (nm)	Crystallite Size (D, nm)	Lattice Strain (e)	H_C (kOe)	M_R (emu/g)	M_S (emu/g)
Ni	81.08 ± 7.39	-	23.80	0.00402	0.17	13.24	48.29
CFO	28.72 ± 2.03	-	29.27	0.00407	1.72	24.68	65.92
Ni@CFO	103.54 ± 11.51	22.46	Ni: 20.87 CFO: 44.70	Ni: 0.00455 CFO: 0.00264	0.67	32.84	80.80

The FESEM micrographs of Ni and CFO nanoparticles and Ni@CFO core-shell nanostructures are displayed in Fig. 5.2(a)–(c). It is evident from the SEM micrographs that the surfaces of the Ni nanoparticles are not smooth and forms an urchin-like structure which get a smooth surfaced spherical shape with the coating of CFO over it. The EDX given at the Fig. 5.2(d), (f), (g) confirms the elemental existence of Co, Fe and O for both CFO nanoparticles and the core-shell Ni@CFO and nickel for the Ni and the Ni@CFO samples. The average sizes of the samples are analyzed by plotting the size distribution curves, as shown in Figs. 5.2(e), (g), (i) and are then tabulated in Table 5.1 with the calculated shell thickness for Ni@CFO.

The TEM micrographs of Ni, CFO and Ni@CFO are depicted in Fig. 5.3(a)-(c). The TEM micrographs provide more prominent views of inner parts of all the samples. For the core-shell Ni@CFO, the HAADF micrograph seen in Figure 5.3(d) reveals dark patches at the

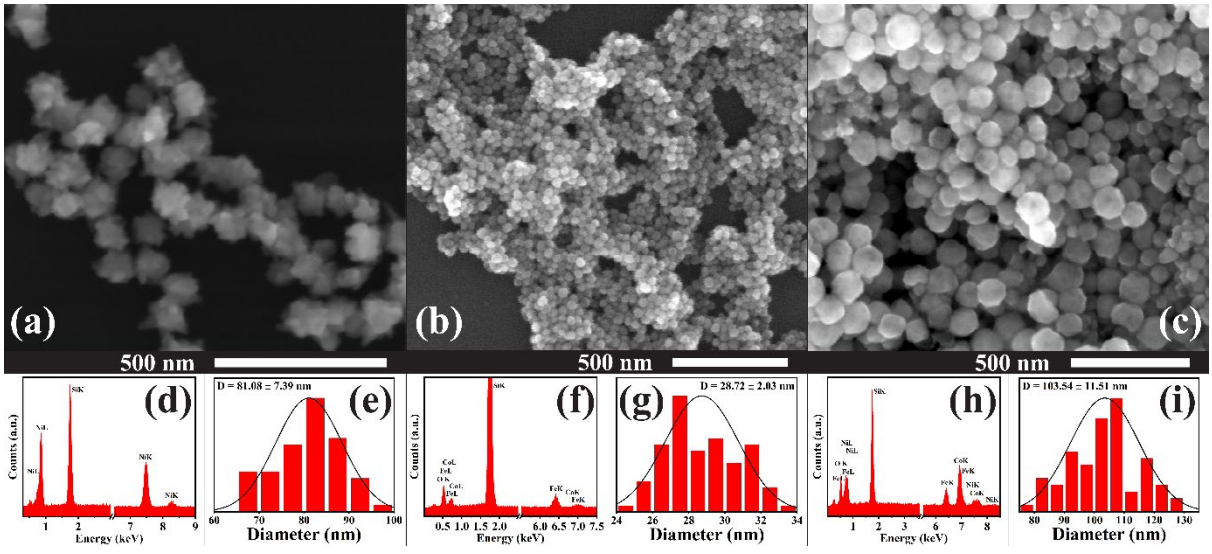

Figure 5.2. FESEM micrographs of (a) Ni, (b) CFO, (c) Ni@CFO, The EDX diagrams of (d) Ni, (f) CFO, and (h) Ni@CFO. The size-distribution plots of (e) Ni, (g) CFO, (i) Ni@CFO

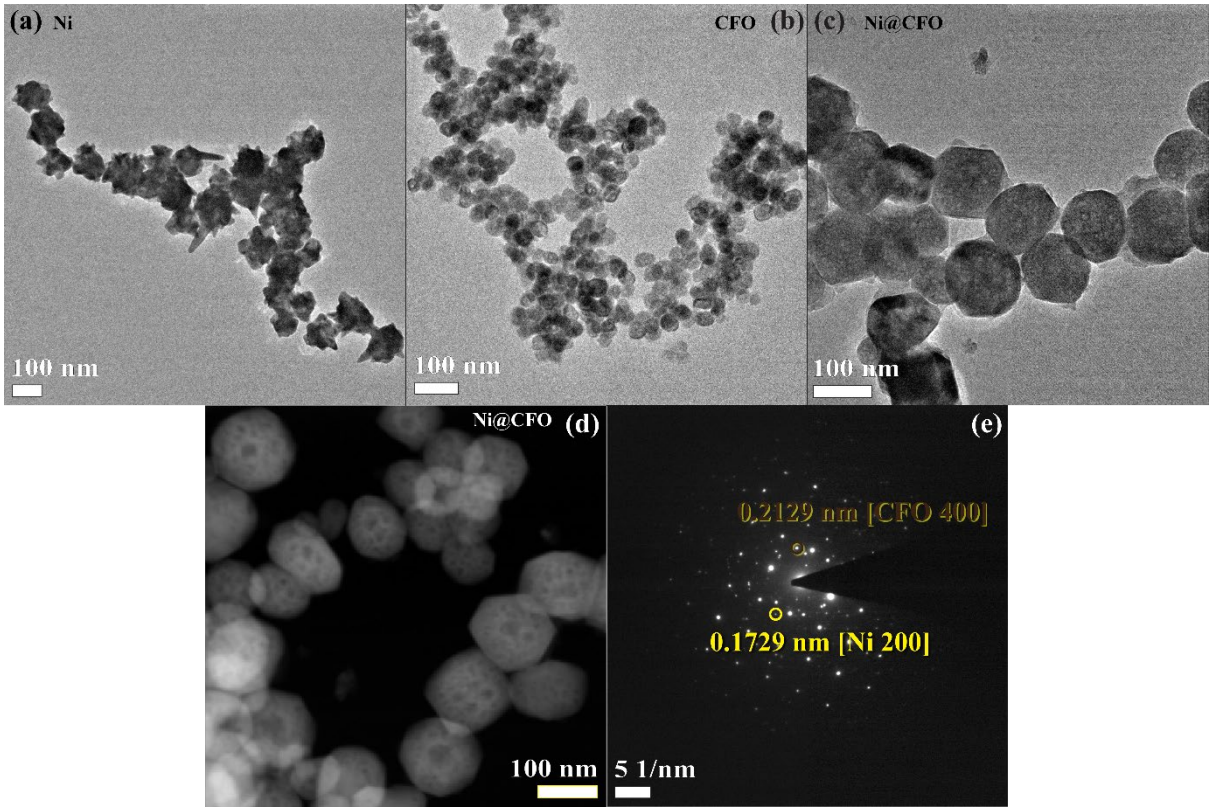

Figure 5.3. TEM micrographs for (a) Ni NPs, (b) CFO NPs, (c) Ni@CFO CS, (d) HAADF micrographs of Ni@CFO CS; (e) SAED pattern of Ni@CFO CS.

centres of the nanostructures, which are essentially the Ni particles at the samples' core. This verifies that the core-shell nanostructures were formed as anticipated. Figure 5.3(e) is an illustration of the SAED pattern of Ni@CFO. This pattern primarily demonstrates the crystalline character of the CS. The distance measured between the two bright spots of the SAED is 0.17 nm and 0.21 nm which matches with the [200] plane of Ni and [400] plane of CFO respectively.

5.3.2 Electric and Magnetic Properties

Microwave absorption is highly connected to the complex permittivity and permeability of an absorber, where the real parts (ε' and μ') represent the storage capacity and the imaginary parts (ε'' and μ'') reflect the loss capacity of electric and magnetic energy, respectively [35], [36]. In Fig. 5.4(a) and 5.4(b), the frequency (f) dependence of real (ε') and imaginary (ε'') parts of relative dielectric constants of CFO and Ni@CFO over the frequency range of 1–17 GHz are displayed. ε' exhibits a resonance peak at around 3 GHz for both samples, which drops with increasing frequency up to roughly 13 GHz and then again rises slightly. However, the ε' for Ni@CFO is larger than that of CFO over the entire frequency range under study, with the largest increase at the resonance peak. The existence of associated surfaces in Ni@CFO

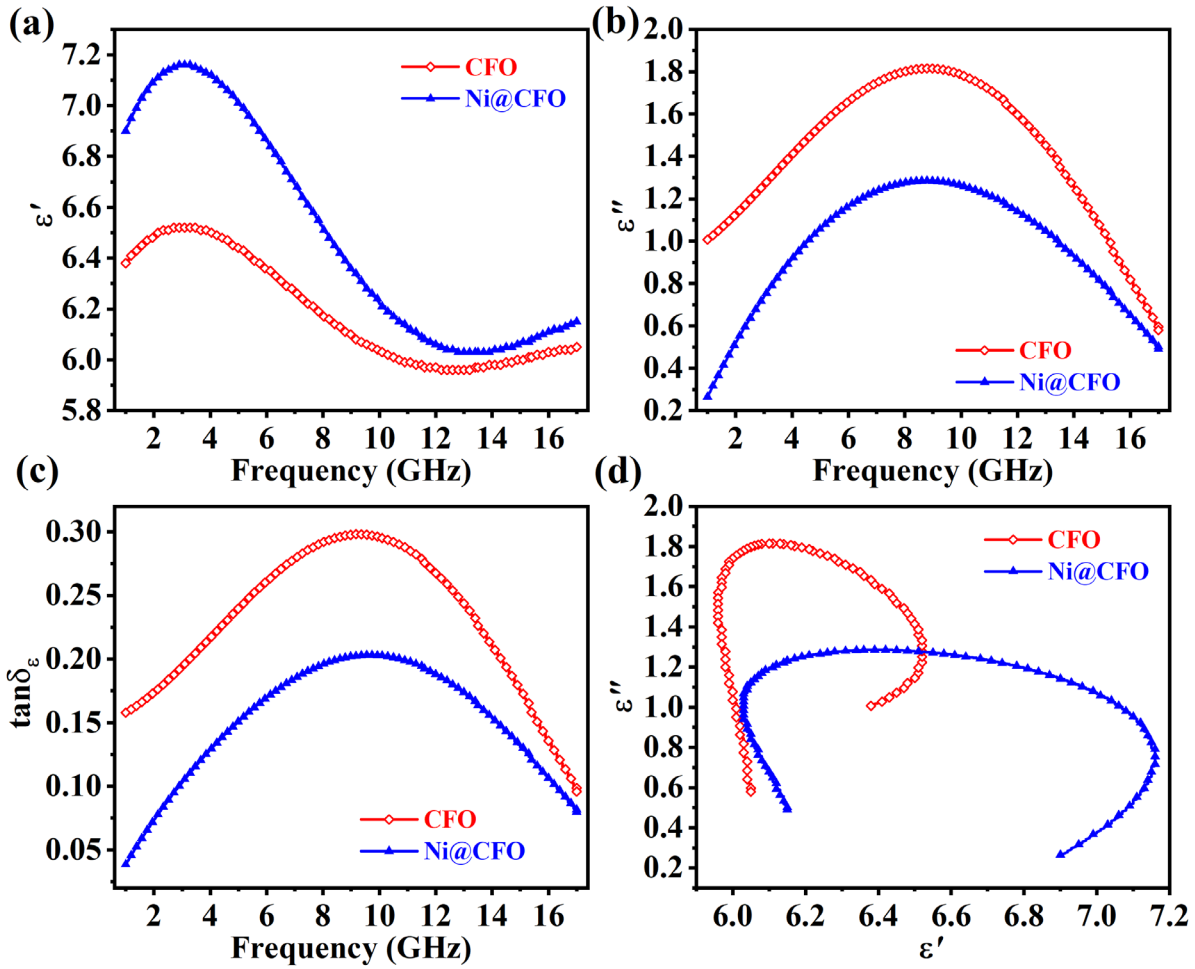

Figure 5.4. Frequency dependence (1–17 GHz) of (a) real (ε′), (b) imaginary (ε″) values of dielectric constant and (c) dielectric loss ($\tan\delta_\varepsilon$) (d) Cole-Cole plots for all samples.

between the Ni core and CFO shell results in an increase in charge carriers due to surface polarization, hence enhancing ε' [37]. Here, the urchin-like structure of Ni nanoparticles is crucial possessing a number of sharp edges. After being coated with CFO, Co^{2+}-Co^{3+} and Fe^{2+}-Fe^{3+} dipoles of CFO material polarize with a high density at the interfaces of these sharp edges. Again, as a result of the uneven structure of the nanoparticles, the total surface accessible for interfacial polarization rises. Therefore, the dipolar resonance of CFO is augmented in Ni@CFO, resulting in a greater ε' close to the resonance frequency. At high frequencies, ε' decays as dielectric relaxation increases with frequency and dipoles lag behind the applied electric field [38]. At the end of the observed frequency range, it tends to rise again to exhibit another resonance peak at higher frequency.

The ε'' is connected to the energy dissipation of accumulated charges, which is directly proportional to the surface-to-volume (STV) ratio of the samples, and is observed to decrease for Ni@CFO core-shell nanostructures since their diameter is roughly six times larger than that of CFO nanoparticles. At frequencies featuring dielectric relaxation, both samples exhibit a

prominent hump. Figure 5.4 demonstrates the frequency dependence of the dielectric loss, $\tan \delta_\mu$. These curves have the same characteristics as ε''. In addition to the reduction of STV ratio, the presence of metallic nickel at the core decreases $\tan \delta_\mu$ compared to that of CFO.

Fig. 5.4(d) depicts Cole-Cole plots, or ε'' versus ε' curves, for CFO and Ni@CFO. According to Eq. 5.1, these curves demonstrate the shape of dielectric polarization based on the Debye theory. In the examined frequency band, the Cole-Cole plots for the samples consist of distorted asymmetric semicircular arcs, suggesting relaxation processes of modified Debye type. These curves also indicate the existence of many types of dipolar relaxations in these heterogeneous systems and the charge carriers responsible for this.

$$(\varepsilon' - \frac{\epsilon_s + \epsilon_\infty}{2})^2 + \epsilon''^2 = (\frac{\epsilon_s + \epsilon_\infty}{2})^2 \quad (5.1)$$

Figure 5.4(d) demonstrates that the deformed semicircular arc of Ni@CFO has a greater number of circles than that of CFO, indicating the presence of a greater number of dipolar relaxations, which implies a bigger dipolar contribution to total dielectric permittivity.

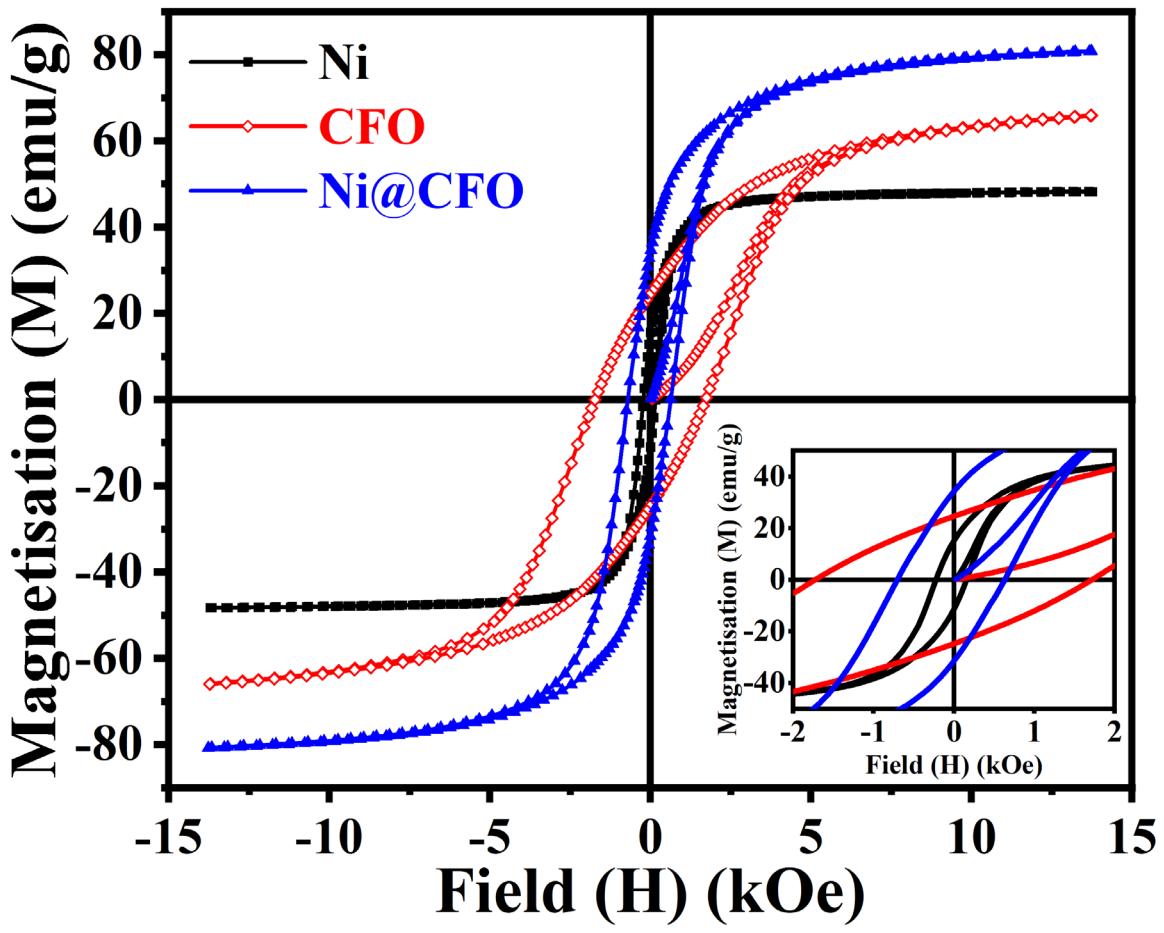

Figure 5.5. M–H plots at 300 K for all the samples.

Figure 5.5 depicts the dependence of the magnetization on the DC magnetic field at 300 K for the Ni@CFO core-shell nanostructure and its component Ni and CFO nanoparticles. The coercivities and remanences of all samples are depicted on an enlarged scale near to the origin in the inset of Figure 5.5. Table 5.1 lists the H_C, M_R, and M_S values derived from these plots. Ni nanoparticles have soft magnetic properties with a coercivity of 0.17 kOe, while CFO nanoparticles exhibit hard magnetic properties with a coercivity of 1.72 kOe. However, at the interfaces of the Ni core and CFO shell in Ni@CFO, the soft magnetic spins of nickel interact with the hard magnetic spins of CFO owing to the near interatomic coexistence. Consequently, despite the large coercivity discrepancies of its component materials, Ni@CFO exhibits a single-phase M-H loop with a coercivity of 0.67 kOe, which is between that of individual Ni and CFO nanoparticles. Again, as a result of the exchange interaction of Ni and CFO spins at the interface of Ni@CFO, the remanence and saturation magnetization of Ni@CFO are greater than those of its component materials.

The real (μ') and imaginary (μ'') components of the relative permeability of CFO nanoparticles and Ni@CFO core-shell are displayed as a function of frequency from 1 to 17 GHz in Fig. 5.6(a) and Fig. 5.6(b). For CFO, μ' shows a modest resonance peak at about 4 GHz, then drops with increasing frequency up to roughly 12 GHz and remains virtually constant thereafter. On the other hand, with Ni@CFO, μ' is shown to decline up to around 6 GHz before remaining essentially constant. The total value of μ' for CFO is discovered to be much greater than that of Ni@CFO. The wavelength for CFO reveals the typical resonance peak of CFO at 8 GHz. In contrast, the plot of μ'' against frequency for Ni@CFO reveals a very weak peak at lower frequency, a lower overall value than that of CFO, and a modest increase at the end of the measured frequency range. According to the Landau–Lifshitz–Gilbert equation [39]–[41], the dynamic magnetic characteristics of ferrimagnets are highly connected to DC magnetic parameters such as magnetic anisotropy and magnetic susceptibility. The high values of μ' and μ'' for CFO are a result of its very strong magnetic anisotropy. At Ni@CFO, the total magnetic anisotropy decreases dramatically due to the presence of Ni, resulting in lower values of μ' and μ'' compared to CFO and a resonance peak shift at lower frequencies that situates outside the measured frequency range for μ'.

In Fig. 5.6(c), the variation of magnetic loss tangent, $\tan\delta_\mu$ with f for CFO nanoparticles and Ni@CFO core-shell nanostructures follow a nearly same trend as the corresponding μ'' vs. f curves. Dynamic magnetic loss is well-known to result primarily from

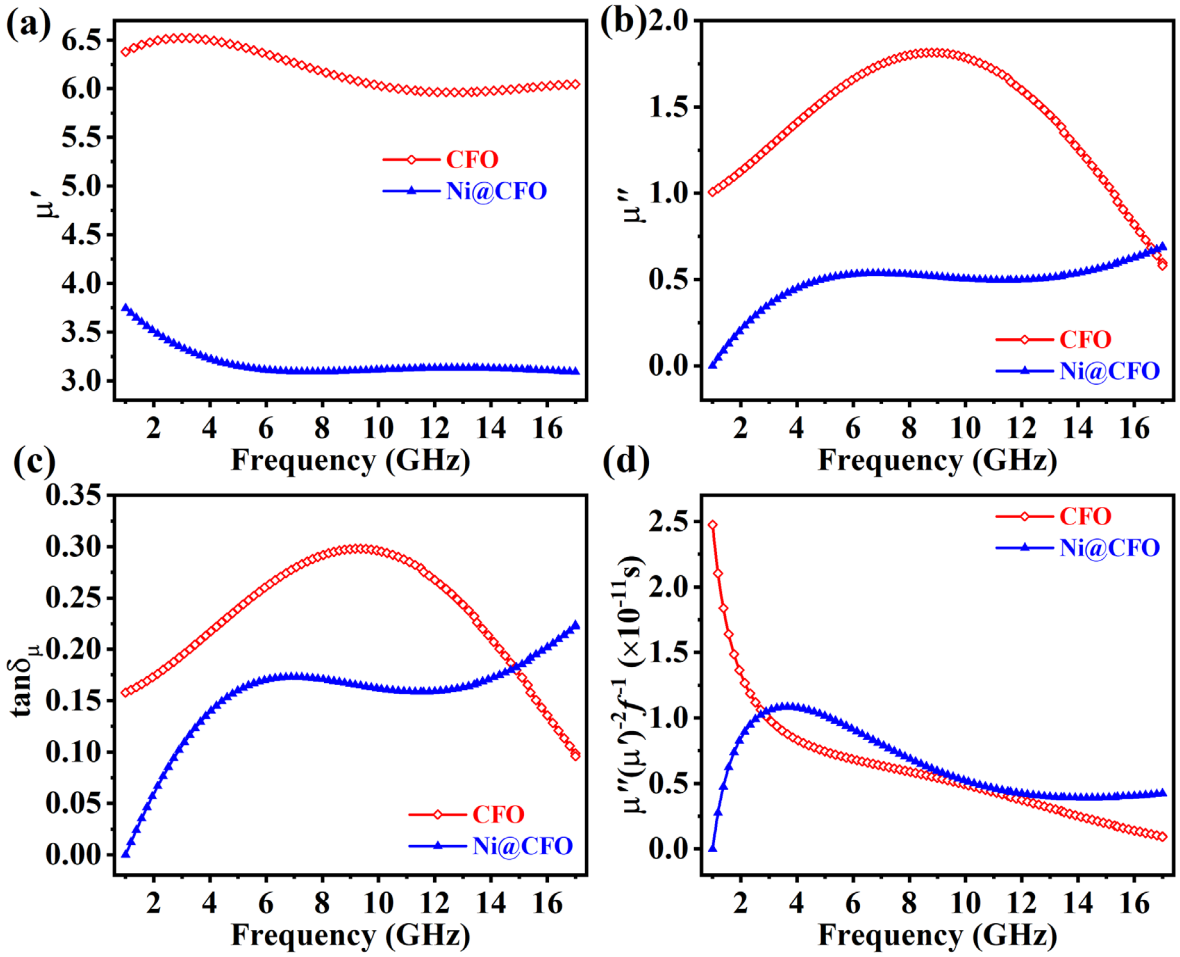

Figure 5.6. Frequency dependence (1–17 GHz) of (a) real (μ′), (b) imaginary (μ″) values of permeability, (c) magnetic loss ($tan\,\delta_\mu$) and(d) $\mu''(\mu')^{-2}f^{-1}$

magnetic hysteresis, domain wall resonance, eddy current effects, natural and exchange resonance. Due to the reduced field intensity, the first two contributions are less effective for samples in the high-frequency range [42]. According to the equation for natural magnetic resonance [43], $2\pi f_r = \frac{4\gamma K}{3\mu_0 M_S}$, where γ is the gyromagnetic ratio (2.8 GHz/kOe for ferrites), the resonance frequency (f_r) for CFO is around 4 GHz. Moreover, the contribution of eddy current loss to μ'' may be written as $\mu''{\sim}2\pi\mu_0\mu'^2(d^2\sigma)$, where d is the sample thickness, σ is the electrical conductivity, and μ_0 is the permeability of free space [44], [45]. If μ'' (or $\tan\delta_\mu$) arises from eddy current loss, according to this equation the $\mu''(\mu')^{-2}f^{-1}$ curves will be constant with frequency [38]. In order to comprehend the potential causes of magnetic loss, the frequency dependency of $\mu''(\mu')^{-2}f^{-1}$ for CFO and Ni@CFO is shown in Figure 5.6(d). A sharp variation in the plot is observed for CFO primarily at lower frequencies up to 4 GHz, after which it maintains a nearly constant non-zero slope, indicating that the magnetic loss in CFO is primarily due to natural resonance and the contribution of eddy current loss is negligible throughout the observed frequency range. In contrast, with Ni@CFO, a minor peak is noticed

at 4 GHz, followed by a fairly constant nature. Consequently, it is obvious from the graph that the contribution to magnetic loss in Ni@CFO originates from the inherent resonance of CFO at lower frequencies, while eddy current loss predominates at higher frequencies. In addition, the existence of the metallic conductor Ni lends credence to this notion.

5.3.3 Microwave absorption properties

The electromagnetic wave absorption qualities of a material are intimately connected with its magnetic and electric properties. Among these features, RL provides information into the material's ability to reduce reflected waves. This may occur through wave absorption, i.e., the transformation of EM waves into other energy, or the transmission of EM waves. Improper impedance matching is required for optimal EM wave propagation. Here, RL is computed using the following equations [44], [45]:

$$Z_{in} = Z_0\left(\frac{\mu_r}{\varepsilon_r}\right)^{1/2} tanh\left[j\left(\frac{2\pi tf}{c}\right)(\mu_r\varepsilon_r)^{\frac{1}{2}}\right] \tag{5.2}$$

$$RL = 20log\left|\frac{(Z_{in}-Z_0)}{(Z_{in}+Z_0)}\right| \tag{5.3}$$

where $\mu_r = \mu' - i\mu''$ and $\varepsilon_r = \varepsilon' - i\varepsilon''$ are relative permeability and permittivity of the material, c, the velocity of light in vacuum, t, the thickness of the composite absorber, Z_0 and Z_{in} are the impedance of free space and input impedance of the absorber, respectively.

A thickness-dependent investigation on EM wave absorption is also conducted for CFO nanoparticles and Ni@CFO core-shell nanostructures in order to build sample-filled epoxy

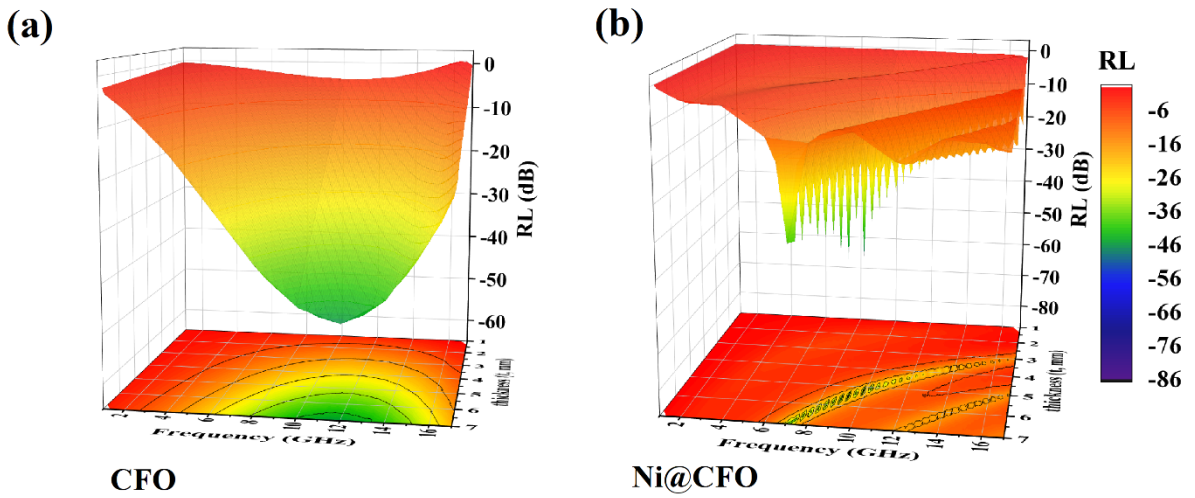

Figure 5.7. 3D plots of reflection loss (RL) of (a) CFO, (b) Ni@CFO.

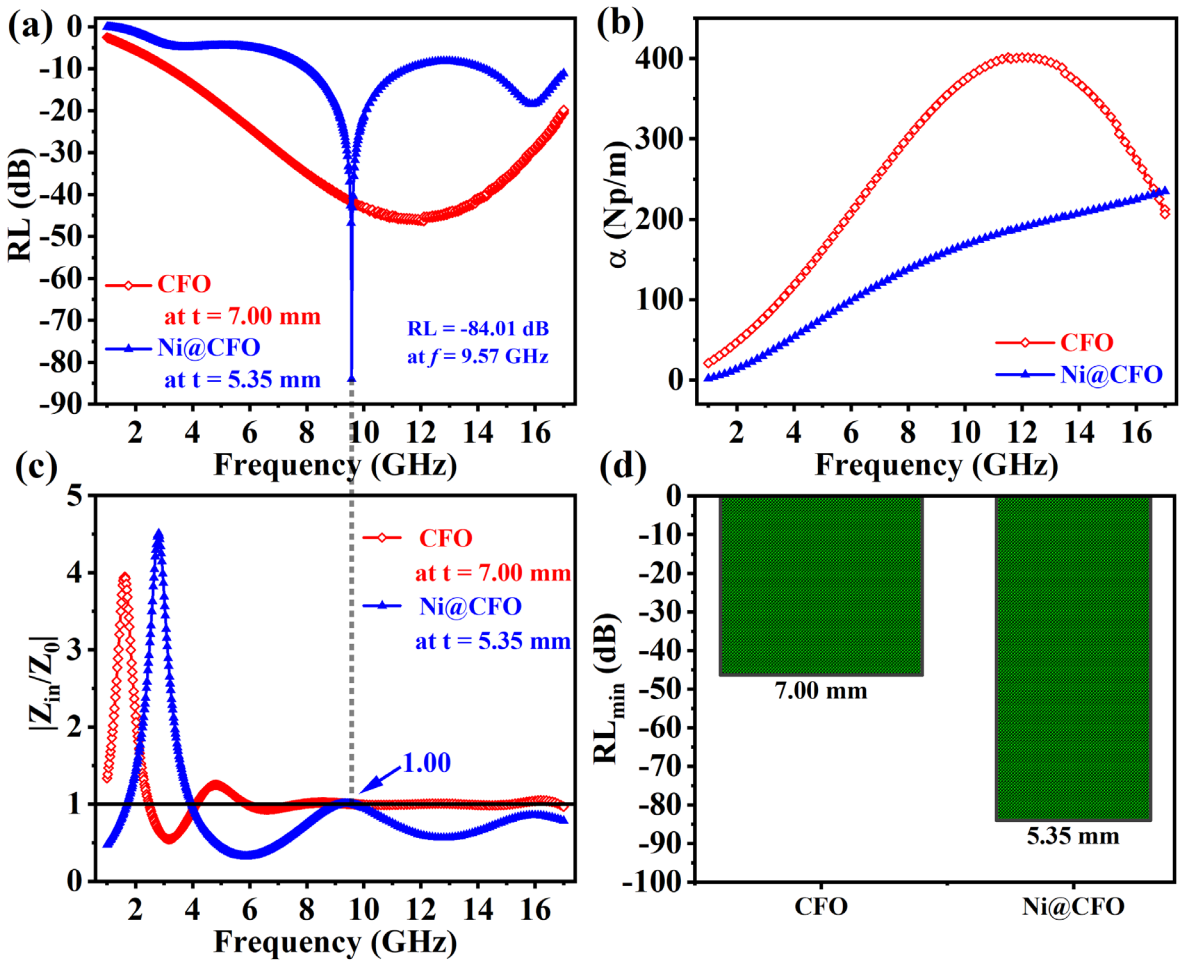

Figure 5.8. (a) Comparative RL versus f plot for the three samples; (b) Frequency dependent attenuation constant (∝), (c) $|Z_{in}/Z_0|$ ratio versus frequency,(d) RL_{min} values at t_m for all samples

composites with the appropriate thickness for practical applications. In Fig. 5.7(a) and (b), frequency-dependent RL is displayed for various thicknesses of 20 wt.% powder sample loaded epoxy resin composites for CFO and Ni@CFO. In Table 5.2, the maximum reflection loss (RL_{max}) determined for all samples for each composite absorber composite absorber thickness (t_m) and frequency (f_m) as well as the total effective bandwidth (BW_{eff}) with $RL < -10$ dB for that t_m in the observed frequency range of 1-17 GHz are listed.

Comparing Ni@CFO core-shell nanostructures with CFO nanoparticles at their respective t_m, Fig. 5.8(a) reveals that the RL_{min} for Ni@CFO core-shell is about -84.01 dB at 9.57 GHz. The BW_{eff} recorded for $RL < -10$ dB in this sample is 6.25 GHz. In Fig. 5.8(c), the $|Z_{in}/Z_0|$ vs. f plots reveal that the optimal impedance matching is reached for Ni@CFO at corresponding f_m = 6.25 GHz, i.e., $|Z_{in}/Z_0| \sim 1.00$. This discovery reveals that the improved EM wave absorption of Ni@CFO is due to its optimal impedance matching, as well as appropriate dielectric and magnetic losses.

The attenuation constant (α) indicates the ability of the material to attenuate EM waves internally and can be calculated by the following equation[44], [45],

$$\alpha = \frac{\sqrt{2}\pi f}{c}\sqrt{(\mu''\varepsilon'' - \mu'\varepsilon') + \sqrt{(\mu''\varepsilon'' - \mu'\varepsilon')^2 + (\mu''\varepsilon' + \mu'\varepsilon'')^2}} \quad (5.4)$$

The α for Ni@CFO core-shell and CFO nanoparticles is calculated and shown in Fig. 5.8.(b). In both samples, α is shown to rise with frequency. The α for CFO grows higher than Ni@CFO, but it drops after 12 GHz and falls below Ni@CFO at the very end of the observed frequency range, while the α for Ni@CFO has a lower overall value, rises almost consistently over the whole frequency range. Fig. 5.8(d) shows a comparison bar plot of the minimal reflection loss of the samples at their respective t_m.

Table 5.2 Maximum reflection loss (RL_{min}), absorber thickness (t_m), frequency (f_m), and effective bandwidth (BW_{eff})

Sample Name	$\boldsymbol{RL_{min}}$**(dB)**	$\boldsymbol{t_m}$**(mm)**	$\boldsymbol{f_m}$**(GHz)**	$\boldsymbol{BW_{eff}}$**(GHz)**
CFO	-46.37	7.00	12.1	13.81
Ni@CFO	-84.01	5.35	9.57	6.25

5.3 Conclusion

In conclusion, metallic Ni nanoparticles, a soft magnetic material, are coated with CFO, a hard magnetic material. In order to achieve efficient exchange coupling, the core-shell structure consisting of Ni as the core and CFO as the shell is effectively synthesized. The single-phase character of the hysteresis loop revealed by the Ni@CFO core-shell structure, together with increased saturation and residual magnetization, and a coercivity with value in between those of Ni and CFO, supports the establishment of exchange coupling between the magnetic spins of Ni and CFO. The thickness-dependent electromagnetic wave absorption properties of Ni@CFO exchange coupled core-shell nanostructures and its shell material as a CFO nanoparticle are examined in depth. As a consequence of the urchin-like structure of Ni, the ε' is enhanced. The ε'', which is directly related to the $\tan\delta_\mu$ and corresponds to the dissipation of accumulated charges, is shown to decrease owing to the significantly greater diameter of Ni@CFO core-shell structures, resulting in a reduced surface-to-volume ratio. The Cole-Cole plot reveals a higher number of dipolar relaxations, indicating a stronger dipolar contribution to total dielectric permittivity. The high values of both the real (μ') and imaginary

(μ'') components of magnetic permeability seen in CFO are the consequence of its very strong magnetic anisotropy. At Ni@CFO, the overall magnetic anisotropy reduces significantly due to the presence of Ni, resulting in poorer magnetic property values compared to CFO. It is assumed that eddy current loss mostly contributes to the magnetic tangent loss. Ni@CFO core-shell is discovered to have a minimal reflection loss (RL) of -84.01 dB at 9.57 GHz. In this sample, the overall effective bandwidth measured for $RL < -10$ dB is 6.25 GHz. The $|Z_{in}/Z_0|$ vs. f plots reveal that the optimal impedance matching is reached for Ni@CFO at corresponding f_m = 6.25 GHz, i.e., $|Z_{in}/Z_0| \sim 1.00$. This reveals that the improved EM wave absorption of Ni@CFO is due to its optimal impedance matching, as well as appropriate dielectric and magnetic losses. The outstanding EM wave absorption of Ni@CFO makes it a mass-efficient and economically beneficial EMA material for a number of high-frequency applications.

References

[1] M. K. Singh, W. Prellier, M. P. Singh, R. S. Katiyar, and J. F. Scott, "Spin-glass transition in single-crystal BiFe O3," *Phys Rev B Condens Matter Mater Phys*, vol. 77, no. 14, Apr. 2008, doi: 10.1103/PhysRevB.77.144403.

[2] J. F. Scott, "Data storage: Multiferroic memories," *Nat Mater*, vol. 6, no. 4, pp. 256–257, Mar. 2007, doi: 10.1038/nmat1868.

[3] I. Žutić, J. Fabian, and S. Das Sarma, "Spintronics: Fundamentals and applications," *Rev Mod Phys*, vol. 76, no. 2, pp. 323–410, Apr. 2004, doi: 10.1103/RevModPhys.76.323.

[4] W. Kleemann, "Magnetoelectric spintronics," in *Journal of Applied Physics*, Jul. 2013. doi: 10.1063/1.4811823.

[5] A. Hoffmann and S. D. Bader, "Opportunities at the Frontiers of Spintronics," *Phys Rev Appl*, vol. 4, no. 4, p. 047001, Oct. 2015, doi: 10.1103/PhysRevApplied.4.047001.

[6] A. J. Cox, J. G. Louderback, S. E. Apsel, and L. A. Bloomfield, "Magnetism in 4d-transition metal clusters," *Phys Rev B*, vol. 49, no. 17, pp. 12295–12298, May 1994, doi: 10.1103/PhysRevB.49.12295.

[7] C. Feng, X. Liu, S. W. Or, and S. L. Ho, "Exchange coupling and microwave absorption in core/shell-structured hard/soft ferrite-based CoFe2O4/NiFe2O4 nanocapsules," *AIP Adv*, vol. 7, no. 5, May 2017, doi: 10.1063/1.4972805.

[8] S. I. Ohkoshi and H. Tokoro, "Hard magnetic ferrite: ε-Fe2O3," *Bull Chem Soc Jpn*, vol. 86, no. 8, pp. 897–907, 2013, doi: 10.1246/bcsj.20130120.

[9] S. I. Ohkoshi, S. Kuroki, S. Sakurai, K. Matsumoto, K. Sato, and S. Sasaki, "A millimeter-wave absorber based on gallium-substituted ε-iron oxide nanomagnets," *Angewandte Chemie - International Edition*, vol. 46, no. 44, pp. 8392–8395, 2007, doi: 10.1002/anie.200703010.

[10] D. T. Zimmerman, J. D. Cardellino, K. T. Cravener, K. R. Feather, N. M. Miskovsky, and G. J. Weisel, "Microwave absorption in percolating metal-insulator composites," *Appl Phys Lett*, vol. 93, no. 21, p. 214103, Nov. 2008, doi: 10.1063/1.3036900.

[11] M. I. Hussein *et al.*, "Microwave Absorbing properties of metal functionalized-CNT-polymer composite for stealth applications," *Sci Rep*, vol. 10, no. 1, p. 16013, 2020, doi: 10.1038/s41598-020-72928-1.

[12] K. Ates, T. Z. Kocaer, S. Ozen, and N. U. Kockal, "Electromagnetic interference shielding effectiveness and microwave absorption performance of plaster mortars containing metal waste chips in X-band frequency range," *Journal of Microwave Power and Electromagnetic Energy*, vol. 57, no. 3, pp. 230–244, Jul. 2023, doi: 10.1080/08327823.2023.2235553.

[13] M. Haddadi. M, B. Das, J. Jeong, S. Kim, and D.-S. Kim, "Near-maximum microwave absorption in a thin metal film at the pseudo-free-standing limit," *Sci Rep*, vol. 12, no. 1, p. 18386, 2022, doi: 10.1038/s41598-022-23119-7.

[14] J. Luo, C. Hunyar, L. Feher, G. Link, M. Thumm, and P. Pozzo, "Theory and experiments of electromagnetic loss mechanism for microwave heating of powdered metals," *Appl Phys Lett*, vol. 84, no. 25, pp. 5076–5078, Jun. 2004, doi: 10.1063/1.1713032.

[15] J. Ma *et al.*, "Systematic study of microwave absorption, heating, and microstructure evolution of porous copper powder metal compacts," *J Appl Phys*, vol. 101, no. 7, p. 074906, Apr. 2007, doi: 10.1063/1.2713087.

[16] K. I. Rybakov, V. E. Semenov, S. V Egorov, A. G. Eremeev, I. V Plotnikov, and Yu. V Bykov, "Microwave heating of conductive powder materials," *J Appl Phys*, vol. 99, no. 2, p. 023506, Jan. 2006, doi: 10.1063/1.2159078.

[17] W. Tang, H. Bosman, Y. Y. Lau, and R. M. Gilgenbach, "The Ohmic heating of particulates in a lossless medium," *J Appl Phys*, vol. 97, no. 11, p. 114915, Jun. 2005, doi: 10.1063/1.1922085.

[18] D. Maity, K. Karmakar, and K. Mandal, "N-N type core-shell heterojunction engineering with MoO3 over ZnO nanorod cores for enhanced solar energy harvesting application in a photoelectrochemical cell," *J Alloys Compd*, vol. 791, pp. 739–746, 2019, doi: https://doi.org/10.1016/j.jallcom.2019.03.292.

[19] J. Hongxia, L. Qiaoling, Y. Yun, G. Zhiwu, and Y. Xiaofeng, "Preparation and microwave adsorption properties of core-shell structured barium titanate/polyaniline composite," *J Magn Magn Mater*, vol. 332, pp. 10–14, Apr. 2013, doi: 10.1016/j.jmmm.2012.11.010.

[20] H. Zeng, S. Sun, J. Li, Z. L. Wang, and J. P. Liu, "Tailoring magnetic properties of core⁄shell nanoparticles," *Appl Phys Lett*, vol. 85, no. 5, pp. 792–794, Jul. 2004, doi: 10.1063/1.1776632.

[21] J. Liu, J. Xu, Z. Liu, X. Liu, and R. Che, "Hierarchical magnetic core-shell nanostructures for microwave absorption: Synthesis, microstructure and property studies," *Sci China Chem*, vol. 57, no. 1, pp. 3–12, 2014, doi: 10.1007/s11426-013-5010-x.

[22] Y. Huang *et al.*, "Preparation and microwave absorption properties of the hollow ZnFe2O4@C composites with core-shell structure," *J Magn Magn Mater*, vol. 502, May 2020, doi: 10.1016/j.jmmm.2020.166543.

[23] W.-I. Liang *et al.*, "In Situ Study of Fe3Pt–Fe2O3 Core–Shell Nanoparticle Formation," *J Am Chem Soc*, vol. 137, no. 47, pp. 14850–14853, Dec. 2015, doi: 10.1021/jacs.5b10076.

[24] G. V. Duong, R. S. Turtelli, and R. Groessinger, "Magnetoelectric properties of CoFe2O4-BaTiO3 core-shell structure composite studied by a magnetic pulse method," *J Magn Magn Mater*, vol. 322, no. 9–12, pp. 1581–1584, May 2010, doi: 10.1016/j.jmmm.2009.09.022.

[25] H. Zeng, J. Li, Z. L. Wang, J. P. Liu, and S. Sun, "Bimagnetic Core/Shell FePt/Fe3O4 Nanoparticles," *Nano Lett*, vol. 4, no. 1, pp. 187–190, Jan. 2004, doi: 10.1021/nl035004r.

[26] S. Chaturvedi, R. Das, P. Poddar, and S. Kulkarni, "Tunable band gap and coercivity of bismuth ferrite-polyaniline core-shell nanoparticles: the role of shell thickness," 2015, doi: 10.1039/c5ra00933b.

[27] S. M. Yusuf, P. K. Manna, M. M. Shirolkar, S. K. Kulkarni, R. Tewari, and G. K. Dey, "A study of exchange bias in BiFeO3 core/NiFe2O 4 shell nanoparticles," in *Journal of Applied Physics*, May 2013. doi: 10.1063/1.4803549.

[28] R. Ghosh Chaudhuri and S. Paria, "Core/shell nanoparticles: Classes, properties, synthesis mechanisms, characterization, and applications," *Chemical Reviews*, vol. 112, no. 4. pp. 2373–2433, Apr. 11, 2012. doi: 10.1021/cr100449n.

[29] J. Liu *et al.*, "Microwave Absorption Enhancement of Multifunctional Composite Microspheres with Spinel Fe3O4 Cores and Anatase TiO2 Shells," *Small*, vol. 8, no. 8, pp. 1214–1221, Apr. 2012, doi: https://doi.org/10.1002/smll.201102245.

[30] M. M. Shirolkar, R. Das, T. Maity, P. Poddar, and S. K. Kulkarni, "Observation of Enhanced Dielectric Coupling and Room-Temperature Ferromagnetism in Chemically Synthesized BiFeO 3 @ SiO 2 Core−Shell Particles," 2012, doi: 10.1021/jp3025683.

[31] A. Gorai, "Study of Exchange Coupled Core-Shell Nanostructures."

[32] D. H. Kim, T. C. Kim, S. H. Lee, S. H. Han, K. S. Han, and C. A. Ross, "Self-assembled growth of Sr(Ti,Fe)O3-CoFe2O4 magnetic nanocomposite thin films," *J Appl Phys*, vol. 121, no. 16, Apr. 2017, doi: 10.1063/1.4982162.

[33] D. H. Kim *et al.*, " Integration of Self-Assembled Epitaxial BiFeO 3 -CoFe 2 O 4 Multiferroic Nanocomposites on Silicon Substrates ," *Adv Funct Mater*, vol. 24, no. 37, pp. 5889–5896, Oct. 2014, doi: 10.1002/adfm.201401458.

[34] A. N. Vicente, G. M. Dip, and C. Junqueira, "The step by step development of NRW method," in *2011 SBMO/IEEE MTT-S International Microwave and Optoelectronics Conference (IMOC 2011)*, 2011, pp. 738–742. doi: 10.1109/IMOC.2011.6169318.

[35] S. F. Soares, T. Fernandes, A. L. Daniel-da-Silva, and T. Trindade, "The controlled synthesis of complex hollow nanostructures and prospective applications†," *Proceedings of the Royal Society A: Mathematical, Physical and Engineering Sciences*, vol. 475, no. 2224, p. 20180677, Apr. 2019, doi: 10.1098/rspa.2018.0677.

[36] M. Alam, S. Talukdar, and K. Mandal, "Multiferroic properties of bilayered BiFeO3/CoFe2O4 nano-hollowspheres," *Mater Lett*, vol. 210, pp. 80–83, 2018, doi: https://doi.org/10.1016/j.matlet.2017.08.097.

[37] M. Qin, L. Zhang, X. Zhao, and H. Wu, "Defect Induced Polarization Loss in Multi-Shelled Spinel Hollow Spheres for Electromagnetic Wave Absorption Application," *Advanced Science*, vol. 8, no. 8, p. 2004640, Apr. 2021, doi: https://doi.org/10.1002/advs.202004640.

[38] Y. Zhang, H. Bin Zhang, X. Wu, Z. Deng, E. Zhou, and Z. Z. Yu, "Nanolayered Cobalt@Carbon Hybrids Derived from Metal-Organic Frameworks for Microwave Absorption," *ACS Appl Nano Mater*, vol. 2, no. 4, pp. 2325–2335, Apr. 2019, doi: 10.1021/acsanm.9b00226.

[39] D. Mandal, A. Gorai, and K. Mandal, "Electromagnetic wave trapping in NiFe2O4 nano-hollow spheres: An efficient microwave absorber," *J Magn Magn Mater*, vol. 485, pp. 43–48, Sep. 2019, doi: 10.1016/j.jmmm.2019.04.033.

[40] T. L. Gilbert, "A phenomenological theory of damping in ferromagnetic materials," *IEEE Trans Magn*, vol. 40, no. 6, pp. 3443–3449, 2004, doi: 10.1109/TMAG.2004.836740.

[41] M. Mehdipour and H. Shokrollahi, "Comparison of microwave absorption properties of SrFe12O19, SrFe12O19/NiFe2O4, and NiFe2O4 particles," *J Appl Phys*, vol. 114, no. 4, p. 043906, Jul. 2013, doi: 10.1063/1.4816089.

[42] P. Liu, Y. Huang, J. Yan, and Y. Zhao, "Magnetic graphene@PANI@porous TiO2 ternary composites for high-performance electromagnetic wave absorption," *J Mater Chem C Mater*, vol. 4, no. 26, pp. 6362–6370, 2016, doi: 10.1039/c6tc01718e.

[43] X. G. Liu, D. Y. Geng, H. Meng, P. J. Shang, and Z. D. Zhang, "Microwave-absorption properties of ZnO-coated iron nanocapsules," *Appl Phys Lett*, vol. 92, no. 17, p. 173117, Apr. 2008, doi: 10.1063/1.2919098.

[44] D. M. Pozar and J. Wiley, "Microwave Engineering Third Edition W WILEY."

[45] S. Hait, A. Gorai, and K. Mandal, "Origin of different microwave absorption in multiferroic Bismuth and Gallium Ferrite," *Mater Lett*, vol. 331, Jan. 2023, doi: 10.1016/j.matlet.2022.133520.

CHAPTER 6

CONCLUSION AND FUTURE STUDY OBJECTIVES

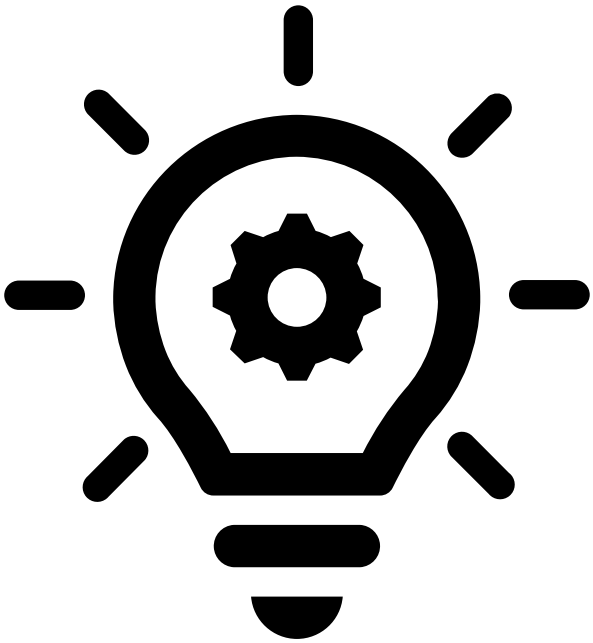

This chapter concludes the outcomes of this thesis and discusses the scopes of future studies.

6.1 Epilogue

The electromagnetic characteristics and microwave absorption capabilities at a frequency range from 1 to 17 GHz have been investigated in depth in this dissertation. Coating with a non-magnetic (Silica, SiO_2) and a magnetic ($CoFe_2O_4$, CFO) layer over manganese ferrite ($MnFe_2O_4$, MnFO) nanohollowspheres has been compared based on the conclusion of a previous study that hollowsphere morphology exhibits increased microwave absorption due to higher scattering, internal reflections, and lower density. In order to optimize the coating thickness, three different coating thicknesses of dielectric SiO_2 and magnetic $CoFe_2O_4$ have been successfully coated over MnFO nanohollowspheres (NHSs), and the electromagnetic wave absorption properties within the commonly used frequency range of 1–17 GHz have been thoroughly examined for both the uncoated and hybridized samples. Bi-layered morphologies with an increased number of associated surfaces and dipoles for electric polarization and an increase in magnetic anisotropy improve dielectric and magnetic loss, which in turn improves electromagnetic (EM) wave attenuation characteristics. The CFO-coated MnFO NHSs have a greater number of connected interfaces and, therefore, spins owing to magnetization, exchange interactions between them, and a synergistic effect generated by many resonance centers. These properties promote dielectric and magnetic loss, which enhances the absorption of electromagnetic waves. The sample with 35 nm coating thickness of CFO (out of 15 nm, 35 nm, and 50 nm), MnFO@CFO-35 exhibits reflection loss (RL) as high as -66.48 dB (shielding > 99.999%) at 6.01 GHz with just 20 wt.% filler concentration in an epoxy matrix and a composite length of 4.46 mm. The MnFO@CFO-35 NHS has a total effective bandwidth of about 1.88 GHz (RL < -10 dB). Sample with 35 nm coating thickness of SiO_2, MnFO/SiO-35 demonstrates RL as high as -61.02 dB at 11.7 GHz with only 20 wt.% filler concentration in an epoxy matrix and a composite length of 4.40 mm. MnFO/SiO-35 NHS has a total effective bandwidth (RL < -10 dB) of about 3.10 GHz. Thus, an optimal layer of CFO on MnFO NHS displays improved EM wave absorption properties, making it a mass-efficient and economically advantageous EMA material for a variety of high-frequency applications.

Bismuth sodium titanate ($Na_{0.5}Bi_{0.5}TiO_3$, or NBT) is a unique Ti-based ferroelectric perovskite oxide that has garnered a great deal of attention because of its strong ferroelectricity, high Curie temperature (T_C ~ 320 ºC), and wide range of attainable dielectric property modifications. In order to reduce the Curie temperature, the material is doped with Sr^{2+} and the structural, dielectric and microwave properties of $Sr_x(Na_{0.5}Bi_{0.5})_{1-x}TiO_3$, SNBTx ($0.25 \leq x \leq 0.75$) prepared using the solid-state reaction technique have been investigated. To implement

magnetic parameters and further enhance the microwave absorption capabilities of SNBT materials, it is coated with magnetic cobalt Ferrite (CFO). Similar studies are performed for cobalt ferrite coated $Sr_{0.5}(Na_{0.5}Bi_{0.5})_{0.5}TiO_3$ or SNBT50 (SNBT50@CFO) composites which exhibits both dielectric and magnetic properties. The Rietveld refinement of the X-ray diffraction pattern at room temperature reveals that the single-phase structure of all SNBT materials with *Pm*3*m* crystal symmetry remained consistent with increasing Sr doping concentration. The composites revealed peaks from both constituent materials without any unexplained peaks, indicating that the constituent materials had been effectively consolidated into a single phase. In order to appreciate the influence of Sr doping on the dielectric characteristics of the materials, the low-frequency dielectric properties of SNBT materials are examined using alternative current impedance spectroscopy across the frequency range of 50 to 1 MHz. The presence of relaxor behavior in these materials has been related to the temperature dependence of the dielectric constant at various frequencies, which produces diffuse peaks. The magnitudes of ε'_m, the maximum value of dielectric constant and T_m, the temperature corresponding to ε'_m are decreased with an increase of Sr^{2+} ion in the materials. There is evidence of relaxational freezing of the Vogel–Fulcher type in the samples. From 1 to 15 GHz, the microwave absorption characteristics of the materials have also been investigated. The aforementioned investigations suggest that SNBT50 is a more promising material for microwave applications than the other two SNBT materials with strong ferroelectricity at room temperature and a respectable permittivity value. The CFO coating greatly enhances the permittivity of SNBT50@CFO composites and introduces permeability. On the other hand, CFO is a good MAM owing to its optimum permittivity and permeability characteristics. Due to interfacial polarization, the synergistic effect between the core and shell, and the introduction of magnetic loss in the sample, the electromagnetic absorption properties of a composite absorber with a length as short as 2.7 mm are improved by up to -20.19 dB with an increased effective absorption bandwidth of 4.56 GHz. It also displays a consistent attenuation that increases continuously over the measured frequency range. Consequently, SNBT50@CFO is a very interesting option for high-frequency multi-disciplinary applications due to its enhanced EM wave absorption capabilities and strong ferroelectricity at ambient temperature.

In the final work, metallic Ni nanoparticles, a soft magnetic material, are coated with CFO, a hard magnetic material. In order to achieve efficient exchange coupling, the core-shell structure consisting of Ni as the core and CFO as the shell is effectively synthesized. The single-phase character of the hysteresis loop revealed by the Ni@CFO core-shell structure,

together with increased saturation and residual magnetization, and a coercivity with value in between those of Ni and CFO, supports the establishment of exchange coupling between the magnetic spins of Ni and CFO. The thickness-dependent electromagnetic wave absorption properties of Ni@CFO exchange coupled core-shell nanostructures and its shell material as a CFO nanoparticle are examined in depth. As a consequence of the urchin-like structure of Ni, the real component of dielectric permittivity is enhanced. The imaginary component of dielectric permittivity, which is directly related to the dielectric tangent loss and corresponds to the dissipation of accumulated charges, is shown to decrease owing to the significantly greater diameter of Ni@CFO core-shell structures, resulting in a reduced surface-to-volume ratio. The Cole-Cole plot reveals a higher number of dipolar relaxations, indicating a stronger dipolar contribution to total dielectric permittivity. The high values of both the real and imaginary components of magnetic permeability seen in CFO are the consequence of its very strong magnetic anisotropy. At Ni@CFO, the overall magnetic anisotropy reduces significantly due to the presence of Ni, resulting in poorer magnetic property values compared to CFO. It is assumed that eddy current loss mostly contributes to the magnetic tangent loss. Ni@CFO core-shell is discovered to have a minimal reflection loss (RL) of -84.01 dB at 9.57 GHz. In this sample, the overall effective bandwidth measured for $RL < -10$ dB is 6.25 GHz. The $|Z_{in}/Z_0|$ vs. f plots reveal that the optimal impedance matching is reached for Ni@CFO at corresponding f_m = 6.25 GHz, i.e., $|Z_{in}/Z_0| \sim 1.00$. This reveals that the improved EM wave absorption of Ni@CFO is due to its optimal impedance matching, as well as appropriate dielectric and magnetic losses.

The maximum RL obtained here is comparable to other promising ferrite-based microwave absorbers as presented in Table 3.3.

6.2. Future Study Objectives

After successful optimisation of both dielectric and magnetic layer over MnFO separately, the best of these results may be merged together in a tri-layer formation. The MnFO coated with optimised CFO layer may again be coated with a thin silica layer to enhance the magnetic and dielectric loss together. In this way, an electromagnetic wave absorbing material can be synthesized with higher reflection loss with high bang width and thinner composite absorber thickness which will facilitate device miniaturization without compromising the absorbing quality.

Again, the sizes of Ni nanoparticles and CFO shells at Ni@CFO exchange-coupled core-shell nanostructures can be varied and optimise for even better and novel microwave absorbing properties. The method of tuning the magnetic properties using exchange coupling may open up a new possibility in the enhancement of magnetic properties itself. A further study in this area is very promising to cater many multidisciplinary applications related to magnetic enhancement such as magnetic hyperthermia, drug delivery, recording media etc.

One of the reasons behind the high reflection loss of these microwave absorbing materials is natural and exchange resonance. These resonances occur at high frequency region. Excited at high frequency region, ferromagnetic materials display the phenomenon known as ferromagnetic resonance (FMR). The FMR is linked to the concepts that a perturbation of the magnetization vectors or magnetic moments / spins would result in a precessional relaxation of the magnetic vector to its new equilibrium position. Therefore, these microwave-absorbent materials may display ferromagnetic resonance when the frequency of the precession equals the frequency of the excitation field, which is typically the case for microwave frequencies. Therefore, these materials may be used in microwave signal processing devices, such as resonators, band-pass / band-stop filters, and phase shifters working between 1 to 70 GHz.

On the other hand, microwave phase shifters are essential for radar applications, communications, and phased array antenna systems. Typical phase shifters typically employ semiconductors, ferroelectrics, and ferrite. A second operating mechanism of ferrite phase shifters is based on the propagation of spin waves in planar ferrites, which is very desirable due to its magnetic tunability across a wide frequency range of 1 to 26 GHz. Ferroelectric phase shifters are characterised by their rapid electric tunability, low power consumption, and exceptionally high loss at frequencies exceeding 5 GHz. By combining ferroelectrics with these EMA materials, it is feasible to create a multiferroic composite which functions as a dual phase adjustable microwave device and operates at frequencies far over 5 GHz.

The EMA materials studied in this dissertation, namely bi-layered MnFO, SNBT50@CFO and Ni@CFO can be further investigated in two-dimensional thin film structures for the purpose of device applications such as band-pass filters, phase shifters, circulators etc.